HIGH FATIGUE RESISTANT ORTHOTROPIC STEEL BRIDGE DECKS

by

Koichi YOKOZEKI

A Dissertation
Presented to Graduate School of
Tokyo City University
in Candidacy of the Degree of
Doctor of Engineering

Tokyo City University
Tokyo, Japan
July 2017

Acknowledgements

I would like to express the deepest appreciation to my advisor Professor Chitoshi Miki of Tokyo City University for his excellent guidance, enthusiasm, and immense knowledge. His guidance helped me in all the time of research and writing of this thesis, and conveyed a spirit of adventure in regard to research. I would like to extend my appreciation to my committee chair Professor Osamu Maruyama of Tokyo City University, for the support of research and writing this thesis, and for valuable comments. I would also like to thank to the rest of my thesis committee: Professor Ikumasa Yoshida, Professor Hiromi Shirahata, Professor Toshihisa Ohtsuka, and Dr. Hidehiko Sekiya of Tokyo City University for their insightful comments and encouragement which incented me to widen my research from various perspectives.

My sincere thanks also goes to Dr. Tomonori Tominaga of Nippon Steel and Sumitomo Metal Corporation, for his kind guidance, and attitude to research. Without his help I could not last doctoral research while working for private company.

This work was supported by the research project funded by members below. I would like to express appreciation to the members: IHI Infrastructure Systems Co., Ltd., JFE Engineering Corporation, JFE Steel Corporation, Kawada Industries, Inc., Kobe Steel, Ltd., Komaihaltec Inc., Mitsui Zosen Steel Structures Engineering Co., Ltd., Miyaji Engineering Co., Ltd., MM Bridge Co., Ltd, Nippon Steel & Sumitomo Metal Corporation, and Yokogawa Bridge Holdings Corp.

At the end but not the least, I would like to thank to my beloved wife Aki who was always my support throughout writing this thesis.

HIGH FATIGUE RESISTANT ORTHOTROPIC STEEL BRIDGE DECKS

Koichi YOKOZEKI
Tokyo City University 2017

Abstract

Orthotropic steel decks are lightweight compared to concrete decks and are used in many long-span bridges and urban expressways. Rehabilitation of bridges by replacing deteriorated concrete decks is also an application of orthotropic steel decks and its demand is increasing. However, many fatigue cracks have been detected in orthotropic steel decks. In particular, fatigue of the connections between longitudinal ribs and transverse ribs is the most significant type of damage found in orthotropic steel decks. Fatigue crack inspections of Japanese urban expressways detected approximately 10,500 cracks and approximately 40% of all cracks were at the longitudinal-rib to transverse-rib connections. Though several types of connections have been proposed in previous studies, fatigue cracks still occur.

Orthotropic steel decks are composed of comparatively thin steel plates down to 6 mm and are subjected to vehicle loads directly. Therefore, these thin flexible steel plates easily deform into the out-of-plane direction, and cause, for example, local bending of deck plates, or torsion and distortion of ribs. The deformed longitudinal and transverse ribs are constrained by each other at the connections, which also induce local out-of-plane bending of the ribs. The out-of-plane bending stresses have not been taken into account for fatigue designs, which treat nominal or in-plane membrane stresses as the acting stresses.

Directions of out-of-plane deformations can be reversed by moving the loading positions. Since actual vehicles run at transversely distributed positions, the loading positions can be located anywhere in the distribution. Out-of-plane bending reversals can cause stress reversals from tension to compression and increase the stress ranges at the joints in orthotropic steel decks.

However, previous studies have not sufficiently considered the three-dimensional deformations caused by in-plane as well as out-of-plane deformations of the ribs at the connections. Some studies have investigated the fatigue strength of a connection with loading by using beam models, which do not cause torsion and distortion of the ribs. The stress reversals by moving the loading conditions should also be taken into account. Insufficient considerations of the loading position can lead to incorrect evaluation results of the fatigue strength. Furthermore, since the stress concentration points in the connections can move as the loading position moves, incorrect loading conditions can result in erroneous crack initiation points.

From the above background, this study investigated the critical loading conditions that can cause the most severe stress conditions for fatigue of various types of connections, while taking account of the above stress occurrence mechanisms. After that, the fatigue strengths of the connections under the critical loading conditions were investigated to propose a suitable structure for orthotropic steel decks. The longitudinal-rib types and slits (or cut outs) on the transverse ribs were varied as parameters since the effect of longitudinal-rib types on fatigue strength have not previously been investigated under the same conditions.

The target fatigue performance was set to 100-year fatigue lives, and was translated to 10^7 cycles of a fatigue design load with the critical loading condition, which implies that the fatigue design load cannot cause stress ranges over constant amplitude fatigue limits. In addition, another objective was to evaluate fatigue lives of connections under actual traffic conditions. It was found that orthotropic steel decks with plate ribs and non-slit connections are the suitable structure and would satisfy 100-year fatigue lives. The results were obtained using the following procedures, separated into chapters.

Chapter 1 reviews literature and found that slits (or cut outs) at connections were fabricated for fitting up of transverse ribs to continuous longitudinal ribs, but the effects of slits on fatigue have not been studied with sufficient consideration of the three-dimensional deformations of longitudinal-rib to transverse-rib connections. The literature review also found that non-slit connections, in which the continuous longitudinal-ribs are welded all around the transverse-rib webs, are also able to be fabricated and can decrease out-of-plane bending at the connections.

Chapter 2 selects a fatigue evaluation method for longitudinal-rib to transverse-rib connections, based on the structural hot-spot stress approach. Since the longitudinal-rib to transverse-rib connections are complex shapes and have complex stress distributions which can change as the loading position moves, the nominal stress approach is hardly applicable. As the results of re-analysis on literature fatigue data, it was found that three-dimensional finite element analyses and the hot-spot stress approach with appropriate modification factors can evaluate the fatigue strength of the joints where out-of-plane bending of thin plates occurs.

Chapter 3 investigates the critical loading conditions and the fatigue strength of the various connections. U-ribs, V-ribs and plate ribs as longitudinal ribs, and the slit and the non-slit transverse ribs were investigated. The shapes of V-ribs and plate ribs are also varied. The critical loading conditions were identified by the combination of the finite element analyses and the hot-spot stress approach. The analyses also took account of the rotations of principal stress directions around box welds and the moving of stress concentration points along weld toes. Fatigue evaluations under the critical loading conditions clarified that applying the non-slit connection instead of the common slit connections can dramatically decrease the hot-spot stress ranges and increase the fatigue strength of the connections.

Chapter 4 conducts fatigue tests on the connections. The fatigue loading simulated the critical loading conditions. The hot-spot stress approach was confirmed to be applicable to longitudinal-rib to transverse-rib connections. Furthermore, the non-slit connections with V-ribs and plate ribs achieved the target fatigue performance, which is fatigue strength corresponding to 10^7 cycles of the design load under the critical loading condition. However, it was also found that U-ribs and V-ribs did not have enough fatigue strength due to fatigue damage at the connection between the deck plates and the ribs. Therefore, orthotropic steel decks with plate ribs and non-slit connections were proposed as a suitable structure.

Chapter 5 evaluates the fatigue lives of the connections under actual traffic conditions by Monte Carlo simulations, since the occurrence of the critical loading conditions is often probabilistic and depends on the transverse distributions of vehicle positions. It was found that the non-slit connections can achieve 100-year fatigue lives for almost all heavy traffic roads in Japan.

Chapter 6 summarizes the results and finding of this study.

Table of Contents

List of Symbols

$ADTT_{al}$	Allowable average daily truck traffic per lane to achieve 100 year fatigue life
$ADEA_{al}$	Allowable average daily truck traffic per lane, equivalent to T load, to achieve 100 year fatigue life
K_t	Factor on acting stress for the thickness effect on fatigue strength, with expression of $(t/t_{ref})^n$, where n is thickness exponent
K_b	Reduction factor on bending component of acting stress for the bending effect on fatigue strength
L	Sum of weld leg lengths and an attached plate thickness in a cruciform joint
L_c	Span length of a longitudinal-rib
N_f	Fatigue life
$n_{eq,axle}$	Number of axles equivalent to T load
$n_{vehicle}$	Number of vehicles
P_{design}	Design load assumed in fatigue test
ΔP	Increased load range for fatigue test
$\Delta P'$	Factored load range, assumed design load in fatigue test
$\mathrm{POS}_{\max}$	Loading position which maximize the factored hot-spot stress of a evaluated weld toe
$\mathrm{POS}_{\min}$	Loading position which minimize the factored hot-spot stress of a evaluated weld toe
t'	corrected thickness to consider the thickness effect on fatigue strength
t_{ref}	Basic thickness, determining basic fatigue strength
$W_{axle,i}$	Weight of vehicle's each axle
W_{T_load}	Weight of T load
y_c	Center of the transverse tire distribution
Z_c	Section modulus of the section including a longitudinal-rib and the effective width of its upper flange (deck plate)
σ_h	Hot-spot stress
σ'_h	Factored hot-spot stress. Factors are thickness effect factor of $(t/25)^{0.25}$ and bending stress reduction factor of 0.8
$\sigma'_{h,\,\mathrm{m}}$	Membrane component of hot-spot stress
$\sigma'_{h,\,\mathrm{b}}$	Membrane component of hot-spot stress
$\sigma'_{h,\,\max}$	Maximum value of factored hot-spot stresses of a weld toe, caused by all loading case
$\sigma'_{h,\,\max,\,node}$	Maximum value of factored hot-spot stresses of *node* in a weld toe, caused by all loading case
$\sigma'_{h,\,\min}$	Minimum value of factored hot-spot stresses of a weld toe, caused by all loading case
$\sigma'_{h,\,\min,\,node}$	Minimum value of factored hot-spot stresses of *node* in a weld toe, caused by all loading case
$\sigma'_{h,\,\mathrm{obv}}$	Hot-spot stress computed using stresses on evaluated (obverse) surface.
$\sigma'_{h,\,\mathrm{rev}}$	Hot-spot stress computed using stresses on reverse surface $\sigma'_{h,\,pos,\,\mathrm{b}}$

$\sigma'_{h,\,pos,\,\mathrm{b}}$	Minimum value of factored hot-spot stresses along a weld toe line when the load case is *pos*
$\sigma'_{h,\,pos,\,\mathrm{u}}$	Maximum value of factored hot-spot stresses along a weld toe line when the load case is *pos*
$\sigma'_{h,\,pos,\,node}$	Factored hot-spot stress of the *node* when the load case is *pos*
$\sigma'_{h,\,test}$	Factored hot-spot stress of a evaluated weld toe caused by a loading position of fatigue test
$\Delta\sigma_{\mathrm{axial,\,95\%}}$	95% survival fatigue strength or constant amplitude fatigue strength of specimens tested with axial loading in terms of nominal stress
$\Delta\sigma_{\mathrm{axial,\,h,\,95\%}}$	95% survival fatigue strength or constant amplitude fatigue strength of specimens tested with axial loading in terms of hot-spot stress
$\Delta\sigma_{\mathrm{bend,\,95\%}}$	95% survival fatigue strength or constant amplitude fatigue strength of specimens tested with bending in terms of nominal stress
$\Delta\sigma_{\mathrm{bend,\,h,\,95\%}}$	95% survival fatigue strength or constant amplitude fatigue strength of specimens tested with bending in terms of hot-spot stress
$\Delta\sigma_f$	Constant amplitude fatigue strength at 2.0×10^6 cycles in terms of nominal stress
$\Delta\sigma_{f,\,h}$	Constant amplitude fatigue strength at 2.0×10^6 cycles in terms of hot-spot stress
$\Delta\sigma'_h$	Factored hot-spot stress range caused by moving load, $\sigma'_{h,\,\max}$ minus $\sigma'_{h,\,\min}$
$\Delta\sigma'_{h,\,node}$	Factored hot-spot stresses range of *node* in a weld toe, caused by all loading case, $\sigma'_{h,\,\max,\,node}$ minus $\sigma'_{h,\,\min,\,node}$

List of tables

List of figures

1. Introduction

1.1. Background

Orthotropic steel decks are lightweight compared to concrete decks and are used in many long-span bridges and urban expressways. Some orthotropic steel deck bridges in Japan are 286 km in total length and 3.77 km^2 in total deck area (Table 1-1, Mori ed. 2010). The lightweight decks have an advantage in urban expressways where foundation capacities are limited, or where construction should be simplified and/or fast. The lightweight decks can also be applied to long-span bridges, in which dead loads are the dominant factor in the design.

Rehabilitations of bridges by replacing deteriorated concrete decks are also an application of orthotropic steel decks and its demand is increasing in Japan. Wolchuck (1987) summarized deck renewals in the United States and explained that orthotropic steel decks are suitable for deck renewal because of their light weight, minimum restriction of traffic during re-decking, increased carrying capacity, long service life and minimum maintenance. Concrete decks of some bridges in Japan have also been damaged and replaced with orthotropic steel decks (Sugisaki and Kobayashi 1991). Due to the thin design thickness of concrete decks, the damage accelerates, especially in bridges designed by the specifications before ver. 1980 (Japan Road Association 1980). Replacements and repair work of the decks accounted for most of the rehabilitation plans for expressways.

However, many fatigue cracks have been detected in orthotropic steel decks (Nunn 1974; Mehue 1990; Jong 2004; Yuge et al. 2004; Miki et al. 2006, 2009). Investigations of the Japanese Metropolitan Expressway detected fatigue damage in 63% and 25% of the open ribs and the closed ribs, respectively, of inspected span orthotropic steel decks (Miki 2009). The fatigue damage was detected even in bridges younger than 10 years. It should be noted that the Metropolitan Expressway has significantly heavy traffic and fatigue cracks would not lead to bridge collapses immediately, even though the bridges would need to be repaired or retrofitted and this increases maintenance costs.

Fig. 1-1 shows locations of fatigue cracks in orthotropic steel decks. Fatigue crack initiation points can be classified into three major types: longitudinal-rib to transverse-rib connections, joints between longitudinal ribs and deck plates (hereinafter, rib-to-deck joints), and vertical stiffener to deck plate joints, indicated as 1, 2, and 3 in Fig. 1-1, respectively. In particular, fatigue of longitudinal-rib to transverse-rib connections is the most significant damage. Investigations of Japanese urban expressways detected approximately 7,000 and 3,500 cracks in closed-rib and open-rib orthotropic steel decks, respectively, and 41% and 91% of them were detected in the longitudinal-rib to transverse-rib connections (Mori ed. 2010, Fig. 1-2). The difference of the percentage is assumed to be due to the second significant fatigue damage at the rib-to-deck joints. This significant damage is only a problem for closed-rib types.

Though several types of longitudinal-rib to transverse-rib connections have been proposed previously, fatigue crack occurrences have not stopped. Many proposals aim to improve the fatigue strength of the connections by changing the slit (cut-out) shapes,

or adding bulkheads or attachments, though some of these modifications would increase fabrication costs. Non-slit connections, in which continuous longitudinal ribs are welded all around to transverse-rib webs, have also been studied and were expected to have high fatigue strength, but these connections have not been widely applied due to their difficult fabrication. Details of previously studied connections are mentioned in "1.2 Literature review".

Conventionally, longitudinal ribs and transverse ribs have been designed as girders with deck plates as upper flanges. Therefore, in-plane bending of the girders and the corresponding stress were considered for the fatigue design in old specifications (Japan Road Association 1980).

On the other hand, actual orthotropic steel decks undergo complex deformations. Orthotropic steel decks are composed of comparatively thin steel plates down to 6 mm and are subjected to vehicle loads directly. Therefore, the thin flexible steel plates easily deform into the out-of-plane direction, and cause, for example, local bending of deck plates, or torsion and distortion of the ribs. The deformed longitudinal ribs and transverse ribs are constrained by each other at the connections, and induce local out-of-plane bending of the ribs. Out-of-plane bending stresses have not been taken into account in conventional fatigue designs, which consider nominal or in-plane membrane stresses as the acting stresses.

Directions of out-of-plane deformations can be reversed by moving the loading positions. Since actual vehicles are distributed in transverse positions, the loading positions can be located anywhere in the distribution. Out-of-plane bending reversals can cause stress reversals from tension to compression and increase the stress ranges at the joints in orthotropic steel decks.

Hot spots, where local stress concentrations occur, can also move along weld toes as the loading positions move. As a rule, hot-spot locations can be determined by the macro stress direction and weld toe shapes. Since deformations can change as the loading positions move, local stress directions can also change, and this results in moving of the hot spots along the weld toes.

However, previous studies did not sufficiently consider three-dimensional deformation and the properties of the fatigue, which can be caused by in-plane as well as out-of-plane deformations of the ribs at the connections. Some studies used beam models to investigate the fatigue strength of the connection with loading on the connection, though those models do not cause the torsion and the distortion of the ribs. The stress reversals by the moving of the loading conditions should also be taken into account. Insufficient considerations of the loading position can lead to incorrect evaluation results of the fatigue strength. Furthermore, since stress concentration points in the connections can move as the loading position moves, incorrect loading conditions can result in erroneous crack initiation points.

Therefore, by taking account of the above stress occurrence mechanisms, this study investigated the critical loading condition that can cause the most severe stress conditions for the fatigue of various types of connections. The fatigue strengths of the connections under the critical loading conditions were investigated in order to propose a suitable structure for orthotropic steel decks. The longitudinal-rib types and slits on the transverse ribs were varied as parameters, because the effects of longitudinal-rib types on fatigue strength have not been previously investigated under the same conditions.

The target fatigue performance was set to 100-year fatigue lives, translated to 10^7 cycles of a fatigue design load with the critical loading condition. In addition, fatigue lives of the connections were evaluated under actual traffic conditions, since occurrence of critical loading conditions can be probabilistic depending on the distributions of the vehicle transverse positions.

From the above backgrounds, the following objectives of this study were established.

1) Select a fatigue evaluation method for longitudinal-rib to transverse-rib connections, where out-of-plane bending of thin plates occurs.
2) Investigate the critical loading conditions for various types of connections by taking account of moving vehicles.
3) Confirm the applicability of the fatigue evaluation method to longitudinal-rib to transverse-rib connections.
4) Investigate the fatigue lives of the connections under the critical loading conditions.
5) Evaluate the fatigue lives of the connections under actual traffic conditions.

1.2. Literature review

1.2.1. Development of longitudinal-rib to transverse-rib connections

(1) Introduction of slits for fabrications

Orthotropic steel decks were developed during the 1940s–50s in Germany, where reconstructions after the 2nd world war were required under a limited steel supply (Seeger 1964). Orthotropic steel decks were structurally more efficient than older steel decks, such as the battle decks developed in the 1930s in the US (Lyse 1938), because deck plates function not only as the top surface but also as the upper flanges of longitudinal ribs and transverse ribs. However, the intersections between longitudinal and transverse ribs have to be fabricated. In the early stages of development, longitudinal ribs were separated at transverse ribs and welded to transverse rib webs by load-carrying fillet welds (Fig. 1-3a).

The discrete longitudinal ribs were altered by continuous longitudinal ribs to avoid load-carrying fillet welds at transverse ribs from the viewpoint of fatigue and fracture (Fielder 2009).

Afterward, slits were introduced on transverse-rib webs in order to easily fabricate the connections with the continuous longitudinal ribs. To fabricate continuous longitudinal ribs with open sections and bottom flanges, longitudinal ribs were inserted into the slits on transverse-rib webs, as shown in Fig. 1-3b (Seeger 1964), or the transverse ribs were moved horizontally. After that, longitudinal ribs were continuously welded on deck plates before assembling the transverse ribs. However, it was difficult to fit the transverse ribs to longitudinal ribs having weld imperfections. Therefore, more efficient fabrications in the 1960s were achieved by enlarging the slit, as shown in Fig. 1-3c (鋼床構造の進捗調査分科会 1982). Another aspect of introducing slits on connections between U-ribs and transverse ribs were to remove stress concentrations from non-slit connections, though the slit created other stress concentration points in U-rib walls (Buckland 2004).

(2) Upper scallop details

Previous studies recommended removing the upper scallops on transverse-rib webs (Fig. 1-4). Upper scallops were added at the connections of three members; deck plates, transverse-rib webs, and longitudinal-rib walls. Miki et al. (1995) conducted fatigue tests on deck panels stiffened by U-ribs, which were loaded by a three-jack system to simulate a running tire, and found that longitudinal-rib to transverse-rib connections without the upper scallop had higher fatigue strength than those with the upper scallops. Mori and Harada (2011) also concluded the upper scallops decreased the fatigue lives by cracks initiating from the weld roots of rib-to-deck joints and propagating in the weld metals. Based on previous studies including the studies above, standard longitudinal-rib to transverse-rib connections recommended by present Japanese specifications do not have the upper scallops for both closed and open ribs, as shown in Fig. 1-4 (Japan Road Association 2014).

(3) Slit (lower cut-out) details for closed ribs

For fatigue improvements of longitudinal-rib to transverse-rib connections, slit and non-slit webs of transverse ribs were compared in European studies, which unfortunately did not sufficiently consider loading positions. Bruls (1991, Chapter 5) and

Kolstein (2001) summarized European research including longitudinal-rib to transverse-rib connections for both U-ribs and V-ribs with three types of transverse-rib webs: non-slit, conventional slit, and improved slit (Fig. 1-5). The improved slit for the U-ribs was proposed by Hibach (1983). It was concluded that the non-slit webs had longer fatigue lives than the slit webs for the U-ribs, and the slit webs functioned better than the non-slit webs for the V-ribs. However, the experimental loads were located on transverse ribs or longitudinal ribs, even though U-rib distortion had a significant effect on fatigue, as indicated by Lehrke (1997). This result means that fatigue load locations should be eccentric to the axes of both the U-ribs and the transverse ribs. The fatigue loads on the transverse ribs are explained as follows. The fatigue at the slit ends can be analyzed by a model composed of a simply supported crossbeam, a short length of longitudinal ribs, and deck plates, because the stress level in the web near the slits is proportional to the shear forces in the transverse ribs and is influenced by the loads introduced locally into the transverse ribs.

The advantage of the non-slit transverse-rib web for U-ribs was also noted in the Japanese development of an orthotropic steel deck with large-size U-ribs, but the advantage was not confirmed experimentally. Katsumata et al. (2000) found that fixing the bottom flanges of U-ribs to transverse-rib webs can decrease the U-rib side stress near the box welds at the slit end by 75%. Mizuguchi et al. (2000, 2004) also recommended fixing the U-rib bottom flanges transversely by welding. Ohashi et al. (2000) found the non-slit webs compared to the slit webs can decrease the stress on longitudinal-rib to transverse-rib connections. Those three studies took moving of the loading position into account. However, Ohashi et al. (2000) also indicated fabrication difficulties of non-slit connections. Those studies did not confirm the fatigue strength and fatigue lives of non-slit connections by fatigue tests or by fatigue assessment with established methods.

Bulkheads, which are inner diaphragms welded in closed longitudinal ribs at the transverse-rib cross section, could improve the fatigue strength of longitudinal-rib to transverse-rib connections, but they lead to load-carrying welded joints (Fig. 1-6a). The bulkheads can decrease the stresses on the U-ribs near the slit ends by fixing out-of-plane deformations of the closed ribs (Katsumata et al. 1999, 2000; Ohashi et al. 2000; Taskopoulos et al. 2003, Conner and Fisher 2006). However, the bulkheads change the conditions of the welds between longitudinal ribs and transverse ribs to load-carrying types, since stresses on transverse-rib webs travel via the bulkheads (Ohashi et al. 2000). Load-carrying welded joints require deeper weld penetrations for complete joint penetrations (Taskopoulos et al. 2003).

Recent studies, most of which take advantage of finite element analyses, found that an inner stiffener welded in the U-ribs at transverse rib cross sections or additional notches of the web slits can likely decrease local stresses on the box weld toes at the slit ends. Suganuma and Miki (2006, 2007a), and Miki and Suganuma (2014) computed structural hot-spot stresses caused by a moving tire load for connection details with and without an inner stiffener, and with various slit shapes (Fig. 1-6b). Fatigue tests for some of the analyzed connection details were also conducted. They concluded that the inner rib can decrease the stresses on both sides of the box welds at the slit ends. Hanji et al. (2013) conducted finite element analyses with local stress approaches to compare the fatigue strength of various details, including a normal type, an enlarged slit type, an improved additional notch type, an inner rib type likely used in the Tokyo Gate Bridge, and a fixed U-rib bottom flange type. The inner rib type and the improved additional

notch type had the lowest and second lowest local stress ranges, respectively, due to the decrease of U-rib wall bending by the inner stiffener and the flexible web slits. Sugiyama et al. (2014) tried to optimize the shape of the improved additional notched slit with finite element analyses and conducted fatigue tests. The proposed additional notched slit was found to decrease stress on the U-rib side weld toe by 75% and to increase fatigue lives in comparison with the normal slit. But the fatigue in that study did not sufficiently consider stress reversal, which is caused by the transversely distributed vehicle positions described in detail in "1.2.3. Loading position effects for fatigue". Therefore, the stress range in the fatigue test would be smaller than possible stress ranges occurring on actual bridges.

Although bulkheads or inner stiffeners would decrease stress ranges occurring at longitudinal-rib to transverse-rib connections, these would increase fabrication costs and thus leading to the increase of total project costs. A cost analysis of orthotropic deck projects conducted by Wolchuck (2004) indicated that the labor cost in the fabrication and election accounts for 80% of the total project cost. Therefore, the additional members and fabrication processes of longitudinal-rib to transverse-rib connections would affect the total project costs. In addition, the cost analysis also indicated that using the non-slit connection as an alternative to the connection with the bulkhead could save up to 15% of the fabrication cost. A part of the cost reduction would come from complete joint penetrations and toe ground of the connection with the bulkheads.

(4) Slit (lower cut-out) details for open ribs

As in the slit details for closed ribs, non-slit details would have high fatigue strength, though it would also have fabrication difficulties. Iwasaki et al. (1992) conducted finite element analyses and found plate ribs with both side surfaces welded to transverse rib webs can decrease the stress on longitudinal-rib to transverse-rib connections compared to the asymmetric slit, which is the standard detail of the Japanese specification (Japan Road Association 2014). The asymmetry slit causes high stress on the box weld at the upper end of the slit. Iwasaki et al. (1992) describes that the non-slit connection requires high fabrication accuracy and the connection with only a lower circle slit is recommended. Fryba and Gajdos (1999) summarized European experimental studies for orthotropic steel decks in railway bridges (Fig. 1-7), and based on their results the connection with a lower "apple" form slit was recommended. Fryba and Gajdos (1999) concluded that non-slit connections show high fatigue strength, but they require advanced welding technology to weld the connections with the smallest possible residual stresses. For the longitudinal-rib to transverse-rib welds, it was recommended to prepare grooves at edges of the transverse-rib web and weld four vertical lines at the same time with automated welding operations. Yamaoka (2010) proposed a retrofit method to bolt angle steel on the connections with the asymmetric slits to make both side surfaces of longitudinal bulb ribs connected to the transverse-rib web. This method would not require high fabrication accuracy but would require additional fabrication costs.

Unfortunately, the previous studies do not sufficiently simulate the behavior of the longitudinal-rib to transverse-rib connections. Most of the experimental and analytical studies were conducted with models composed of simply supported transverse ribs and short lengths of longitudinal ribs and deck plates. Loads were put on the simply supported transverse ribs, except in ERRI D 191 research program, in which longitudinal ribs were loaded but out-of-plane deformations of the ribs were not induced. (Fryba and

Gajdos 1999). However, as Miki et al. (1991a) and Tateishi et al. (1995) showed, transverse-rib webs are under bending and the bending stresses on the webs are almost similar values to membrane stresses. This observation might mean that loads not positioned on but at a distance from the transverse ribs could cause maximum or minimum stresses on longitudinal-rib to transverse-rib connections. Zhang et al. (2016) conducted finite element analyses on deck panel models with various types of longitudinal-rib to transverse-rib connections and a tire load moving both longitudinally and transversally. The connections with the apple form slit were again recommended, but they did not show the critical loading positions used to determine the stress ranges of the connections.

1.2.2. Complex deformation shape of orthotropic steel decks

(1) Out-of-plane bending of deck plates

Since the deck plate support vehicle loads directly, local areas of the deck plates can easily deform in the out-of-plane direction. Nunn and Cuninghame (1974a, b) conducted static loading tests on deck panels with five U-ribs or five V-ribs, and found that out-of-plane components are dominant in stresses measured on deck plates. The measured points were adjacent to the rib-to-deck joints, and the measured stress directions were transverse. Cullimore (1981) conducted static loading tests and finite element analyses on a deck panel model with two V-ribs. They found that the transverse bending moment in the deck plate was greater than the longitudinal bending moment, and the highest stress in the deck plate occurred locally under the wheel load. The highest stresses result from the transverse bending moment caused by the local out-of-plane deformation of the deck plates.

The stresses in the deck plates reverse due to the out-of-plane deformation of the deck plates. Nirasawa (1992) conducted finite element analyses on a deck panel model with five U-ribs between main girders and concluded that the transverse stresses in the deck plate adjacent to the rib-to-deck joints reverse as the wheel loading passes the stress reference point. The stress reversal was explained as the combination of global deflection of the orthotropic plate and local out-of-plane bending of the deck plates. Ono et al. (2005) conducted static loading tests on a deck panels with three U-ribs and found the similar stress behavior. Both Cullimore (1981) and Ono et al. (2005) noted that the stress reversal should be taken into account in the fatigue evaluation of the rib-to-deck joints. The stress reversal can cause not only the stress range increase, but also the average stress change, as was confirmed later to affect the fatigue of the joints (Inokuchi et al. 2008; Kainuma et al. 2008, 2016).

In addition to the deck plate side, the longitudinal-rib side of the rib-to-deck joints is also subjected to transverse bending. Cullimore (1981) conducted static loading tests and finite element analyses, as mentioned above, and found that the transverse bending moment at the longitudinal ribs adjacent to the joints was reversed. It was also found that the stresses in orthotropic steel decks with V-ribs were less than those with U-ribs, in later of which the distortions when subjected to wheel loads have an increased bending moment. Ono et al. (2005) explained that the directions of the local transverse bending of the longitudinal ribs adjacent to the joints depend on the transverse position of the wheel loading.

(2) Three-dimensional deformations of longitudinal-rib to transverse-rib connections

As in the deck plates, longitudinal ribs and transverse ribs are also forced to deform in the out-of-plane direction. The longitudinal ribs and transverse ribs are designed as girders with a deck plate as the upper flange of both, and in-plane bending of the girders was conventionally considered for fatigue design in old specifications (Japan Road Association 1980). However, the ribs are also subjected to out-of-plane deformations such as the out-of-plane bending of plates, and torsion and distortion of the ribs. Fig. 1-8a and b show examples of in-plane deformations, and the mix of in-plane and out-of-plane deformations, respectively.

The deformed longitudinal ribs and transverse ribs are constrained by each other at the connections, which induce local out-of-plane bending of the ribs. Miki et al. (1991) and Tateishi et al. (1995) conducted field measurements of strains at longitudinal-rib to transverse-rib connections with both open and closed longitudinal ribs and clarified that similar values of membrane and bending stresses are caused on the transverse-rib web side of the connections. Miki et al. (1991) also conducted modal analyses to identify the cause of out-of-plane bending stresses on transverse-rib webs and found rotations of the web about the transverse axis is dominant in the case of closed ribs, whereas rotations of the web about the vertical axis were found to occur in the case of open-rib decks.

As mentioned above, torsion and distortion of closed longitudinal ribs lead to local stresses at the connections (Leendertz 2008; Delesie et al. 2008). Lehrke (1997) calculated the out-of-plane bending stress on closed-rib walls caused by closed-rib distortions and found that the influence line of the distortion-induced stress is independent of the influence surface of the in-plane bending moment of the longitudinal ribs. Katsumata (1999) found that rotations of U-ribs with cross-section shapes fixed by inner diaphragms cause significant stress leading to fatigue damage at the U-rib sides weld toes at the slit ends. Unfortunately, those calculations did not obtain reliable local stresses due to stress singularities in the analyses, as indicated by Lehrke (1997). In addition, Poisson's effect could also cause out-of-plane bending on the closed-rib walls (Wolchuck 1992).

At connections between the open ribs and transverse ribs with the slits, one side of the open-rib walls are welded to the transverse-rib webs, as recommended by the Japanese specification (Japan Road Association 2014). In this connection, the deck plates at the slits deform locally into the out-of-plane direction. Iwasaki et al. (1992) conducted finite element analyses and found high out-of-plane bending stress occurred on the deck plate.

1.2.3. Loading position effects for fatigue

(1) Critical loading conditions for fatigue of the connections

Since the stresses at the longitudinal-rib to transverse-rib connections can be caused by the torsion and the distortion of the ribs, large local stress at the connection can be caused by eccentric loading. Beales (1990) conducted static loading tests on V-rib deck panel models and showed the tire positions that cause minimum (maximum compression) surface stress on the transverse-rib web adjacent to the slit end are not on the axes of either the V-rib or the transverse rib, as shown in Fig. 1-9. Miki et al. (1995) conducted static loading tests on a deck panel model with U-ribs and found that the tire positions that maximize both the membrane and the bending stresses on the slit end of the transverse-rib web are not on the connection but at a distance away from the center

axes of both the U-rib and the transverse ribs. More recent works with finite element analyses also found the critical loading positions for U-ribs to transverse-rib connections (Hanji et al. 2013; Harada et al. 2016).

Those loading positions should be taken into account for fatigue evaluations, since the fatigue of the welded joints is dominated by the maximum stress range, although the stress history on the joints also affects fatigue lives. Therefore, Miki et al. (1995) indicated that a fatigue investigation without consideration of the loading positions cannot simulate actual fatigue cracks and fatigue strength.

In addition, as the loading position moves, the torsion and the distortion deformation of the ribs can be reversed. The deformation reversal results in stress reversal at the longitudinal-rib to transverse-rib connections where out-of-plane bending stress caused by the torsion and the distortion are dominant. Therefore, both tension and compression surface stresses occur at the connection, since the transverse positions of the vehicles are distributed. The critical loading condition, which is the most severe condition, is that vehicles run over positions causing the maximum and the minimum stresses on the connections.

Furthermore, the probabilities of the maximum stress range occurrence can affect the fatigue lives of longitudinal-rib to transverse-rib connections. Since vehicle positions are not always the critical loading conditions, statistical simulations are required to estimate fatigue lives of longitudinal-rib to transverse-rib connections. Beales (1990) conducted statistical simulations to estimate the fatigue lives of connections between V-ribs and transverse ribs in the case of slit and non-slit transverse-rib webs by using the stress obtained by static loading tests and the fatigue strength obtained by component fatigue tests. Yan et al. (2016) also conducted similar simulations to estimate the fatigue lives of a orthotropic steel deck with U-ribs by finite element analysis.

(2) Distributed transverse positions of vehicles

In actual traffic conditions, the transverse positions of vehicles are not fixed but distributed. Leonard (1969) and Takada (2009a) measured transverse vehicle distributions in England and Japan, respectively. The measurements resulted in distributions similar to normal distributions with standard deviations of 300–330 mm and 179 mm (Fig. 1-10). The results indicate that transverse vehicle distributions have to be taken into account for the fatigue investigations of orthotropic steel decks, since stress on longitudinal-rib to transverse-rib connections can be reversed from compression to tension, as mentioned above. However, it should be noted that both of the above investigations stated that vehicle transverse distributions would depend on road width.

Eurocode stipulates that transverse traffic distributions should be taken into account in steel deck designs, though Japanese and American specifications do not (European Committee for Standardisation 2003; Japan Road Association 2014; American Association of State Highway and Transportation Officials 2012). The vehicle transverse distribution for design recommended by Eurocode is similar to a normal distribution. American specifications for the load and resistance factor design (LRFD) describe design loads positioned to the most severe conditions for fatigue, regardless of the present position of traffic lanes, because traffic lanes could be changed in the future. In the case of LRFD, maximum or minimum stresses on evaluated joints will be considered. However maximum stress ranges will be overlooked since the vehicle transverse position is not distributed.

1.2.4. Fatigue improvements of the rib-to-deck joints

(1) Two types of fatigue cracks

Rib-to-deck joints have the fatigue problem of cracks initiated from the weld root and propagated into deck plates or welds (deck cracks or bead cracks in the following). According to investigation of bridges under service, both types of cracks have been reported at longitudinal-rib to transverse-rib connections and at the middle part between a transverse rib and the next transverse rib.

(2) Required weld penetrations and throat thicknesses for bead cracks

The fatigue strength of bead cracks initiated from weld roots of rib-to-deck joints can be improved by sufficient weld penetrations and weld throat thicknesses. Maddox (1974) conducted fatigue tests on component joints and concluded that both fillet welded and butt welded rib-to-deck joints gave similar fatigue strength of bead cracks in terms of bending stress in the weld, where the fillet welded and the butt welded models corresponded to 0% and 100% penetrations, respectively. Though the study did not take account of the global structural behavior of deck panels, the result meant that thicker welds provide higher fatigue strength. Suganuma and Miki (2007b) computed the notch stress on the weld root by finite element analyses on a full bridge model with 75% penetrated and fillet welded rib-to-deck joints. The result shows the lack of weld penetrations increased the deck side stress by 16% and caused stress concentrations at the weld material side of the tip of the weld root, where no stress concentration was observed in the 75% penetration case. Hirayama et al. (2015) conducted fatigue tests with a running wheel load on deck panel specimens, and no bead cracks were observed after 0.89 million cycles of a 147 kN double tire on a 75% penetration model, compared to cracks penetrating the weld bead after 0.25 million cycles of 147 kN on a fillet welded model. Based on such investigation results, $\geqq$75% penetrations are required by JSHB, and also $\geqq$80% penetrations by AASHTO LRFD, and $\leqq$2 mm un-welded thickness by Eurocode (European Committee for Standardisation 2006; Japan Road Association 2014; American Association of State Highway and Transportation Officials 2012). AASHTO LRFD also prohibited weld melt-through, which can decrease the fatigue strength of rib-to-deck joints (Sim et al. 2009).

(3) Stress reduction by surfacing support

Behaving as a part of structural members, surfacing or pavements decrease stresses of orthotropic steel decks but the decrease depends on temperature. Nunn and Cuninghame (1974a) conducted static loading tests on U-rib deck panel specimens with and without 38-mm asphalt surfacing. Stress reductions at rib-to-deck joints after asphalt surfacing were up to 20% compared to un-paved deck panels. Fields measurements by Iwasaki et al. (1997) showed that the stresses of orthotropic steel decks increase linearly to the asphalt temperature increase up to 40°C**.** By using field measurements and static loading tests, Cheng et al. (2004a) found stresses of orthotropic steel decks with 30–35 mm asphalt surfacing became similar to those without surfacing when the asphalt temperature reached 45°C. Hence, the surfacing behaves as a part of the deck plate but the stiffness has a temperature dependency.

However, the stress reductions by the surfacing are less effective on the ribs than on the deck plates. Takada et al. (2010) conducted field measurements on a bridge with

U-ribs in summer and winter, where the temperature difference between seasons was approximately 20°C. The measurement found differences between stresses in summer and winter were 1.8–1.9 and 3.0–3.5 times, respectively, on decks and ribs. This result means that stresses on deck plates can easily be decreased by surfacing compared to stresses on ribs. The ineffectiveness of the surfacing to the rib stress reduction was implied by previously published analysis results, which indicate that the increase of the deck plate thickness from 14 to 20 mm can decrease the stress on the longitudinal-rib to transverse-rib connections by only 20% approximately (Wang and Feng 2008).

Due to the temperature dependency and the character of less effective reduction of rib stresses, the surfacing was basically not taken into account in this study. Another reason for neglecting the surfacing was that uncertain mechanical properties of the surfacing could lead to a non-conservative estimation of fatigue strength by overestimating its stiffness in finite element analysis. It should be noted that fatigue assessments by models without the surfacing would provide conservative results, because the existence of the surfacing basically reduces the stress working on orthotropic steel decks.

(4) Deck plate stiffening for fatigue of rib-to-deck joints

Increasing deck plate thickness could improve the fatigue strength of deck cracks from the weld roots of rib-to-deck joints. Suganuma and Miki (2007b) computed the notch stress on the weld root by finite element analyses on a full bridge model and found that thicker deck plates can decrease the notch stress but the reduction range is smaller in the case where U-rib deformations are dominant than in the case where the deck plate bending is dominant. Some running wheel tire tests on deck panel models found stresses on the deck plate and propagation rates of the deck cracks can decrease by increasing the deck plate thickness (Cheng et al. 2004b; Inokuchi et al. 2011; Murakoshi et al. 2012; Saito 2013). From such investigation results, JSHB requires a minimum deck plate thickness of 16 mm for closed longitudinal ribs (Japan Road Association 2014). AASHTO LRFD and Eurocode require 16 mm for all orthotropic steel bridges, though Eurocode allows 14 mm deck plates in the case that the surfacing is thicker than 70 mm (European Committee for Standardisation 2006; American Association of State Highway and Transportation Officials 2012).

In addition, stiffer surfacing materials can dramatically improve the fatigue strength of rib-to-deck joints. Stiffer surfacing materials, such as steel fiber reinforced concrete (SFRC), high or ultra-high performance concrete, and the combination of them have been reported in many previous studies (Jong and Kolstein 2004; Buitellar et al. 2004; Ono et al. 2005, 2009; Miki et al. 2007; Kodama et al. 2010; Dieng et al. 2013; Zhang et al. 2016). For example, Ono et al. (2005, 2009), and Miki and Suganuma (2014) conducted static and cyclic loading tests on U-rib deck panels loaded by running tires. In the static loading tests, SFRC decreased stresses near rib-to-deck joints by up to approximately 80% compared with stresses on a non-paved deck panel, and the stress reductions were larger than the other alternate approaches, which were bolting a stiffening plate on the deck plate and filling concrete in the U-ribs. The fatigue tests with two sets of 69 kN double tires in the tandem arrangement (138 kN in total) resulted in fatigue crack initiations in the non-paved deck after 0.50 million cycles, but no crack was detected in the SFRC deck after 4.4 million cycles.

1.2.5. Fatigue improvements of rib longitudinal joints

Fatigue strength of on-site welded longitudinal joints of the closed ribs can be decreased by weld defects and is significantly affected by the weld root gap. Kondo et al. (1982) conducted 4-point bending fatigue tests on U-rib models having welded longitudinal joints with backing splice plates. They found that the fatigue strength of the joints was significantly decreased when the root gap was zero and concluded that the reduction may be due to the incomplete penetration of the groove welds. Cuninghame (1982) also conducted 4-point bending fatigue tests on V-rib models with three types of longitudinal joints, including butt welded joints. It was recommended that the longitudinal joints of the types tested are treated as BS5400 class D ($\Delta\sigma_f$=91 N/mm^2) of the fatigue strength at 2.0 × 10^6 cycles in this case, a designer can ensure an adequate standard of welding, as confirmed by non-destructive testing techniques capable of detecting root defects (Cuninghame 1982).

Fatigue strength of on-site bolted longitudinal joints is higher than those of welded joints. Fujii et al. (1993) conducted compression fatigue tests on U-rib models having butt welded and bolted joints and concluded that the fatigue strength of bolted joints can be designed by JSSC class C ($\Delta\sigma_f$=125 N/mm^2) compared to butt welded joints classified into JSSC class F ($\Delta\sigma_f$=65 N/mm^2). The Japanese fatigue design recommendation (日本道路協会 2002) stipulates that the on-site longitudinal joints of closed ribs should be bolted with a countermeasure against inner surface corrosion caused by the hand holes for bolted joints.

Rib longitudinal joints have another fatigue initiation point at the box welds between deck plates and the scallop of longitudinal ribs. The scallops are holed to avoid overlap between transverse deck-to-deck butt welds and rib-to-deck joint welds or rib longitudinal joints. Ohashi et al. (1997) conducted field measurements and found that stresses on the U-rib walls near the scallop ends can be >98 N/mm^2 and suffer stress reversal. In order to reduce the stress, the longitudinal length of the scallops was recommended to be ≦80 mm by the Japanese fatigue design recommendation (日本道路協会 2002).

1.3. Outline of dissertation

Chapter 1 reviewed related literature. It was found that the slit (or cut out) at the connections was introduced for fabrication procedures of fitting up transverse ribs to continuous longitudinal ribs, but the effect of the slit on fatigue has not been studied with sufficient consideration of the three-dimensional deformations of longitudinal-rib to transverse-rib connections. The literature review also found that the non-slit connection, in which continuous longitudinal ribs are welded all around to the transverse-rib webs, are also able to be fabricated and this design can decrease out-of-plane bending at the connections.

Chapter 2 selects a fatigue evaluation method for the longitudinal-rib to transverse-rib connection, based on the structural hot-spot stress approach. Since the longitudinal-rib to transverse-rib connections are complex shapes and have complex stress distributions that can change as the loading position moves, a nominal stress approach is hardly applicable. As the results of re-analysis of literature fatigue data, it was found that three-dimensional finite element analyses and the hot-spot stress approach with appropriate modification factors can evaluate the fatigue strength at joints where out-of-plane bending of thin plates occurs.

Chapter 3 investigates the critical loading conditions and the fatigue strength of the various connections. Connections with U-ribs, V-ribs and plate ribs as longitudinal ribs, and with slit and the non-slit transverse ribs were investigated. The shapes of V-ribs and plate ribs were also varied. The critical loading conditions were identified by the combination of finite element analyses and the hot-spot stress approach. The analyses took account of rotations of principal stress directions around box welds and the moving of stress concentration points along weld toes. Fatigue evaluations under the critical loading conditions clarified that applying non-slit connections instead of common slit connections can dramatically decrease the hot-spot stress ranges and increase the fatigue strength of the connections.

Chapter 4 describes the fatigue tests conducted on the connections. The fatigue loading simulated the critical loading conditions. The hot-spot stress approach was confirmed to be applicable to the longitudinal-rib to transverse-rib connections. Furthermore, the non-slit connections with V-ribs and plate ribs achieved the target fatigue performance, which is fatigue strength corresponding to 10^7 cycles of the design load under the critical loading condition. However, it was also found that U-ribs and V-ribs did not have enough fatigue strength due to fatigue damage at the rib-to-deck joints. Therefore, orthotropic steel decks with the plate ribs and non-slit connections were proposed as suitable structures.

Chapter 5 evaluates the fatigue lives of the connections under actual traffic conditions by Monte Carlo simulations, since the critical loading conditions do not always occur. The simulation took account of transverse distributions of vehicle positions. It was found that the non-slit connections can achieve 100-year fatigue lives for almost all heavy traffic roads in Japan.

Chapter 6 summarizes the results and finding of this study.

Table 1-1 Orthotropic steel deck bridges of Japanese expressways (Mori, 2010)

Location (Owner)	Rib type	Total length [km]	Deck area [10^3m^2]	Average span length [m]
City expressways (shown in (b))	**Total**	**230.2**	**2790**	**64.4**
	Open rib	80.8	851	57.1
	Closed rib	149.4	1939	69.1
Intercity expressway including near city region (NEXCO)	**Total**	**29.7**	**518**	**125.3**
	Open rib	2.4	27	109.1
	Closed rib	27.3	491	127.0
Links between two major islands (Honshu-Shikoku Bridge Expressway)	**Total**	**26.0**	**466**	**232.1**
	Open rib	0.0	0	0.0
	Closed rib	26.0	466	232.1
Total	**Total**	**285.9**	**3774**	**72.8**
	Open rib	83.2	878	57.9
	Closed rib	202.7	2896	81.5

Table 1-2 Stress correction by thickness factor, $\Delta\sigma'=(t/t_{ref})^n \Delta\sigma$ for plates thicker than t_{ref}

	JSSC	IIW
Basic thickness t_{ref}	25	25
Effective thickness t_{eff}	t	Max (t, 0.5L)
Thickness exponent n		
(a) Cruciform and T joints	0.25*	0.3 (0.2)
(b) Ends of longitudinal welds	0	0.3 (0.2)
(c) Butt welds	0.25	0.2 (0.1)
(d) BM, longitudinal welds, and attachments at plate edges	0	0.1

*n=0 for non-load-carrying and fully penetrated load carrying cruciform joints with attached plate thickness of ≦12 mm

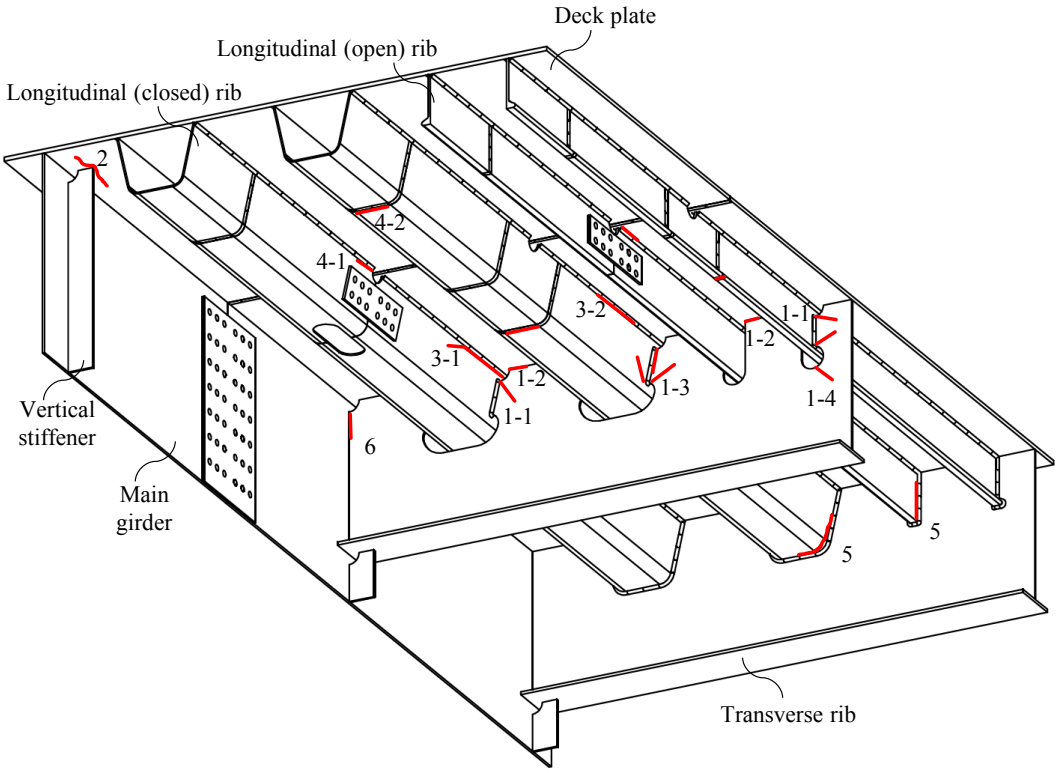

a) Fatigue crack locations

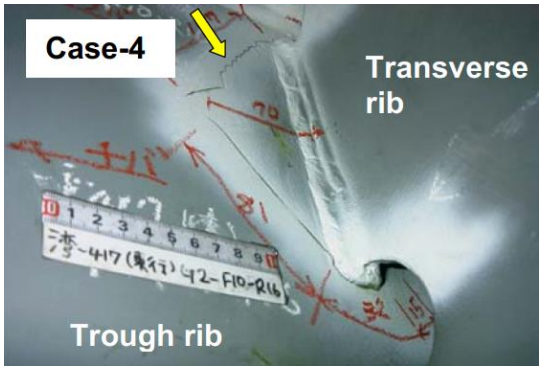

b) A crack detected at 1-3 (Yuge et. al 2004)

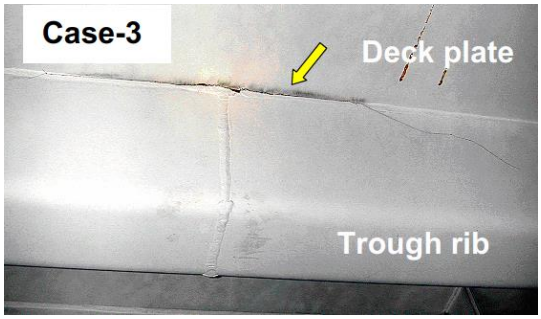

c) A crack detected at 3-2 (Yuge et. al 2004)

Fig. 1-1 Fatigue cracks in orthotropic steel decks

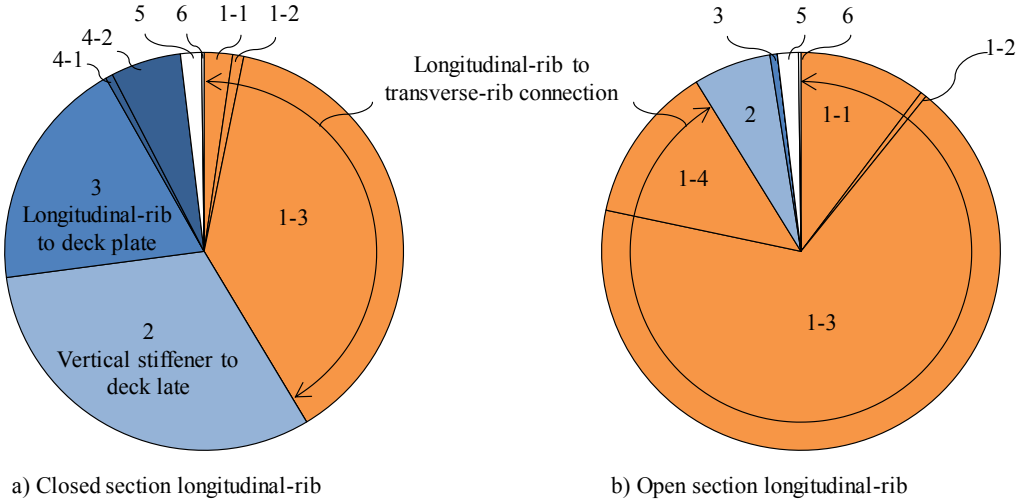

Fig. 1-2 Ration of fatigue crack initiation points (reproduced from Mori 2010)

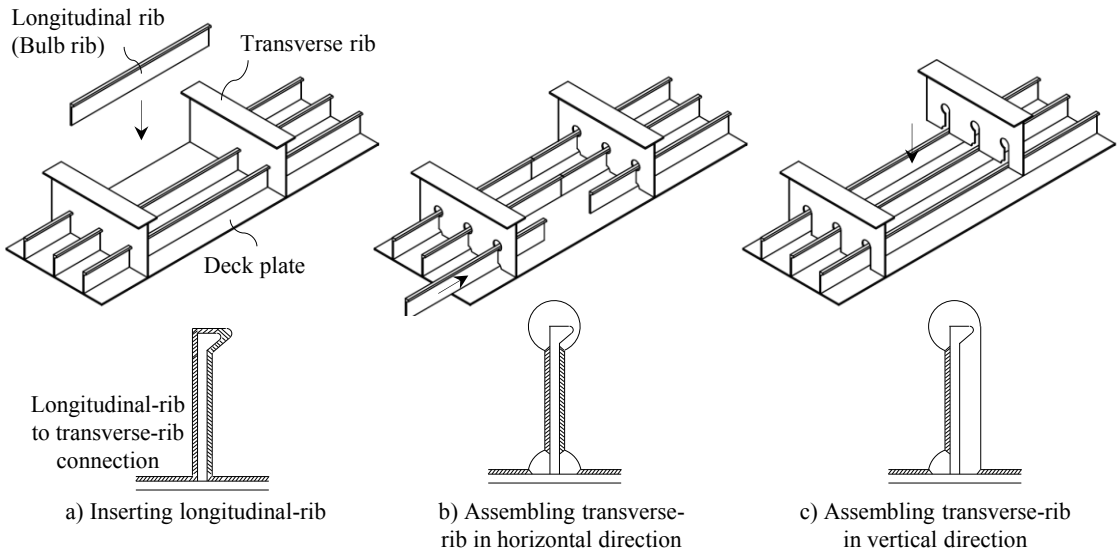

Fig. 1-3 Fabrication procedures for orthotropic steel decks with bulb-ribs

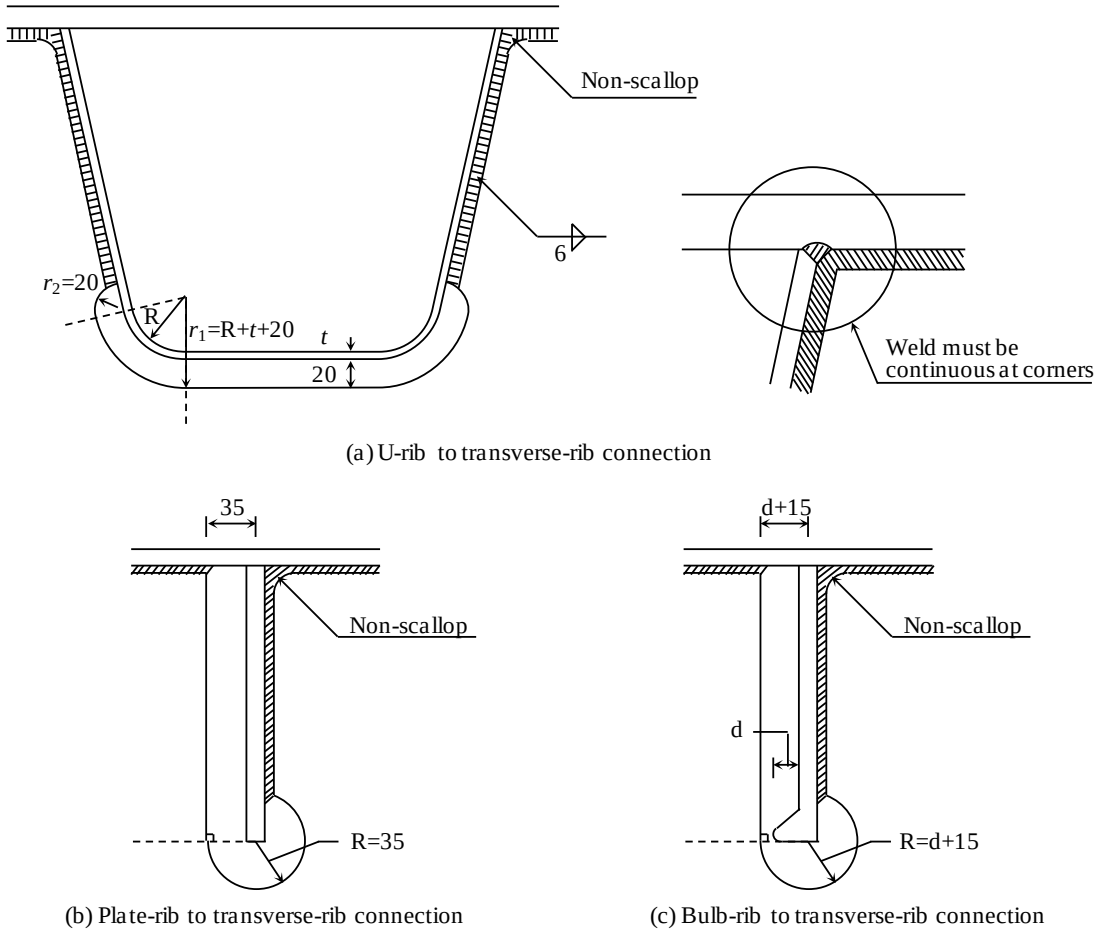

Fig. 1-4 Longitudinal-rib to transverse-rib connections without upper scallop (Japan Road Association 2014)

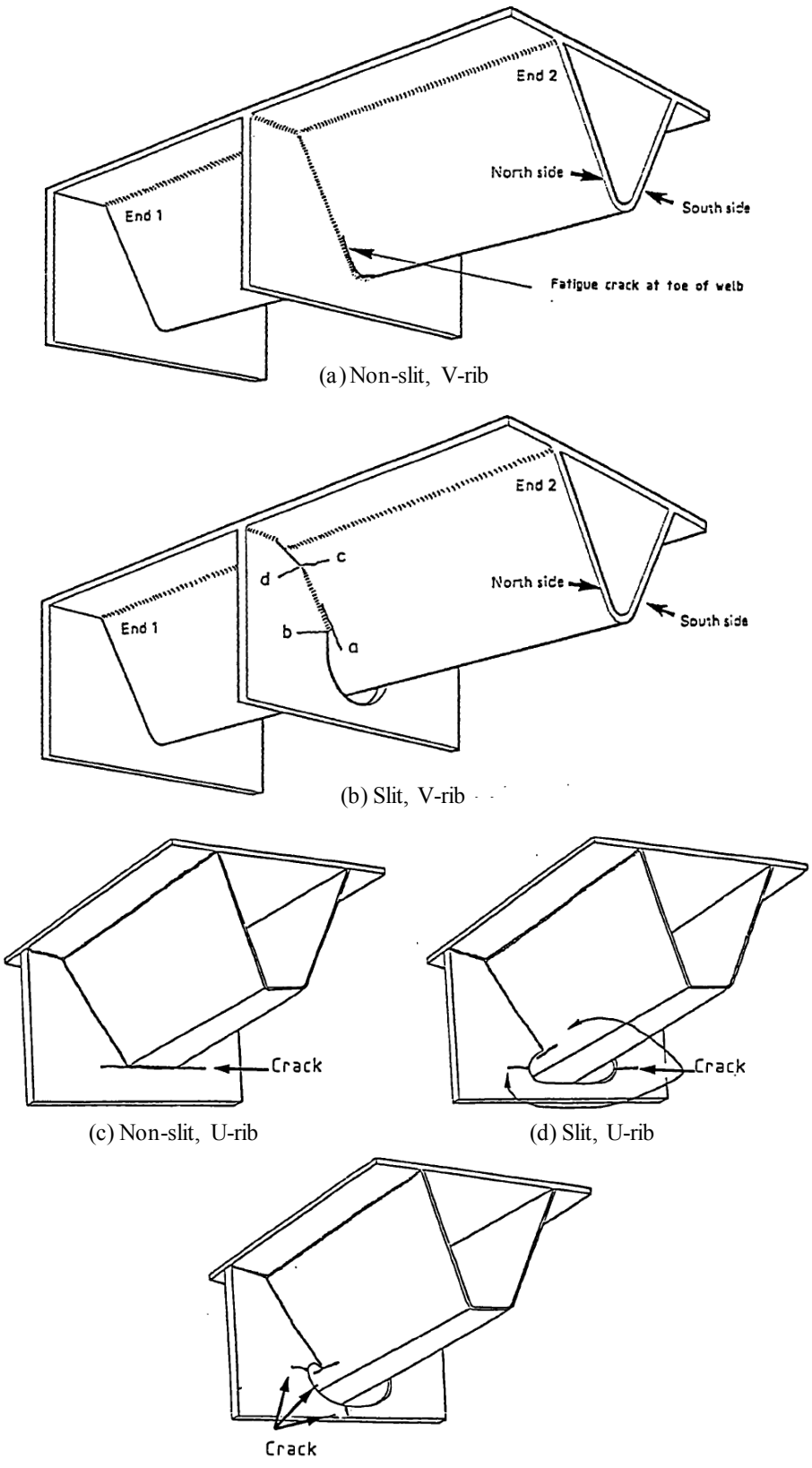

Fig. 1-5 Longitudinal-rib to transverse-rib connections evaluated in Bruls (1991)

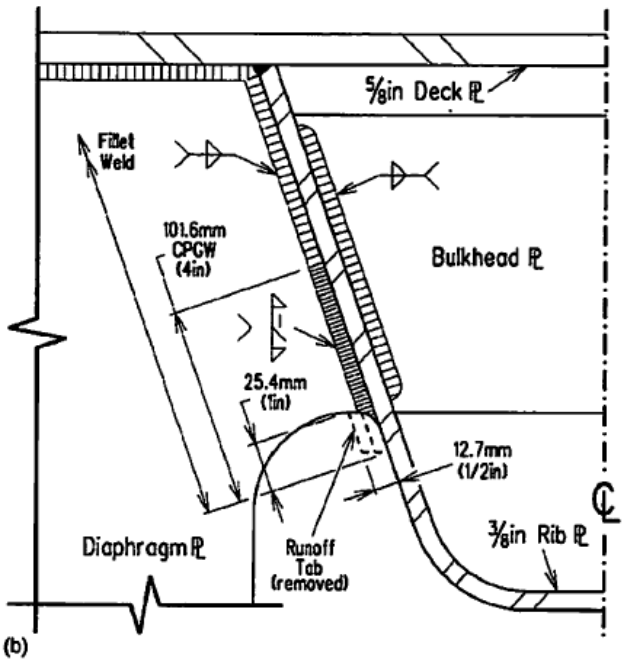

(a) U-rib to transverse-rib connection with bulkheads (Taskopoulos et al. 2003)

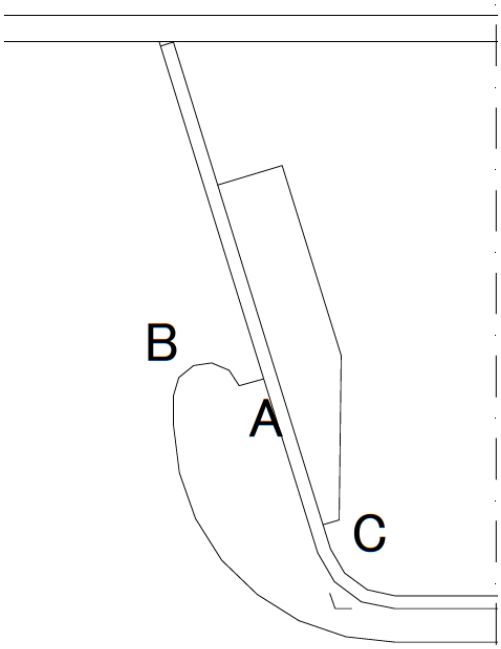

(b) U-rib to transverse-rib connection with inner stiffener (Suganuma and Miki 2007)

Fig. 1-6 U-rib to transverse-rib connections with inner attachments

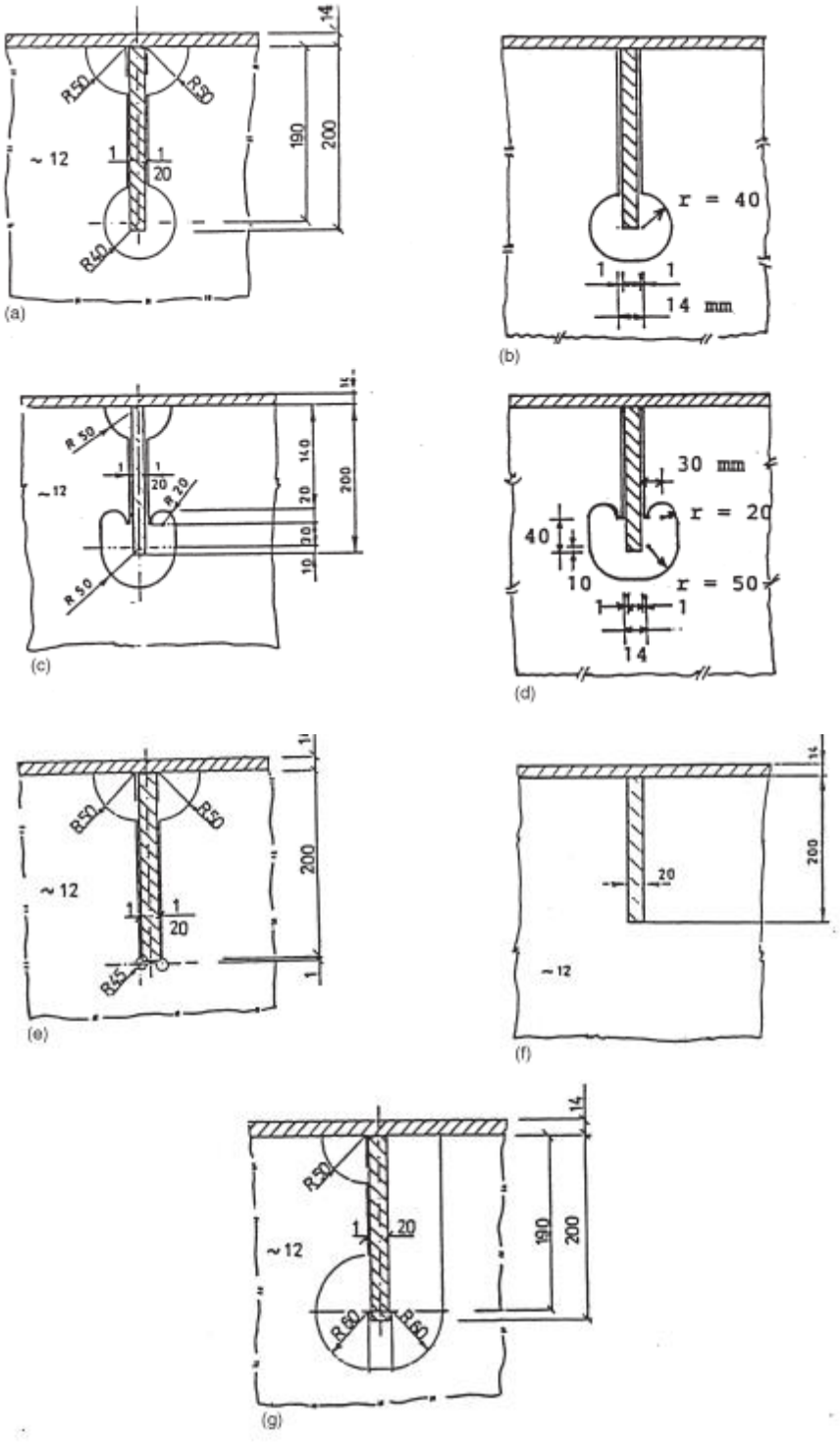

Fig. 1-7 Plate-rib to transverse-rib connections (Fryba 1999)

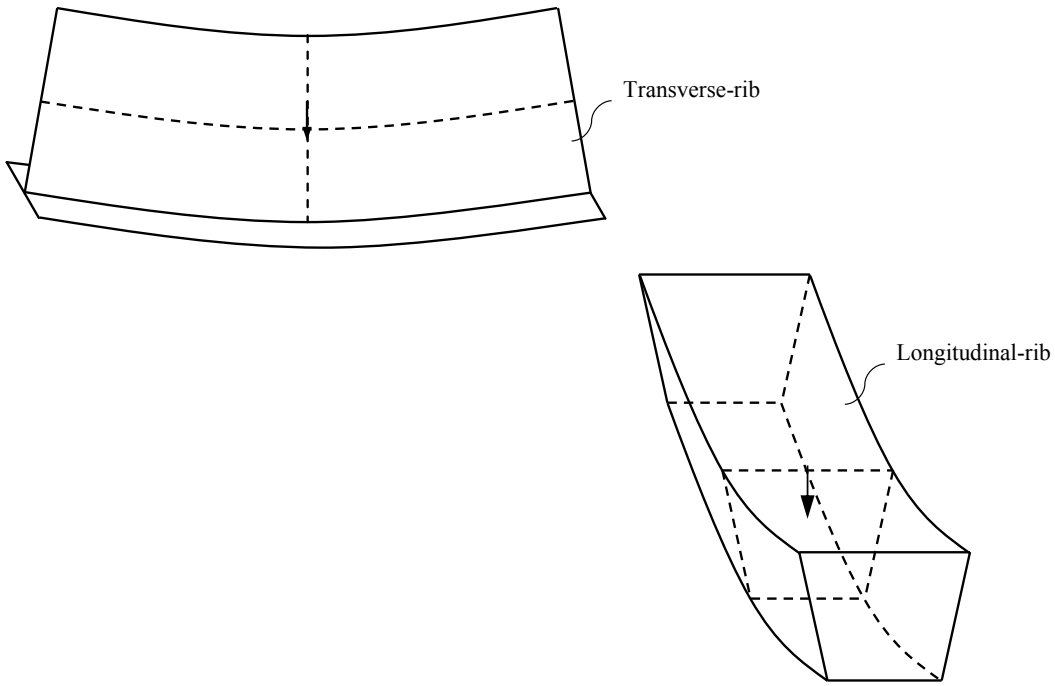

(a) Flexural bending of ribs

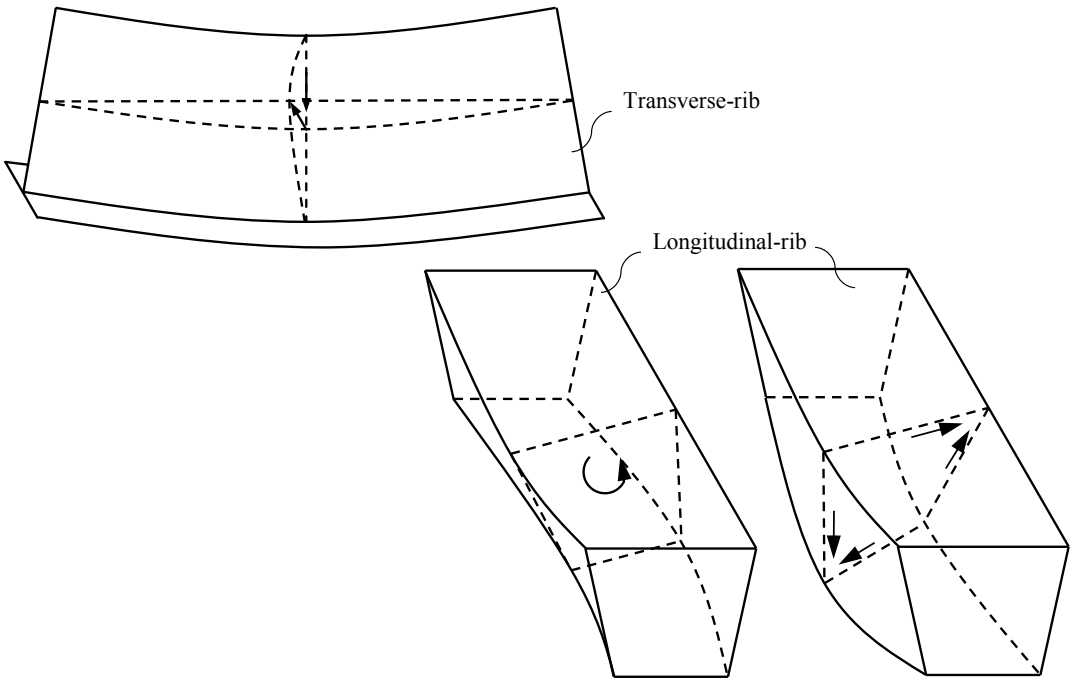

(b) Mix of in-plane and out-of-plane deformations

Fig. 1-8 Estimated deformations of longitudinal and transverse-ribs

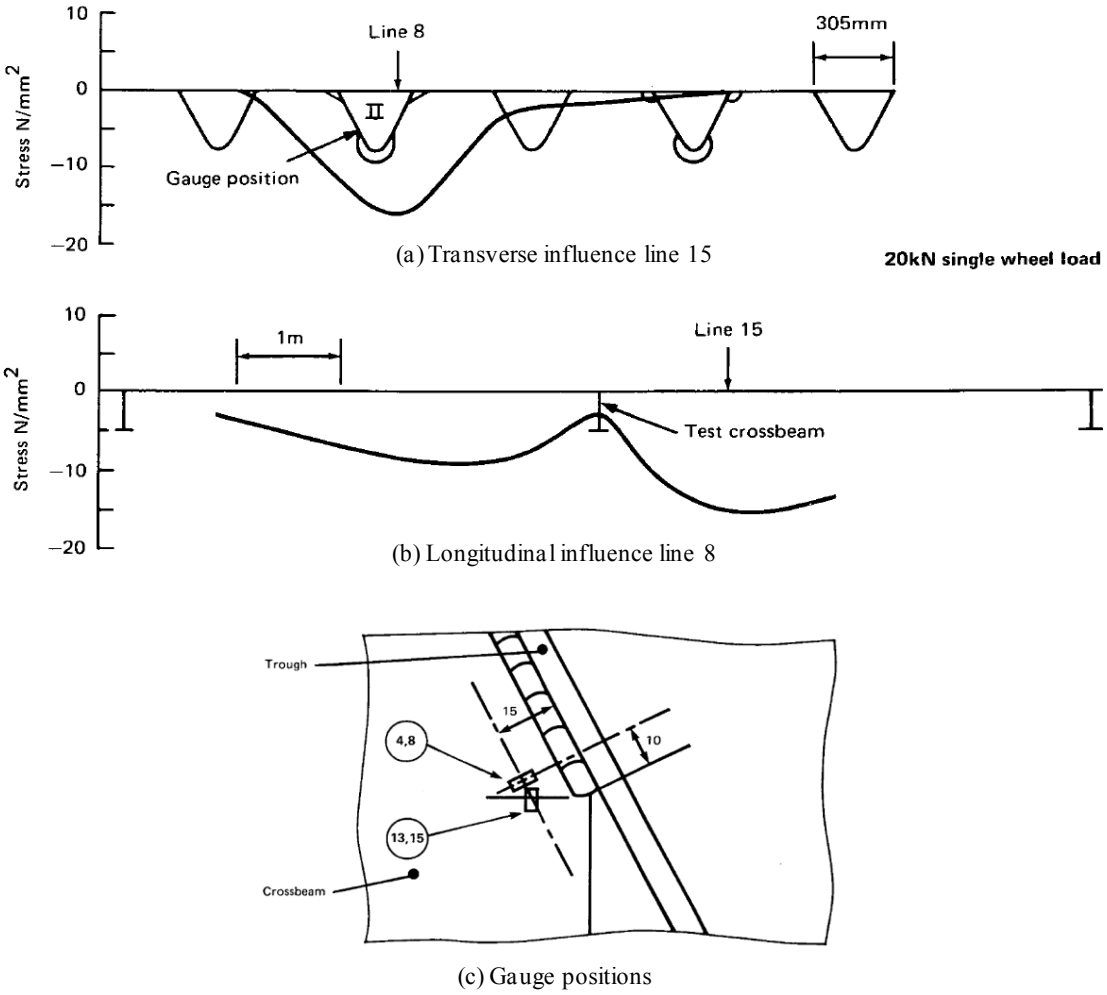

(a) Transverse influence line 15

(b) Longitudinal influence line 8

(c) Gauge positions

Fig. 1-9 Influence line of strain gauge 13 at the transverse rib web near to the slit end (Beales 1990)

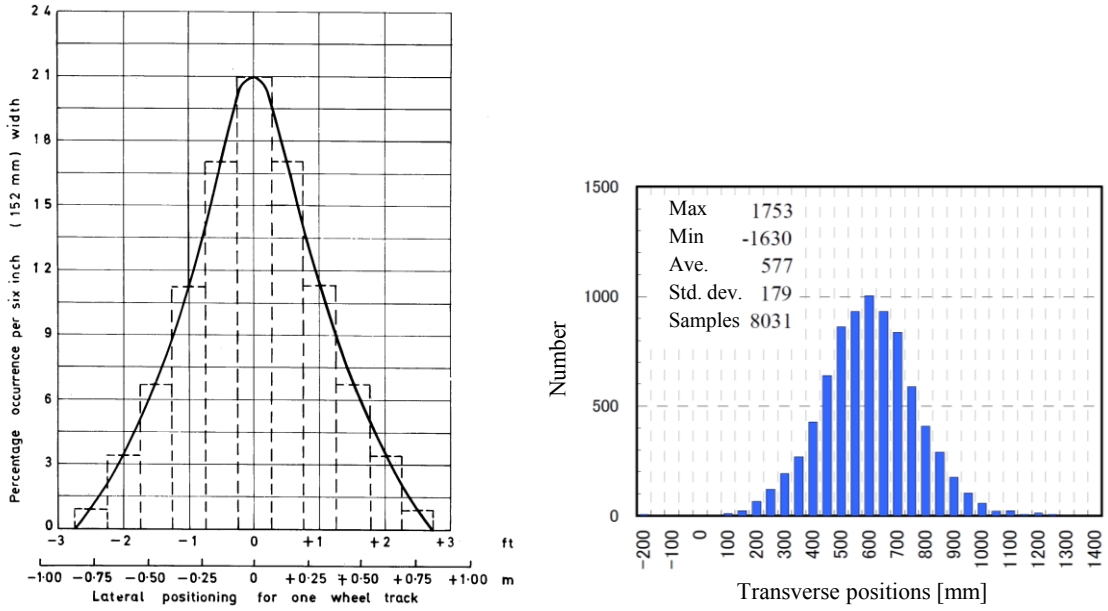

a) Transverse distribution of commercial vehicle wheel units (Leonald 1969)

b) Transverse distribution of left wheel units of middle-size truck (Takada 2009a, translated from *Japanese*)

Fig. 1-10 Transverse distribution of wheel units

2. Proposal of fatigue assessment approaches for orthotropic steel decks

2.1. Introduction

Conventionally, longitudinal ribs and transverse ribs have been designed as girders with deck plates as upper flanges. Therefore, in-plane bending of the girders and the corresponding membrane stress were considered by a nominal stress approach in old specifications (Japan Road Association 1980).

In real situations, orthotropic steel decks are subjected to complex deformations. Orthotropic steel decks are composed of comparatively thin steel plates down to 6 mm and subjected to vehicle loads directly. The thin flexible steel plates easily deform in the out-of-plane direction, with local bending of deck plates, or torsion and distortion of the ribs. The deformed longitudinal ribs and transverse ribs are constrained by each other at the connections, and this constraint also induces local out-of-plane bending of the ribs.

To evaluate fatigue of the connections where stress distributions are complex, a nominal stress approach is not suitable. The nominal stress approach, in which nominal stress is the average stress of the cross section where the stress distribution is not disturbed by the joints (Fig. 2-1a), is the most simple fatigue assessment procedure. However, nominal stress cannot be defined in the longitudinal-rib to transverse-rib connection, since three-dimensional deformation causes complex stress distributions at the complex shape connections (Fig. 2-1b)

In addition, hot spots, where local stress concentrations occur, can move along weld toes as loading positions move. As a rule, hot-spot locations can be determined by the macro stress direction and weld toe shapes. However, since deformations can change as the loading position moves, local stress directions also can change, and the result is moving of hot spots along weld toes (Fig. 2-2). For example, a hot-spot location is the side of the box weld at the joint between a U-rib and a slit transverse rib when a longitudinal in-plane tension force acts on the U-rib, whereas the hot-spot location is the bottom of the box weld when out-of-plane bending about the longitudinal axis acts on the U-rib wall (Fig. 2-2a, b). Since the deformation of longitudinal-rib to transverse-rib connections can change as the loading position moves, hot spots are not fixed points (Fig. 2-2c).

In this chapter, a more suitable fatigue assessment approach is investigated for fatigue assessment of longitudinal-rib to transverse-rib connections. To calculate the local stress at the connections which deform three-dimensionally, the applicability of hot-spot stress approach is investigated (Sec. 2.2). After that, a stress calculation equation is determined by taking account of two features, comparatively thin steel plates and out-of-plane bending stresses, which are known to affect the fatigue strength of orthotropic steel decks (Sec. 2.3). The effects are investigated by using literature fatigue test results and finite element analyses. Finally, the corresponding fatigue design curve is selected from fatigue data for various types of models (Sec. 2.5).

2.2. Hot-spot stress applicability to longitudinal-rib to transverse-rib connections

2.2.1. Determination of local stress and hot spots

To evaluate fatigue of longitudinal-rib to transverse-rib connections where stress distributions are complex and hot-spot locations can move along the weld toes, structural hot-spot stress (hereinafter referred to as hot-spot stress) is expected to be applicable. The hot-spot stress approach can obtain geometrical stress concentrations and estimate fatigue strength without fatigue tests (Radaj 2006). The fatigue strength corresponding to hot-spot stress can be provided by one or a few lines in the S-N diagram regardless of the joint shape (DNV 2006; Hobbacher 2007). The applicability of hot-spot stress has been investigated for various fields: ship structures (Maddox 2002; Lotsberg and Sigurdssn 2006; Fricke 2010), tubular joints, and bridge structures (Miki 1994).

In addition to the geometrical stress concentration caused by a joint itself, more details such as weld shapes can cause an additional stress concentration, which is the so-called notch stress. The notch stress can be calculated by the effective notch stress approach or other methods (Radaj 2006). However, calculating the hot-spot stress costs less than calculating the notch stress concentration, and it can have sufficient accuracy in the case that the weld toe conditions are as-welded.

Furthermore, hot spots can be identified by the hot-spot stress approach even in the case that the hot spot moves along the weld toes by moving loading positions. In this study, hot-spot stresses were calculated by stress extrapolation methods, as shown in Fig. 2-3, provided by the IIW recommendations shown in the following equations (Hobbacher 2007).

$$\sigma_h = \begin{cases} 1.67\sigma_{0.4t} - 0.67\sigma_{1.0t}, & \text{2-1a} \\ 3.0\sigma_{4\text{mm}} - 3.0\sigma_{8\text{mm}} + 1.0\sigma_{12\text{mm}}, & \text{2-1b} \end{cases}$$

where σ and its indexes refer to the surface stresses normal to the weld toes and the distances from the weld toes to the reference points. Equations 2-1a and b were used for the plate surface side (types A and C in Fig. 2-4) and the plate edge side weld toes (type B in Fig. 2-4). For the plate surface side weld toes, hot spots can be determined by calculating the hot-spot stress distribution along the weld toes (Fig. 2-3a). Here, it should be noted that the actual weld toes are wavy-shaped weld toes and hot spots calculated by the procedure above is the engineering approach.

2.3. Thickness and bending effects

2.3.1. Previous studies

Two features of longitudinal-rib to transverse-rib connections are thin steel plates and out-of-plane bending stress. These features should be taken into account for fatigue assessment by the hot-spot stress approach. The hot-spot stresses have been confirmed to have certain accuracy for the assessment of longitudinal-rib to transverse-rib connections (Conner and Fisher 2006; Kozy et al. 2011; Aygul et al. 2012; Miki and Suganuma

2014; Zhang et al. 2015). Because the two features are known to affect fatigue strength and fatigue lives, they enhance the accuracy, as stated in the following sentences.

First, the thickness effect, which has been studied over the decades as part of the size effect of fatigue, can also affect the fatigue strength of longitudinal-rib to transverse-rib connections, because longitudinal-rib to transverse-rib connections are composed of relatively thin steel plates of 6-16 mm. Many specifications and recommendations take account of fatigue strength reductions of plates thicker than the basic thickness of 25 mm in IIW and JSSC recommendations (Hobbacher 2013; Japanese Society of Steel Construction 2012). Conversely, some investigations found that the thickness effect extends to plates thinner than 25 mm. As a result of fatigue tests under bending loads and of crack propagation analyses under axial as well as bending loads, Miki (1987) showed that the thickness effect with an exponent of approximately 0.25 was suitable for cruciform and T joints of 9–75 mm thickness. As a result of analyzing experimental data in the literature, Gurney (1995) showed the thickness effect with a less severe exponent than 0.25 extended at least to a thickness of 10 mm. Kihl and Sarkani (1997) conducted constant and random amplitude fatigue tests on cruciform joints of 6–25 mm thickness, and they concluded that the rule of the thickness effect with an exponent of 0.25 is conservative for low-stress high-cycle conditions (greater than 10^5 cycles) compared with the test results.

In addition to the thickness effect on thinner plates, thickness exponents should also be determined or selected from established specifications or recommendations. In the early stages of size effect investigations using cruciform and T joints, a thickness exponent of 0.25 was proposed. In the present recommendations, various thickness exponents are provided, such as those shown in Table 1-2 (Hobbacher 2013; Japanese Society of Steel Construction 2012). However, applicability of the recommendation to the hot-spot stress approach has not been clarified.

Second, it is known that out-of-plane bending, as compared to axial loads, can increase fatigue strength or fatigue lives of welded joints. To take account of the bending effect, previous studies have proposed reduction factors for bending stress, such as 0.6 and 0.8 for the nominal stress approach (Lotsberg and Sigurdsson 2006; Japanese Society of Steel Construction 2012, respectively), and 0.7 for local stress approaches (Fischer and Fricke 2014). Since out-of-plane bending stress can account for more than half of the stresses near longitudinal-rib to transverse-rib connections, the bending effect should be taken into account, but it has not been confirmed to be applicable to the hot-spot stress approach.

2.3.2. Analysis of fatigue data literature

Coefficients of the thickness and the bending effects in terms of hot-spot stress were investigated by using fatigue test results found in the literature. Hot-spot stresses were computed by consistent finite element analyses in this study to minimize the influences of computation environment differences, such as finite element mesh sizes. The thickness and the bending effects were investigated by fatigue data of out-of-plane gusset and cruciform joints, corresponding to the types A and C, respectively, since enough fatigue data were available. Then the fatigue design curve was selected to provide a safe estimation for all types of fatigue data including the type B component models and structural models, which can have fatigue strengths that are different and smaller in many cases compared to component models (e.g., Anami 2000).

(1) Literature fatigue test results

Fatigue test results of non-load-carrying cruciform and out-of-plane gusset joints with as-welded conditions were corrected to investigate thickness and bending effects (Kamakura et al. 1979; Shimokawa et al. 1985; Maddox 1987, 2011; Miki 1987; Vosikovsky 1989; Yagi 1991; Sakano 1994, 2004; Anami 2001; Huo 2005; Park 2008; Wang 2009; Araki 2012; Mori 2012; Kim 2013; Sakino 2015). Table 2-1 shows the numbers of fatigue data sets in a matrix of thickness and model types taken from the literature. Fatigue data included cruciform joints with a thickness from 6 to approximately 100 mm tested under both axial and bending loads. The available fatigue data of out-of-plane gusset joints tested under axial loads were smaller in number than those of cruciform joints and limited to data of plates thinner than 25 mm. However, the data were enough to investigate the thickness effect for the longitudinal-rib to transverse-rib connections of orthotropic steel decks, which are normally composed of 6-16 mm plates.

Table 2-2 shows a summary of the fatigue data, and more details of the fatigue data are shown in Appendix-A Table A-1–4 and Fig. A-1–7. In this study, fatigue data sets with only fatigue lives shorter than 10^6 cycles were not used in this study, because those fatigue data sets may not be enough to estimate fatigue strength at 2.0×10^6 cycles. The load types were axial, with 4- and 3-point bending cyclic loads with stress ratios of zero or larger than zero. Definitions of fatigue failure were complete failure in all literature data of the component models. Though the materials of fatigue data varied from mild to high strength steels such as HT780 or HT80 (Shimokawa 1985; Anami 2001), the effect of material strength on the fatigue strength of welded joints was not significant.

(2) 2.0×10^6 fatigue strength determination for thickness effect investigation

The mean fatigue strength at 2.0×10^6 cycles in terms of hot-spot stresses ($\Delta\sigma_{f,h}$) was determined based on the IIW recommendation (Hobbacher 2007). The fatigue strengths were calculated with linear regression of hot-spot stress data calculated by multiplying nominal stresses written in the literature by the stress concentration factors. The linear regression regarded fatigue lives as dependent variables. Since short fatigue lives may have different phenomena from high cycle fatigue, test results under high stress ranges that could cause shorter fatigue lives than 10^5 cycles were eliminated from analyses in this study. On the other hand, it was indicated that run-out data should be used to estimate the mean curves of test results in the S-N diagram (Marquis 2002). All fatigue data sets were analyzed without run-out data, which was not included in some fatigue data sets. Such analyses provide conservative estimations of the mean curves.

(3) Hot-spot stress computation by finite element analyses

The hot-spot stresses were computed by elastic finite element analyses using ABAQUS 6.13. An elastic modulus of 205 kN/mm^2 and Poisson's ratio of 0.3 were set in the analyses.

Component specimens and their welded joints were modeled by 6-node solid elements (Fig. 2-5a, b). One-eighth and one-fourth symmetric models were applied for axial and bending load tests, respectively. The solid element sizes were 0.1 times the main plate thicknesses. Inner un-welded surfaces of fillet welded joints were also modeled as surfaces where the main and attached plates could be separated without

contacting each other. Thus, two plates could be overlapped in these models, though this does not happen in real situations. However, the welded joints can have weld root gaps and the gaps can keep two plates separated in a real situation.

Hot-spot stresses were computed as structural stresses by the stress extrapolation methods provided by the IIW recommendations, as shown in Equations 2-1a and b (Hobbacher 2007).

2.3.3. Existence of thickness effect on thicknesses less than 25 mm

The differences between the effects of thicknesses in terms of hot-spot stress and nominal stress first were investigated. Fig. 2-6a and b shows graphs of the stress concentration factors of cruciform, T, and out-of-plane gusset joints as the vertical axes and the thicknesses and the width-thickness ratios of the component joint models as the horizontal axes. More detailed results are shown in Appendix-A Table A-5–7. The stress concentration factors of cruciform and T joints were almost 1.0 regardless of the thickness and the width-thickness ratios. Therefore, analyses of thickness and bending effects in terms of hot-spot stress can give similar results to those in terms of nominal stress. On the other hand, the stress concentration factors of out-of-plane gusset joints were likely to increase as the width-thickness ratio became larger, though only a small correlation existed between stress concentration factors and thicknesses. Therefore, analyzing the thickness effect by the nominal stress approach would include the noises from model dimensions, and the hot-spot stress approach can eliminate the noises. In addition, since the thick plate specimens tended to have a small width-thickness ratio, in which the stress concentration factors were comparatively small, and since actual structures would have larger width-thickness ratios, the fatigue evaluation for thick plate specimens by the nominal approach might not be safe.

Fig. 2-7a shows the relations between corrected thicknesses and fatigue strengths of cruciform joints, and their linear regression lines. More detailed results are shown in Appendix-A Table A-5–7 and Fig. A-8, 9. The corrected thicknesses were determined by the following equations (Gurney 1989, 1999).

$$t' = \min(t_1, 0.5L) \qquad \text{2-2a}$$

$$L = t_2 + 2a \qquad \text{2-2b}$$

Here t' is the corrected thickness; t_1, t_2 are the main plate and attached plate thicknesses, respectively, and a is the weld leg length.

The thickness effects on axially loaded cruciform joints and bending loaded T joints existed down to at least 6-mm thickness with exponents of 0.23 and 0.35, respectively. The result that the thickness effect on cruciform joints can be extended to relatively thinner plates was also suggested in previous research (Miki 1987; Gurney 1995; Kihl and Sarkani 1997). The steeper thickness exponents of the bending loaded T joints were also obtained by Yagi (1991) with fatigue tests on geometrically similar component models under both axial and bending loads. From Fig. 2-7a and previous study results, the thickness effects in terms of hot-spot stress and an exponent of 0.25 could be extended to 6 mm for cruciform joints. Though the thickness exponents of bending loaded T joints were steeper than 0.25, a lower exponent applied to plates thinner than the basic thickness can provide safe estimations. The corrected thickness indicated in Equation

2-2 can be applied to determine the thickness factor, but simply using a main plate thickness equal to or larger than the corrected thickness can give safe fatigue estimations.

Fig. 2-7b shows the relations between thickness and fatigue strength of out-of-plane gusset joints. Thickness effects on axial and bending loaded joints existed down to 8 and 12 mm thicknesses, respectively, and the exponents were 0.28 and 0.35, respectively. The existence of the thickness effect in terms of nominal stress has already been indicated in the literature (Sakano 1994, 2004; Hobbacher 2007), and can be applied to out-of-plane gusset joints with relatively thicker plates. As is similar to cruciform and T joints, thickness effects in terms of hot-spot stresses and an exponent of 0.25 could be extended to plates thinner than 25 mm.

In this study, hereinafter, the thickness exponent of 0.25 was applied to plates with a thickness of 6-25 mm. However, it should be noted that more investigation is required to apply that rule for general fatigue design, since fatigue data was limited in this study.

2.3.4. Fatigue strength increase of bending stress

Fig. 2-8 compares fatigue data of axially and bending loaded joints with a thickness of 6-25 mm. The vertical axis is the hot-spot stress modified by the thickness effect factor $(t/25)^{0.25}$. The figure does not include fatigue data of plates thicker than 25 mm, which are rarely used for orthotropic steel decks and can cause non-conservative fatigue estimations by thickness exponents of 0.25 according to Fig. 2-7. Fig. 2-8 also shows 95% survival curves connected to constant amplitude fatigue limits. To compare axial and bending loaded joints, the axial-bending ratio is defined as follows.

$$\text{ratio} = \begin{cases} \Delta\sigma_{\text{axial},95\%} / \Delta\sigma_{\text{bend},95\%} & (\text{nominal stress approach}) \quad \text{2-3a} \\ \Delta\sigma_{\text{axial,h},95\%} / \Delta\sigma_{\text{bend,h},95\%} & (\text{hot-spot stress approach}) \quad \text{2-3b} \end{cases}$$

where $\Delta\sigma_{\text{axial, 95\%}}$ and $\Delta\sigma_{\text{bend, 95\%}}$ are the 95% survival fatigue strength or constant amplitude fatigue limits in terms of nominal stress for axial and bending loads, respectively, and $\Delta\sigma_{\text{axial, h, 95\%}}$ and $\Delta\sigma_{\text{bend, h, 95\%}}$ are those in terms of hot-spot stress. Bending factors were investigated based on these ratios.

In the comparison of the 95% survival curves, the reduction factor of 0.8 for bending stresses was applicable to the hot-spot stress approach. The axial-bending ratios of cruciform joints were 0.74 and 0.76 at 2.0×10^6 cycles with constant amplitude fatigue limits, respectively. These ratios indicate that the reduction factor of 0.8 for bending stress, suggested by JSSC (2012), can give safe fatigue estimations in the hot-spot stress approach. The axial-bending ratios of out-of-plane gusset joints were 0.68 and 0.86 at 2.0×10^6 cycles and a constant amplitude fatigue limit, respectively. Though the axial-bending ratio at constant amplitude limit was larger than 0.8, the ratio of the JSSC-E class to the bending loaded model data in Fig. 2-8b at a constant amplitude fatigue limit (84 N/mm^2) was 0.74. Here, the JSSC-E class is the fatigue design curve suitable for the hot-spot stress approach by taking account of thickness and bending effects, as described in the following section. In addition, a bending stress reduction factor of 0.8, suggested by JSSC (2012), was selected and applied in this study.

2.4. Fatigue design curve

2.4.1. Re-analysis of fatigue data literature

(1) Fatigue test results in the literature

The selection of a fatigue design curve for the hot-spot stress approach while taking thickness and bending effects into account was investigated by using fatigue data including component and structural models with types A, B and C hot spots. Since the fatigue strength of welded joints depends on joint types even in the hot-spot stress approach, and since types A, B and C hot spots appear in the longitudinal-rib to transverse-rib connections, determination of fatigue design curves required the fatigue data of the three types of hot spots. In addition, since the fatigue strength of structural models can be lower than those of component models, the fatigue data of structural models were used. Those fatigue data were limited in thicknesses, so their thickness effects were not investigated in this study.

Table 2-2 shows a summary of the fatigue data (Kamakura et al. 1979; Shimokawa et al. 1985; Maddox 1987, 2011; Miki 1987; Vosikovsky 1989; Yagi 1991; Sakano 1994, 2004; Anami 2001; Huo 2005; Park 2008; Wang 2009; Araki 2012; Mori 2012; Kim 2013; Sakino 2015, Yagi 1991; Miki 1994; Schumacher 2006; Yamaoka 2010; Kim 2013; Cheng 2015). Each literature source used different crack lengths as the fatigue failure, N_f, as shown in Table 2-2.

(2) Hot-spot stress computation by finite element analyses

The determination of hot-spot stresses of component models were described above. The structural specimens were modeled by 4-node shell elements (Fig. 2-5c). The shell elements were applied to reduce the numbers of degree of freedom and computation costs. Welded joints were modeled with increased thicknesses to simulate the stiffness based on previous research, as shown in Fig. 2-5d (Machida 1992). The sizes of the shell elements were 0.1 times the main plate thicknesses near the evaluated weld toes and the sizes of larger elements were up to 50 mm far from the weld toes. Full models were used except for half symmetric models for ship brackets.

Before analyzing the fatigue data, the difference of the hot-spot stresses between solid and shell element results was investigated. Fig. 2-9 shows stress extrapolations for hot-spot stresses based on solid and shell element results for axially loaded cruciform joints and bending loaded out-of-plane gusset joints. The errors of hot-spot stresses based on shell element results from those based on solid element results were smaller than 3%. Therefore, it is possible to evaluate hot-spot stresses computed by using both element results at the same time. However, the surface stresses of the solid element results were larger than those of the shell element results in the area within 0.3t. Some stress concentrations might be due to local geometries, such as weld toe shapes, and such local stress concentrations could not be computed by shell elements. The concept of the hot-spot stress approach is to obtain the stress concentration factor not by local geometries but by joint detail (structural stresses).

2.4.2. Applicability of JSSC-E class

Fig. 2-10 shows the fatigue strength of the literature data and fatigue class JSSC-E provided by the JSSC recommendation. The vertical axes of Fig. 2-10a and b are the hot-spot stresses and the hot-spot stresses factored by the equations below.

$$\sigma'_{\boldsymbol{h}} = \left(\boldsymbol{t}/25\right)^{0.25}\left(\sigma_{\boldsymbol{h},\mathrm{m}} + 0.8\sigma_{\boldsymbol{h},\mathrm{b}}\right) \quad \text{2-4a}$$

$$\sigma_{\boldsymbol{h},\mathrm{m}} = \left(\sigma_{\boldsymbol{h},\mathrm{obv}} + \sigma_{\boldsymbol{h},\mathrm{rev}}\right)/2 \quad \text{2-4b}$$

$$\sigma_{\boldsymbol{h},\mathrm{b}} = \left(\sigma_{\boldsymbol{h},\mathrm{obv}} - \sigma_{\boldsymbol{h},\mathrm{rev}}\right)/2 \quad \text{2-4c}$$

where $\sigma_{h,\,\mathrm{m}}$ and $\sigma_{h,\,\mathrm{b}}$ are membrane and bending components of hot-spot stresses, respectively, and $\sigma_{h,\,\mathrm{obv}}$ and $\sigma_{h,\,\mathrm{rev}}$ are hot-spot stresses calculated based on obverse and reverse surface stresses. As shown by the results of the previous section, the thickness factor and the bending reduction factor were determined to $(t/25)^{0.25}$ and 0.8. The thickness factor was applied to any type of joints of all thickness ranges, though JSSC recommendations provide the thickness factor for only cruciform and butt welded joints with plates thicker than 25 mm. Fig. 2-10b shows the fatigue strength of plates thinner than 25 mm only, since the thickness exponents of 0.25 can be non-conservative for plates thicker than 25 mm. Such plates are rarely applied to orthotropic steel decks.

Almost all fatigue data satisfied fatigue class JSSC-E in Fig. 2-10b. Though fatigue data sets had 95% survival curves with 77 N/mm2 at 2.0×10^6 cycles, which is 4% smaller than that of JSSC-E class, fatigue data except for type C component models were plotted above the JSSC-E curve. In addition, the 95% survival curve of each type model (e.g., type A component model) was above the JSSC-E class, except the 95% survivals of type C component models were across the JSSC-E curve and located below the JSSC-E curve at approximately $\leqq 1.0 \times 10^6$ cycles. However, the objective of this study, 100-year fatigue strength, is $>1.0 \times 10^6$ cycles. Therefore, the fatigue evaluation using the hot-spot stress modified by Equation 2-4a and the fatigue design curve of class JSSC-E is applicable to fatigue assessment of longitudinal-rib to transverse-rib connections. It should be noted that the abovementioned type C component model results and some of the in-plane gusset joint results were plotted below the constant amplitude fatigue limit of JSSC-E.

Applying the thickness and the bending stress reduction factors enhanced the fatigue assessment. The width between the lower and upper 95% survival curves of fatigue data in terms of factored hot-spot stresses was 30% smaller than that in terms of hot-spot stresses. However, some type B component model results were in the excessively high fatigue strength region even after the factors were applied (Fig. 2-10b). Though it is a safe evaluation, additional investigation is needed to understand these results.

2.5. Summary

In this chapter, a fatigue assessment approach was determined for longitudinal-rib to transverse-rib connections. To calculate the local stresses at the connections that deform three-dimensionally, applicability of the hot-spot stress approach was investigated. After that, a stress calculation equation was determined by taking account of two features of orthotropic steel decks. The features are comparatively thin steel plates and out-of-plane bending stresses, which are known to have an effect on fatigue strength. The effects were investigated by using the literature of fatigue test results and finite element analyses. Finally, a corresponding fatigue design curve was selected from fatigue data including various types of models. The following are the conclusions obtained.

1) The hot-spot stress approach can be applied for fatigue assessment of longitudinal-rib to transverse-rib connections, where three-dimensional deformations are caused and hot spots move as loading positions move.
2) A thickness factor with an exponent of 0.25 and bending stress reduction factor of 0.8 can be applicable to the hot-spot stress approach. The thickness effect could be extended to plates thinner than 25 mm. In addition, the width between the lower and upper 95% survival curves of fatigue data in terms of factored hot-spot stresses was 30% smaller than that in terms of hot-spot stresses.
3) JSSC-E class can provide safe estimations of fatigue strength and fatigue lives for the factored hot-spot stresses, except for type C hot spots under a relatively high stress range approximately equal to or higher than 100 N/mm^2 and type B hot spots under stress ranges lower than the constant amplitude fatigue limit of JSSC-E class.

Table 2-1 Numbers of literature fatigue data sets for each model and each thickness

Model	Type	Load	Thickness (t_{min}-t_{max} means $t_{min}<t\leqq t_{max}$) [mm]					
			6-10	10-16	16-25	25-40	40-63	63-103
Component	A	Axial	7	2	8	3	1	4
	A	Bending	1	2	3	3	3	4
	B	Axial	4	1	-	-	-	-
	C	Axial	3	3	1	2	-	-
	C	Bending	-	2	1	-	-	2
Structure	A	Axial	1	-	1	-	-	-
	A	Bending	-	-	-	-	-	-
	B	Axial	1	-	-	-	-	-
	C	Axial	-	-	-	-	-	-
	C	Bending	2	3	1	-	-	-

*Non-load-carrying joints

Table 2-2 Summary of literature fatigue data

Reference	Model	HS	Stress	*t* [mm]	Failure definition
Component joints					
Shimokawa (1985)	Out-of-plane gusset	A	Membrane	30	Complete failure
Anami (2000)	Out-of-plane gusset	A	Membrane	16	Complete failure
Huo (2005)	Out-of-plane gusset	A	Membrane	8	Complete failure
Park (2008)	Out-of-plane gusset	A	Membrane	20	Complete failure
Wang (2009)	Out-of-plane gusset	A	Membrane	8	Complete failure
Maddox (2011)	Out-of-plane gusset	A	Membrane	30	Complete failure
Araki (2012)	Out-of-plane gusset	A	Membrane	12	Complete failure
Mori (2012)	Out-of-plane gusset	A	Membrane	12	Complete failure
Kim (2013)	Out-of-plane gusset	A	Membrane	10	Complete failure
Sakano (1994)	Out-of-plane gusset	A	Bending	25	Complete failure
	Out-of-plane gusset	A	Bending	75	Complete failure
Sakano (2004)	Out-of-plane gusset	A	Bending	75	Complete failure
Araki (2012)	Out-of-plane gusset	A	Bending	12	Complete failure
Kim (2013)	Out-of-plane gusset	A	Bending	14	Complete failure
Sakino (2015)	Out-of-plane gusset	A	Bending	15	Complete failure
Yamada (1984)	In-plane gusset	B	Membrane	10	20 mm (2.0) [a]
Miki (1993)	Web gusset	B	Membrane	9	40 mm (4.4) [a]
Kondo (2002)	In-plane gusset	B	Membrane	10	20 mm (2.0) [a]
Fricke (2006)	Scallop	B	Membrane	12	No info. available
Kamakura (1979)	Cruciform	C	Membrane	9	Complete failure
	Cruciform	C	Membrane	20	Complete failure
Maddox (1987)	Cruciform	C	Membrane	13	Complete failure
	Cruciform	C	Membrane	50	Complete failure
	Cruciform	C	Membrane	100	Complete failure
Yagi (1991)	Cruciform	C	Membrane	10	Complete failure
	Cruciform	C	Membrane	22	Complete failure
	Cruciform	C	Membrane	40	Complete failure
	Cruciform	C	Membrane	80	Complete failure
Miki (1987)	Cruciform	C	Bending	9	Complete failure
	Cruciform	C	Bending	16	Complete failure
	Cruciform	C	Bending	50	Complete failure
Vosikovsky (1989)	Cruciform	C	Bending	16	Complete failure
	Cruciform	C	Bending	26	Complete failure
	Cruciform	C	Bending	52	Complete failure
	Cruciform	C	Bending	78	Complete failure
	Cruciform	C	Bending	103	Complete failure
Yagi (1993)	Cruciform	C	Bending	22	Complete failure
	Cruciform	C	Bending	40	Complete failure
	Cruciform	C	Bending	80	Complete failure
Structure models					
Yagi (1991)	Bracket	A	Membrane	22	100 mm (4.5) [b]
Kim (2013)	Web gusset	A	Membrane	9	30 mm (3.3) [b]
Yamaoka (2010)	Orthotropic steel deck	B	Membrane	9	40 mm (2.5) [a]
Schumacher (2006)	Pipe to pipe	C	Bending	12.5	Through-thickness
	Pipe to pipe	C	Bending	20	Through-thickness
Cheng (2015)	Pipe to pipe	C	Bending	8	Through-thickness
	Pipe to pipe	C	Bending	10	Through-thickness
	Pipe to pipe	C	Bending	12	Through-thickness

HS: Hot-spot type, Stress: stress gradient over thickness – Membrane (M) or Bending (B),
[a] twice of plate edge crack length at fatigue failure (c / t_1), [b] surface crack length c at fatigue failure (c / t_1)

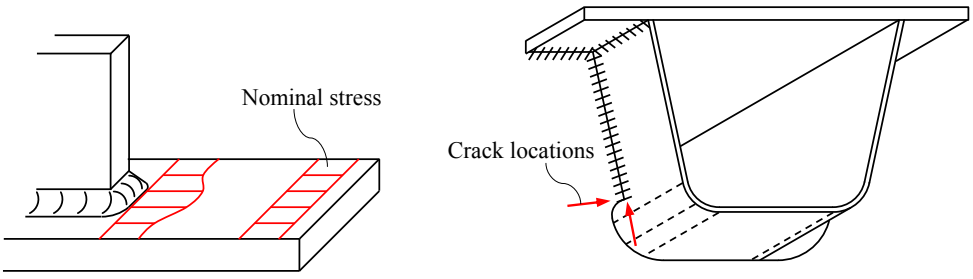

a) Simple joints b) Longitudinal-rib to transverse-rib connections

Fig. 2-1 Difficulty of nominal stress approach application to longitudinal-rib to transverse-rib connections

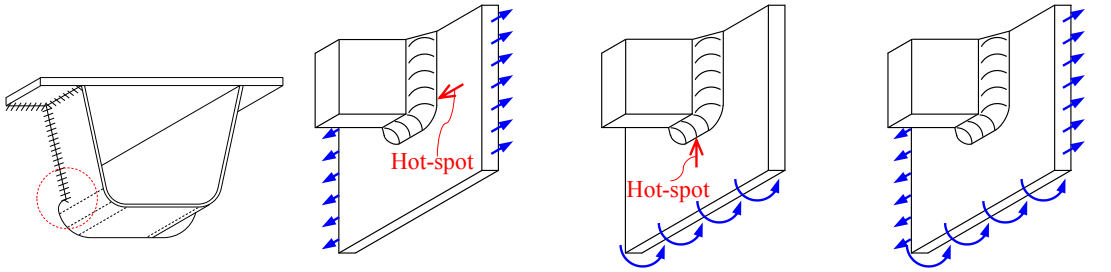

a) Connection between U- and transverse-rib

b) Hot-spot under in-plane tension

c) Hot-spot under out-of-plane bending

d) Mix of in-plane tension and out-of-plane bending

Fig. 2-2 Move of the hot-pot at welded joints between U- and transverse-ribs

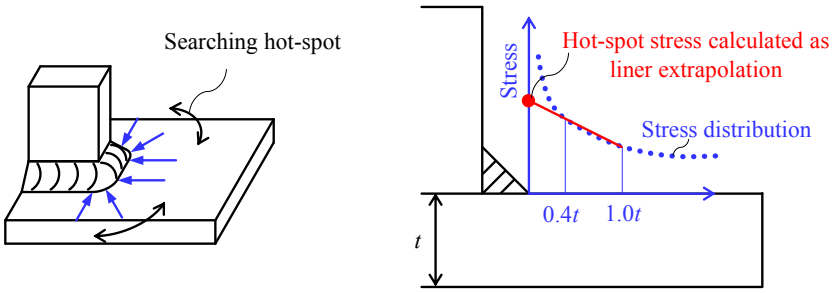

a) Hot-spot stress calculations at plate surface side weld toes

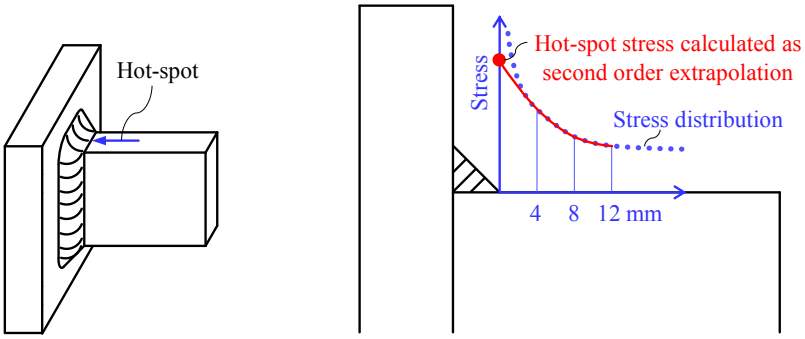

a) Hot-spot stress calculations at plate edge side weld toes

Fig. 2-3 Hot-spot stress calculations

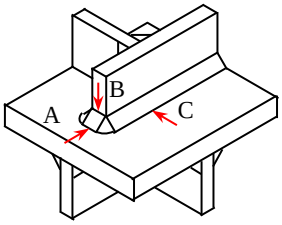

Fig. 2-4 Weld toe types

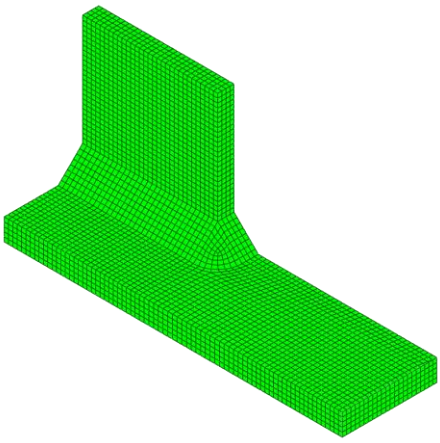

a) Out-of-plane gusset joints

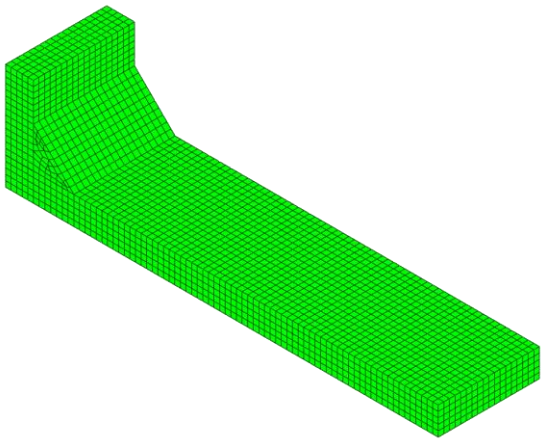

b) Cruciform joints

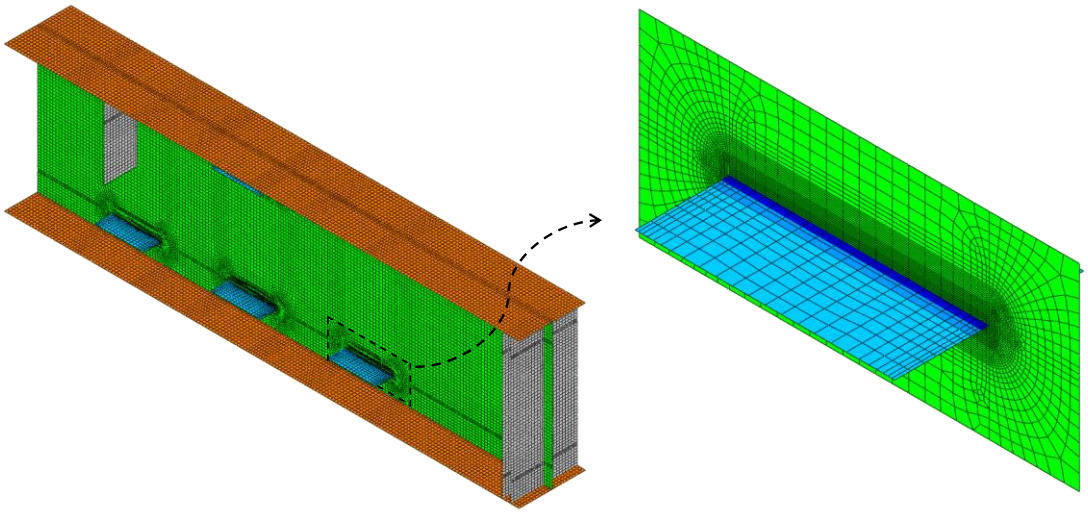

c) Structure model (web gusset of plate girder)

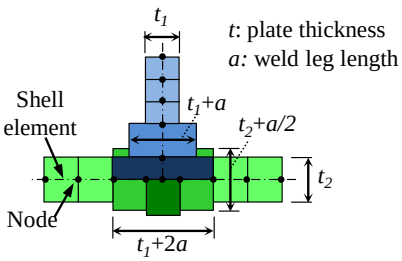

d) Shell element thickness at welded joints

Fig. 2-5 Finite element models

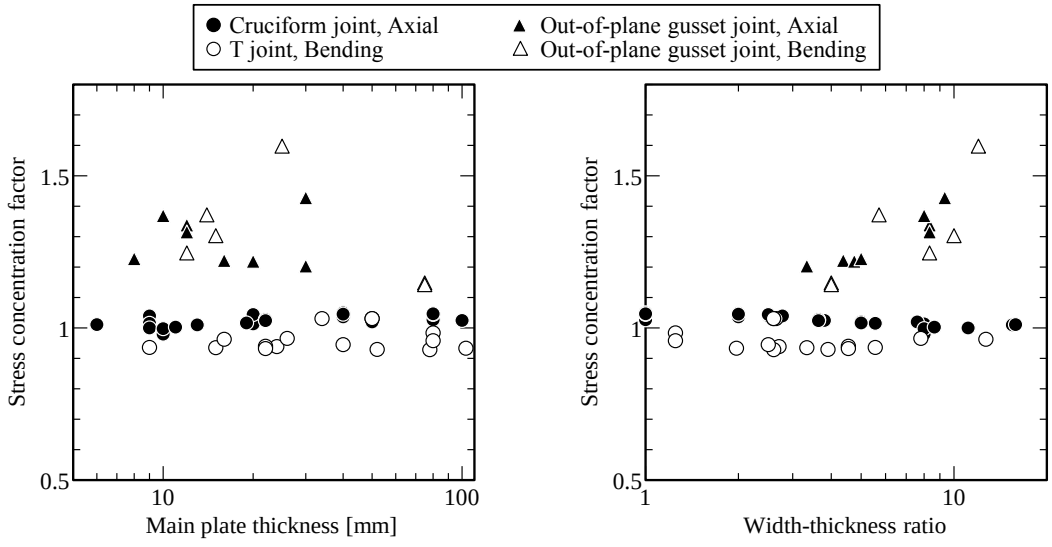

a) Effect of thickness b) Effect of width-thickness ratio

Fig. 2-6 Influence of thickness and width-thickness ratios on stress concentration factors

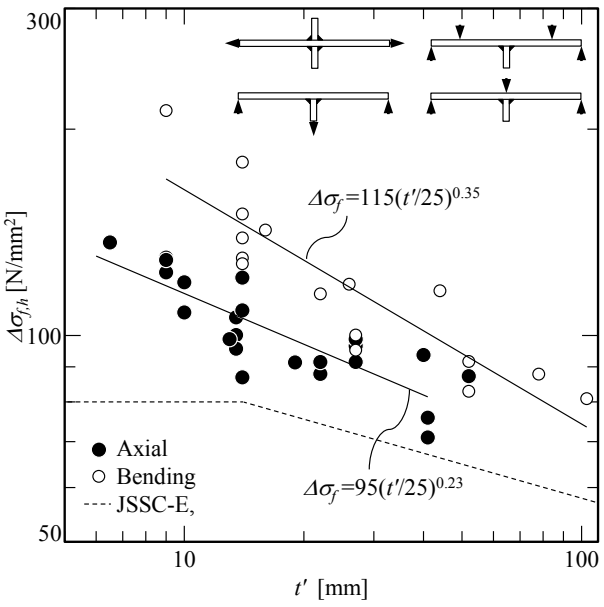

a) Cruciform and T-joints

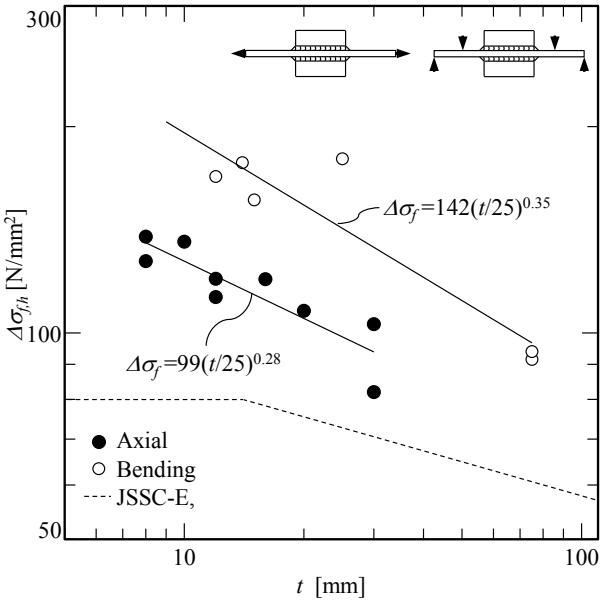

b) Out-of-plane gusset joints

Fig. 2-7 Relations between thicknesses and fatigue strength

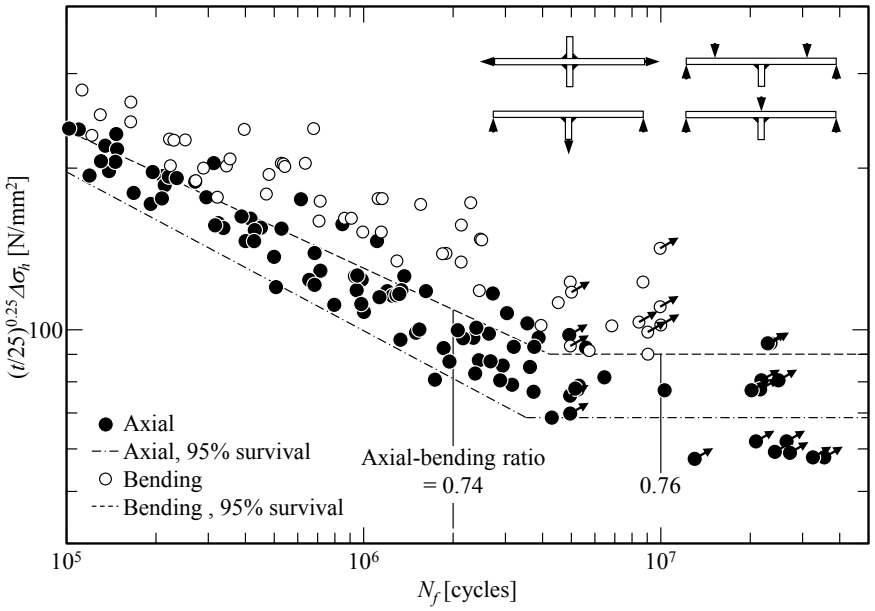

a) Cruciform and T-joints

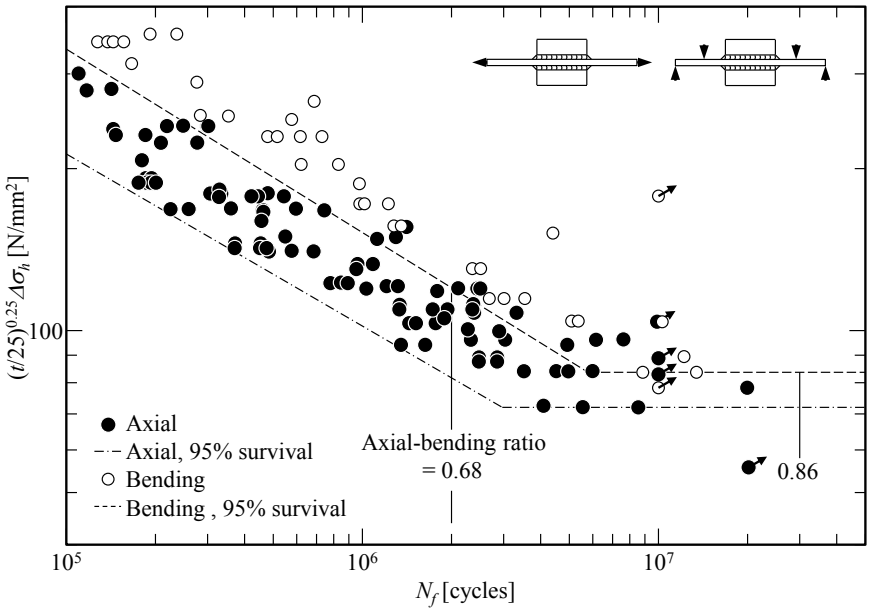

b) Out-of-plane gusset joints

Fig. 2-8 Fatigue strength comparison between axially- and bending-loaded joints

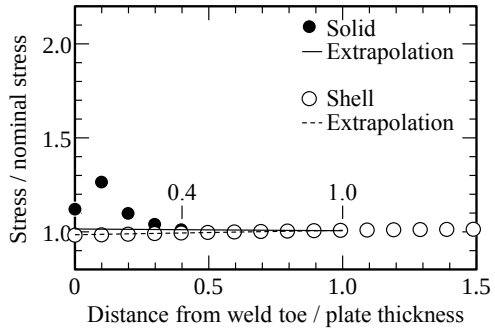

a) Axially loaded cruciform joints with 9 mm thickness (Kamakura, 1979)

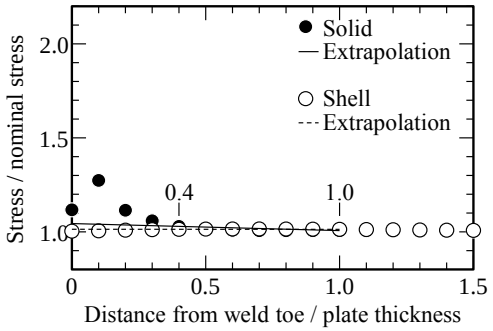

b) Axially loaded cruciform joints with 20 mm thickness (Kamakura, 1979)

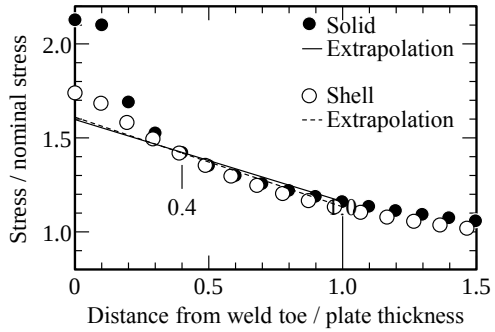

c) Bending loaded out-of-plane gusset joints with 25 mm thickness (Sakano, 1994)

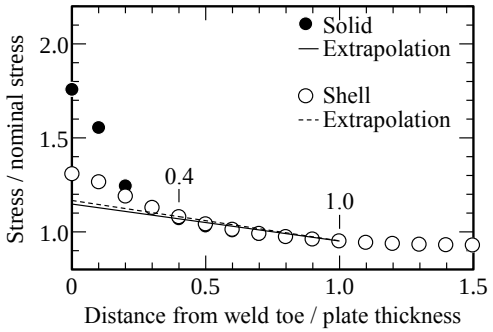

d) Bending loaded out-of-plane gusset joints with 75 mm thickness (Sakano, 1994)

Fig. 2-9 Comparison of solid elements and shell elements

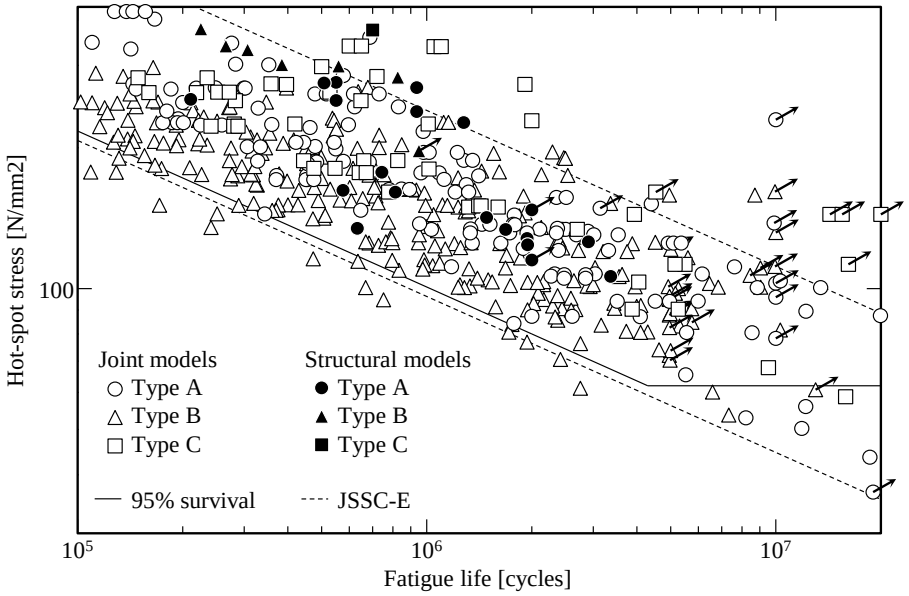

a) Distribution of fatigue data, without taking account of thickness and bending factor
(Fatigue data covers all thicknesses)

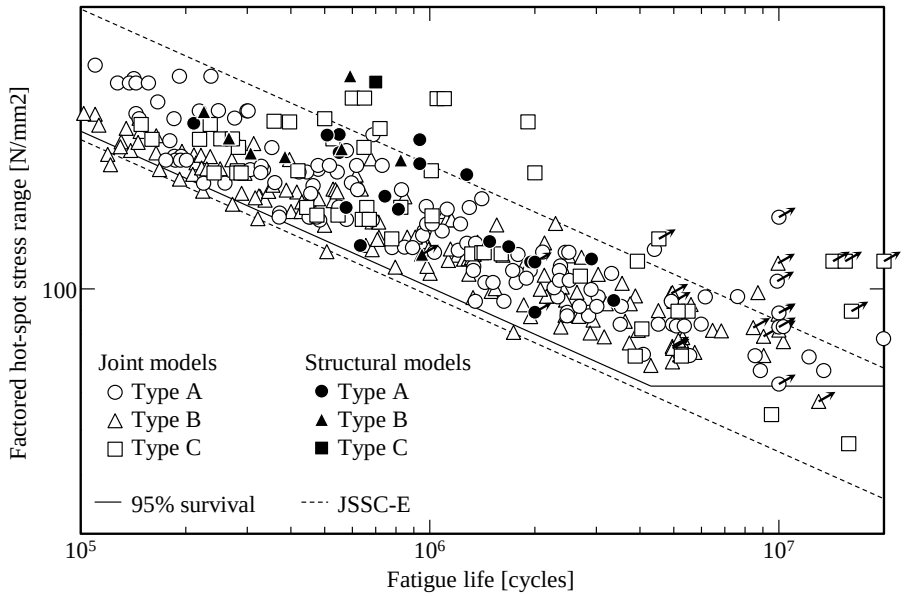

b) Distribution of fatigue data, with taking account of thickness and bending factor
(Fatigue data includes only $t \leqq 25$ mm due to applicability limit of thickness factor)

Fig. 2-10 Fatigue strength in terms of hot-spot stress and factored hot-spot stress

3. Investigations of fatigue resistant structures for orthotropic steel decks

3.1. Introduction

Orthotropic steel decks, which have light weight, are placed in many long-span bridges and city expressways for renewal of deteriorated reinforced concrete decks. However, orthotropic steel decks have serious fatigue problems that require improvement. Fatigue cracks initiated from longitudinal-rib to transverse-rib connections are the largest in number and account for approximately 40% of all cracks, according to investigation of Japanese expressway bridges under service (Mori ed. 2010).

Longitudinal-rib to transverse-rib connections without scallops and slits are expected to have high fatigue strength. The upper scallops were introduced on transverse-rib webs to avoid overlapping of longitudinal-rib to transverse-rib and rib-to-deck welds. However, afterward, eliminating scallops was recommended based on previous research (Miki et al. 1995). On the other hand, lower slits (or cut outs) were introduced for efficient fabrication of longitudinal-rib to transverse-rib connections with continuous longitudinal-ribs (Seeger 1964). Eliminating fatigue cracks around lower slits has been attempted by changing slit shapes and/or adding attachments such as bulkheads and inner stiffeners (Ohashi et al. 2000; Taskopoulos et al. 2003, Conner and Fisher 2006, Miki and Suganuma 2014; Hanji et al. 2013). Longitudinal-rib to transverse-rib connections without scallops and slits (hereinafter, non-slit connections) have also been reported to be capable of reducing stress on the connections (Kolstein 2001; Katsumata et al. 2000). The slits can be eliminated by managing manufacturing techniques, such as checking weld root gaps.

However, previous studies of longitudinal-rib to transverse-rib connections did not sufficiently consider the moving loading position. The positions of a vehicle moving in the longitudinal direction are transversely distributed (Leonard 1969). Furthermore, critical loading positions, which are the positions causing maximum and minimum stresses on longitudinal-rib to transverse-rib connections, are a distance away from the evaluated connections (Miki et al. 1995). Therefore, fatigue tests or fatigue assessments without taking account of the critical loading positions can result in incorrect fatigue strength and crack initiation points compared to those of actual bridges. The critical loading positions have not been clarified except for some U-rib slit connections (Suganuma and Miki 2006).

From the background above, the following objectives of this chapter were established.

1) Clarify critical loading conditions that are the most severe for the fatigue of longitudinal-rib to transverse-rib connections.
2) Evaluate and compare fatigue strengths of slit and non-slit connections under the critical loading conditions.

3.2. Models and analysis method

3.2.1. Connection models

The fatigue strengths of 32 models with U-ribs, V-ribs, and plate ribs were evaluated (Table 3-1). The connections are named and followed by two characters that indicate the rib type and slit/non-slit condition, such as connection US indicating the U-rib and the slit connection. The fatigue assessments used deck panel models (Fig. 3-1 to Fig. 3-4), with the each type of connections. The evaluated connections in the deck panel models were the intersections between each longitudinal rib and the center transverse ribs, though it should be noted that deformations of longitudinal ribs adjacent to main girders could be significantly affected by boundary conditions at deck plate ends supported by main girders, which are different from actual boundary conditions. The deck panel models were actual-size partial models composed of main girders, three or more longitudinal ribs, and three or four transverse ribs. The deformation of these structural members should be taken into account when the stress conditions of longitudinal-rib to transverse-rib connections are evaluated (Suganuma and Miki 2007). The appropriate stress conditions of longitudinal-rib to transverse-rib connections are considered difficult to obtain by using smaller models, such as models with only one transverse rib.

Fig. 3-1 shows the shapes of the deck panel models and the connections with closed-section longitudinal ribs. Connections US, UN, VS, and VN were evaluated to investigate the effect of rib shapes and the slit on the fatigue strength of the connections. connections VN_1 through VN_6 were evaluated to investigate the dimensions of V-ribs on the fatigue strength of the connections. The cross section of the U-rib and its slit detail were decided for a common cross section applied to orthotropic steel decks in Japan and the recommended standard detail, respectively (Japan Road Association 2014). The V-rib cross section was decided to have the same radius as in the bending plate process and approximately the same section area as that of the U-rib. Connection VN was used to investigate the effect of cross sections on rib distortions and distortion-induced stress on longitudinal-rib to transverse-rib connections indicated in previous studies (Leherke 1997; Delesie et al. 2008; Katsumata et al. 2000).

Fig. 3-2 to Fig. 3-4 show shapes of the deck panel models and the connections with open-section longitudinal ribs. Connections PS, PC and PN were evaluated to investigate the effects of the slit on the fatigue strength of the connections. Connections PN_{10}–PN_{29} were evaluated to investigate the effects of plate rib and transverse rib dimensions on the fatigue strength of the connections. The plate rib cross sections of connections PS, PC, and PN were decided to have approximately the same cross section modulus as a commonly used bulb rib with 230-mm height and 11-mm thickness, where the effective width of the deck plates was taken into account for the cross sections. The slit detail of connection PS was based on the recommended standard detail with its radius enlarged to 45 mm, which could improve fatigue strength according to investigations of the Metropolitan Expressway in Japan (Mori ed. 2010).

Inner diaphragms were installed in the deck panel models with the U- and the V-ribs to simulate actual structural conditions. Diaphragms are installed at the longitudinal connections of actual structures for protection against corrosion. In this study, the effect of inner diaphragms on fatigue strength was also investigated, since it can increase stresses on longitudinal-rib to transverse-rib connections (Katsumata et al. 2000).

Longitudinal-rib span lengths were decided based on common lengths of actual

structures in Japan. The span lengths of the U- and the V-ribs were taken as the upper limit length for the standard orthotropic steel deck described in the recommendation for fatigue designs of steel road bridges (日本道路協会 2002). The common span length of open cross-sectional longitudinal ribs in Japan is 1250-2000 mm, and so the span length of the plate-ribs was taken as two-thirds of that of the U-rib and the V-ribs in order to make the total lengths of all deck pane models equal.

The weld leg length was taken as 6 mm, except the length was 8 mm for joints between the plate ribs and the non-slit transverse ribs. The 8-mm length was used to keep adequate weld throats against enlarged 2-mm weld root gaps for efficient assembling of connection PN.

Though surfacing has been known to affect stresses of orthotropic steel decks, it was neglected in this study due to the uncertainty of its mechanical properties for finite element analyses. The surfacing would decrease the stress of orthotropic steel decks up to a certain temperature. Therefore, deck panel models without surfacing result in safe fatigue evaluations.

3.2.2. Evaluated weld toes

Fig. 3-5 shows evaluated weld toes, where stresses would be concentrated, to be evaluated for fatigue assessment of longitudinal-rib to transverse-rib connections. Numerous hot spots along weld toe lines mean somewhere on the toe line will be a hot spot. Weld toe numbers of 1 and 2 were given to the transverse- and longitudinal-rib side weld toes, respectively, of welded joints between longitudinal and transverse ribs. In the case of connection PS, weld toe numbers of 3 and 4 were given to the transverse rib and deck plate side weld toes, respectively, of welded joints between the transverse rib and the deck plate. It should be noted that weld toe 4 has almost no fatigue cracks according to investigations in the Japanese expressways. In the following descriptions, weld toes are named as the connection name combined with two numbers indicating the evaluated part number (Fig. 3-5a–d) and weld toe number (Fig. 3-5e–k), such as weld toe US-31 indicating hot spot 1 in evaluated part 3 of connection US.

3.2.3. Loads

Fig. 3-6 shows the load model and positions for stress analyses. The load model of 100 kN, uniformly distributed on the loading area simulating a double tire, was decided based on a fatigue design load (T load) specified in the Specification for Highway Bridges (Japan Road Association 2014). The T load is one axle, which simplifies the rear tandem axle of trucks. This study used the simplified load model to clarify relations between load positions and hot-spot stresses of evaluated connections.

The load position, which means the center of the double tire load where no loading was put, was moved in the longitudinal and transverse directions. By using the coordinate system with x and y for the longitudinal and transverse directions, respectively, and the origin at the middle of the center transverse ribs of the models, loads were positioned at x=-1200, -1000, …, +1200 mm of each lane at y=-800, -640, …, +800 mm in the case of the deck panel models with connections US, UN, and VN, and x=-800, -700, …, +800 mm of each lane at y=-800, -640, …, +800 mm in the case of the deck panel models with connections PS and PN.

3.2.4. Finite element analysis conditions

Elastic finite element analyses were conducted by using ABAQUS 6.13 with the following conditions. Finite element models were composed of 4-node shell elements with reduced integration, as shown in Fig. 3-7a. The mechanical properties of steel were 205 kN/mm^2 for the elastic modulus and 0.3 for Poisson's ratio. Boundary and loading conditions were simply supported main girders with pressure on the deck plates.

The sizes, shapes, and applied thicknesses of shell elements around hot spots were controlled to compute the stress concentration at welded joints. The elements were shaped as substantially rectangle with sizes equal to or smaller than 0.2 times thicknesses, as shown in Fig. 3-7b. In the case that hot spots were at the plate edge, 2 mm was applied to the element sizes. The thicknesses at welded joints were increased based on previous research to simulate increased stiffness, as shown in Fig. 3-7c (Machida 1992). The other parts of the deck panel models were meshed at a relatively coarse size up to 100 mm. Since only the evaluated parts were fine-meshed, the deck panel models of connection PS and PN had different meshes, but both models were geometrically the same.

No imperfections, including welding residual stresses and geometrical imperfections, were input in the finite element models. Not including welding residual stresses, which were assumed as tension stresses near yielding stresses, means that the effect of the stress ratio on fatigue strength was small.

3.2.5. Hot-spot stress computation procedures

Hot-spot stresses were computed as structural stresses by stress extrapolations which took account of thickness and bending effects by the following equations, as discussed in the previous chapter.

$$\sigma'_h = K_t\left(\sigma_{h,m} + K_b\sigma_{h,b}\right) \quad \text{3-1a}$$

$$K_t = \left(t/25\right)^{0.25} \quad \text{3-1b}$$

$$K_b = 0.8 \quad \text{3-1c}$$

$$\sigma_{h,m} = \left(\sigma_{h,obv} + \sigma_{h,rev}\right)/2 \quad \text{3-1d}$$

$$\sigma_{h,b} = \left(\sigma_{h,obv} - \sigma_{h,rev}\right)/2 \quad \text{3-1e}$$

where K_t and K_b are factors of thickness and bending effects on fatigue strength, $\sigma_{h,m}$ and $\sigma_{h,b}$ are membrane and bending components of hot-spot stresses, and $\sigma_{h,obv}$ and $\sigma_{h,rev}$ are hot-spot stresses based on evaluated (obverse) and reverse surface stresses. Hot-spot stresses based on surface stresses were calculated as the following equations.

$$\sigma_h = \begin{cases} 1.67\sigma_{0.4t} - 0.67\sigma_{1.0t} & \text{3-2a} \\ 3\sigma_{4\,\mathrm{mm}} - 3\sigma_{8\,\mathrm{mm}} + \sigma_{12\,\mathrm{mm}} & \text{3-2b} \end{cases}$$

where σ on the right side of the equation is surface stress of the reference point, perpendicular to the weld toe lines, and the subscripts of σ mean the distance from the weld toes to the reference points. Equation 3-2a was applied for types A and C hot-spots, and Equation 3-2b for type B hot spots, as shown in previous chapter, Fig. 2-4.

Fig. 3-8 shows the procedure to determine the hot spots with the weakest fatigue strength. The procedure comprises the following: determining the characteristic stresses of each hot spot for all loading cases (Fig. 3-8b–e), determining the critical loading positions causing maximum and minimum hot spot stresses, and hot-spot stress ranges of each hot spot (Fig. 3-8f, g), determining the weakest fatigue strength hot spot (Fig. 3-8h, i) of the connections.

Fig. 3-8c and d show the procedure to determine the characteristic stresses, which are the maximum and minimum value of hot-spot stresses along the weld toe line. The results of PN-21 are shown in the figure as an example. The hot spots were composed of several nodes in the finite element model, so that hot-spot stresses were not a unique value for the hot spot but can be calculated at several nodes. Here, the hot-spot stresses at the nodes were modified for the bending and the thickness effects by Equation 3-1a. Furthermore, the hot-spot stress distributed along the weld toe line, and the nodes having the maximum and minimum hot-spot stresses (hereinafter, called characteristic stresses) of the weld toe changes as the load position moves (Fig. 3-8c, d). Hence, the characteristic stresses of the weld toe can be missed if the evaluated nodes are fixed. To take account of the distribution change, the characteristic stresses were searched along the weld toe line for each loading case. The following descriptions show the procedure to determine the characteristic stresses with numerical expressions. Let *pos*=1–*n* be the loading cases and *node*=1–*m* be the node numbers composing the evaluated weld toe lines, and then the hot-spot stress of each node for each loading case is expressed as the following equations.

$$\begin{aligned}\sigma'_{h,pos,node} = {} & \sigma'_{h,1,1}, \sigma'_{h,1,2}, .., \sigma'_{h,1,m}, \\ & \sigma'_{h,2,1}, \sigma'_{h,2,2}, .., \sigma'_{h,2,m}, \\ & \vdots \\ & \sigma'_{h,n,1}, \sigma'_{h,n,2}, .., \sigma'_{h,n,m}\end{aligned} \qquad 3\text{-}3$$

The characteristic stresses along the weld toe line for each loading case are expressed as the following equations.

$$\sigma'_{h,pos,\mathrm{u}} = \max\left(\sigma'_{h,pos,1}, \sigma'_{h,pos,2}, .., \sigma'_{h,pos,m}\right) \qquad 3\text{-}4a$$

$$\sigma'_{h,pos,\mathrm{b}} = \min\left(\sigma'_{h,pos,1}, \sigma'_{h,pos,2}, .., \sigma'_{h,pos,m}\right) \qquad 3\text{-}4b$$

$$pos = 1,2,..,n \qquad 3\text{-}4c$$

In the case that only one node composes a target weld toe, such as PN-22, $\sigma'_{h,pos,\mathrm{u}}$ and $\sigma'_{h,pos,\mathrm{b}}$ are the same value as $\sigma'_{h,pos,1}$.

Fig. 3-8f and g show the procedure to determine the loading cases causing the maximum and minimum hot-spot stresses, which are $\sigma'_{h,\max}$ and $\sigma'_{h,\max}$, respectively. The actual vehicle load moves in both longitudinal and transverse directions and results in variation of the characteristic stresses ($\sigma'_{h,pos,\mathrm{u}}$ and $\sigma'_{h,pos,\mathrm{b}}$), as mentioned above. Hence, $\sigma'_{h,\max}$, $\sigma'_{h,\min}$, and their ranges were determined by the following equations, after iterating the procedure to determine the characteristic stresses for all loading cases.

$$\sigma'_{h,\max} = \max\left(\sigma'_{h,1,\mathrm{u}}, \sigma'_{h,2,\mathrm{u}}, .., \sigma'_{h,n,\mathrm{u}}\right) \quad \text{3-5a}$$

$$\sigma'_{h,\min} = \min\left(\sigma'_{h,1,\mathrm{b}}, \sigma'_{h,2,\mathrm{b}}, .., \sigma'_{h,n,\mathrm{b}}\right) \quad \text{3-5b}$$

$$\Delta\sigma'_h = \sigma'_{h,\max} - \sigma'_{h,\min} \quad \text{3-5c}$$

The load positions causing $\sigma'_{h,\max}$ and $\sigma'_{h,\min}$ are called POS_{max} and POS_{min} in this study. Loadings on POS_{max} and POS_{min} alternately can cause the largest hot-spot stress ranges ($\Delta\sigma'_h$) of hot spots and were considered as the critical loading condition in this study.

On the other hand, hot-spot stress ranges can also be calculated for each node in the following equations.

$$\sigma'_{h,\max,node} = \max(\sigma'_{h,1,node}, \sigma'_{h,2,node}, .., \sigma'_{h,n,node}) \quad \text{3-6a}$$

$$\sigma'_{h,\min,node} = \min(\sigma'_{h,1,node}, \sigma'_{h,2,node}, .., \sigma'_{h,n,node}) \quad \text{3-6b}$$

$$\Delta\sigma'_{h,node} = \sigma'_{h,\max,node} - \sigma'_{h,\min,node} \quad \text{3-6c}$$

$$node = 1,2,..,m$$

The hot-spot stress range calculated by Equation 3-5c might have a larger value than the hot-spot stress ranges of each node in the weld toe lines (Equation 3-6c). However, it has not been clarified whether Equation 3-5c or Equation 3-6c is appropriate for fatigue evaluation in the case that the hot-spot stress distribution along the weld toe lines changes as the loading positions move. Therefore, Equation 3-5c was applied as a safe evaluation in this study.

Fig. 3-8i shows the procedure to determine the weakest fatigue strength hot spots of the connections. The hot spots having the largest hot-spot stress ranges were assumed to be the location where a fatigue crack would initiate first in the connections, though the fatigue strengths or the fatigue lives of weld toes can be determined not only by the hot-spot stress range but also many other parameters, such as stress ratio, notch shape, and so on. In the case that two or more hot spots have almost the same hot-spot stress ranges, the one with the higher stress ratio than the other was selected.

3.3. Critical loading conditions for three-dimensionally deformed connections

3.3.1. Hot-spot location moving

Fig. 3-9 shows the hot-spot stress distributions along the weld toes that are the load cases causing the maximum and the minimum hot-spot stresses at the evaluated weld toes (load A and B in Fig. 3-9, respectively). Each of the weld toes in Fig. 3-9 has the largest hot-spot stress ranges of each of the models except for PS-32 and PN-31. Though PS-23 and PN-32 have the largest hot-spot stress ranges in the connections, they were weld toes at plate edges and composed of only one node. In the following description, “hot spot” means the node where the largest tension or compression hot-spot stresses were caused in each of the weld toes.

The hot-spot locations along weld toes were moved as the loading position moved. The hot-spot locations were different from load A to load B in all of the weld toes except for US-32 (Fig. 3-9b–f). The hot spots of US-32 were located at the bottom center of the box weld when both the maximum and the minimum hot-spot stresses, respectively, were caused (Fig. 3-9a). However, the hot spots of US-32 also moved to the side of the box weld in the case of load C. The hot spots of VS-32, PS-32, and PN-31 were located at the corner of the box welds in both or either case of loads A and B (Fig. 3-9b, c, e).

Fig. 3-10 shows the ratio of hot-spot stress ranges of nodes ($\Delta\sigma'_{h,\,\mathrm{node}}$) to the hot-spot stress ranges of weld toes ($\Delta\sigma'_{h}$). The ratio were calculated as Equation 3-6c with the evaluated points fixed to the side, the bottom and the corner of the welds, as shown in Fig. 3-10.

The hot-spot stress ranges calculated under fixed evaluated points were smaller than those calculated by Equation 5 ($\Delta\sigma'_{h}$) for all cases shown in Fig. 3-10, except for US-32. Therefore, the fatigue evaluation using hot-spot stresses with fixed evaluated points can overlook the maximum hot-spot stress ranges.

The hot-spot stress ranges at the bottom of US-32 and VS-32 were 100% and 97% of $\Delta\sigma'_{h}$, respectively (Fig. 3-10). In addition, out-of-plane bending stress components ($0.8\Delta\sigma'_{h,b}$) accounted for 88% and 72% of the hot-spot stress ranges of US-32 and VS-32, respectively. Therefore, out-of-plane bending of the U-rib and the V-rib walls about the longitudinal axis (Fig. 2-2c) could be the dominant deformation.

The hot-spot stress range at the side of PS-32 was 91% of $\Delta\sigma'_{h}$ and the bending stress component accounted for 96% of the hot-spot stress range. Therefore, out-of-plane bending of the plate rib about the vertical axis was dominant in the weld toe.

The hot-spot stress ranges at the side and the bottom of PN-31 were only 51% and 70% of the hot-spot stress range, respectively. This result shows that the hot-spot locations were different from the corner to the bottom of the box weld toe when the maximum and the minimum hot-spot stresses were caused (Fig. 3-9e).

3.3.2. Differences between conventional and proposed design procedures

Fig. 3-11 shows factored hot-spot stresses of connection US caused by both the conventional and the proposed design procedures. Here, the conventional design procedure indicates loading on the evaluated ribs and assumes only flexural bending. The proposed design procedure indicates loads moving in both longitudinal and transverse directions, and assumes the three-dimensional deformation of connections.

The factored hot-spot stress range caused by the proposed design procedure was approximately 6 times larger than that of the conventional design procedure. In addition, the hot spots, where the maximum factored hot-spot stresses in absolute values were caused, were different depending on the design procedure. Therefore, the conventional design procedure can overlook the acting stresses in structures under service.

3.3.3. Loading position for maximum and minimum hot-spot stresses

Fig. 3-12 and Fig. 3-13 show the relations between load positions and hot-spot stresses (hereinafter referred to as influence surfaces) for weld toes in slit and non-slit connections, respectively. Influence surfaces have two horizontal axes indicating load positions and a vertical axis indicating one with larger absolute values of $\sigma'_{h,pos,\mathrm{u}}$ and

$\sigma'_{h,pos,b}$ caused by the corresponding load positions. Fig. 3-12 and Fig. 3-13 show the influence surfaces of hot spots at part 3 (the intersection between the left side of the center longitudinal ribs and the transverse ribs). The loading positions causing maximum and minimum hot-spot stresses, which are POS_{max} and POS_{min}, respectively, for each hot spot are also indicated in Fig. 3-12 and Fig. 3-13 as circle and cross marks.

POS_{max} and POS_{min} for hot spots in slit connections as well as connection UN were not on the center axes of the longitudinal or the transverse ribs; they were a distance away from the centers of the evaluated connections in both longitudinal and transverse directions. Furthermore, POS_{max} and POS_{min} were on different lanes (Fig. 3-12, Fig. 3-13a, b). For example, POS_{max} and POS_{min} of connection US were located at x=-800 mm of the lanes at y=-320 and +320 mm, respectively. The critical loading positions located on lanes distant from the center axes of the longitudinal ribs could be the results of distortion-induced stress at US-32 and UN-32', and stresses on PS-23', induced by shear deformation of the transverse-rib webs, as described in the following sections.

On the other hand, in the case of influence surfaces of VN-32' and PN-21', POS_{min} was located on the longitudinal ribs, whereas POS_{max} and POS_{min} were located on different lanes, as in US-32, UN-32', and PS-23'.

From the result of POS_{max} and POS_{min} located on different lanes, hot-spot stress ranges caused at the longitudinal-rib to transverse-rib connections in bridges under service could not be simulated by fatigue tests with cyclic design loads on a fixed position or a fixed lane; these ranges correspond to the stress ranges caused by constant amplitude and running wheel fatigue tests, respectively. For example, a constant amplitude fatigue test for US-32 with load range P on POS_{max} , can cause only 56% of the hot-spot stress range caused by the moving load with weight P according to the analysis results.

Locations of POS_{max} and POS_{min} were different depending on the longitudinal-rib shapes and whether slits existed. Therefore, critical loading conditions should be clarified for each investigated connection.

Fig. 3-14 shows the relation between transverse distances from rib centers to load centers and the ratios of out-of-plane bending components when the maximum and the minimum hot-spot stresses were caused. The evaluated weld toes are longitudinal-rib side weld toes of welded joints at part 3 except for PS-33', which is the transverse-rib side weld toe of welded joints between the transverse rib and the deck plate.

The bending component ratios tended to be higher as the transverse distances from the rib centers to the load centers increased. As confirmed by Fig. 3-12, the load centers were transversely distant from the rib centers in the case of the slit connections. In addition, out-of-plane bending of the longitudinal ribs would be dominant for the maximum and the minimum hot-spot stresses of weld toes in the slit connections, as stated below (3.5.2). From the above results, POS_{max} and POS_{min} of weld toes in the slit connections were transversely distant from the longitudinal-rib center because out-of-plane bending caused by those eccentric loadings is dominant for hot-spot stresses of the slit connections.

3.3.4. Inner diaphragm effects

The influence surfaces of hot spots in connection US and UN were affected by the existence of the inner diaphragms. Fig. 3-15a and b show the differences between the sides below and above the center transverse rib (diaphragm and non-diaphragm side) of the influence surface of US-32. The diaphragm side of the influence surface has POS_{max}

and POS_{min} of the whole influence surface on lanes at y=-320 and +320 mm, respectively. On the other hand, the non-diaphragm side has POS_{max} and POS_{min} on lanes at y=+160 and -320 mm, respectively, which were transversely inverse to those of the diaphragm side. Fig. 3-15c and d show the differences between the influence surfaces of UN-32 and UN-32', which are weld toes at the diaphragm and non-diaphragm side of the center U-rib. The influence surfaces of UN-32 and UN-32' could be taken as influence surfaces relatively affected and un-affected by the inner diaphragm. The influence surface with the diaphragm effect has POS_{min} on the center axis of the U-rib, which is the lane at y=0 mm, compared to POS_{min} of the influence surface without the diaphragm effect, located on the lane at y=-160 mm.

However, influence surfaces of weld toes in connection VN were less or almost not affected by the existence of the inner diaphragm. Fig. 3-15e and f show the influence surfaces of VN-32 and VN-32', as in Fig. 3-15c and d. Both influence surfaces were almost flip vertical images of the other, and POS_{max} and POS_{min} were mirrored about the center transverse rib.

The results above indicate that hot-spot stresses of connections with the U-rib are affected by the existence of the inner diaphragms, whereas the connections with the V-rib are less affected. Those differences result from the difference between the U-rib capable of distortion and the V-rib having a triangle cross section, which is stable and hardly distorted, as described in the following section.

3.4. Stress occurrence mechanisms

Fig. 3-16 shows deformations of the deck panel models of connections US, UN, and -VN under loading located eccentric to the center axes of the longitudinal ribs to investigate the effect of rib types on distortion-induced stress on longitudinal-rib to transverse-rib connections. The loading position was POS_{max} for US-32 and its position was mirrored about the center transverse rib. The figure shows deformations of cross sections at the longitudinal-rib to transverse-rib connection (x=0 mm), loading positions (x=±800 mm), and at the middle of the loading positions (x=±400 mm). The figures for deformation of longitudinal-rib to transverse-rib connection cross sections also indicate hot-spot stresses caused by the eccentric position loading on the hot spots.

POS_{max} and POS_{min} of PS-23' could be transversely located on the lanes distant from the evaluated plate rib, since the loading on those positions causes shear forces in the transverse-rib web, and this results in deformation of the slits. It should be noted that POS_{max} and POS_{min} of PS-23' were distant from the transverse rib in the longitudinal direction.

3.4.1. Connection US

Significantly large hot-spot stress at US-32 could be caused mainly by bending of the U-rib walls when the eccentric position loading rotated the U-rib cross section with the inner diaphragm (Fig. 3-16c). The U-rib cross section at x=-400 mm, the inner diaphragm section, was rotated counterclockwise without any distortion by the loading at POS_{max} for US-32. The rotated cross section caused its lower flange to move to the positive direction about the y-axis, and the U-rib walls adjacent to the ends of the slit on the transverse-rib web were bent to the positive direction about the y-axis. Tension and

compression hot-spot stresses were on the U-rib wall side weld toes, corresponding to the bending directions of the U-rib walls. The bending component accounted for 82% of the hot-spot stress of US-32. From the deformation and the composition of the hot-spot stress, the rotation of the U-rib with the inner diaphragm and the restraint by the transverse-rib web were considered to result in the significant large bending stress of US-32.

The relatively small hot-spot stress at US-32 could be caused mainly by bending of U-rib walls when the eccentric position loading distorted the U-rib cross section without the inner diaphragms (Fig. 3-16d). The U-rib cross section at x=+400 mm, without the diaphragm, was distorted by the eccentric loading located at the non-diaphragm side. The distortion caused its lower flange to move to the negative direction about the y-axis, and the U-rib walls adjacent to the ends of the slit on the transverse-rib web were bent to the negative direction about the y-axis. Compression and tension hot-spot stresses occurred on the U-rib wall side weld toes, corresponding to the bending directions of the U-rib walls. The bending component accounted for only 30% of the hot-spot stress of US-32. Here, the hot-spot stresses were smaller than one-fourth of those caused by loading on the diaphragm side. U-rib deformation and the restraint by the transverse-rib web resulted in the bending stress on the U-rib wall as with the inner diaphragm effect, but the bending direction was inversed due to the lower flange moving to the negative direction about the y-axis, compared to the positive direction in the case with the diaphragm.

The difference of the U-rib cross-section deformation resulting from the diaphragm effect resulted in the difference between the influence surfaces of the diaphragm side and the other side. As described in the previous section, the non-diaphragm side of the influence surface of US-32 had POS_{max} and POS_{min} on lanes at y=+160 and -320 mm, respectively, which were transversely inverse to those of the diaphragm side at y=-320 and +320 mm (Fig. 3-15a, b). The difference of POS_{max} and POS_{min} could be the result from the bending direction of the U-rib walls, as shown in Fig. 3-16 due to the existence of the inner diaphragm. In addition, hot-spot stresses of US-32 were smaller in the case of the U-rib without the inner diaphragm than in the case of the U-rib with the diaphragm.

3.4.2. Connections UN and VN

Almost no significant bending deformation was observed in connection UN compared to the bent U-rib walls adjacent to the slit ends of connection US, but the diaphragm effects were still observed in connection UN, as in connection US. The U-rib cross section at x=-400 mm, the inner diaphragm section, was not deformed but fixed under the loading on the diaphragm side (Fig. 3-16c). On the other hand, the U-rib cross section at x=+400 mm was distorted to a diamond-like shape under loading on the non-diaphragm side. Furthermore, compared to the loading on the diaphragm side, the loading on the non-diaphragm side caused almost twice the hot-spot stress at UN-32, which is the U-rib corner additionally displaced in the vertical direction by the cross-section distortion. The difference of the cross-section deformation by the diaphragm effects resulted in the difference of the influence surface of UN-32 and UN-32' (Fig. 3-15c, d). In addition, the increased hot-spot stress by the additional vertical displacement of the U-rib corner resulted in the UN-32' POS_{min}, which was located at the lane distant transversely from the U-rib center axis (Fig. 3-15d).

However, almost no significant bending deformation as well as diaphragm effects

were observed in connection VN. The V-rib cross sections at x=+400 and -400 mm were almost fixed and had nearly no deformations regardless of the diaphragm existence (Fig. 3-16e, f). Furthermore, the hot-spot stress of VN-32 and VN-32' under loading on the diaphragm and the non-diaphragm side, respectively, were almost the same value, which was 60% smaller than the hot-spot stress of UN-32' shown in Fig. 3-16d. The V-ribs having the triangle cross section, which is stable and less distorted, resulted in influence surfaces similar to those of VN-32 and VN-32', and a smaller hot-spot stress than that of UN-32'.

3.4.3. Connections PS and PN

Deformation of connection PS had differences in the levels between both ends of the slits, but differences were not observed in the continuous transverse-rib web of connection PN. Fig. 3-17a and b show the deformations of connections PS and PN under the loading at POS_{max} for PS-23'. The figures also show the hot-spot stress of hot spot 3 of connection PS and hot spot 2 of connection PN, all of which were hot spots of the transverse-rib side weld toes of welded joints. The hot-spot stress of PN-22 was 77% smaller than that of PS-23' in Fig. 3-15. Eliminating the slits in the continuous transverse-rib web decreased the hot-spot stress of the connection by eliminating hot spot 3 of connection PS, where significant high stresses were concentrated due to the shear deformations of the slits.

3.5. Fatigue assessments of the connections

3.5.1. The weakest hot spot of each connection

The fatigue strength of the longitudinal-rib to transverse-rib connections were compared with the fatigue strength of the hot spots considered to have the weakest fatigue strength of each connection. Fig. 3-18 and Fig. 3-19 show hot-spot stress ranges of the evaluated hot-spots in the deck panel models with closed and open ribs, respectively. The evaluated hot spots did not include the longitudinal ribs adjacent to the main girders of the deck panel models, which were significantly affected by the boundary conditions of the deck plates supported at the main girders, as mentioned above. The hot-spot stress ranges in the figure are the differences between $\sigma'_{h,max}$ and $\sigma'_{h,min}$, and are caused by loadings alternately to POS_{max} and POS_{min}. Since connections US, UN, and VN behaved differently depending on whether the inner diaphragms were introduced, the hot-spot stress ranges of those connections are indicated for both cases with and without the diaphragm. The compositions of the hot-spot stresses, meaning tension-membrane and -bending, and compression-membrane and -bending, are also shown in Fig. 3-18 and Fig. 3-19.

The hot spots taken as the weakest of each connection were US-32, UN-32', VS-32, VN-32', PS-23', and PN-42. The weakest hot spots were longitudinal-rib side weld toes of welded joints between the longitudinal and transverse ribs, except for PS-23' at the upper end of the slit on the transverse-rib web. In the case without a diaphragm in the closed ribs, the weakest hot spots for connection US changed to US-31, whereas the weakest hot spots of the other connections did not change regardless of the diaphragm existence.

3.5.2. Fatigue strength improvement by applying the non-slit connections

Fig. 3-20 to Fig. 3-22 show the hot-spot stress ranges, the stress ratios, and the bending ratios of the weakest hot spots of the connections, respectively, where the stress ratios were calculated as $\sigma'_{h,\min} / \sigma'_{h,\max}$, and the bending ratios were calculated as $\Delta\sigma'_{h,b} / \Delta\sigma'_{h}$. Table 3-2 also summarizes these values.

Applying the non-slit connections instead of the slit-connections decreased the hot-spot stress ranges for the U- and the V-ribs by 65% and 33%, respectively (Fig. 3-20a, b). However, in the case of the non-diaphragm connection, the hot-spot stress range of the U-rib model was increased by 1% when the non-slit connection was applied, whereas the range of the V-rib model was decreased by 22% (Fig. 3-20a). These results mean that the non-slit connection can improve the fatigue strength of the connections with the inner diaphragm adjacent to the connection, but has less effect on the fatigue strength improvement of the connections without the inner diaphragms in the case of the U-rib.

Fig. 3-21 shows the bending ratios of the weakest hot spots. Applying the non-slit connection decreased the bending ratios of the U- and the V-rib connections by 53% and 49%, respectively (Fig. 3-21a). As assumed from the cross-section deformation (Fig. 3-16), the improvement of applying the non-slit connection was the result of eliminating the slit where the U-rib walls bent and significant hot-spot stresses occurred. Since the significant U-rib wall bending occurred only in the case that the diaphragm constrained the U-rib cross-section deformation, the hot-spot stress ranges were not so changed from connection US to UN in the case of the non-diaphragm. On the other hand, the V-rib had resistance against cross-section deformation even without the diaphragm and behaved almost similarly regardless of the diaphragm existence, as mentioned in the above sections. Therefore, the hot-spot stress range of the V-rib model was decreased by applying the non-slit connection regardless of the diaphragm existence.

Applying the non-slit connection instead of the slit connection also decreased hot-spot stress ranges for the plate rib by 58%, whereas the hot-spot stress ranges of the cut-out connection (connection PC) were similar to that of the non-slit connection (Fig. 3-20c).

Fig. 3-22 shows stress ratios of the weakest hot spots with the upside-down vertical axis. Applying the non-slit connection decreased stress ratios of all longitudinal-rib type connections. The stress ratios of the slit or the cut-out connections were $\geqq$ -1.0, meaning the tension stresses are larger than the compression stresses. On the other hand, the stress ratios of the non-slit connection were $\leqq$-2.5, meaning the non-slit connection restrained the tension stress occurrence. This characteristic of the non-slit connection also contributed to enhancement of the fatigue lives. From the viewpoint of the stress ratio, the fatigue lives of connection PN were better than those of connection PC.

3.5.3. Fatigue strength improvement by the V-rib

In Fig. 3-20 and Fig. 3-22, connection VN had the smallest hot-spot stress range as well as the lowest stress ratio of the five connections' weakest hot spots. The range, 66 N/mm^2, was almost the fatigue limit of JSSC-E class. Furthermore, the hot-spot stress ranges of VN-32 and VN-32', which are the diaphragm and the non-diaphragm side weld toes, were almost same. Those results mean that connection VN had the highest fatigue strength of the seven connections in Fig. 3-20. The smaller hot-spot stress range and the lower stress ratio of VN-32' compared to those of UN-32' were achieved by the

triangle cross section of the V-rib, which was hardly distorted.

Fig. 3-23 shows the relations between rib stiffness and the hot-spot stress ranges at the weakest hot spots. The horizontal axes are Z_c / L_c, where Z_c is the cross section modulus and L_c is the span length of the longitudinal rib. The selection of the vertical axis was based on the simplified assumption that the stress of a point-loaded simple beam is in inverse proportion to Z_c / L_c, even though plate theory should be strictly applied.

The hot-spot stress of connection VN was smaller than that of connection UN by 19%, even though the stiffness (Z_c / L_c) of connection VN was smaller than that of connection UN. Based on the simplified assumption mentioned above, connections VN, VN_1, and VN_4 have efficient cross sections with small values of $\Delta\sigma_h \times Z_c / L_l$ (Fig. 3-23a). These results would be due to the comparatively high resistance of those connections against cross-section distortion, since connections VN and VN_1 have shallower rib walls and connection VN_4 has a thicker plate.

3.5.4. Fatigue strength improvement of the plate-rib connections

Fig. 3-23b shows relations between rib stiffness and the hot-spot stress ranges at the weakest hot spots of the plate-rib non-slit connections. The data shows hot-spot stress ranges at transverse-rib side weld toes of connections except for connection PN and -PN_{10}, which have the weakest hot spots at the longitudinal-rib side welded toes.

The relations show an inverse proportion with slopes shallower than -1, even though almost all the data were from transverse-rib side weld toes. Hot-spot stress range varied among connections PN_{16}, PN_{12}, PN_{17} or PN_{26}, PN_{22}, PN_{27}, which had the same longitudinal ribs and transverse-rib webs heights of 400, 500, 600 mm, respectively.

Fig. 3-24 shows the relations between steel weights per unit area of deck surface and the hot-spot stress ranges of the weakest hot spots. Three types of arrows indicate increase of plate-rib height, transverse-rib web height and transverse-rib flange width with other dimensions fixed. Increasing the transverse-rib web height decreased the hot-spot stress range more efficiently than increasing the longitudinal-rib height (where "efficiently" means the ratio of the hot-spot stress range decrease to the steel weight increase). The transverse-rib flange width had almost no effect on the hot-spot stress range.

In the connections with a span length of 2250 mm, only connection PN_{25} and PN_{27} had hot-spot stress ranges lower than the fatigue limit of JSSC-E class (Fig. 3-23b). Since connection PN_{25} has a comparatively heavy plate rib with 19-mm thickness, connection PN_{27}, with 16-mm thickness was selected as a suitable structure in the case that a longitudinal-rib span length up to 2250 mm is applied.

3.5.5. Suitable structure for longitudinal-rib to transverse-rib connections

In Fig. 3-24, the V-rib non-slit connections were the most "efficient" structure. However, the fatigue strength of the joints between the closed longitudinal ribs and deck plates were low and fatigue cracks were not yet eliminated. Therefore, this study proposes connection PN as the high fatigue strength connection.

3.6. Summary

This chapter investigated critical loading positions for longitudinal-rib to transverse-rib connections and their fatigue strengths under the critical loading conditions by using the hot-spot stresses computed by finite element analyses. The thickness and the bending effects were taken into account for hot-spot stress modification. Based on the results, the following conclusions were obtained.

1) Critical loading positions causing maximum and minimum hot-spot stresses on longitudinal-rib to transverse-rib connections are located at a distance away from the evaluated connections. Furthermore, those positions are different depending on the longitudinal-rib type and the slit existence on the transverse-rib webs.
2) Eliminating the slit on the transverse-rib webs can improve the fatigue strength of the longitudinal-rib to transverse-rib connections. The hot-spot stress ranges of connection UN and PN were smaller than those of US and PS by 65% and 58%, respectively, where the inner diaphragms were attached in the U-ribs at 400 mm from the transverse-rib.
3) Using V-ribs would further enhance the fatigue strength of non-slit connections. The hot-spot stress range of connection VN was 39% smaller than that of connection UN.
4) Hot-spot stresses of the connections between U-ribs and transverse-rib webs are significantly affected by the existence of inner diaphragms adjacent to the connections. The hot-spot stresses ranges of connection US and UN were increased and decreased by the inner diaphragms.

Table 3-1 Analysis models for fatigue assessments of longitudinal-rib to transverse-rib connections

Model / Connection	Longitudinal-rib		Slit	t_d	Parameter
	Type	Span [mm]			
US	U	2500	Slit	16	
UN	U	2500	Non-slit	16	Longitudinal-rib
VS	V	2500	Slit	16	type (closed) and
VN	V	2500	Non-slit	16	slit shapes
VN_1–VN_5	V[a]	2500	Non-slit	16	
PS	Plate	1667	Slit[b]	12	
PC	Plate	1667	Slit[c]	12	Slit shapes
PN	Plate	1667	Non-slit	12	
PN_{10}–PN_{19}	Plate	1500	Non-slit	16	Dimensions of plate
PN_{20}–PN_{29}	Plate	2250	Non-slit	16	and transverse ribs

[a] Five types of V-sections, [b] Large slit, [c] small cut-out

Table 3-2 Characteristic stress ranges and stress ratios of longitudinal-rib to transverse-rib connections, computed by finite element analyses

	With diaphragm				Without diaphragm			
Connection	Hot spot	$\Delta\sigma'_h$ [N/mm^2]	R	Ψ	Hot spot	$\Delta\sigma'_h$ [N/mm^2]	R	Ψ
US	32	228	-0.78	0.88	31'	79	-2.96	0.20
UN	32'	56	-8.79	0.39	32'	80	-4.39	0.41
VS	32	99	-0.71	0.72	32'	85	-0.72	0.57
VN	32'	66	-7.92	0.36	32'	67	-7.92	0.36
VN_1	32'	78	-6.17	0.44	32	73	-9.11	0.41
VN_2	32'	64	-3.58	0.46	32	59	-5.64	0.43
VN_3	32'	49	-4.28	0.44	32	47	-5.77	0.41
VN_4	32'	39	-5.33	0.43	32	38	-6.19	0.39
VN_5	32'	60	-2.52	0.54	32	50	-3.57	0.45
PS	N/A	N/A	N/A	N/A	23'	184	-0.93	0.15
PC	N/A	N/A	N/A	N/A	31	73	-0.18	0.46
PN	N/A	N/A	N/A	N/A	42	76	-2.47	0.31
PN_{10}	N/A	N/A	N/A	N/A	42*	69	-1.74	0.27
PN_{11}	N/A	N/A	N/A	N/A	21*	55	-1.90	0.31
PN_{12}	N/A	N/A	N/A	N/A	21*	51	-1.78	0.30
PN_{13}	N/A	N/A	N/A	N/A	21*	69	-2.12	0.35
PN_{14}	N/A	N/A	N/A	N/A	21*	55	-1.80	0.29
PN_{15}	N/A	N/A	N/A	N/A	41*	44	-1.28	0.38
PN_{16}	N/A	N/A	N/A	N/A	31*	59	-1.42	0.42
PN_{17}	N/A	N/A	N/A	N/A	31	52	-2.98	0.46
PN_{18}	N/A	N/A	N/A	N/A	31*	51	-1.35	0.35
PN_{19}	N/A	N/A	N/A	N/A	21*	51	-1.92	0.30
PN_{20}	N/A	N/A	N/A	N/A	21*	80	-4.89	0.09
PN_{21}	N/A	N/A	N/A	N/A	21*	69	-2.07	0.43
PN_{22}	N/A	N/A	N/A	N/A	21*	65	-1.96	0.42
PN_{23}	N/A	N/A	N/A	N/A	21*	84	-2.26	0.44
PN_{24}	N/A	N/A	N/A	N/A	21*	68	-1.93	0.41
PN_{25}	N/A	N/A	N/A	N/A	21*	54	-1.64	0.39
PN_{26}	N/A	N/A	N/A	N/A	21*	79	-1.90	0.51
PN_{27}	N/A	N/A	N/A	N/A	21*	59	-2.10	0.37
PN_{28}	N/A	N/A	N/A	N/A	21*	65	-1.57	0.39
PN_{29}	N/A	N/A	N/A	N/A	21*	65	-2.19	0.42

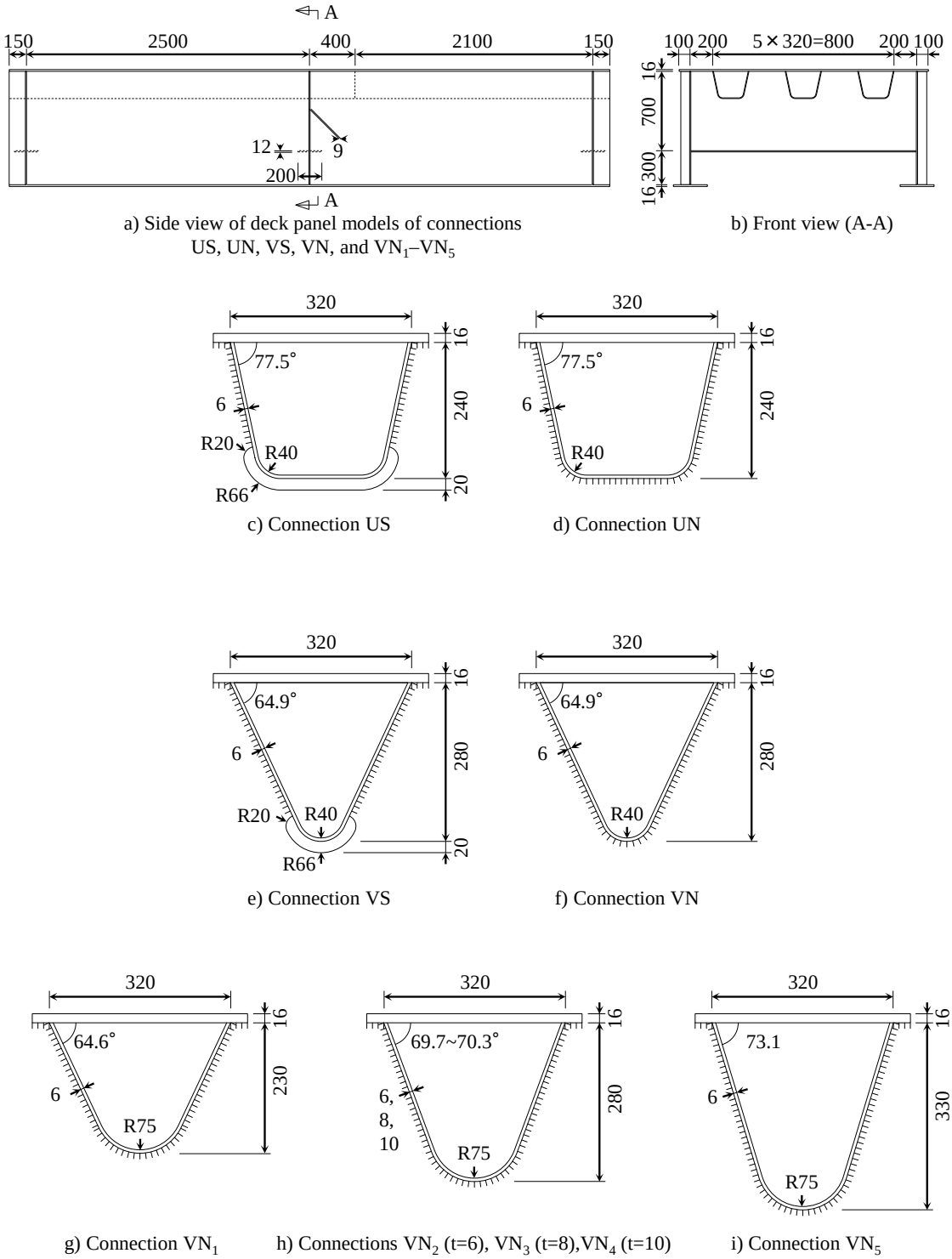

a) Side view of deck panel models of connections US, UN, VS, VN, and VN_1–VN_5

b) Front view (A-A)

c) Connection US

d) Connection UN

e) Connection VS

f) Connection VN

g) Connection VN_1

h) Connections VN_2 (t=6), VN_3 (t=8),VN_4 (t=10)

i) Connection VN_5

Fig. 3-1 Analysis models with closed-section longitudinal-ribs (models US, UN, VN, VN_1–VN_5)

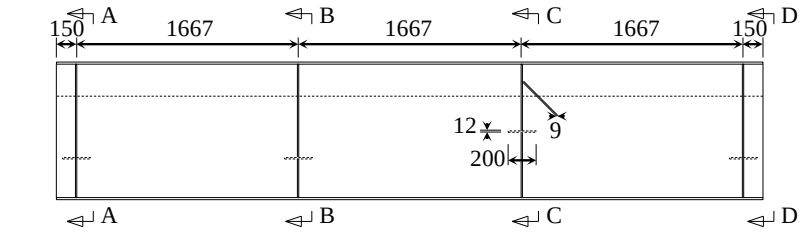

a) Side view of deck panel models of connections PS and PN

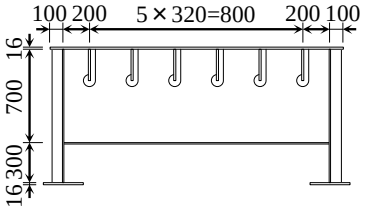

b) A-A, B-B, D-D cross sections

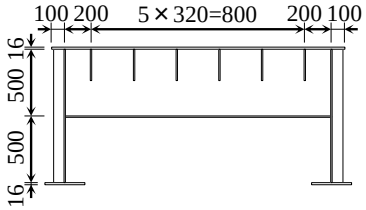

c) C-C cross section

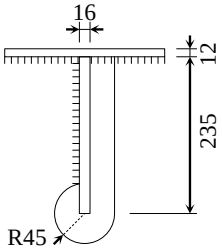

d) Connection PS

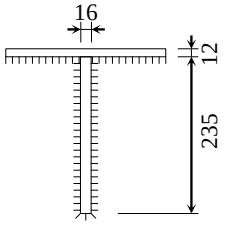

e) Connection PN

Fig. 3-2 Analysis models with open-section longitudinal-ribs (model PS, PC)

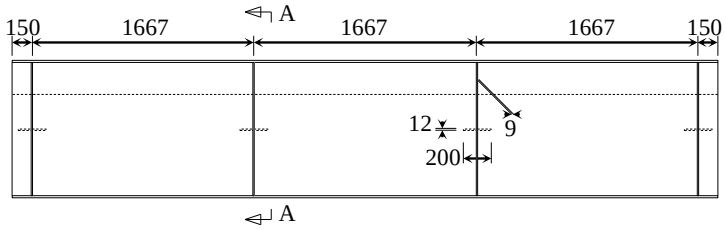

a) Side view of deck panel model of connection PC

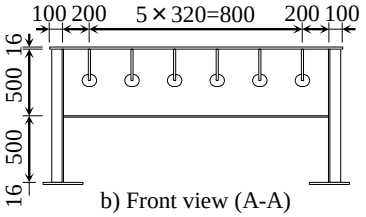

b) Front view (A-A)

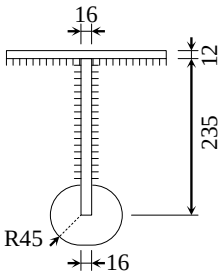

c) Connection PC

Fig. 3-3 Analysis models with open-section longitudinal-ribs (model PN)

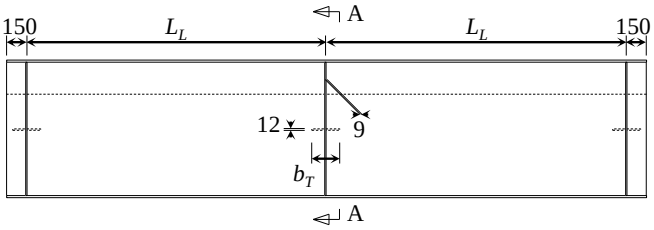

a) Side view of deck panel models of connections PN_{10}–PN_{29}

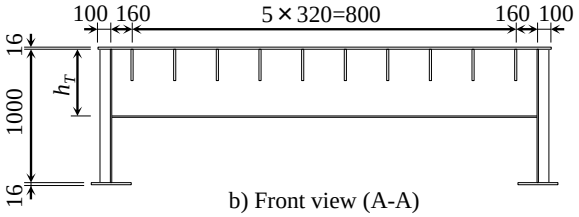

b) Front view (A-A)

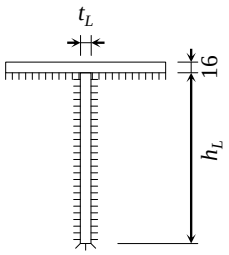

c) Connections PN_{10}–PN_{29}

Connection	Longitudinal-rib			Transverse-rib	
	L_L [mm]	h_L [mm]	t_L [mm]	h_T [mm]	b_T [mm]
PN_{10}	1500	183	16	500	200
PN_{11}	1500	235	16	500	200
PN_{12}	1500	256	16	500	200
PN_{13}	1500	162	19	500	200
PN_{14}	1500	217	19	500	200
PN_{15}	1500	304	19	500	200
PN_{16}	1500	256	16	400	200
PN_{17}	1500	256	16	600	200
PN_{18}	1500	256	16	500	100
PN_{19}	1500	256	16	500	300
PN_{20}	2250	183	16	500	200
PN_{21}	2250	235	16	500	200
PN_{22}	2250	256	16	500	200
PN_{23}	2250	162	19	500	200
PN_{24}	2250	217	19	500	200
PN_{25}	2250	304	19	500	200
PN_{26}	2250	256	16	400	200
PN_{27}	2250	256	16	600	200
PN_{28}	2250	256	16	500	100
PN_{29}	2250	256	16	500	300

Fig. 3-4 Analysis models with plate ribs and non-slit transverse-rib webs (models PN_{10}–PN_{29})

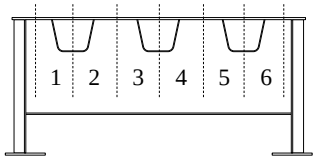

a) Part numbers of the deck panel models with U-ribs

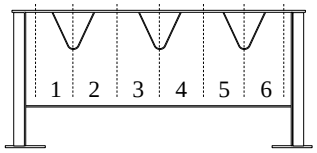

b) Part numbers of the deck panel models with V-ribs

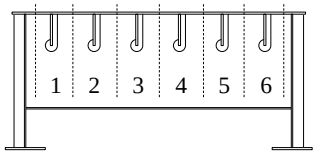

c) Part numbers of the deck panel models of connections PS, PC, PN

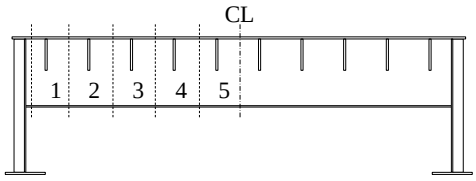

d) Part numbers of the deck panel models of connections PN_{10}–PN_{29}

Weld toe name
e.g. US- 3 2
local number
global number
PN- 2 2'
' means reverse side surface of transverse-rib

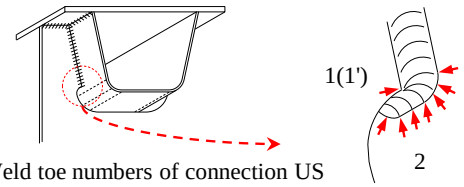

e) Weld toe numbers of connection US

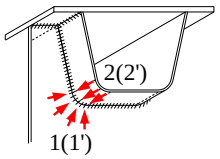

f) Weld toe numbers of connection UN

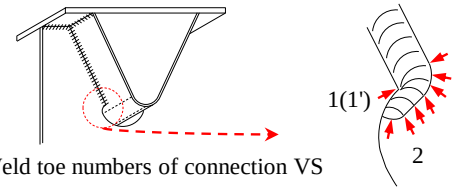

g) Weld toe numbers of connection VS

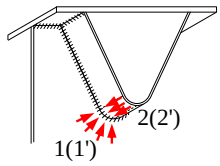

h) Weld toe numbers of connections VN, VN_1–VN_5

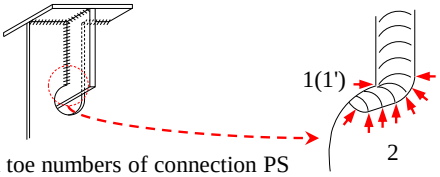

i) Weld toe numbers of connection PS

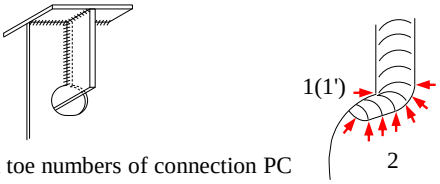

j) Weld toe numbers of connection PC

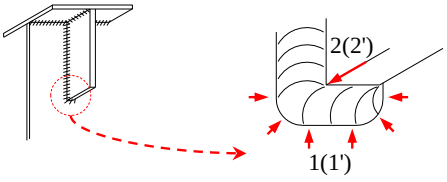

k) Weld toe numbers name of connection PN, PN_{10}–PN_{29}

Fig. 3-5 Evaluated weld toes of longitudinal-rib to transverse-rib connections

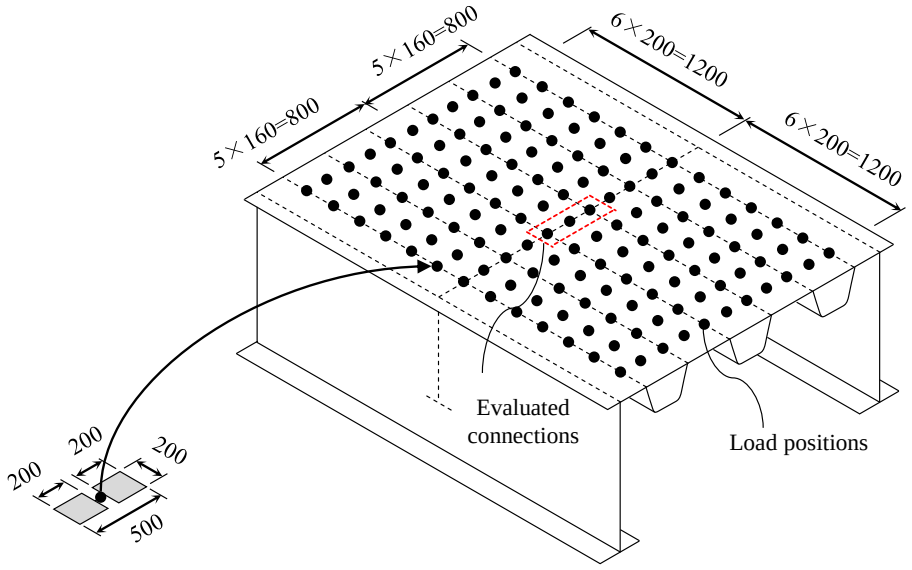

a) Load model

b) Load positions for deck panel models of connections US, UN, VN

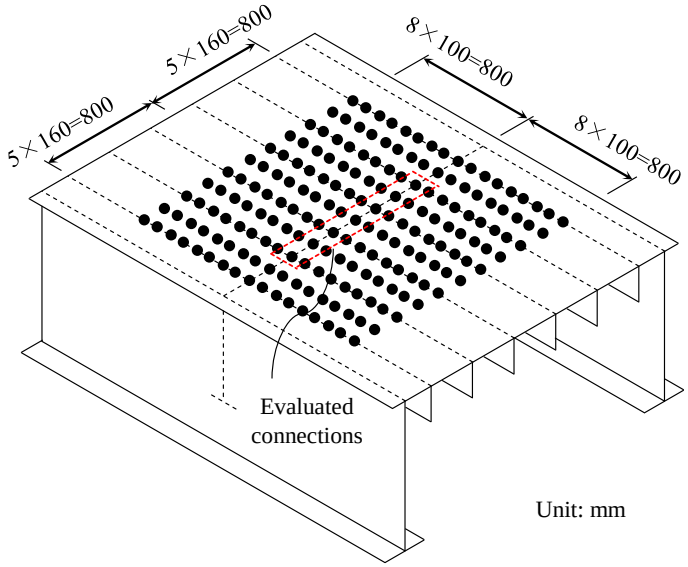

c) Load positions for deck panel models of connections PS. PC, PN

Fig. 3-6 Load model and load positions

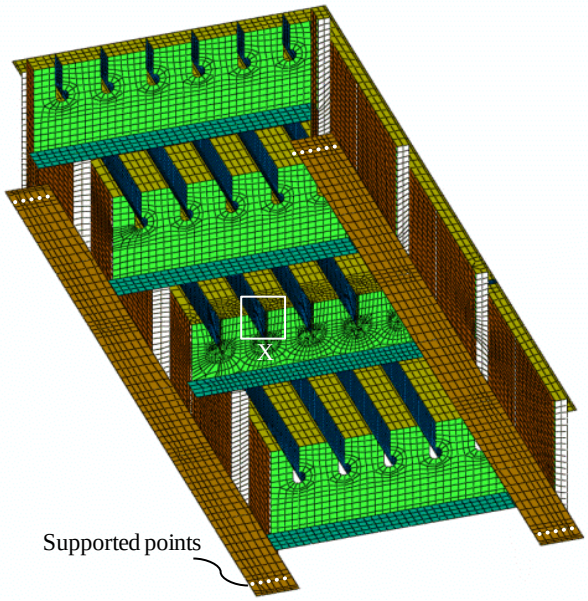

(a) Overall view

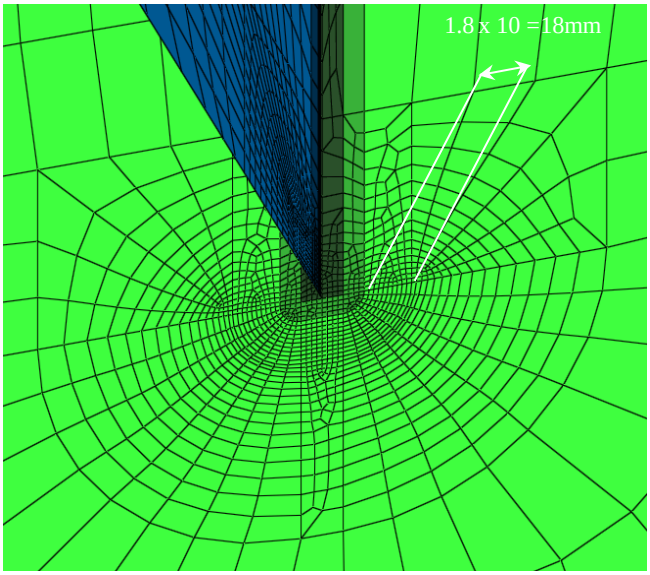

(b) Welded joints between longitudinal and transverse ribs (X part)

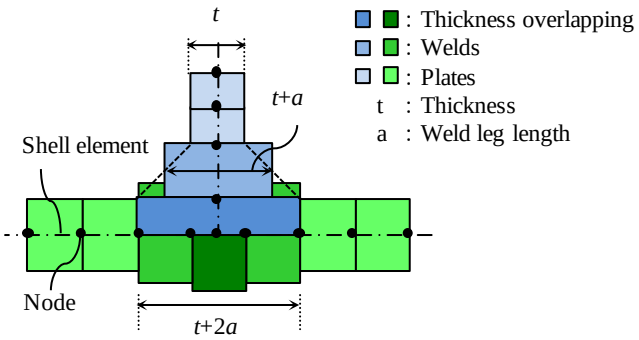

(c) Thickness of welded joints

Fig. 3-7 Finite element model

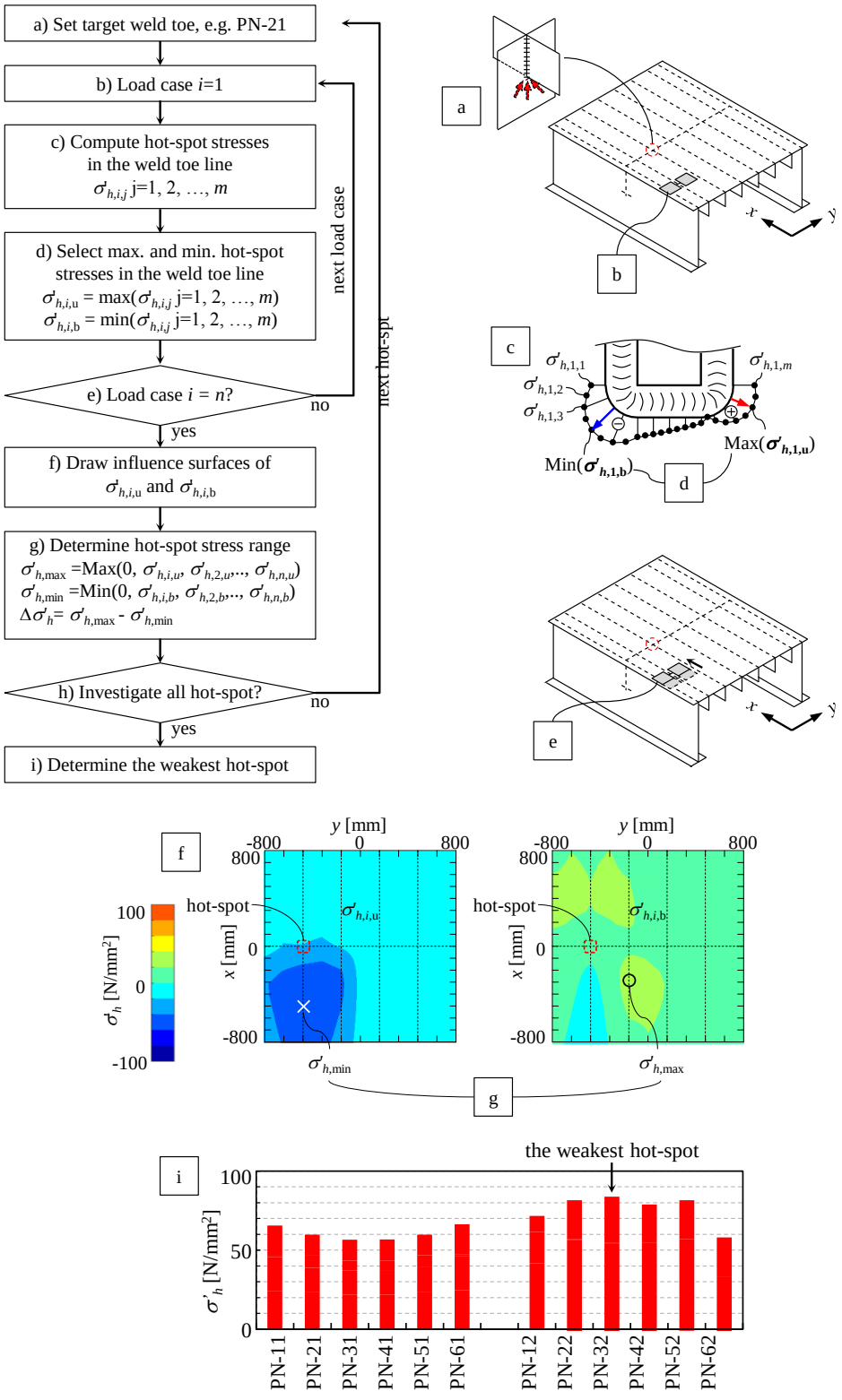

Fig. 3-8 Hot spot stress computation procedure

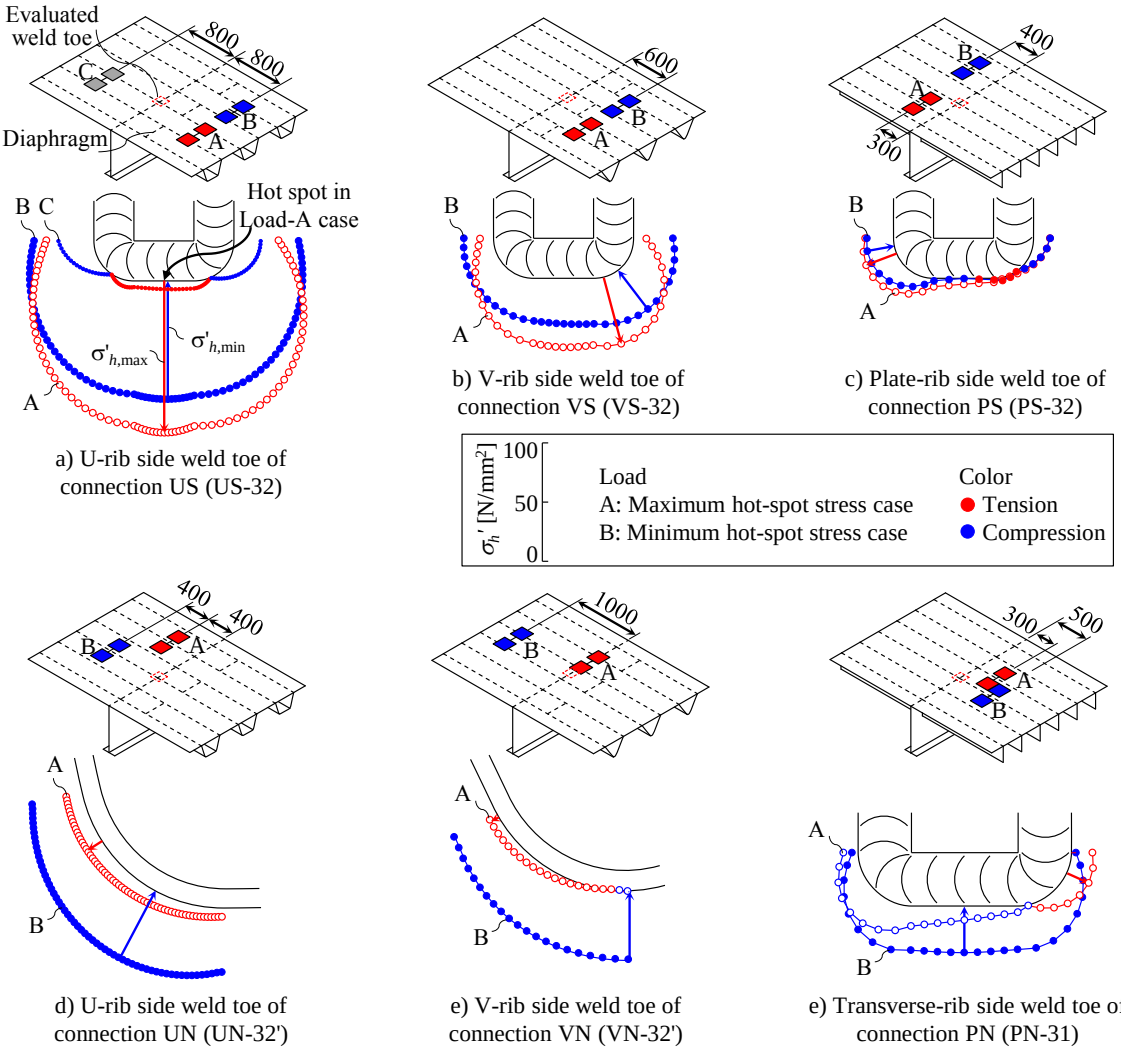

Fig. 3-9 Hot-spot locations caused by characteristic load cases
(The loading positions are those maximizing and minimizing hot-spot stresses, as a rule)

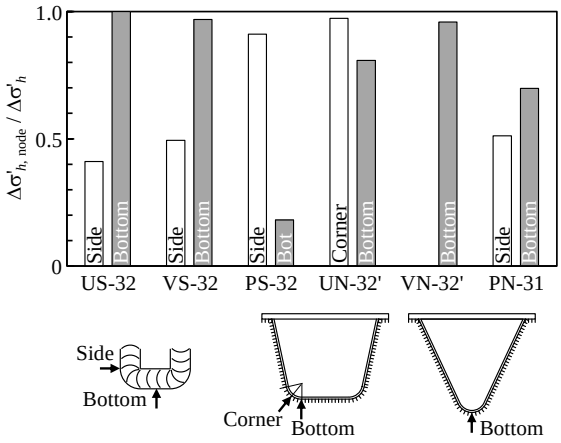

Fig. 3-10 Ratio of hot-spot stress ranges of nodes ($\Delta\sigma'_{h,node}$) to hot-spot stress ranges of

weld toes ($\Delta\sigma'_h$)

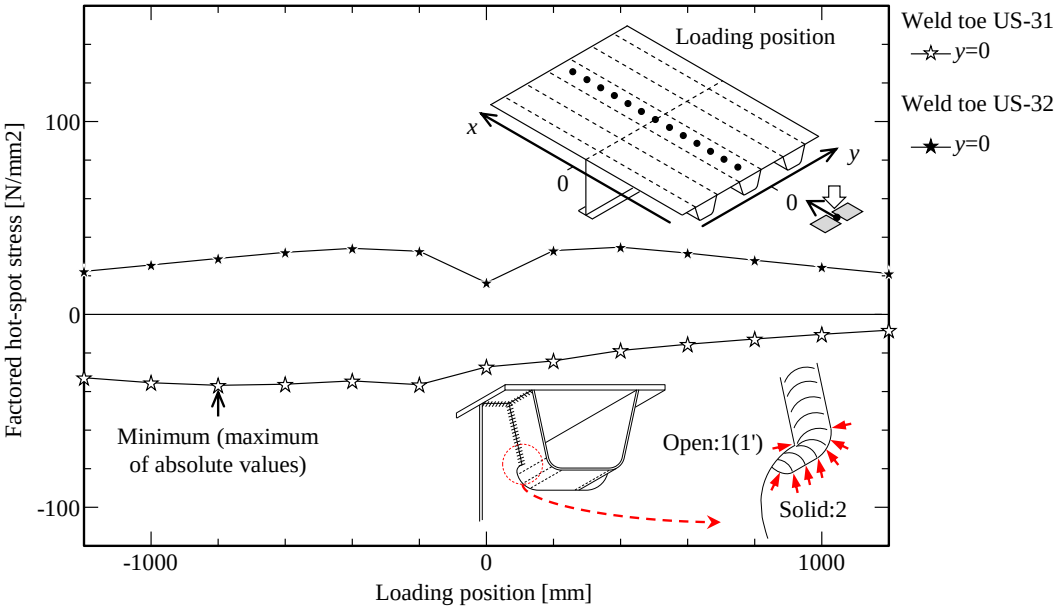

a) Factored hot-spot stresses caused by loads on evaluated U-rib

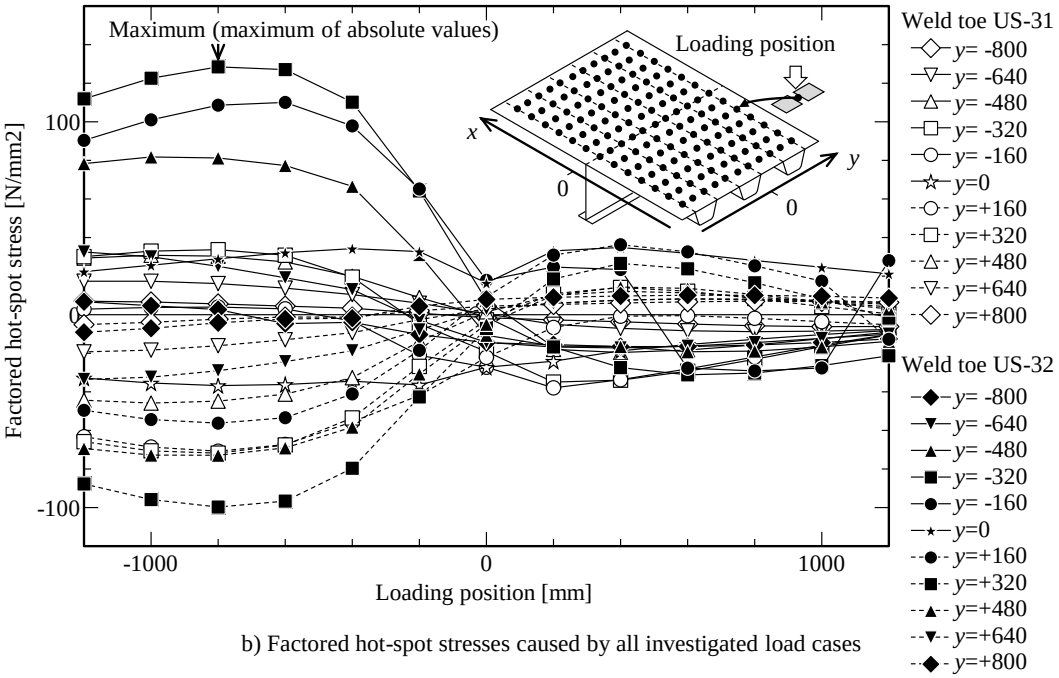

b) Factored hot-spot stresses caused by all investigated load cases

Fig. 3-11 Factored hot-spot stresses of connection US, caused by conventional and proposed design procedures

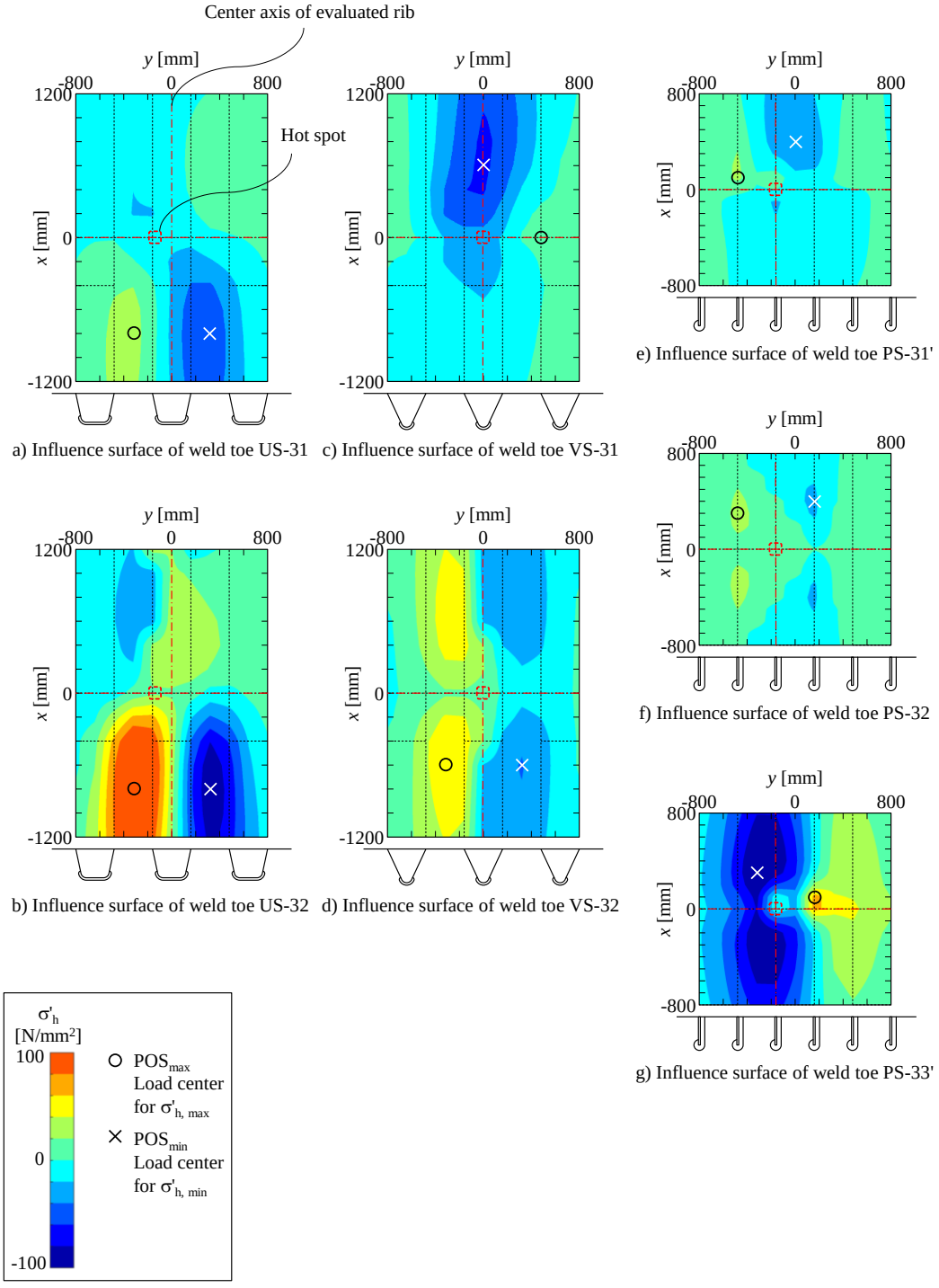

Fig. 3-12 Influence surfaces of slit connection

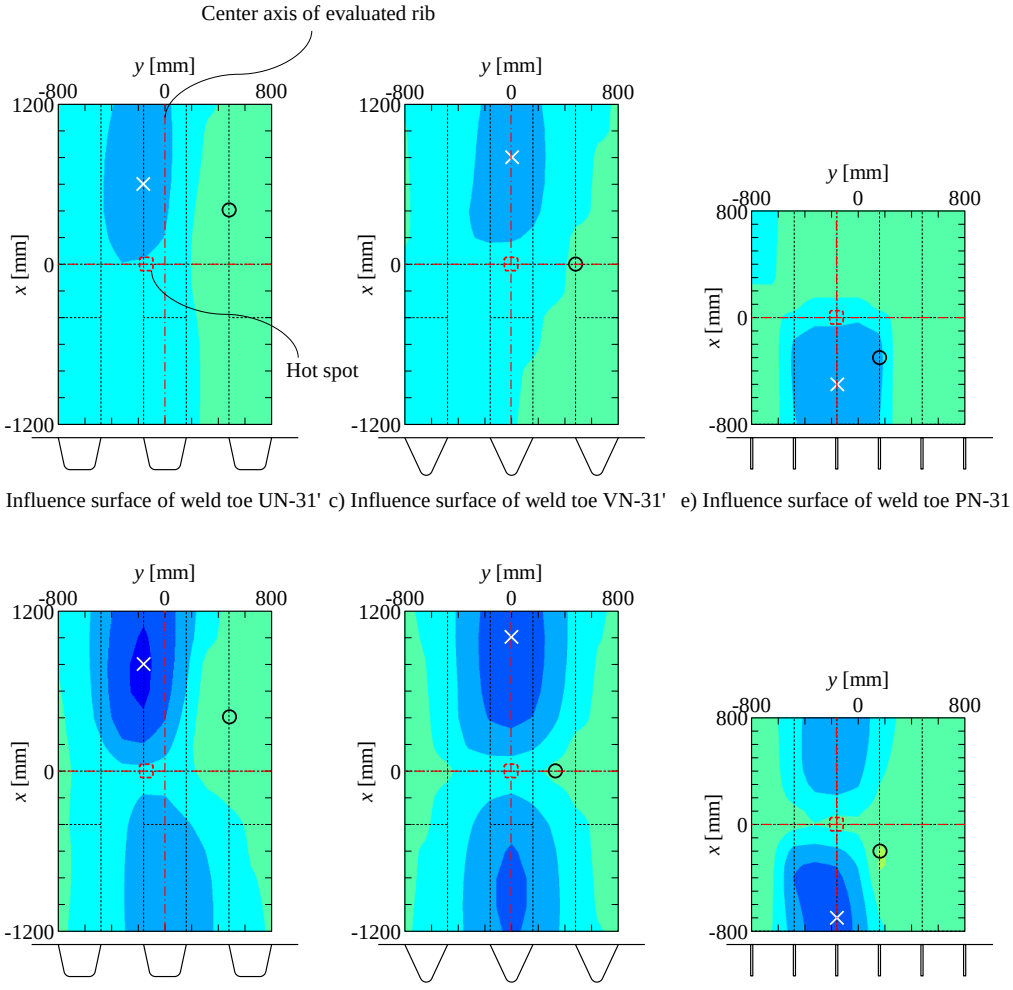

a) Influence surface of weld toe UN-31' c) Influence surface of weld toe VN-31' e) Influence surface of weld toe PN-31

b) Influence surface of weld toe UN-32' d) Influence surface of weld toe VN-32' f) Influence surface of weld toe PN-32

Fig. 3-13 Influence surfaces of non-slit connections

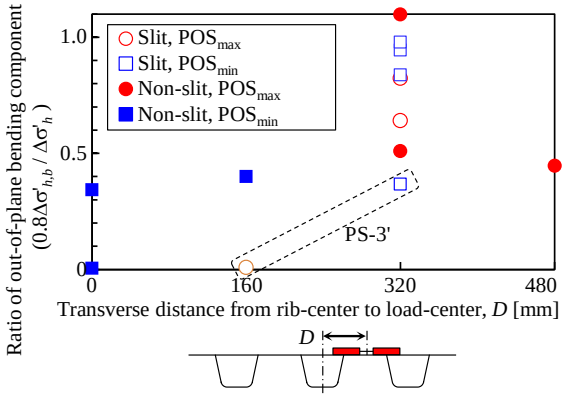

Fig. 3-14 Relations between transverse distances from rib-centers to load centers and ratios of out-of-plane bending components when the maximum and the minimum hot-spot stresses were caused

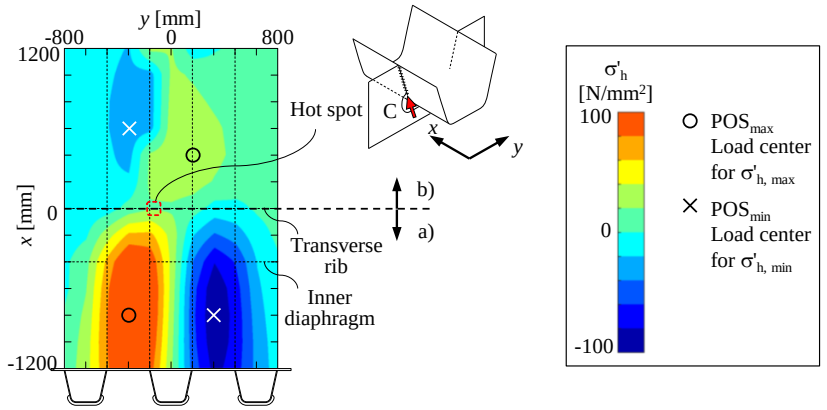

a) and b) Influence surface of weld toe US-32 with and without diaphragm effects

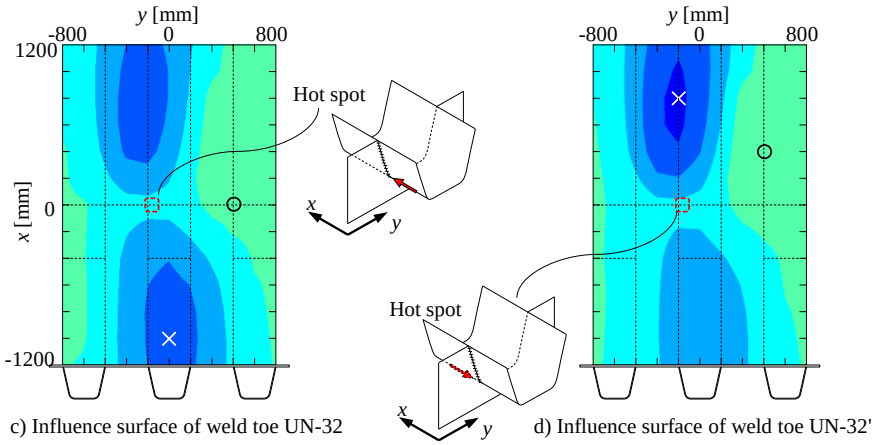

c) Influence surface of weld toe UN-32

d) Influence surface of weld toe UN-32'

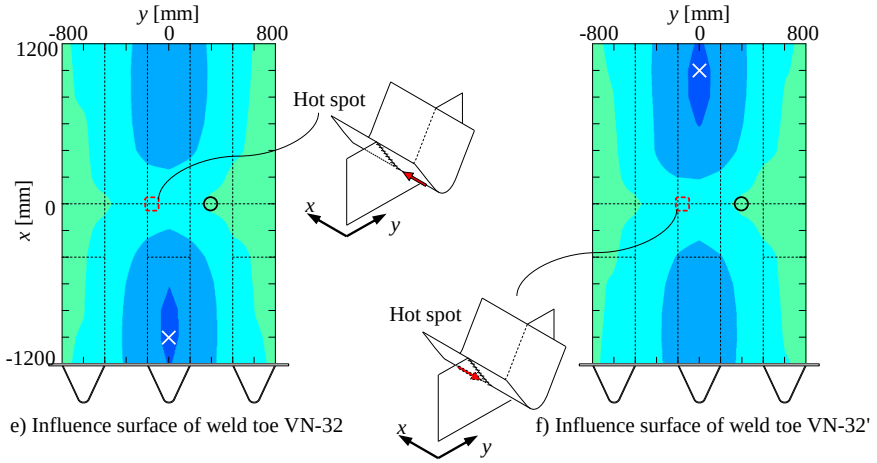

e) Influence surface of weld toe VN-32

f) Influence surface of weld toe VN-32'

Fig. 3-15 Diaphragm effects on the influence surfaces

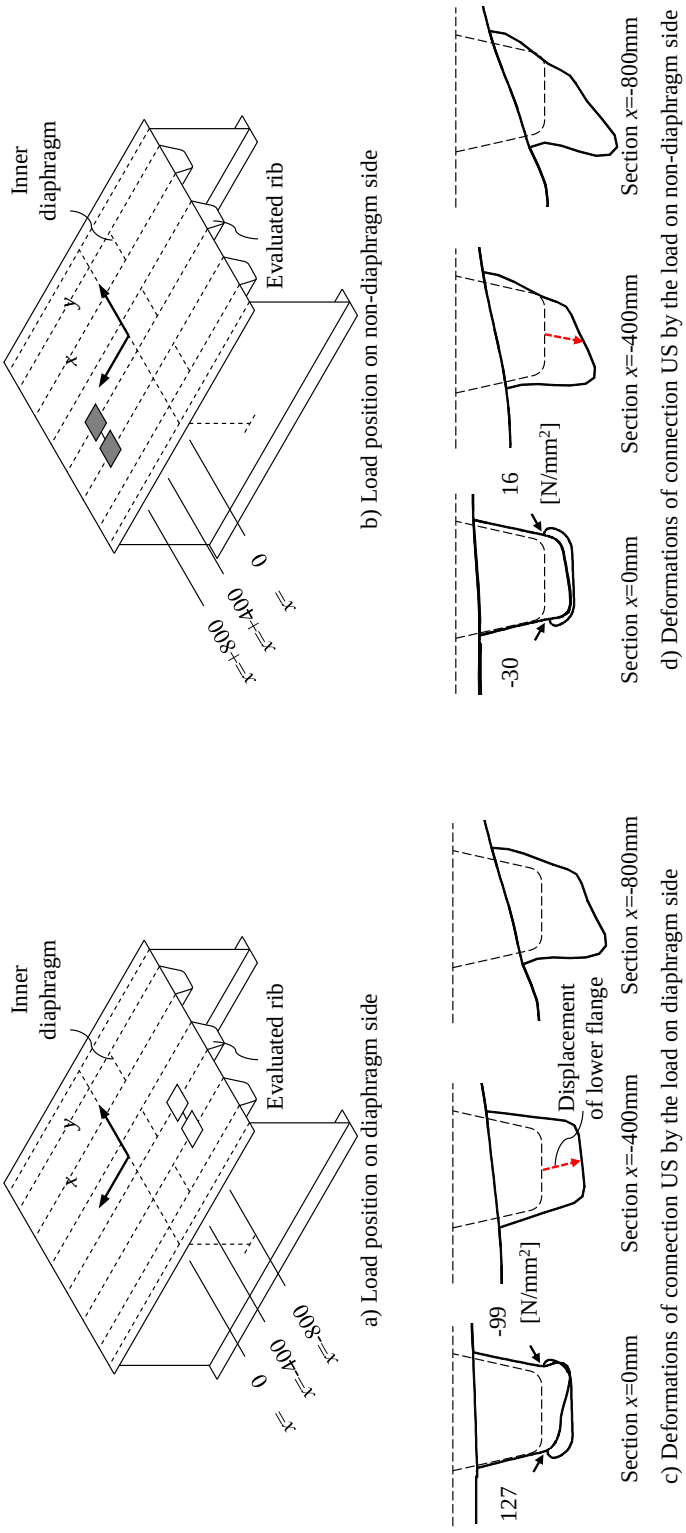

Fig. 3-16 Deformation of closed longitudinal-ribs, deformation × 200

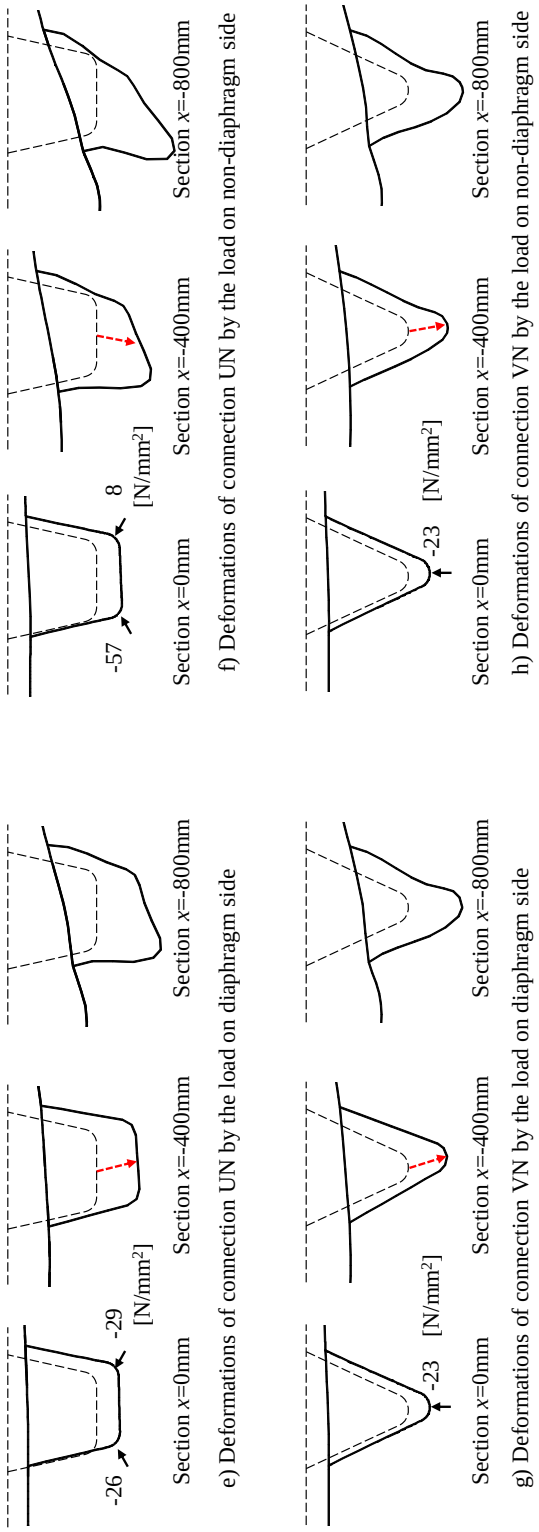

Fig. 3-16 Deformation of closed longitudinal-ribs (continue), deformation × 200

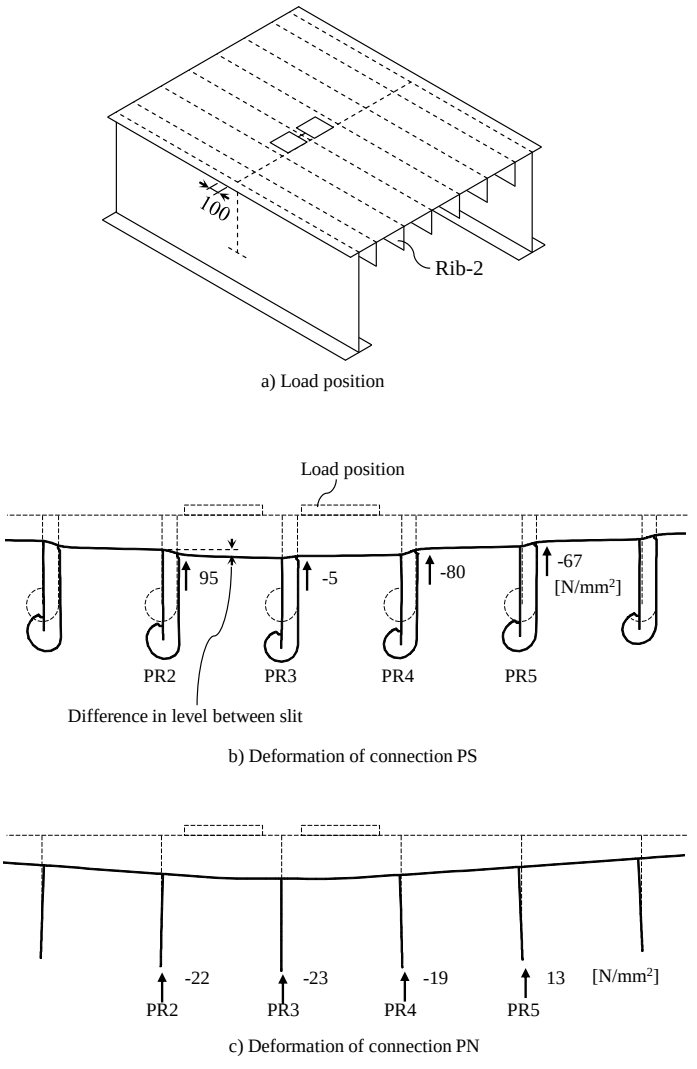

Fig. 3-17 Diaphragm effects on the influence surfaces, deformation × 300

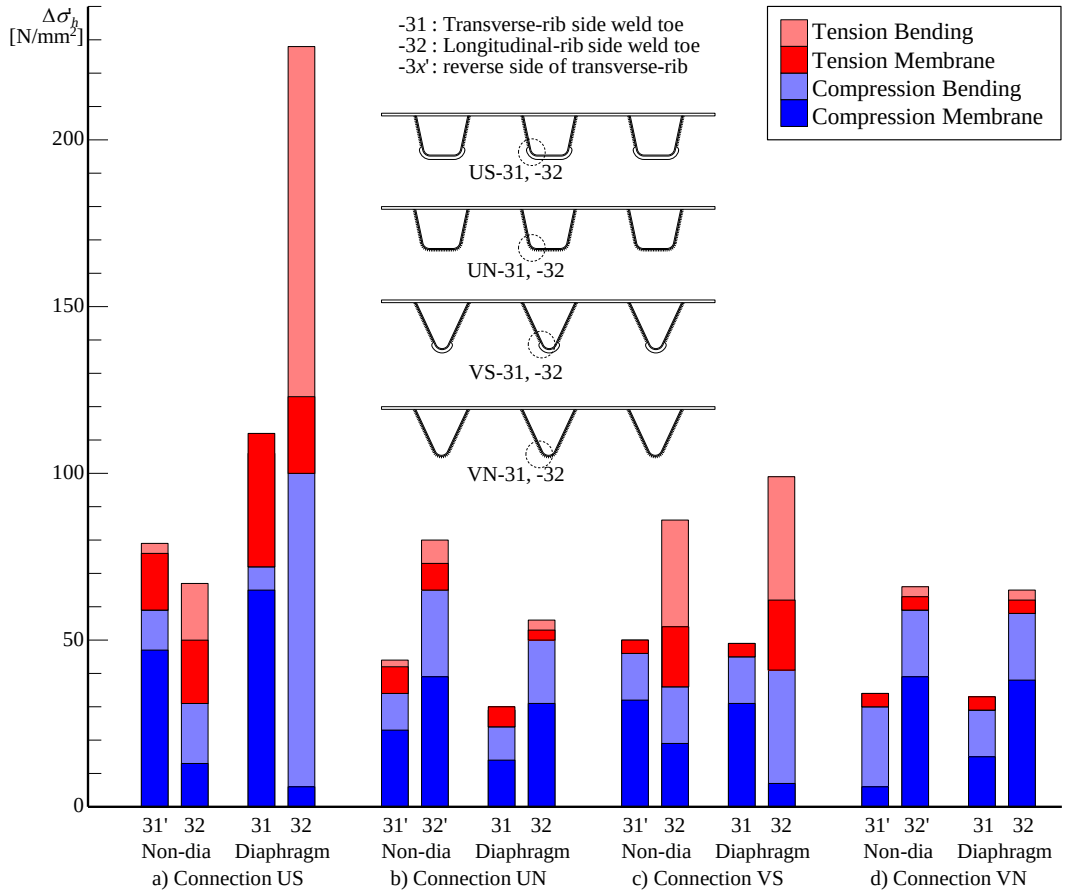

Fig. 3-18 The weakest hot-spots of the closed-rib models

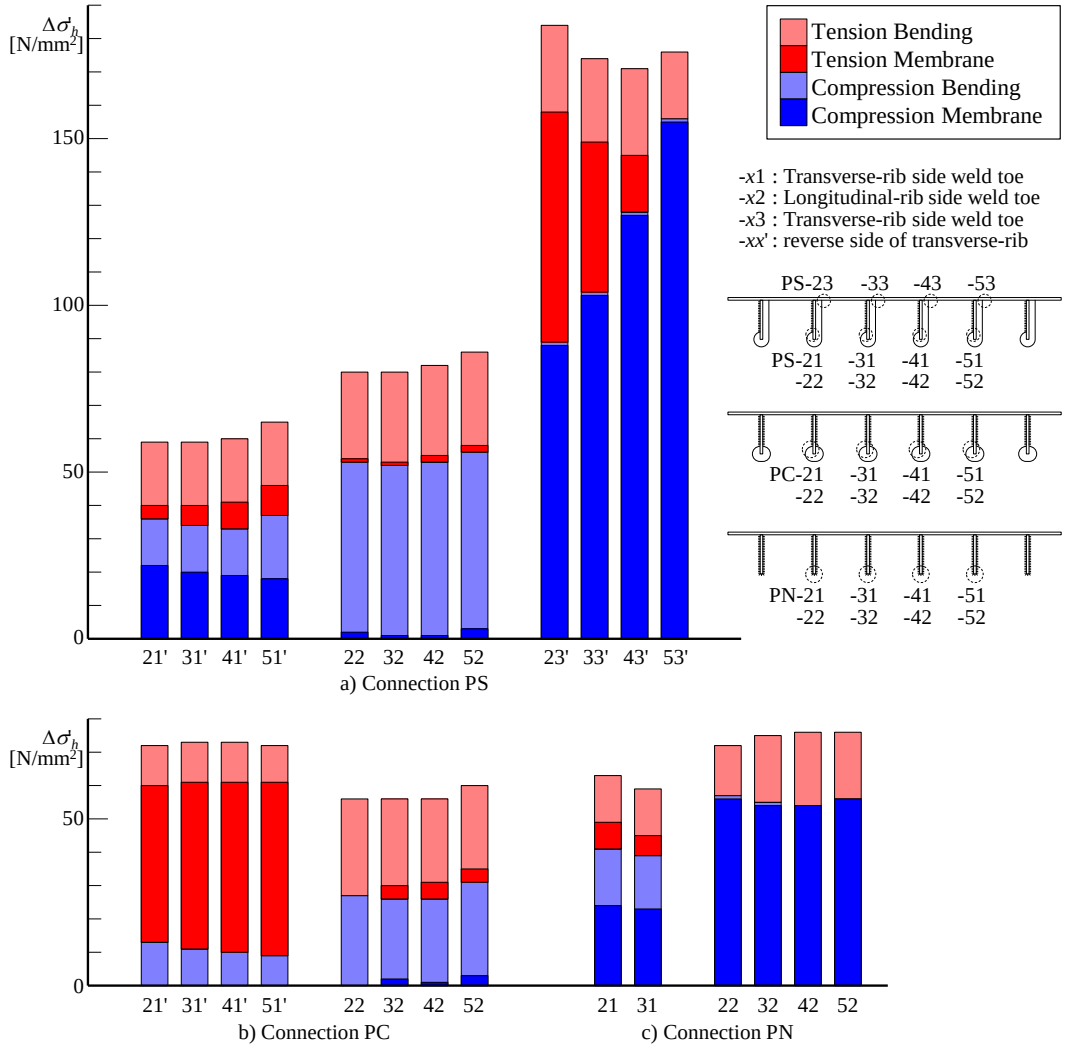

Fig. 3-19 The weakest hot-spots of the open-rib models

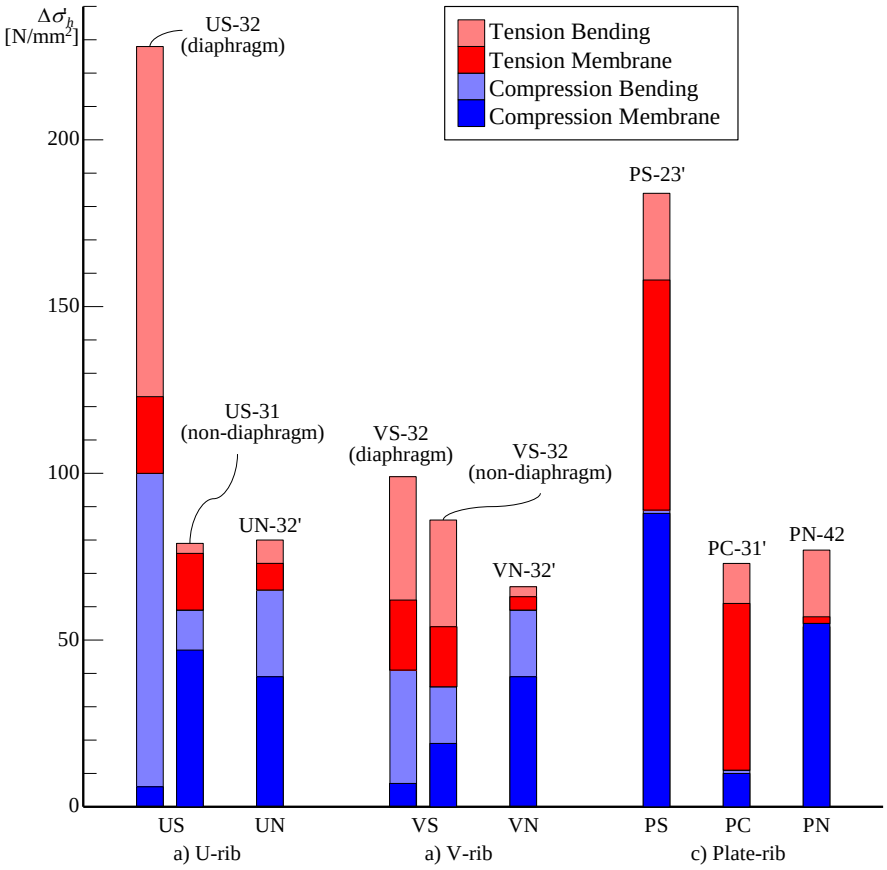

Fig. 3-20 Reduction of hot-spot stress rages by applying non-slit connections

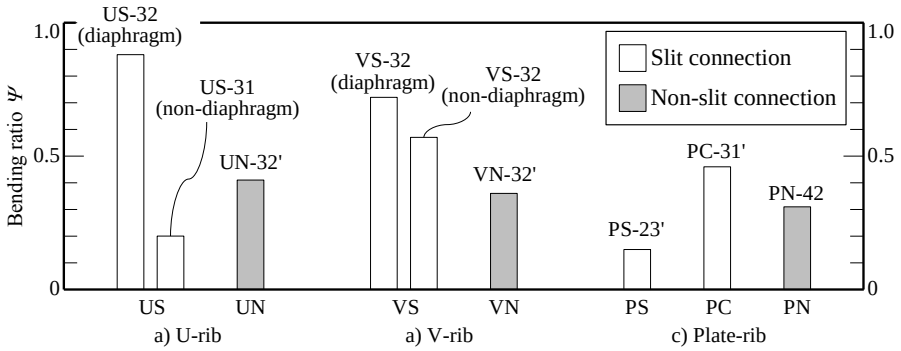

Fig. 3-21 Reduction of out-of-plane bending stress by applying non-slit connections

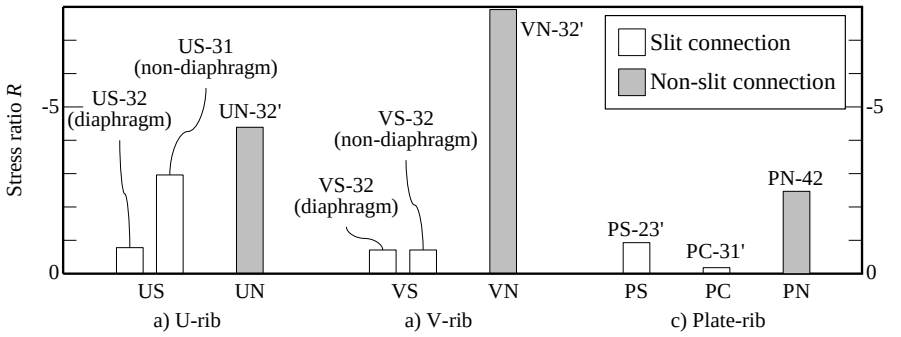

Fig. 3-22 Reduction of tension stress occurrence by applying non-slit connections

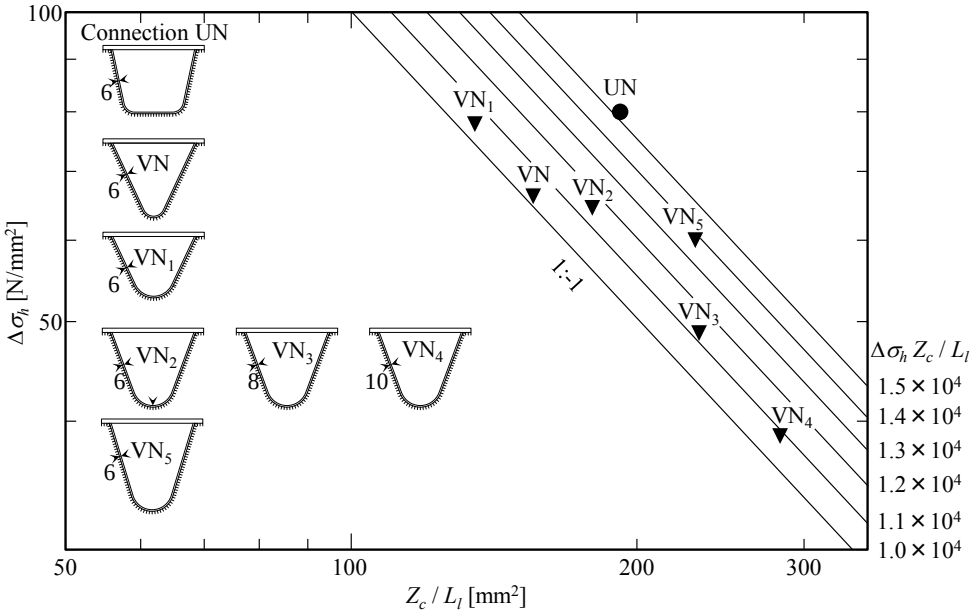

a) Connections with closed-ribs

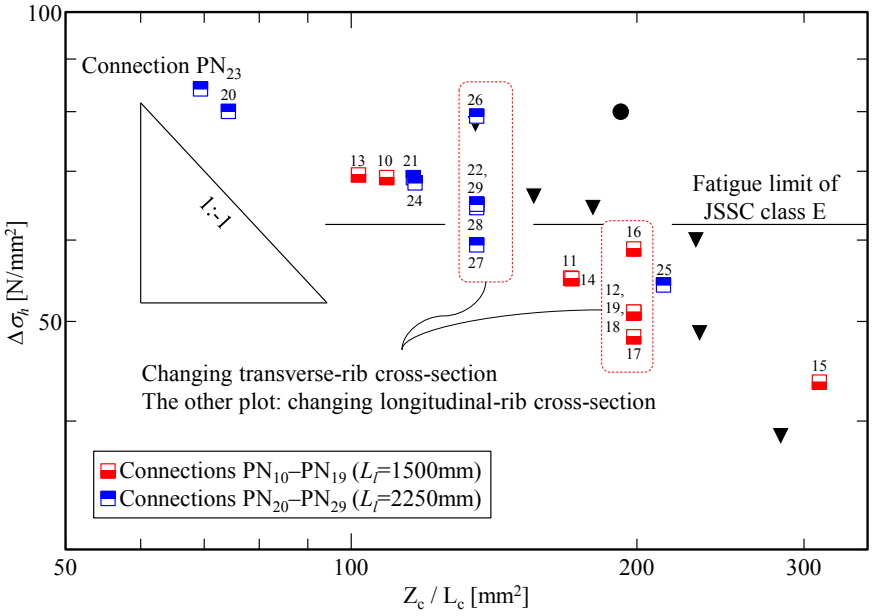

a) Connections with open-rib

Z_c: Section modulous of a longitudinal-rib cross-section including effective width of deck plate
L_l: Span length of longitudinal-rib

Fig. 3-23 Relationships between rib stiffness and the hot-spot stress ranges

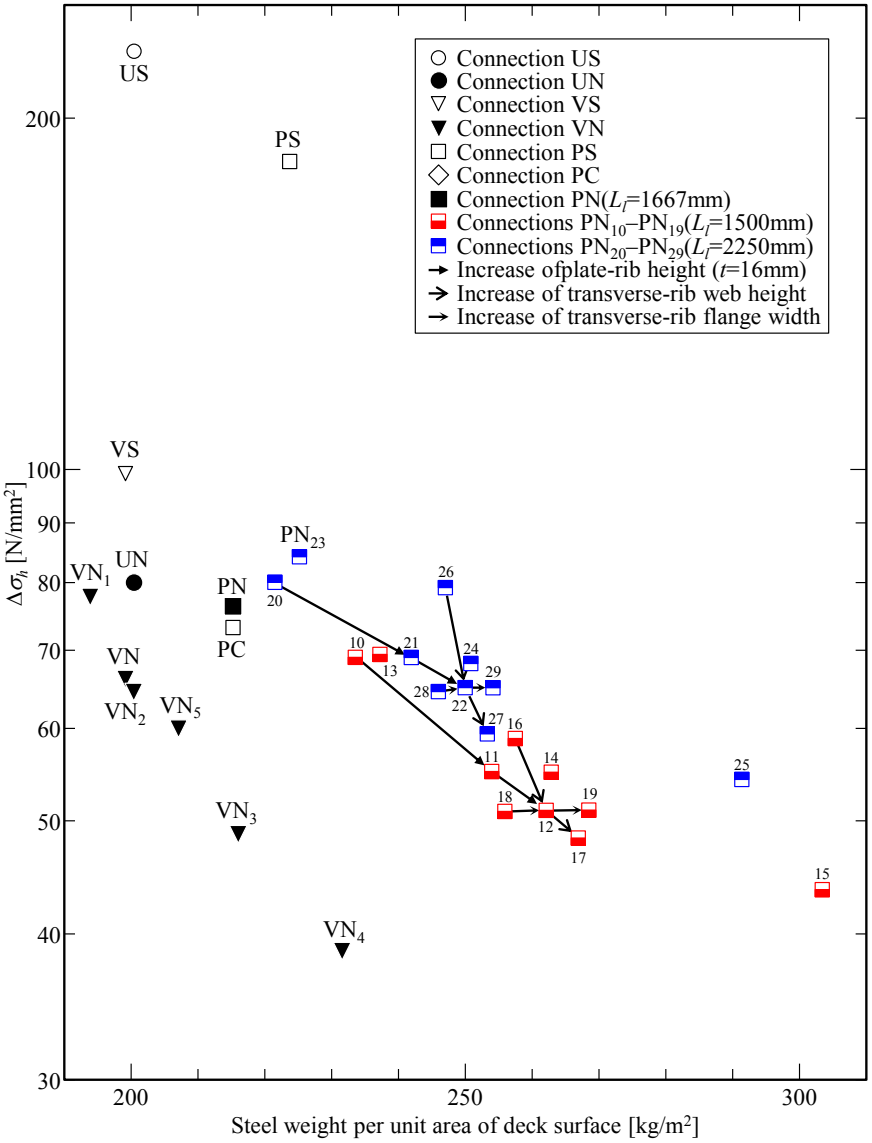

Fig. 3-24 Relations between hot-spot stress ranges and steel weights of the connections

4. Fatigue strength verification

4.1. Introduction

Fatigue improvement for longitudinal-rib to transverse-rib connections is important for developing orthotropic steel decks with high fatigue strength. Orthotropic steel decks suffer serious fatigue problems, especially fatigue cracks initiated from the longitudinal-rib to transverse-rib connections; this cracks account for approximately 40% of all fatigue cracks in orthotropic steel decks (Mori ed. 2010). However, previous studies of longitudinal-rib to transverse-rib connections have not sufficiently considered moving of the loading position (Katsumata et al. 2000; Ohashi et al. 2000; Kolstein 2001; Taskopoulos et al. 2003, Conner and Fisher 2006, Miki and Suganuma 2014; Hanji et al. 2013). The positions of vehicles move in the longitudinal direction and are transversely distributed (Leonard 1969; Takada 2009a). Furthermore, critical loading positions, causing maximum and minimum stresses on longitudinal-rib to transverse-rib connections are a distance away from the evaluated connections (Miki et al. 1995).

From the background above, the fatigue evaluation method was proposed to take moving of load positions into account (Chapter 3). The method used the hot-spot stress approach with factors, 0.8 and $(\text{thickness}/25)^{0.25}$, for the bending and the thickness effects on fatigue, respectively, since the longitudinal-rib to transverse-rib connections have comparatively thin steel plates down to 6 mm and both membrane and bending stresses. As the results of the evaluation, critical loading positions were found to be a distance away from the evaluated longitudinal-rib to transverse-rib connections in all cases of the six types of connections. The critical loading positions were those causing the maximum and the minimum factored hot-spot stresses on the connections, and they were considered to be dominant for fatigue damage. Hence, the fatigue strength of the connections must be evaluated under those loading conditions.

The applicability of the factored hot-spot stress approach has not been investigated for longitudinal-rib to transverse-rib connections. Based on the re-analyzing of literature data (Chapter 2), the approach was found to provide safe fatigue evaluations against JSSC-E class (Japanese Society of Steel Construction 2012). However, the literature data did not include models of orthotropic steel decks. In addition, the re-analyzing used basic fatigue test results of component models to determine the thickness and bending effects, though it was reported that the fatigue strength of the component models and structural models could be different (Anami 2000). The hot-spot stress of the longitudinal-rib to transverse-rib connections were computed by shell element models of finite element analyses, because it can decrease computation costs dramatically compared to the costs of solid element models. However, finite element models, especially shell element models, cannot simulate shapes and stiffness of welded parts. Therefore, the applicability of the factored hot-spot approach needed to be investigated for stress analyses by shell element models.

From the background above, the following objectives of this chapter were established.

1) Clarify the fatigue strength of longitudinal-rib to transverse-rib connections by fatigue tests simulating critical loading conditions.
2) Investigate the applicability of the factored hot-spot stress approach to longitudinal-rib to transverse-rib connections.
3) Validate shell element FEA applicability to confirm the validity of critical loading conditions determined by FEA and applied to fatigue test conditions.

4.2. Fatigue tests under critical loading conditions

4.2.1. Panel specimens for three-dimensionally deformed connections

Four deck panel models were fabricated for fatigue tests, as shown in Table 4-1 and Fig. 4-1. Models U and P included the slit and the non-slit connections to investigate the applicability of the hot-spot stress approaches to both types of connections, since U-rib and plate-rib slit connections (connections US and PS), are a common detail applied to Japanese bridges, and U-rib and plate-rib non-slit connections (connections UN and PN), are expected to have high fatigue strength. Models V and PL included only the non-slit connections with V-rib and Plate-rib (connections VN and PN_{27}). Model PL was prepared to investigate the fatigue behavior of plate-rib non-slit connections under running as well as constant position tandem axis loadings, which are closer to actual vehicle loading compared to constant position double tire loadings of the other models. Connection names in this chapter are same as previous chapter.

The models made of JIS SM400A steels were fabricated by a common assembling procedure that checks for weld root gaps and weld leg length. As written in the recommendations (Federal Highway Administration 2012), transverse-ribs were fitted-up to longitudinal ribs previously welded to deck plates, and welded to longitudinal ribs and deck plates. The main girders of the models were also welded to deck plates before assembling the transverse ribs. Weld root gaps between longitudinal and transverse ribs were designed as 2 mm only for plate-rib non-slit connections to enable the fit-up of the transverse ribs (Fig. 4-2), compared to 1 mm for the other connections. Therefore, the weld root gaps of the plate-rib non-slit connections were 4 mm maximum with 0 mm gaps at the other side surface of the plate ribs. The weld leg lengths of fillet welds of non-slit connections were controlled to be larger than 6 mm plus weld root gaps, whereas those of the other joints were larger than 6 mm, as shown in Table 4-1 Deck panel models for fatigue tests. Welds of rib-to-deck joints of the closed rib models were designed as 75% partial penetrations.

As mentioned in the previous chapter, common designs in Japan were applied to cross sections of longitudinal ribs, slit shapes, and span lengths of longitudinal ribs except for the design of Model PL (Japan Road Association 2014). The V-rib cross section was decided to have the same radius as the cross section used in the bending plate process and approximately the same cross section area as those of the commonly used U-rib. The plate-rib cross section was decided to have approximately the same cross section modulus with a commonly used bulb rib with 230-mm height and 11-mm thickness, where the effective width of the deck plates was taken into account for the sections. The slit detail of connection PS was based on the recommended standard with its radius enlarged to 45 mm, which could improve fatigue strength according to investigations of

the Metropolitan Expressway in Japan (Mori ed. 2010). Model PL was designed to have lower hot-spot stress ranges than the constant amplitude fatigue limit of JSSC-E class, after the thickness and the bending effect were taken into account.

The inner diaphragms were welded in U- and V-ribs by 4-mm fillet welds to simulate actual structural conditions. The diaphragms are installed at the longitudinal connections of actual structures for protection against corrosion. In this study, the effect of the inner diaphragms on fatigue strength was also investigated, since they can increase stresses on longitudinal-rib to transverse-rib connections (Katsumata et al. 2000).

4.2.2. Evaluated weld toes

Fig. 4-3 shows evaluated weld toes in the models. Numerous arrows along weld toe lines mean a hot spot will be somewhere on the toe line. Weld toes 1 and 2 were given to transverse- and longitudinal-rib side weld toes of the welded joints between the longitudinal and transverse ribs (Fig. 4-3b, c, e, g, i). In the case of connection PS, weld toes 3 and 4 were given to the transverse-rib and deck-plate side weld toes of welded joints between the transverse rib and the deck plate (Fig. 4-3g). It should be noted that weld toe 4 has almost no fatigue problem according to the investigations of Japanese expressways. In the following descriptions, weld toes of each type of connection are named as the connection name combined with two numbers indicating the evaluated part number and the weld toe number, such as US-31 indicating weld toe 1 in part 3 of connection US.

4.2.3. Static loading tests: validation of FEA applicability

Static loading tests were conducted before each fatigue test to investigate the stress behavior at surfaces near evaluated weld toes and to check the differences between the measured stress and the FEA results for validation of the FEA from the previous chapter. Static loading tests in the running wheel tests investigated the stress behavior around evaluated weld toes. The static loading tests included the principal stress directions, since the directions were assumed to be rotated, according to FEA results.

Fig. 4-1 shows the load cases. Loads were transferred from a 500 kN hydraulic jack to the models via rubber plates to simulate tire load conditions, as shown in Fig. 4-4b, or a running wheel machine was located on the models, as shown in Fig. 4-4c. The static loadings by the running wheel were conducted while moving the wheel position in 200-mm intervals.

The maximum loads of the static loading tests were the same as those for the fatigue tests when both static loading and fatigue test were conducted with those loading position. The maximum loads were 100 kN when only static loading tests were conducted with those loading positions. Static loadings were conducted not only with the load cases shown in Fig. 4-1, but also other load cases. Details of the other load cases are described in Appendix-B.

Strains and strain concentrations were measured at surfaces near the evaluated weld toes to investigate the stress behavior and to check differences between the measured stress and the FEA results. For all evaluated weld toes, uni-axial or tri-axial strain gauges with 1-mm gauge length were attached at points distant from the surface intersections of the two plates by 20 mm or from plate edges by 10 mm, as shown in Fig. 4-5. The strain gauge locations were determined to measure stresses without the effects of the weld toe shapes. Furthermore, stress concentrations were measured at weld toes

PL-21 and 22 by five strain gauges arranged in a row at 2-mm intervals. The first strain gauges were attached on points as near to the weld toes as possible.

4.2.4. Constant amplitude fatigue tests: validation of fatigue strength

Table 4-3 shows sequences, load ranges, and frequencies of fatigue tests with the load cases shown in Fig. 4-1. Additional fatigue tests for rib-to-deck joints were conducted by single tire loads located at the centers of models U and V.

Constant amplitude fatigue tests were conducted for all four models with loading positions expected to cause maximum and/or minimum hot-spot stresses on the longitudinal-rib to transverse-rib connections. Loading cases were named with uppercase letters for the target connections followed by lowercase letters ‘a’ and ‘b’, such as USa. The loads simulated a double tire for models U, V, and P, and double tires of tandem axes for model PL. The loads for models U, V, and P were applied to simulate the critical loading conditions clarified by the hot-spot stress computations in the previous chapter, and the loads for model PL simulated the situation closer to actual vehicle loading.

The load ranges of constant amplitude fatigue tests were basically determined to simulate the hot-spot stress ranges caused in actual bridges based on the FEA results. In actual bridges, stresses on the weld toes change from tensile to compressive depending on the load positions. However, the stresses at the weld toes were fixed to tensile or compressive cyclic stresses in the fatigue tests. To simulate the hot-spot stress ranges by the stress reversal under constant amplitude cyclic loading, the load ranges for fatigue tests were increased as follows.

$$\Delta P = \frac{\Delta \sigma'_h}{\sigma'_{h,test}} P_{design} \qquad 4\text{-}1$$

where ΔP, P_{design} represent the increased load range and the design load (= 100 kN), respectively, and $\Delta \sigma'_h$, and $\sigma'_{h,test}$ represent the hot-spot stress ranges caused by the moving positions of loads and fatigue tests based on the FEA results, respectively. The design load was determined from the Japan Road Association (2014). It should be noted that ΔP varies for each weld toe because $\Delta \sigma'_h$, and $\sigma'_{h,t}$ of each weld toe are different. The load ranges of the fatigue tests were increased when no fatigue cracks were expected, based on the computed hot-spot stress, or no cracks were detected after 5.0 million cycles of fatigue tests. The stress ratios were set to approximately zero.

Fatigue failure events were defined as the surface crack propagation from the weld toe to the base material in this study. Fatigue crack initiations and propagations were monitored by strain gauges (Fig. 4-5), and magnetic particle examinations.

Unexpected fatigue cracks at rib-to-deck joints were detected underneath the load positions during the fatigue tests for models P and V, and the unexpected cracks of model P were repaired. The fatigue cracks of model P were initiated from the deck-plate side weld toes of the rib-to-deck fillet welded joints. Because these cracks were not reported in the investigations of actual bridges, the fatigue tests were continued after removing the cracks by grinding, re-welding the ground part and reinforcing new weld toes by ultrasonic impact treatments. The main reason for the unexpected cracks was the increase of the load range by Equation 4-1 to simulate the hot-spot stress ranges of the longitudinal-rib to transverse-rib connection by moving the load position. The hot-spot stresses

at the weld toe of un-expected cracks were greater than 200 N/mm^2.

The un-expected fatigue cracks of model V were detected on the weld bead surface of the rib-to-deck 75%-penetration welded joint after finishing the constant amplitude fatigue tests. The running wheel fatigue tests were continued without repairing the rib-to-deck joint crack, which might have been initiated from the weld root after the constant amplitude fatigue tests. The rib-to-deck joint cracks were considered to not affect the fatigue tests for the longitudinal-rib to transverse-rib connections.

4.2.5. Running wheel fatigue tests: validation of fatigue lives

Running wheel fatigue tests were conducted for models V and PL to investigate fatigue behaviors of the non-slit connections under situations closer to actual vehicle loadings, as shown in Fig. 4-4c. The running wheel machine had two sets of double tires arranged as tandem axes with 1400-mm distance, and the machine was moved back and forth by a chain.

Load ranges, or the weight of the running wheel machine, were set to 198 kN. Even though it would be heavier than the design fatigue loads, the load could not cause enough hot-spot stress ranges to initiate fatigue cracks according to the FEA results. Heavier load ranges would increase stress ranges and fatigue damage possibilities, but tire collapse would be a danger in actual wheel tires.

Fatigue crack initiations and propagations were monitored by strain gauges (Fig. 4-5), and magnetic particle examinations were conducted at intervals of approximately 0.5–0.7 × 10^5 cycles.

4.3. Static loading test results

4.3.1. Validation of FEA results used for fatigue test condition

Fig. 4-6 shows comparisons between the measured and the computed stress on surfaces near the evaluated weld toes. The lengths and directions of arrows indicate the magnitudes and directions of principal stresses. The measured stresses were calculated from measured strain by an elastic modulus of 205 kN/mm^2. The computed stresses were the results of the FEA from the previous chapter.

For all evaluated toes, the directions of the measured principal stress were similar to those of the computed stresses. In the case of strains measured in connection PS, as shown in Fig. 4-6a, the measured directions differed from the computed directions by -9 to +9 degrees. The differences were -5 to +7 degrees in the case of connection VN shown in Fig. 4-6b. The comparison was conducted for a measured point having a stress magnitude larger than 10 N/mm^2. From the comparison above, the stress distributions were confirmed to be simulated well in FEA.

However, the magnitudes of the measured stresses tended to be larger than those of the computed stresses especially at weld toes on plate edges. The magnitudes of the measured strain at weld toes on plate edges were higher than those of the computed strain by an average of 19% and a maximum of 36% in the case of Fig. 4-6a. The hot-spot stresses calculated from measured strains were also higher than those from the FEA results. Magnitudes of the measured strain at weld toes on plate surfaces were higher than those of the computed strains by 1.5% on average and 17% maximum.

4.3.2. Inelastic strain behaviors at weld toes

Fig. 4-7 shows inelastic strain behaviors observed at plate surfaces and plate edges near the evaluated weld toes on plate edges when compression stress acted on the strain gauges. Fig. 4-7b–d show strains measured at plate surfaces near PS-23 (PS-23'), PS-43 (PS-43'), and PS-53 (PS-53'). Fig. 4-7a show the locations of the strain gauges. The strains at PS-43 and PS-53 behaved like compression yielding when 100 kN of load PSa acted, compared to the linear relation between tensile strain at PS-23 and the load. Fig. 4-7f and g show strains measured at plate surfaces and edges near PN-42 and PN-42', respectively. Fig. 4-7e shows the locations of those strain gauges. The strains at PN-42 and PN-42' also behaved like compression yielding under 210 kN of load PNa. In addition, similar inelastic strain behaviors were observed at PS-33 and PS-33' under 100 kN of load PSc, PL-22 and PL-22' under 198 kN of load PLr, PL-32 and PL-32' under 856 kN of load PLa, and PL-42 and PL-42' under 633 kN of load PLb. All of these inelastic strains were observed at weld toes on plate edges in connection PS and PN, where the compression stress acted.

The inelastic strains might arise from the compression residual stress introduced during fabrication procedures. The strain levels at the gauges immediately before inelastic strain behavior started were smaller than the material yielding strains, which were more than 1500 μ according to mill sheets. These strains could mean that additional residual stresses existed at the weld toes on plate edges. Though welding procedures are known to cause tensile residual stresses near to the yielding of base materials, it has also been reported that residual stress levels could change depending on the welding procedures. In previous study, compression residual stresses were also observed at weld toes on plate edges, whereas the specimens were different from the longitudinal-rib to transverse-rib connection (Fricke and Doerk 2004). Furthermore, the base materials can have residual stress distributions along the thicknesses as a result of the steel plate rolling. However, it should be noted that controlling residual stresses at the weld toes would be difficult due to complex fabrication procedures of longitudinal-rib to transverse-rib connections and the compression residual stress could not be expected.

4.4. Fatigue test results

4.4.1. Constant amplitude fatigue test results

Table 4-4 summarizes the fatigue test results. The table shows load cycles as the cycles for fatigue failure (N_f) or cycles of the end of the fatigue test in cases that no cracks were detected. Surface fatigue cracks were detected at slit connections of models U and P, and non-slit connections of models V and PL, as shown in Fig. 4-8 and Fig. 4-9. No cracks were detected in non-slit connections of models U and P by both visual inspections and strain monitoring. Though fatigue cracks at weld toes VN-32 and VN-32' were detected after 0.05 million cycles of the running wheel loading of load VNra, those cracks were considered to be caused by the constant amplitude fatigue test of load VNa; this test was conducted right before running wheel loading, because those cracks were not propagated after 0.50 million cycles of running wheel loading. The constant amplitude loading of load VNa gave a 1.2 times larger load range than that of the running wheel loading, and might have caused fatigue cracks at weld toes VN-32 and VN-32',

but those cracks were overlooked. In addition, the running wheel loading of load VNrb, which was run on the next V-rib, did not cause any damage after 0.17 million cycles.

Fatigue failures were determined from the lengths of the surface fatigue cracks. Fig. 4-10 shows the relations of fatigue crack lengths to load cycles. Fig. 4-10a shows the crack lengths in the base materials; these lengths could be zero in the cases that fatigue cracks were detected on weld toes but not yet propagated into the base materials. Fig. 4-10b shows fatigue crack lengths including cracks along the weld toes. The cracks initiated at the box weld toes on plate surfaces (US-22, US-32, PS-14, PS-24, PL-31, and PL-41) were propagated into the base materials. Fatigue failures for those cracks were defined as crack propagations from the weld toes into the base materials in this study. However, the crack initiated at the weld toes on plate edges, which was PS-23, was initiated at the plate edge and not propagated into the base material during fatigue tests. The fatigue failure for that crack was defined as crack propagation into the plate surface, i.e., a through-thickness crack in this study. In addition, the cracks at the weld toes perpendicular to transverse weld, which were VN-32 and VN-32', were also not propagated into the base material. The fatigue failures for those cracks were defined as the surface crack lengths of three times the plate thickness under the assumption that crack aspect ratios were one-third in this study. The surface crack lengths were 22-40 mm at the fatigue failures.

The lengths of the cracks at weld toes US-22 and US-32 propagated at accelerated speed, whereas propagation of the crack at weld toe PS-14 was decelerated. Crack propagation rates are known to increase as the crack length increases in simple component joints under membrane stress. The reason for the crack deceleration could be the decrease of effective stress ranges at crack tips by complex stress conditions including the bending stress component at longitudinal-rib to transverse-rib connections.

Fig. 4-11 shows strains measured at surfaces near the cracked weld toes. The strain history indicates that cracks initiated before they were detected visually and tensile residual stresses existed at some weld toes. The measured strain ranges dropped at weld toes US-22, US-23, PL-31, and PL-41, or increased at weld toe PS-24, before cracks were detected. This result means cracks initiated before visual detections. Furthermore, the strains measured under almost no external forces dropped at weld toes PS-24, PL-31, and PL-41. This result indicates tensile residual stresses existed. On the other hand, measured strain ranges were slightly or not changed at weld toes VN-32, VN-32', and PL-23. Though the strain range at weld toe PL-23 changed slightly after the crack on it was detected, it could be affected not only by the crack at weld toe PL-23 but also the crack at weld toe PL-24. The less-sensitive strain at weld toe PL-24 might be related to the compression residual stress, which was estimated to exist at weld toes similar to weld toe PL-24 as the results of the static loading tests. The strain measurement points at weld toes VN-32 and VN-32' were at some distance away from the cracks and could result in less sensitivity of the strain ranges. Unfortunately, strains at weld toe PL-14 were not measured.

4.4.2. Running wheel fatigue test results

Table 4-4 includes running wheel fatigue test results. No changes were observed at the longitudinal-rib to transverse-rib connections after all running wheel fatigue tests of model V and PL. The measured strains at the evaluated weld toes in longitudinal-rib to transverse-rib connections were also not changed during the fatigue tests. However, the

cracks at rib-to-deck joints of model V were caused by the constant amplitude fatigue test and propagated during the running wheel fatigue tests. The detail of the rib-to-deck joint crack of model V is shown in Appendix-B.

4.5. Fatigue assessment

4.5.1. Fatigue strength assessment under critical loading conditions

Fig. 4-12 shows the relations between load ranges and the fatigue test results of the longitudinal-rib to transverse-rib connections. This figure also shows the design curve, which is connected to a point at 10^7 cycles of the fatigue design load with a slope of -1/3 under the assumption that a constant amplitude fatigue limit can connect to a point at 10^7 cycles. The design curve shows one possibility and should be determined for each project. The design load was determined from the Japan Road Association (2014).

Though Fig. 4-12a has a vertical axis of the load range in the fatigue tests, vehicle loads can move and cause larger stress ranges than the stress range caused during the fatigue tests, as described above. Therefore, in Fig. 4-12b, the load ranges were factored to express the magnitude of vehicle loads that would cause the stress ranges at the evaluated weld toes, as in the following equation.

$$\Delta P' = \frac{\sigma'_{h,test}}{\Delta\sigma'_h}\Delta P_{test} \qquad 4\text{-}2$$

where $\Delta P'$, ΔP_{test} represent the factored load range and the load range in the fatigue test, respectively, and $\Delta\sigma'_h$, and $\sigma'_{h,test}$ represent the hot-spot stress ranges caused by 100 kN moving position loads and 100 kN fatigue tests based on the FEA results, respectively.

In Fig. 4-12b, the fatigue test results of connections VN and PN were plotted above the design curve and those of connections US and PS were plotted below the design curve. Though the fatigue test result of connection UN was plotted below the design curve, it was run-out data. Therefore, connections VN and PN could achieve 10^7 cycles of the fatigue design load, and connections US and PS could not. Connection UN could possibly have higher fatigue strength than the design curve, but more investigations are required to confirm its fatigue strength.

However, fatigue cracks were initiated at rib-to-deck joints of models U and V plotted below the design curve (Fig. 4-12b). Therefore, orthotropic steel decks with connection VN cannot achieve the objective fatigue life, though its longitudinal-rib to transverse-rib connection had high fatigue resistance.

Fig. 4-12b shows the factored load range as the vertical axis. This figure indicates that connection PS would have lower fatigue strength than the design curve, which is different from the result in Fig. 4-12a. Therefore, the fatigue test without taking account of moving of the load position could result in incorrect fatigue strength.

4.5.2. Hot-spot stress applicability to longitudinal-rib to transverse-rib connections

Fig. 4-13 shows the relations between $\Delta\sigma'_h$ and fatigue lives (N_f) of the longitudinal-rib to transverse-rib connections, which were obtained from the FEA and the fatigue tests. The figures show not only the results of failure but also the results of run-out in

the plot above JSSC-E class. All results were conservative results against JSSC-E class, though some results showed excessively high fatigue strength. Therefore, the fatigue of the longitudinal-rib to transverse-rib connections could be conservatively evaluated by the hot-spot stress approach combined with the factors for the thickness and the bending effect, and the design curve of JSSC-E class.

Though fatigue cracks were initiated from weld toes PS-14 and PS-24, these cracks would be not initiated in actual bridges. The results of weld toes PS-14 and PS-24, shown in Fig. 4-13 as open rectangular marks, were located at lower fatigue strengths than the results of weld toe PS-23, shown as solid rectangular marks. These results seems to indicate that the fatigue strength of connection PS could be determined by weld toes similar to PS-14 and PS-24, which are deck-plate side weld toes of box welds at the upper ends of the slits rather than weld toe similar to PS-23, which are transverse-rib side weld toes of the same welds. However, almost no cracks have been reported at the deck-plate side weld toes in investigations of actual bridges (Mori 2010). Those unexpected fatigue crack initiations (PS-14, -24) may be partly due to the differences of loads and surfacing between the fatigue tests and the actual bridges. The loads of the fatigue tests were located at a fixed position and caused tension cyclic stresses on weld toes PS-14, PS-24 and PS-23, whereas vehicle loads on an actual bridges can cause stress reversals on the weld toes. The surfacing would reduce stresses of weld toes near the deck plates, but were ignored in this study mainly because of the uncertain stiffness of surfaces and the lesser effect on stress reductions for longitudinal-rib to transverse-rib connections, as described in the literature review of this dissertation. Further investigations are required to clearly understand the result of connection PS.

The fatigue strength of connection PN can be determined by the cracks on the transverse-rib side weld toes of the box welds at longitudinal-rib to transverse-rib joints, even though the longitudinal-rib side weld toes have higher hot-spot stress ranges. The results of the transverse-rib side weld toes, PL-31 and PL-41, show lower fatigue strengths than the results of the longitudinal-rib side weld toes, PN-42, PL-32, and PL-42 (Fig. 4-13). In addition, the transverse-rib side weld toes, PL-21, had higher hot-spot stress in experiments than that in the FEA, especially when compared to the longitudinal-rib side weld toe PL-22, which had lower hot-spot stress in the experiments than that in the FEA. The longitudinal-rib side weld toes had similar detail to weld toe PS-23, all of which showed high fatigue strength and can be classified into type B hot spots.

Fig. 4-14a–c show $\Delta\sigma'_h - N_f$ relations of each type of hot spots in the longitudinal-rib to transverse-rib connections as well as in literature data from Chapter 2. The literature data of in-plane gusset joints are plotted in Fig. 4-14b as reference, but were not used for comparisons because the type B hot spots investigated in this study were on the edges of plates welded to other plates with box welds and are geometrically different from the hot spots of in-plane gusset joints. The results of type A and type C hot spots in the longitudinal-rib to transverse-rib connections were plotted during 95%–5% survival ranges of literature data regardless of the tension or the compression working stresses. Therefore, the factored hot-spot stress approach provides accurate estimation for type A and C hot spots. The compression working stress could result in fatigue cracks due to tensile residual stresses observed in the strain measurements during the fatigue tests. However, the results of type B hot spots in the longitudinal-rib to transverse-rib connections were plotted above the 5% survival line of the literature data, regardless of the

tension or compression working stresses. The high fatigue strength evaluation might be affected by compression residual stresses, which were observed in the strain measurements during the static loading tests. However, further investigations are required to confirm existences and mechanisms of the compression residual stress at type B hot-spots. In addition, further investigations on weld shapes would support further understanding of the fatigue test results.

4.6. Summary

This chapter investigated the actual fatigue strength of the longitudinal-rib to transverse-rib connections and applicability of the factored hot-spot stress approach by taking account of the thickness and the bending effects by means of fatigue tests on deck panel models. Since vehicle loads can move and cause higher stress ranges at weld toes than can fixed position loads, the fatigue strength of the longitudinal-rib to transverse-rib connections were tested under critical loading conditions that cause maximum or minimum factored hot-spot stresses on the weld toes. The applicability of shell element models was also investigated by comparisons between measured and computed local stresses.

1) The fatigue strength of non-slit connections with V-ribs and plate ribs satisfied the fatigue strength equivalent to 10^7 cycles of the fatigue design load (T load), whereas the fatigue strength of the rib-to-deck joints of the U-rib and V-rib models were insufficient to 10^7 cycles of the fatigue design load under the condition that a 15% strain drop measured on rib-to-deck weld beads was regarded as N_f.
2) The factored hot-spot stress approach with the design curve of JSSC-E class provides conservative estimations for the fatigue strength of longitudinal-rib to transverse-rib connections. The estimations for type A and C hot spots are accurate enough, though the estimations for type B hot spots are excessively conservative.
3) Finite element analyses with the shell element models simulate stress conditions around weld toes in the longitudinal-rib to transverse-rib connections except for weld toes on plate edges of connections PS and PN, which have higher stresses than those computed by the finite element analyses.
4) Compressive residual stresses existed on some weld toes on plate edges and affected the fatigue test results.

Table 4-1 Deck panel models for fatigue tests

Model	Longitudinal-rib		Connection	
	Cross section	Span length [mm]	Type	Name
U	U-rib	2500	Slit and non-slit	US and UN
V	V-rib	2500	Non-slit	VN
P	Plate rib (h235 × t16 mm)	1666	Slit and non-slit	PS and PN
PL	Plate rib (h256 × t16 mm)	2250	Non-slit	PN_{27}

Table 4-2 Weld root gaps and leg lengths

Model (Connection)	Location number	Gap [mm]	Leg length [mm]	
			S1[a]	S2[b]
U (US)	1	0.5	6.2	
	2	0.9	6.5	
	3	1.5	7.0	
	4	0.6	7.0	
U (UN)	5	0.5	8.0	
	6	1.5	8.0	
V (VN)	30	1.6	7	
	3	1.0	8.5	
	4	1.7	8.5	
P (PS)	1	2.5	9	
	2	2.5	9	
	3	2.5	9	
	4	2.6	9	
	5	1.4	8	
P (PN)	30	1.0	10	
	3	2.0	11	
	3*	0.0	9	
	40	1.9	11	
	4	2.9	11	
	4*	0.0	11	
PL (PN_{24})	20	1.8	16.5	14.5
	2	1.7	9	11
	2*	2.0	10	12
	30	2.7	13.5	13
	3	3.1	10	10
	3*	0.4	9	11
	40	1.7	13	12
	4	2.5	10	10
	4*	1.1	10	11

Location

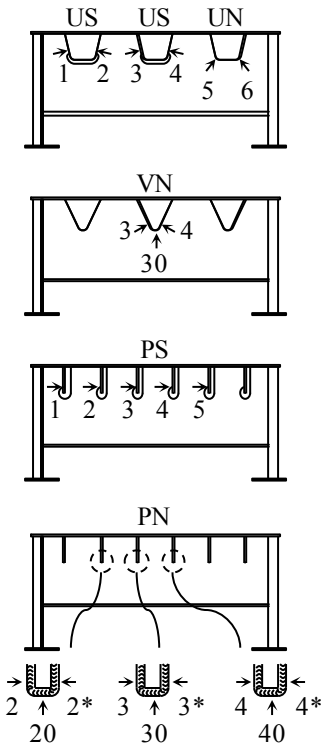

[a]S1: Longitudinal-rib side
[b]S2: Transverse-rib side

Table 4-3 Fatigue test procedure

Model	Test type	Load			
		Case	Range [kN]	Frequency [Hz]	Cycles [million]
U	Constant amplitude	USa	100	2.6	3.00
	Constant amplitude	UWa	75	2.5	3.00
	Constant amplitude	UNa	100	2.7	4.62
V	Constant amplitude	VWa	75	5.1	5.50
	Constant amplitude	VNa	120	3.5	5.00
			245	2.8	3.00
	Running wheel	VNra	198	0.09	0.50
	Running wheel	VNrb	198	0.09	0.17
P	Constant amplitude	PSa	195	3.0	5.35
			290	3.0	5.30
	Constant amplitude	PNa	205	3.0	5.40
			405	1.6	1.04
PL	Running wheel	PLr	198	0.12	2.00
	Constant amplitude	PLa	846	1.0	0.49
	Constant amplitude	PLb	623	1.2	0.86

Table 4-4 Fatigue test results

Model	Load			Status
	Case	Rage [kN]	Cycles [million]	
U	USa	100	0.70	Failure at weld toe US-22
	USa	100	1.48	Failure at weld toe US-32
	UWa	75	0.20	15 % strain drop at rib-to-deck joints (UW-35)
	UWa	75	0.35	15 % strain drop at rib-to-deck joints (UW-45)
	UNa	100	4.62	No crack observed
V	VWa	75	2.00	15 % strain drop at rib-to-deck joints (VW-45')
	VWa	75	2.25	15 % strain drop at rib-to-deck joints (VW-35')
	VNa	245	3.00[a]	Failure at weld toe VN-32
	VNa	245	3.00[a]	Failure at weld toe VN-32'
	VNra	198	0.50	No crack observed[a]
	VNrb	198	0.17	No crack observed
P	PSa	195	5.35	No crack observed
	PSa	290	1.25	Failure at weld toe PS-14
	PSa	290	2.33	Failure at weld toe PS-23
	PSa	290	3.48	Failure at weld toe PS-24
	PNb	205	5.40	No cracks observed
	PNb	410	1.04	No cracks observed
PL	PLr	198	2.00	No cracks observed
	PLa	846	0.41	Failure at weld toe PL-31
	PLb	642	0.86	Failure at weld toe PL-41

[a] Though the cracks were detected after 0.05 million cycles of the wheel running fatigue test, the cracks were considered to be caused by load VNa

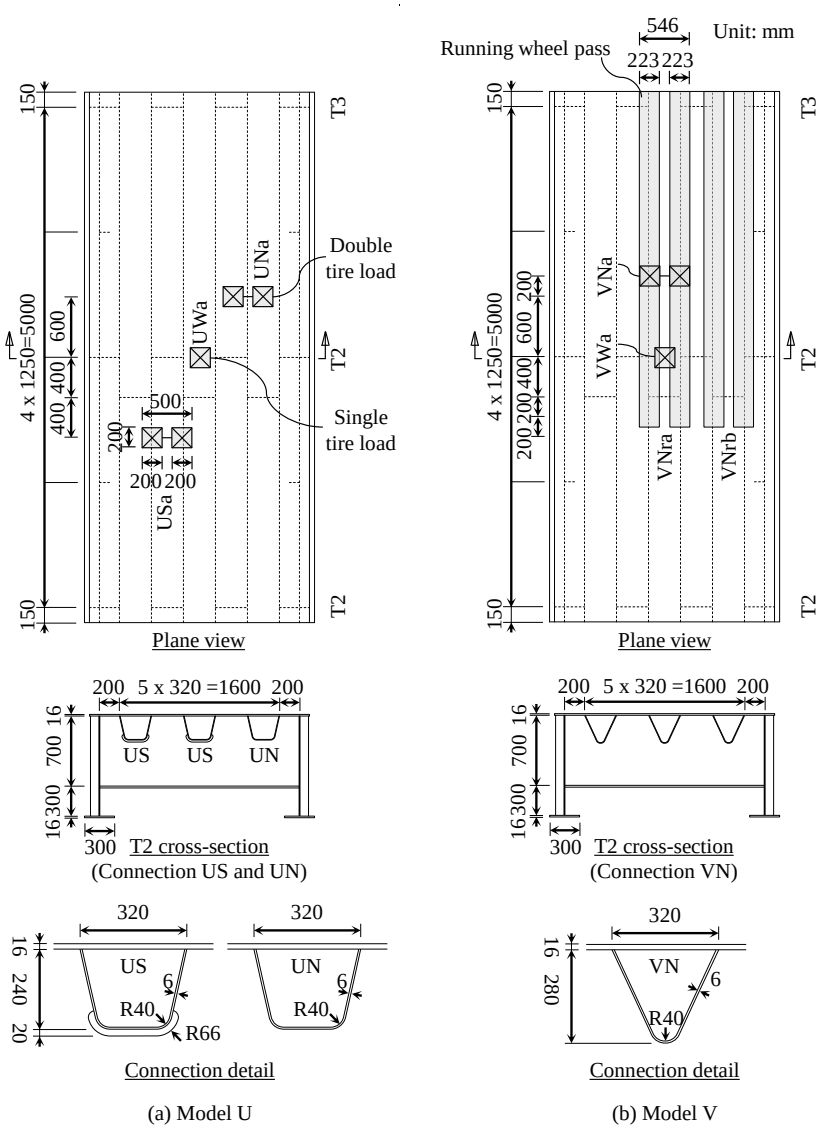

Fig. 4-1 Models and load cases

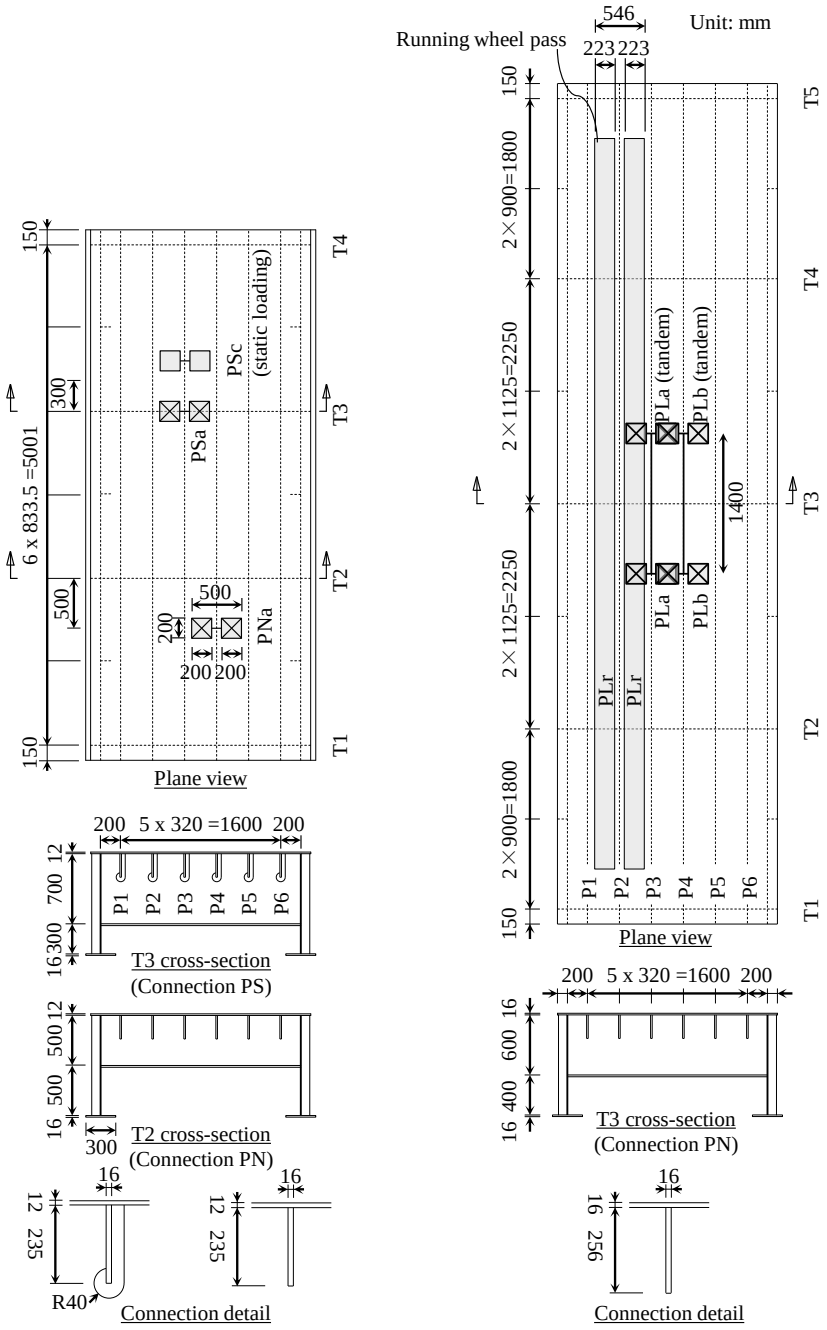

Fig. 4-1 Models and load cases (continue)

a) Before welding b) After welding

Fig. 4-2 Pictures of the connection between the plate-rib and the non-slit transverse-rib of model PL, before and after welding

Unit: mm
Brackets mean reverse surfaces

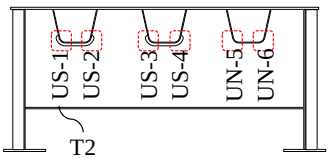

(a) Part names of model U

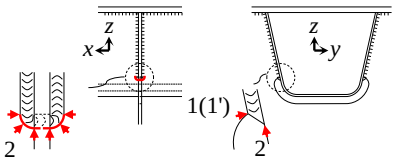

Side view Front view
(b) Weld toe numbers in connection US

Weld toe name
=[Part name] + [Weld toe number]

e.g. US31'

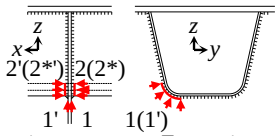

Side view Front view
(c) Weld toe numbers in connection UN

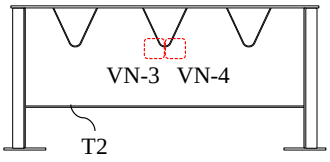

(d) Part names of model V

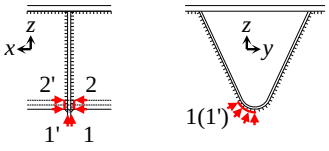

Side view Front view
(e) Weld toe numbers in connection VN

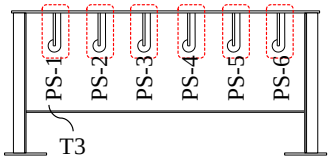

(f) Part names of model P
(Connection PS)

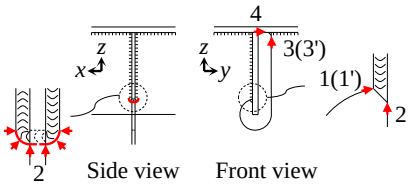

Side view Front view
(g) Weld toe numbers in connection PS

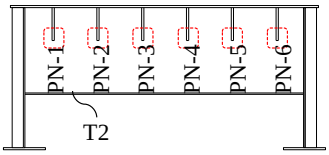

(h) Part names of model P
(Connection PN) [a]

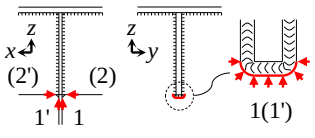

Side view Front view
(i) Weld toe numbers in connection PN[a]

[a] Weld toe names for T3 cross-section of Model PL are same as (h) and (i) instead of 'PN' replaced to 'PL'

Fig. 4-3 Names of hot-spots

(a) Overview of constant amplitude fatigue test

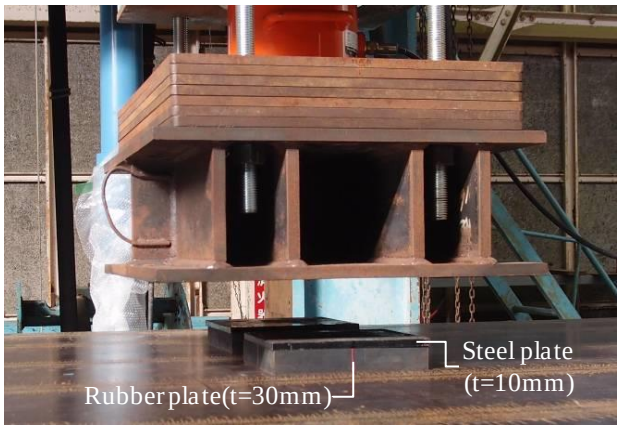

(b) Condition of load point in (a)

(c) Overview of running wheel fatigue tests

Fig. 4-4 Pictures of fatigue tests

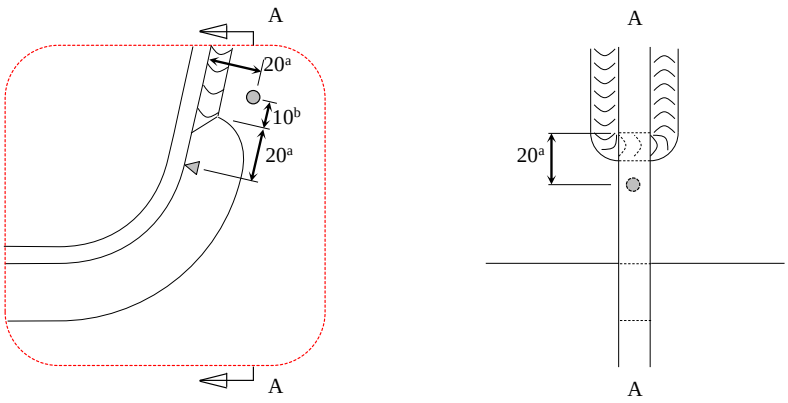

[a]20 mm from intersections of plate surfaces or edges
[b]10 mm from plate edges

Fig. 4-5 Strain gauge locations (Gauges at US21 and US22 as examples)

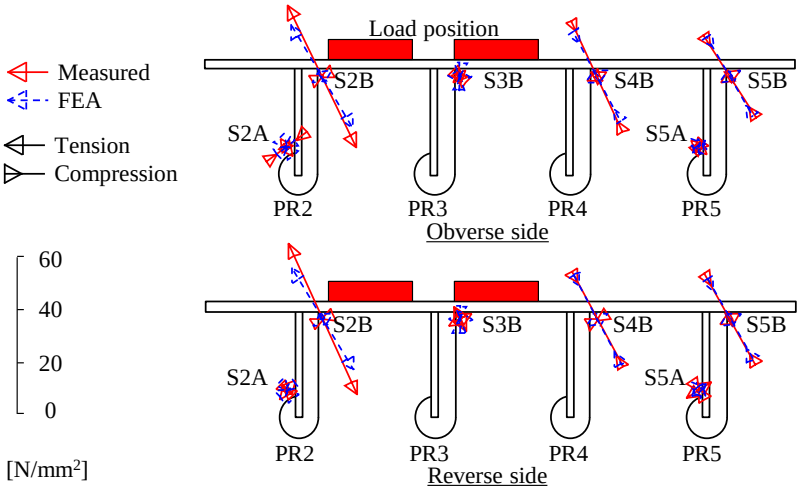

(a) Model P, connection PS , load PNa

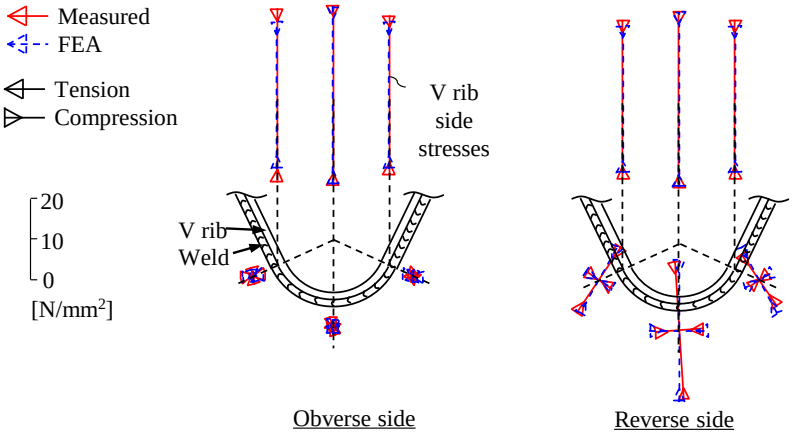

(b) Model V, Center V-rib, load VNa

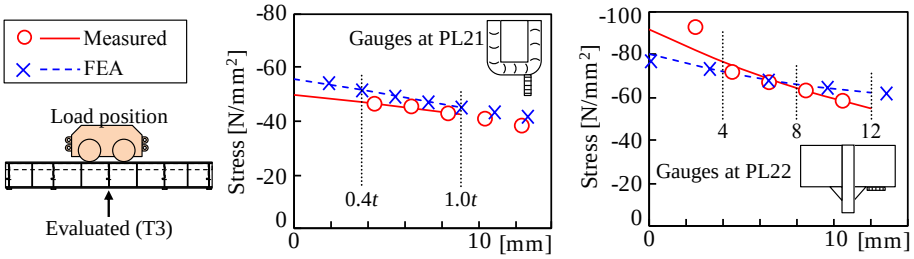

(c) Model PL, second plate-rib from left main girder, load PLr

Fig. 4-6 Measured and computed stresses at surfaces near to hot-spots

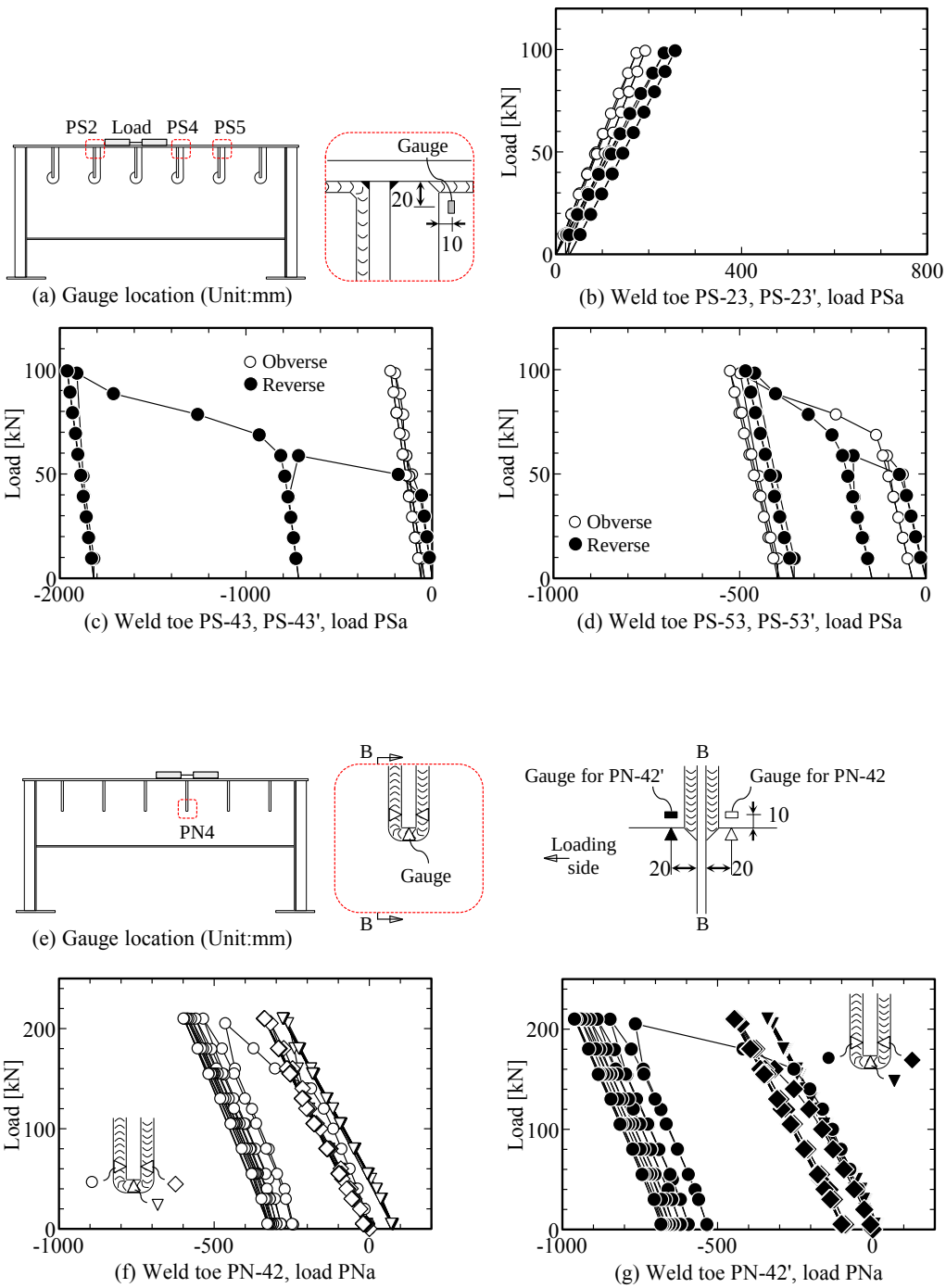

Fig. 4-7 In-elastic strain behaviors at weld toes

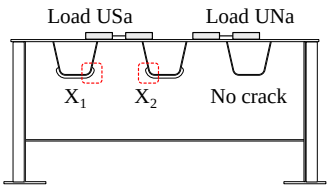

(a) Cracks in connections US

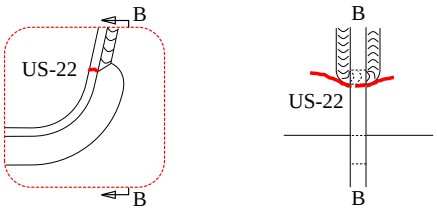

(b) Enlarged view of X_1, crack at US-22

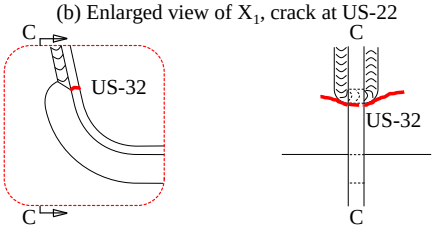

(c) Enlarged view of X_2, crack at US-32

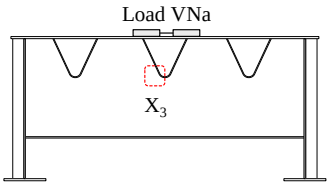

(d) Cracks in connections VN

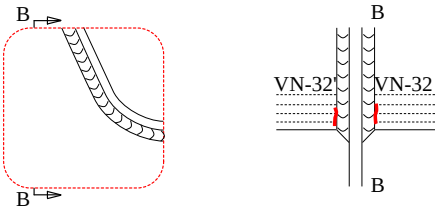

(e) Enlarged view of X_3, cracks at VN-32, VN-32'

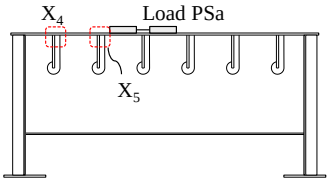

(f) Cracks in connections PS

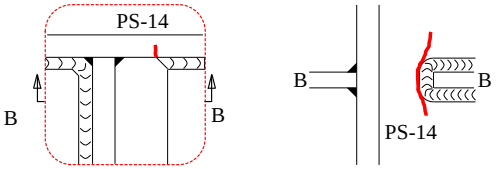

(g) Enlarged view of X_4, crack at PS-14

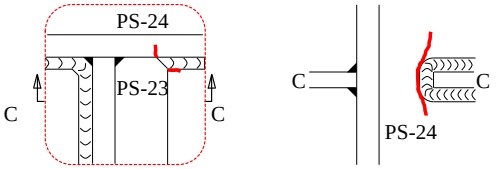

(h) Enlarged view of X_5, crack at US-32

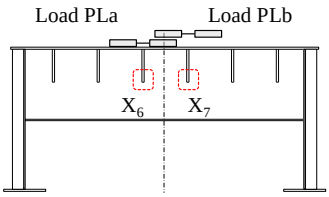

(i) Cracks in connections PL

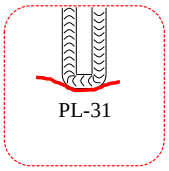

(j) Enlarged view of X_6, crack at PL-31

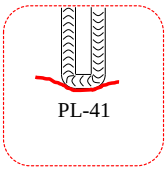

(k) Enlarged view of X_7, crack at PL-41

Fig. 4-8 Fatigue crack locations

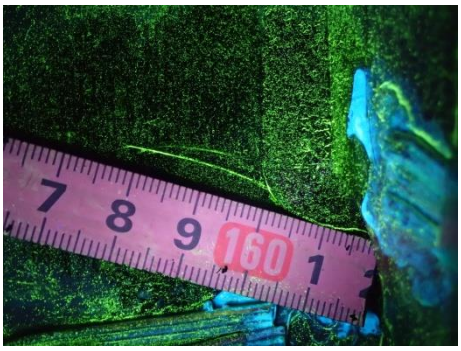

(a) Crack at US-22

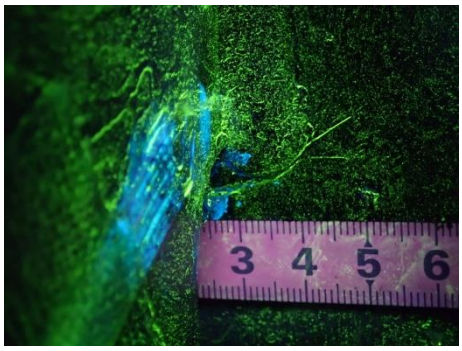

(b) Crack at US-32

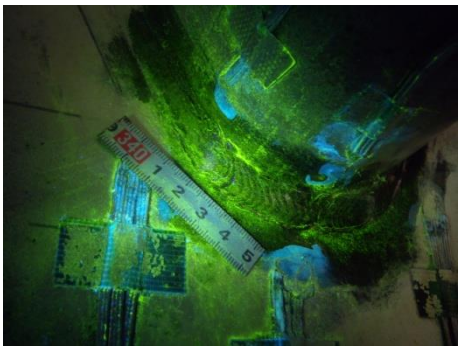

(c) Crack at VN-32

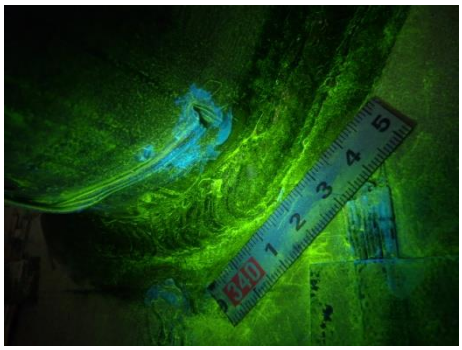

(d) Crack at VN-32'

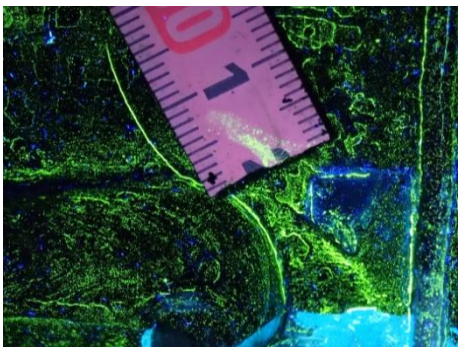

(e) Crack at PS-14

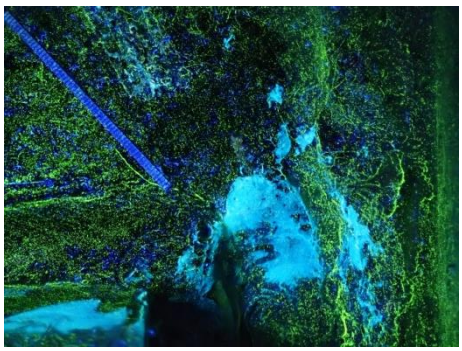

(f) Crack at PS-24

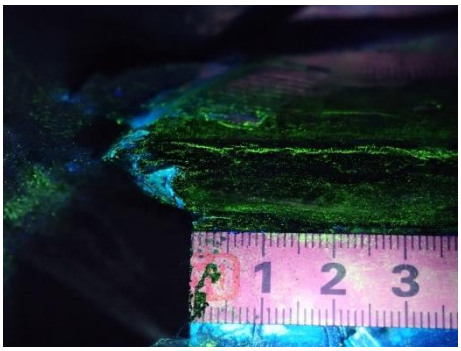

(g) Crack at PS-23

Fig. 4-9 Pictures of fatigue cracks

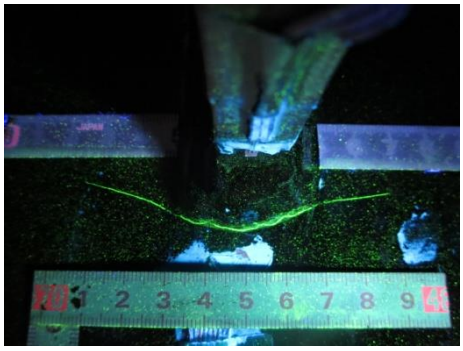

(h) Crack at PL-31

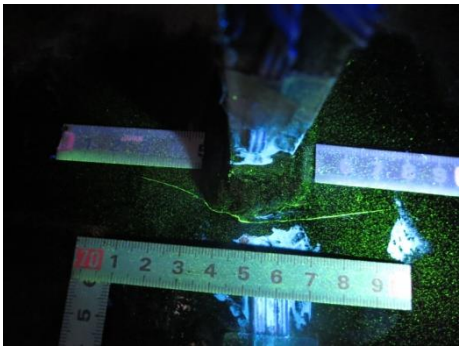

(i) Crack at PL-31'

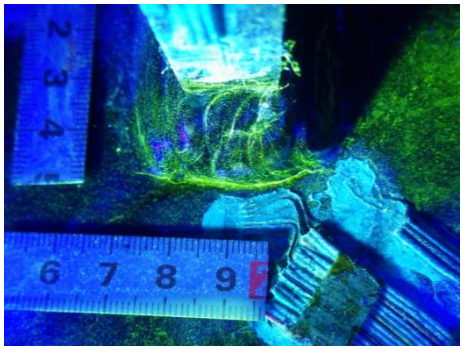

(j) Crack at PL-41

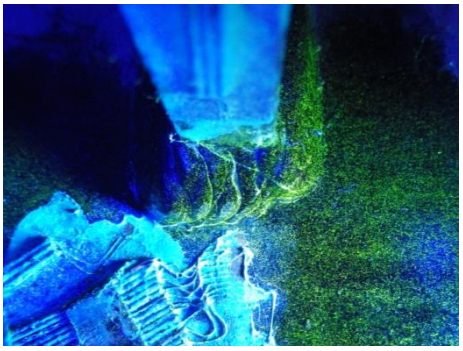

(k) Crack at PL-41'

Fig. 4-9 Pictures of fatigue cracks (continue)

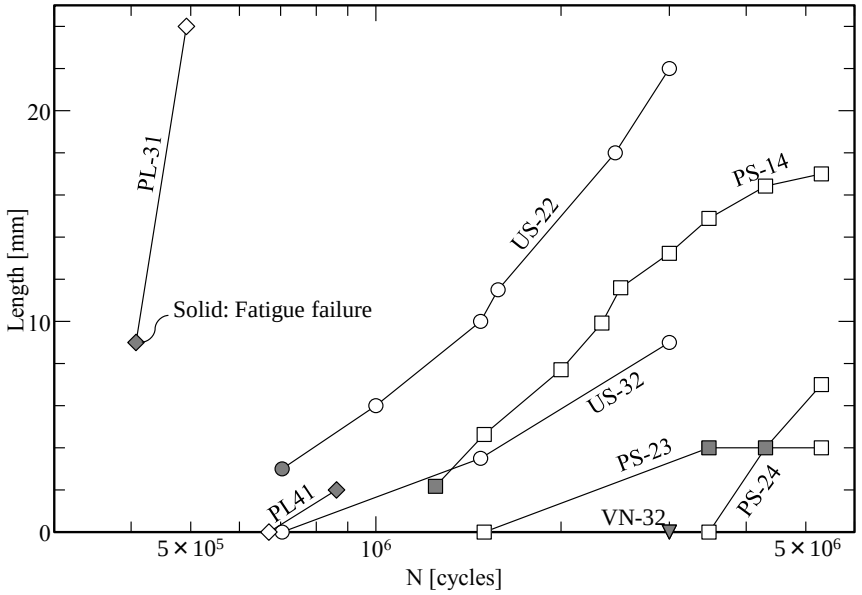

(a) Crack length in base material

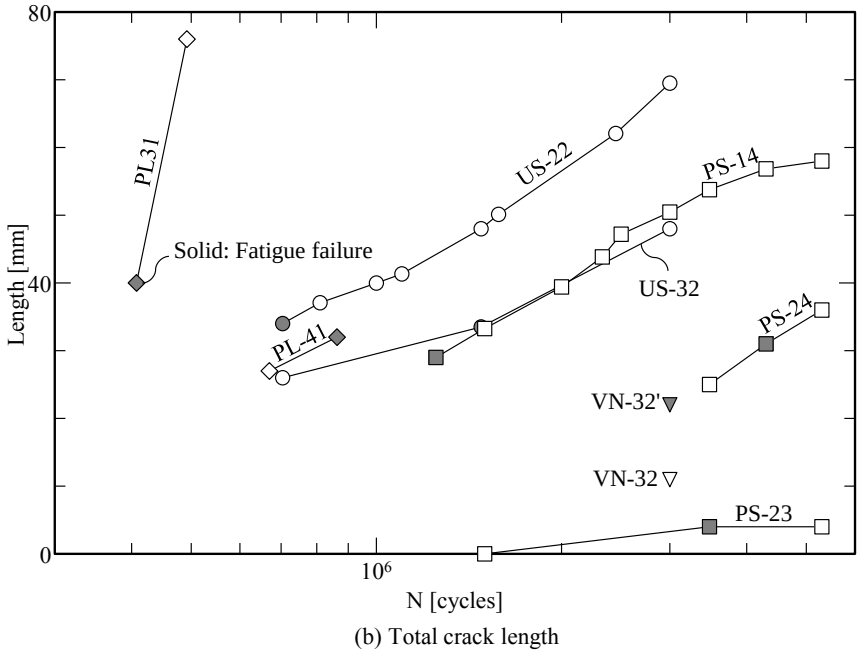

(b) Total crack length

Fig. 4-10 Fatigue crack lengths

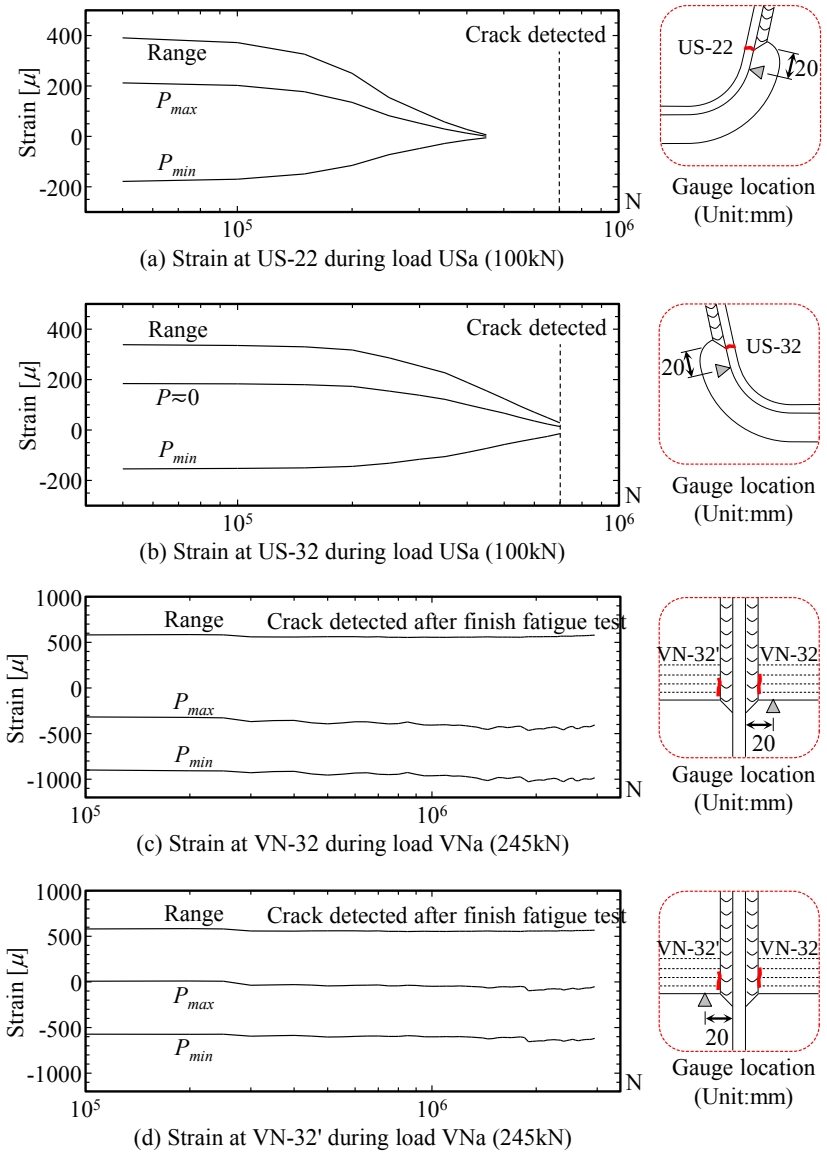

Fig. 4-11 Strains at cracked weld toes

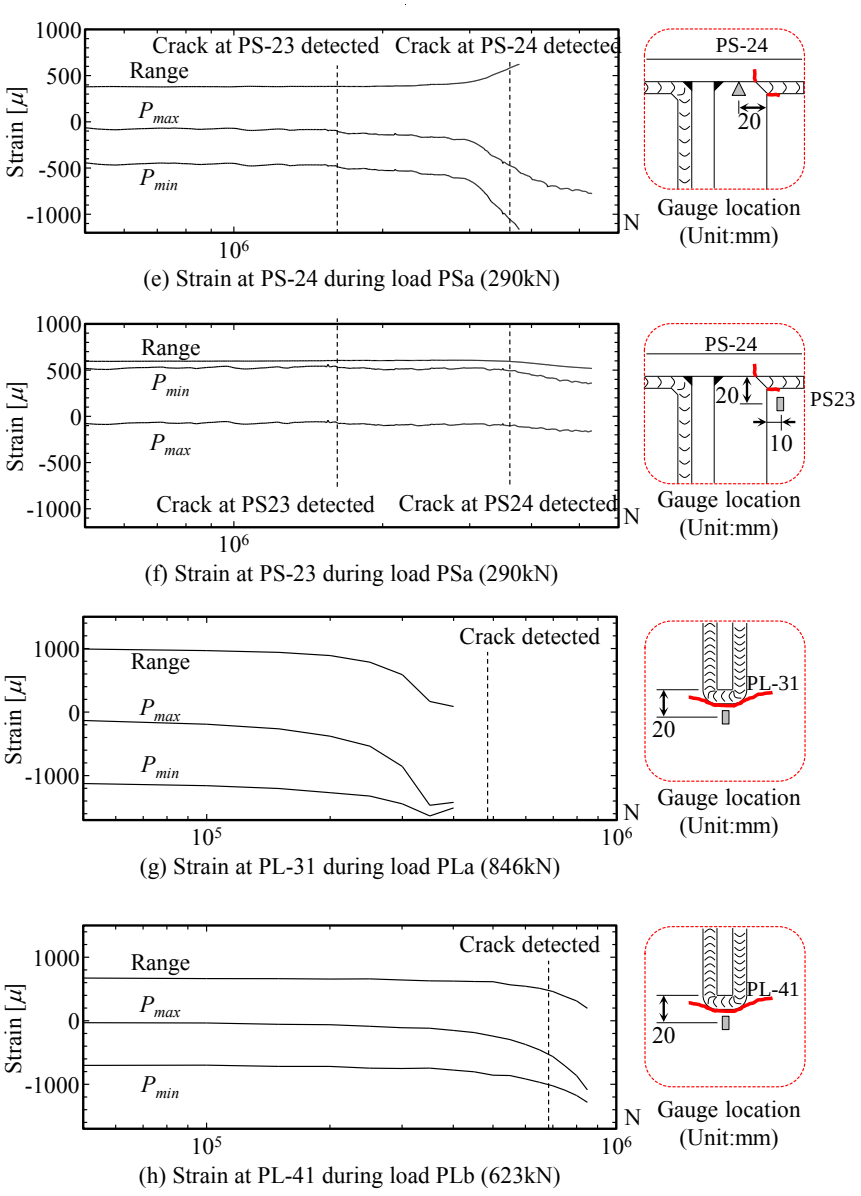

Fig. 4-11 Strains at cracked weld toes (continue)

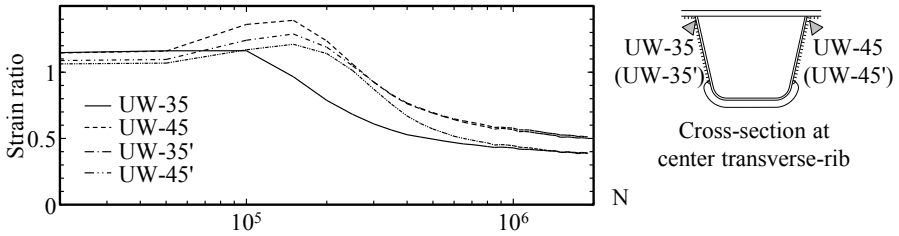

(a) Strain ratios at rib-to-deck joints of model U during load UWa (75kN)

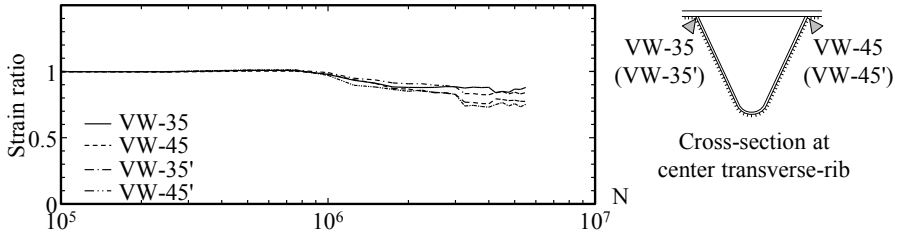

(b) Strain ratios at rib-to-deck joints of model V during load VWa (75kN)

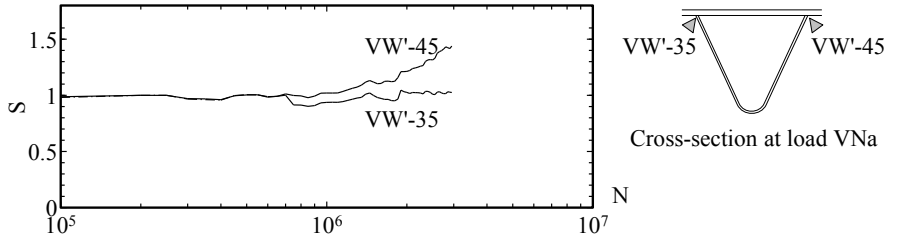

(c) Strain ratios at rib-to-deck joints of model V during load VNa (245kN)

Fig. 4-11 Strains at cracked weld toes (continue)

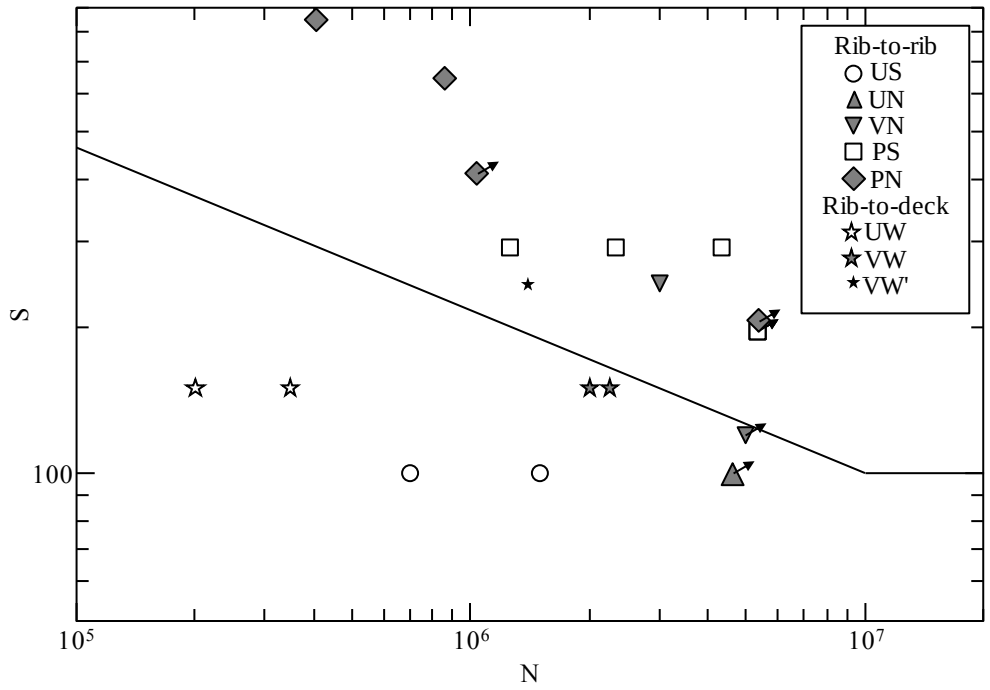

(a) Evaluation by load ranges in fatigue tests

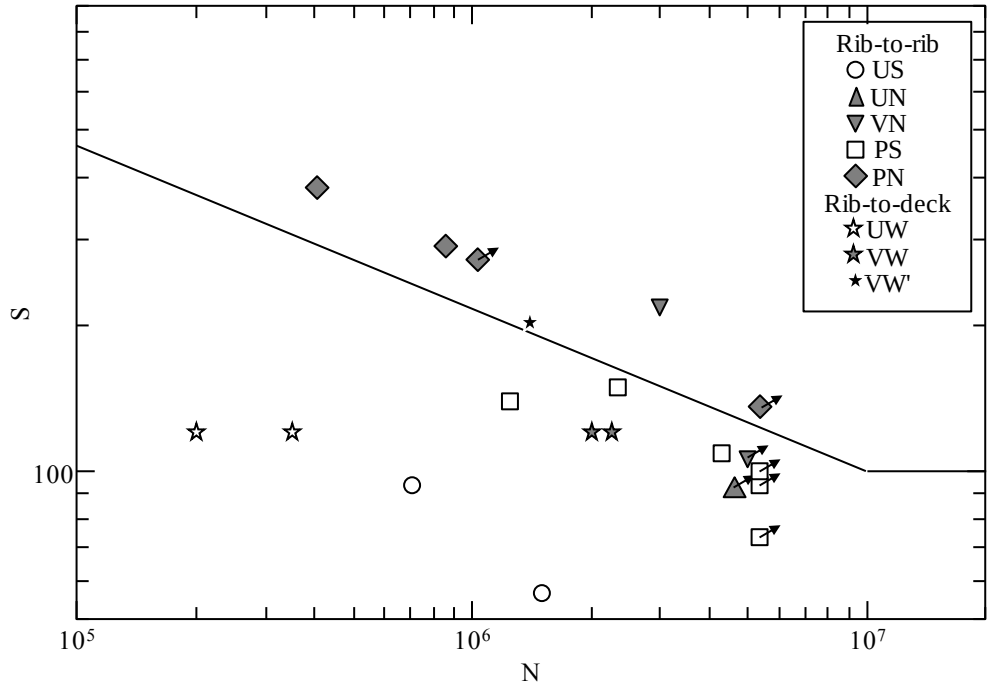

(b) Evaluation by factored load ranges

Fig. 4-12 Fatigue assessment of longitudinal-rib to transverse-rib connections in format of load ranges

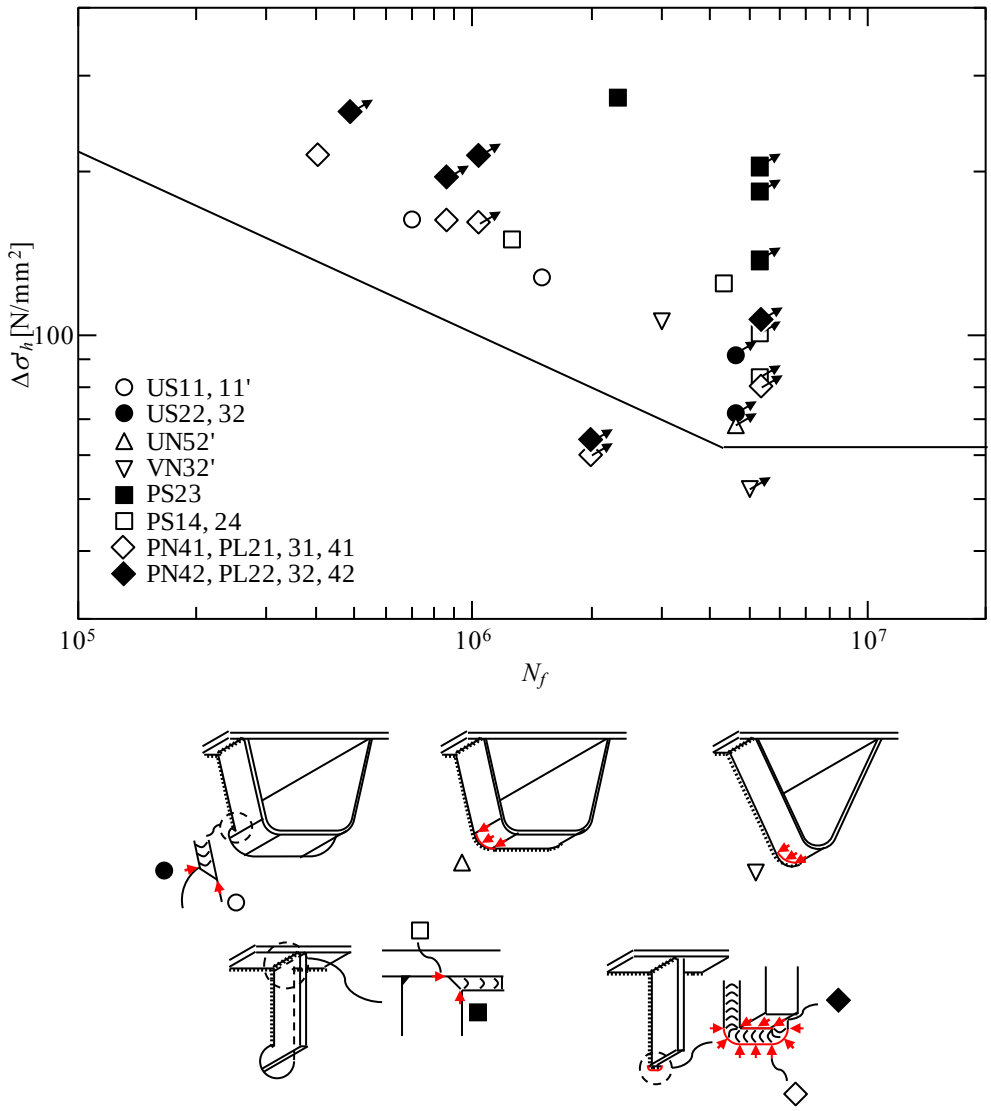

Fig. 4-13 Relationships between $\Delta\sigma'_h$ and N_f

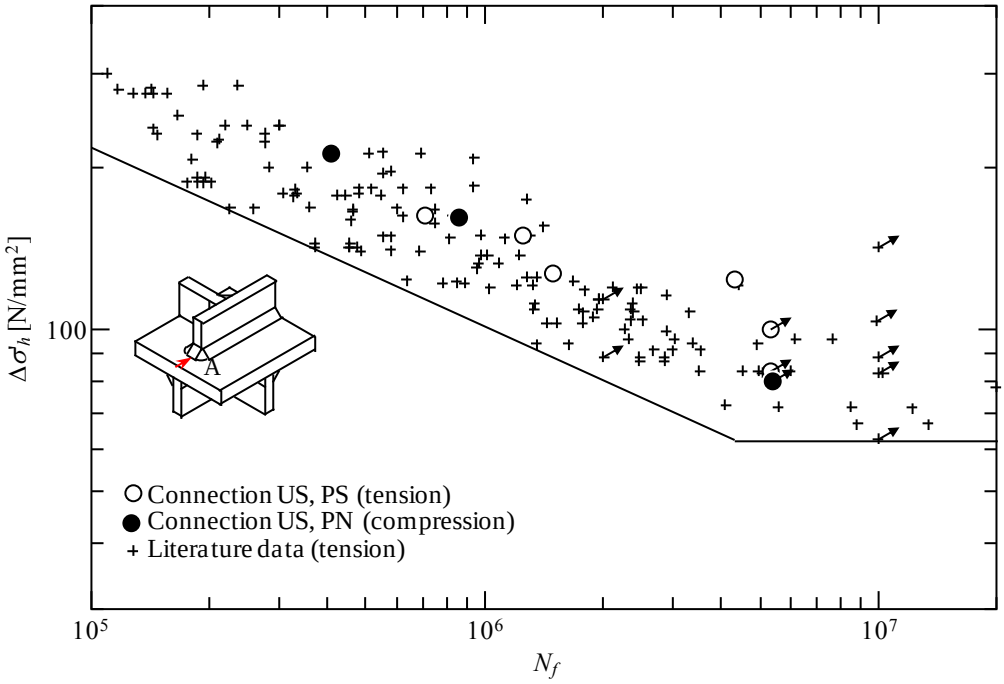

(a) Results of type-A hot-spots (including literature data)

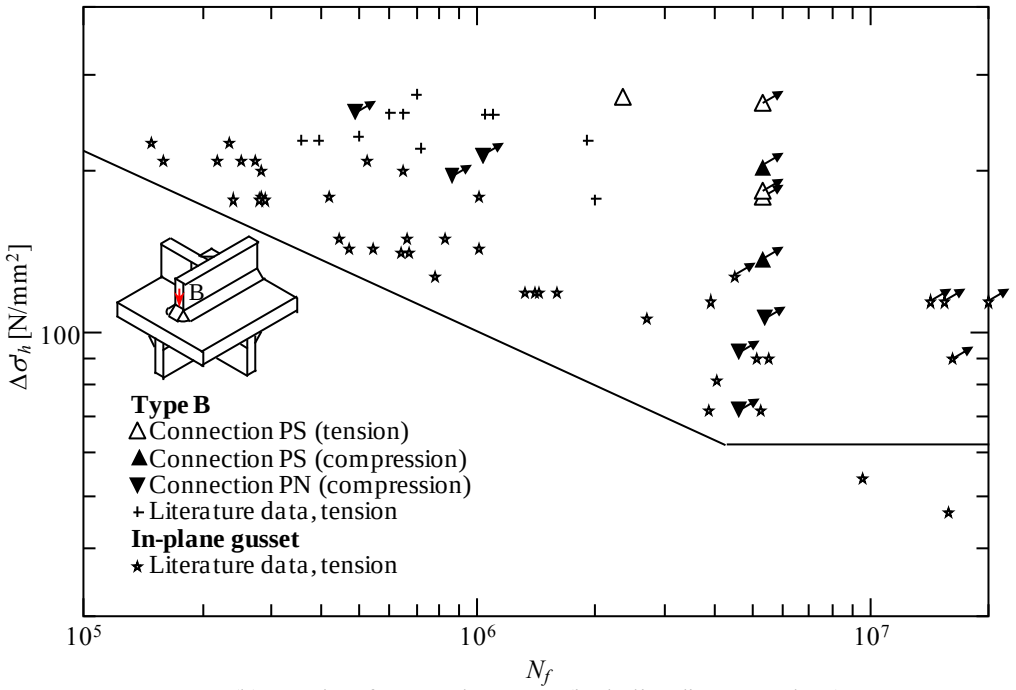

(b) Results of type-B hot-spots (including literature data)

Fig. 4-14 Relationships between $\Delta\sigma'_h$ and N_f for each types of hot-spots

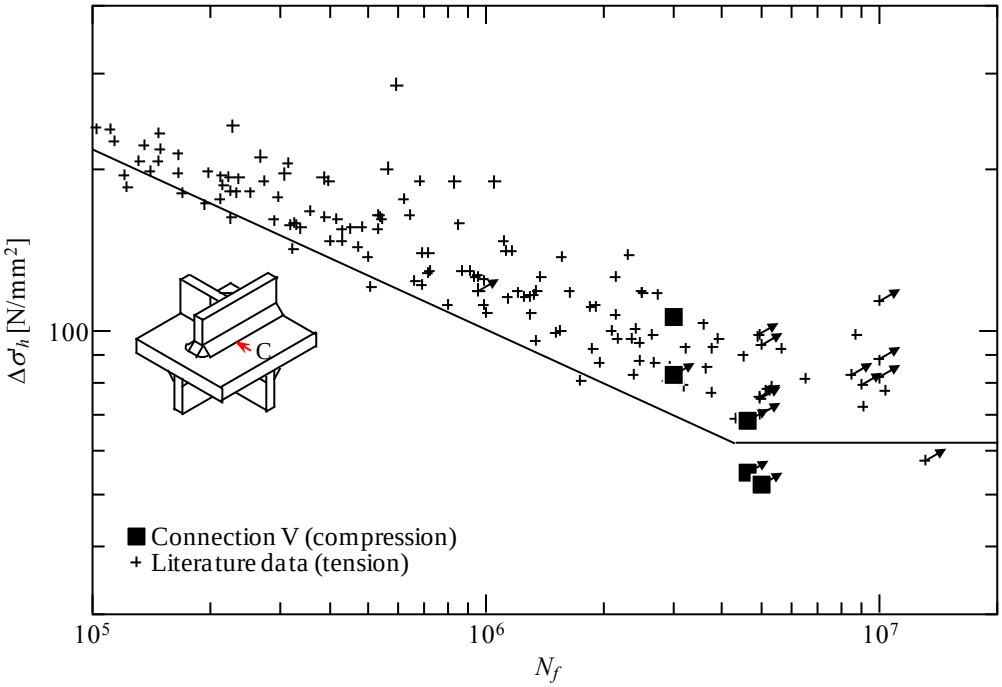

(d) Results of type-C hot-spots (including literature data)

Fig. 4-14 Relationships between $\Delta\sigma'_h$ and N_f for each types of hot-spots (continue)

5. Fatigue life estimation under actual traffic conditions

5.1. Introduction

Orthotropic steel decks, even though they have fatigue problems at welded connections, are required for long-span bridges, city expressways, and re-decking of deteriorated RC-decks. Fatigue cracks at longitudinal-rib to transverse-rib connections accounted for approximately 40% of all cracks in an investigation of bridges in service. Therefore, improving the longitudinal-rib to transverse-rib connections is important (Mori ed. 2010). Several longitudinal-rib to transverse-rib connections have been proposed for fatigue improvement (Katsumata et al. 2000; Ohashi et al. 2000; Kolstein 2001; Taskopoulos et al. 2003, Conner and Fisher 2006, Miki and Suganuma 2014; Hanji et al. 2013). However, these investigations do not sufficiently clarify the critical loading conditions for fatigue of the connections. Loadings are a distance away from the connections but cause maximum strain at the connections. Because traffic loadings in service could run in the longitudinal direction and each vehicle could have a different transverse position (Leonard 1969; Takada et al. 2009a), the fatigue evaluation should take account of the critical loading conditions (Miki et al. 1995).

Though Chapter 3 clarified the factored hot-spots stress ranges ($\Delta\sigma'_h$) of several longitudinal-rib to transverse-rib connections, the relations between $\Delta\sigma'_h$ and fatigue lives are uncertain. Chapter 3 described the finite element analyses and found the load positions causing maximum and the minimum factored hot-spot stresses on the longitudinal-rib to transverse-rib connections (POS_{max}, POS_{min}) with U-ribs, V-ribs, and plate ribs, and the slit and the non-slit transverse-rib webs. Since POS_{max} and POS_{min} were on different lanes in all cases of longitudinal-rib to transverse-rib connections, $\Delta\sigma'_h$ cannot be caused by one vehicle but can be caused by at least two vehicles. Since those vehicles run on transversely distributed positions, $\Delta\sigma'_h$ occurs at certain probabilities. Therefore, fatigue lives obtained by fatigue tests simulating the most severe conditions for longitudinal-rib to transverse-rib connections are smaller than fatigue lives of longitudinal-rib to transverse-rib connections in service.

From the background above, the following objectives of this chapter were established.

1) Investigate the fatigue lives of the longitudinal-rib to transverse-rib connection under traffic loading with transversely distributed running positions.

5.2. Monte Carlo simulations for fatigue life estimations

5.2.1. Evaluated weld toes

The weld toes in the deck panel models presented in Chapter 3 were evaluated. Fig. 5-1 shows evaluated weld toes for fatigue life simulations. The evaluated weld toes were expected to have the lowest fatigue strength of the models based on the factored hot-spot stress ranges computed in Chapter 3 and the fatigue test results in Chapter 4. The transverse-rib side weld toes (weld toe PN-31) were selected for the plate-rib non-slit connection (connection PN), since fatigue cracks were initiated at the transverse-rib side weld toes, even though the longitudinal-rib side weld toes had larger hot-spot stress ranges in the fatigue tests and would have larger hot-spot stress ranges in actual bridges.

Fig. 5-1 shows the relations between positions of the double tire load and the factored hot-spot stresses (influence surfaces), which were computed in Chapter 3. In this chapter, the factored hot-spot stresses caused by load models were calculated from the influence surface.

5.2.2. Simulation cases

Table 5-1 shows simulation cases, variables of which were load models, transverse distributions of tire positions. Fig. 5-2 and Table 5-2 show load models and total weights of vehicle models. Only the left side tires of vehicles were simulated, since the influence areas for the hot-spot stresses were not so wide.

Cases S1–S3 and T1 adopted simplified one axle and tandem axles of double tires, respectively. Case S1–S3 was based on the design fatigue load (T load) of Japanese specifications (Japan Road Association 2014). Since the T load is a simplified design load and assumes a combined axle from tandem axles, case T1 adopted tandem axles to investigate the effects of load simplification on the fatigue life estimation results. Transverse distributions of tire positions followed normal distributions with standard deviations of 0, 165, and 330 mm (Fig. 5-4). Since the transverse distribution depends on lane width (Leonard 1969; Takada et al. 2009a), the effect of the distribution width was investigated. The basic standard deviation, 165 mm, was determined from the measurement of actual traffic conditions in Hanshin expressways (Takada et al. 2009a).

Cases A1–A5 adopted a traffic model including two-, three- and four-axle vehicles in order to estimate actual traffic conditions. The dimensions of vehicles were determined based on previous research (Miki et al. 1986). The weights of the vehicles followed log-normal distributions based on traffic measurement in one of the heaviest traffic roads in Tokyo (Tamakoshi et al. 2006).

The hot-spot stress ranges can change depending on dimensions such as thickness of plates in orthotropic steel decks or span length of the longitudinal ribs. On the other hand, the shapes of the influence surfaces might not change if the shapes of the longitudinal-rib to transverse-rib connections are constant. Therefore, the influence surfaces of the vertical (σ'_h) axis were factored by 0.8, 0.9, 1.1 and 1.2 to investigate the effects of the hot-spot stress ranges on fatigue life estimation results.

5.2.3. Fatigue damage computation procedure

Fig. 5-5 shows the Monte Carlo simulation procedure to estimate fatigue lives under each simulation case. First, the center of the transverse tire distribution (y_c) was set to

-720 mm. Second, vehicles were randomly generated with the weight and the transverse positions following each of the distributions. The stress histories caused by the vehicles were calculated by linear interpolations of the influence surfaces. Equivalent axles were also counted by the following equation.

$$n_{eq,axle} = \Sigma_i \left(W_{axle,i} / W_{T\_load} \right)^3 \qquad 5\text{-}1$$

where $n_{eq,axle}$ represents the number of axles equivalent to T load, and $W_{axle,i}$ and W_{T_load} represent the weight of each axle of a vehicle and T load, respectively. When the number of vehicles ($n_{vehicle}$) reached 20,000, the stress histories were converted to fatigue damage (D) by rain-flow counting, as described below. The allowable average daily truck traffic per lane ($ADTT_{al}$) and the equivalent axles of $ADTT_{al}$ ($ADEA_{al}$) for 100-year fatigue lives were estimated using the fatigue damage by the following equations.

$$\boldsymbol{ADTT_{al}} = \frac{\text{Fatigue life}}{365\,\text{day} \times 100\,\text{year}} = \frac{\boldsymbol{n_{vehicle} / D}}{36{,}500} \qquad 5\text{-}2a$$

$$\boldsymbol{ADEA_{al}} = \frac{\text{Fatigue life}}{365\,\text{day} \times 100\,\text{year}} = \frac{\boldsymbol{n_{eq,axle} / D}}{36{,}500} \qquad 5\text{-}2b$$

$ADTT_{al} = n$ represents the weld toes having a 100-year fatigue life if the average daily truck traffic is equal to or lower than n. $ADEA_{al} = m$ represent the weld toes having a 100-year fatigue life if the average daily axle equivalent to the T load is equal to or lower than m.

The rain-flow counting procedure described by Endo et al. (1981) was used to calculate fatigue damage accumulations through variable amplitude stress histories. First, the stress histories were converted into histories of peak-valley differences (A_0, A_1, ..., A_n), which represent the stress ranges of each monotonic increasing or decreasing sequence of the stress histories. Then, the peak-valley differences were converted to fatigue damage accumulations based on Miner's rule with the cut-off limit of JSSC-E class for variable amplitude stress (28 N/mm^2).

The abovementioned simulation process was conducted on a developed program written in Ruby.

5.3. Estimated fatigue lives

5.3.1. Effect of transverse distributions of tire positions

Table 5-3 shows the results of Monte Carlo simulations in formats of allowable average daily truck traffic per lane for 100-year fatigue lives ($ADTT_{al}$) and the equivalent axles ($ADEA_{al}$).

Fig. 5-6 shows $ADTT_{al}$ of simulation cases for simplified load models with the standard deviations of the transverse distribution being 0, 165, 330 mm. $ADTT_{al}$ for all hot spots investigated were increased as the transverse distribution expanded. Therefore, the

narrower transverse distribution could be more severe for the fatigue of longitudinal-rib to transverse-rib connections. In addition, the standard deviation of 165 mm could be smaller than usual but would provide safe estimations.

Fig. 5-7a shows the transverse distributions of tire positions that caused minimum fatigue lives for US32 in each of the simulation cases, S2 and S3. Fig. 5-7b shows the front view of the influence surface of US32. The center of the transverse distribution (y_c) was the lane where maximum factored hot-spot stress ranges were caused by the passing of one T load in the case that the standard deviation was 165 mm, whereas the maximum factored hot-spot stress ranges caused by the passing of several T loads ($\Delta\sigma'_h$) can be larger. On the other hand, y_c was located between lanes for the maximum and the minimum factored hot-spot stresses of the influence surfaces ($\sigma'_{h,\max}$, $\sigma'_{h,\min}$) in the case that the standard deviation was 330 mm. This result means that the stress ranges by one vehicle are dominant for the fatigue of longitudinal-rib to transverse-rib conditions in the case that the transverse distributions of tire positions are limited, for example, due to a narrow road width.

5.3.2. Allowable *ADTT* under actual traffic conditions

Fig. 5-8 shows the fatigue life estimation results for each of simulation cases, S2, T1, and A3, all of which had a transverse distribution with the standard deviation of 165 mm.

Connection PN, which was proposed as a fatigue resistant structure in Chapter 3, was evaluated to be applicable to *ADTT* of approximately 1,800 (PN-32) and 9,500 (PN-31) vehicles. Though the estimated fatigue life of PN-31 was smaller than that of PN-32, fatigue cracks were initiated from the PN-31 transverse-rib web side weld toes. It should be noted that hot-spot stresses measured at PN-32 were larger than those of PN-31 even in fatigue tests. From the fatigue test results, the fatigue lives of connection PN could be determined from fatigue cracks at PN-31. Therefore, $ADTT_{al}$ of connection PN could be estimated as approximately 9,500.

The results of simulation case A3 showed the largest $ADTT_{al}$, which mean the longest fatigue lives, for all hot spots investigated, and simulation cases T1 and S2 showed the second largest and the last, respectively. Therefore, the simplified load model, T load, provides a conservative fatigue estimation compared to more detailed traffic models. The simplified model was applied in Chapter 3, but it resulted in a conservative estimation, though the tandem axle is common for heavy axles. On the other hand, $ADEA_{al}$ was ordered differently from hot spot to hot spot. The order might be affected by the shapes of the influence surfaces, which were different for all hot spots investigated.

5.3.3. Relations between the hot-spot stress ranges and the fatigue lives

Fig. 5-9 shows the relations between the factored hot-spot stress ranges and the fatigue lives from the results of simulation case A1-5, in which the influence surfaces were factored by 0.8, 0.9, …, 1.2. Hence, the figure shows five plots for each hot spot. The resulting fatigue lives are expressed in the format of $ADTT_{al}$ and $ADEA_{al}$ for 100-year fatigue lives. By using Fig. 5-9 as the fatigue design curve, longitudinal-rib to transverse-rib connections could be designed. The required factored hot-spot stress ranges can be determined from traffic conditions and Fig. 5-9, and structural dimensions can be determined to satisfy the obtained factored hot-spot stress ranges. It should be noted that the design procedure above applies only to the connections and traffic condi-

tions investigated in this study.

$ADTT_{al}$ of the non-slit connections reached approximately 4,000 vehicles or 300 axles or more. These connections could have 100-year fatigue lives for many of the heavy traffic roads. $ADTT_{al}$ and $ADEA_{al}$ which correspond to the constant amplitude fatigue limit of JSSC-E class (62 N/mm^2) for UN32, VN32, PN32, and PN31, were approximately 2,000, 4,000, 4,000, and 7,000 vehicles, and 150, 300, 300, and 600 equivalent axles. As described in Chapter 4, the fatigue tests resulted in no fatigue crack initiations from PN32, even though the hot-spot stresses were higher than those of PN31 where cracks were initiated. From the test results, $ADTT_{al}$ and $ADEA_{al}$ of non-slit plate-rib connections could be those of PN31.

The relations between the factored hot-spot stress ranges and $ADTT_{al}$ or $ADEA_{al}$ depended on the hot spots. For example, $ADTT_{al}$ of PN31 was approximately four times larger than those of VN32 in similar stress ranges. PN31 had an influence surface with a peak at only one side about the center transverse rib, whereas VN32 had peaks at both sides about the center transverse rib (Fig. 5-1). The VN32 influence surface could cause a stress increase by the tandem axles, whereas the PN31 influence surface could not. In addition, $ADTT_{al}$ by the tandem axles was larger than that by the simplified axle in the results for PN31, whereas the order was reversed for VN32. From these results, the difference between the influence surfaces of PN31 and VN32 could affect the difference of $\Delta\sigma'_h - ADTT_{al}$ relations.

5.4. Summary

This chapter conducted Monte Carlo simulations to investigate the relations between the factored hot-spot stress ranges and fatigue lives of the longitudinal-rib to transverse-rib connections under traffic loading with transversely distributed running positions. The simulations were based on the influence surfaces of the factored hot-spot stresses on the longitudinal-rib to transverse-rib connections and the investigations of traffic on bridges in service. As results, the following results were obtained

1) Actual traffic simulations showed that the allowable average daily truck traffic for connection PN was 9,500 vehicles.
2) Fatigue lives of longitudinal-rib to transverse-rib connections can be designed by the hot-spot stress approach and traffic simulations.
3) Fatigue lives were affected by not only the factored hot-spot stress ranges but also the shapes of the influence surfaces.
4) Fatigue lives of longitudinal-rib to transverse-rib connections decrease as the transverse distribution of tire positions becomes narrow.

Table 5-1 Simulation cases

Case	Traffic model	Distribution[a] [mm]	K_{is}[b]
S1	S	0	1.0
S2	S	165	1.0
S3	S	330	1.0
T1	T	165	1.0
A1	A	165	0.8
A2	A	165	0.9
A3	A	165	1.0
A4	A	165	1.1
A5	A	165	1.2

[a]Standard deviation of transverse tire distribution,
[b]Factor for the hot-spot stresses of the influence surfaces,
[c]Taking account of cut off limit of JSSC-E class for variable amplitude

Table 5-2 Traffic models

Traffic model	Vehicle model	Frequency	Vehicle weight			
			W_0 [kN][a]	W_{min} [kN][b]	μ[c]	σ[d]
S	Simplified fatigue load	1.00	200	-	-	-
T	Tandem fatigue load	1.00	200	-	-	-
A	Two axel truck	0.55	56	16	1.75	0.17
	Three axel truck	0.29	154	37	2.19	0.16
	Four axel trailer	0.16	216	50	2.33	0.21

[a]Most frequent value, [b]Minimum value, [c]Mean of log-normal distribution,
[d]Standard deviation of log-normal distribution

Table 5-3 Simulation results

	$ADTT_{al}$[a]					$EQAX_{al}$[b]				
	US	UN	VN	PS	PN	US	UN	VN	PS	PN
S1	7	108	367	20	194	7	108	367	20	194
S2	14	168	559	26	235	14	168	559	26	235
S3	16	234	828	27	345	16	234	828	27	345
T1	49	405	894	92	1885	12	101	223	23	471
A1	332	4020	15263	579	28839	27	344	1252	48	2411
A2	223	2712	8597	398	15656	19	219	722	33	1316
A3	152	1735	5617	277	9513	13	146	474	24	794
A4	113	1267	3671	211	6241	10	105	312	17	518
A5	89	894	2543	160	4120	7	75	214	13	347

[a] Allowable average daily truck traffic per lane for 100 year fatigue lives,
[b] Allowable average daily equivalent axles per lane for 100 year fatigue lives (equivalent to 200kN axle)

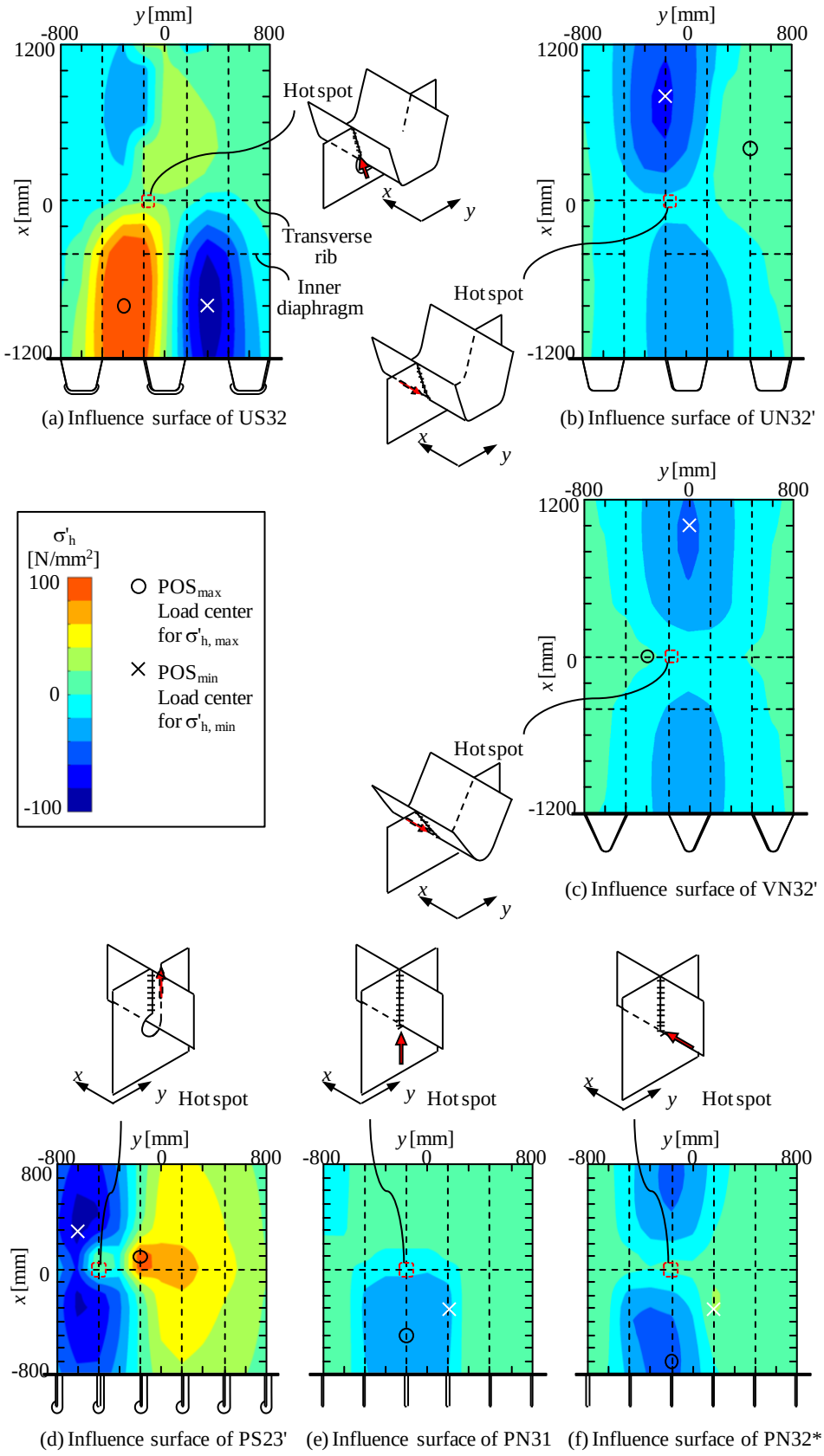

Fig. 5-1 Influence surfaces of evaluated hot-spots

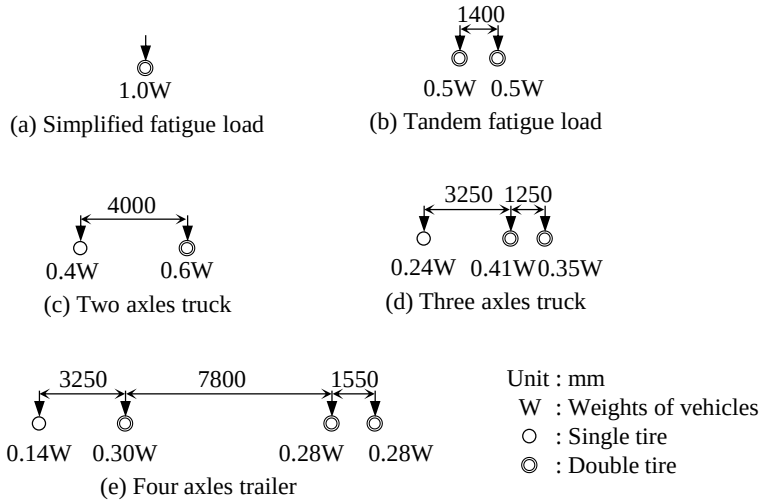

Fig. 5-2 Load models

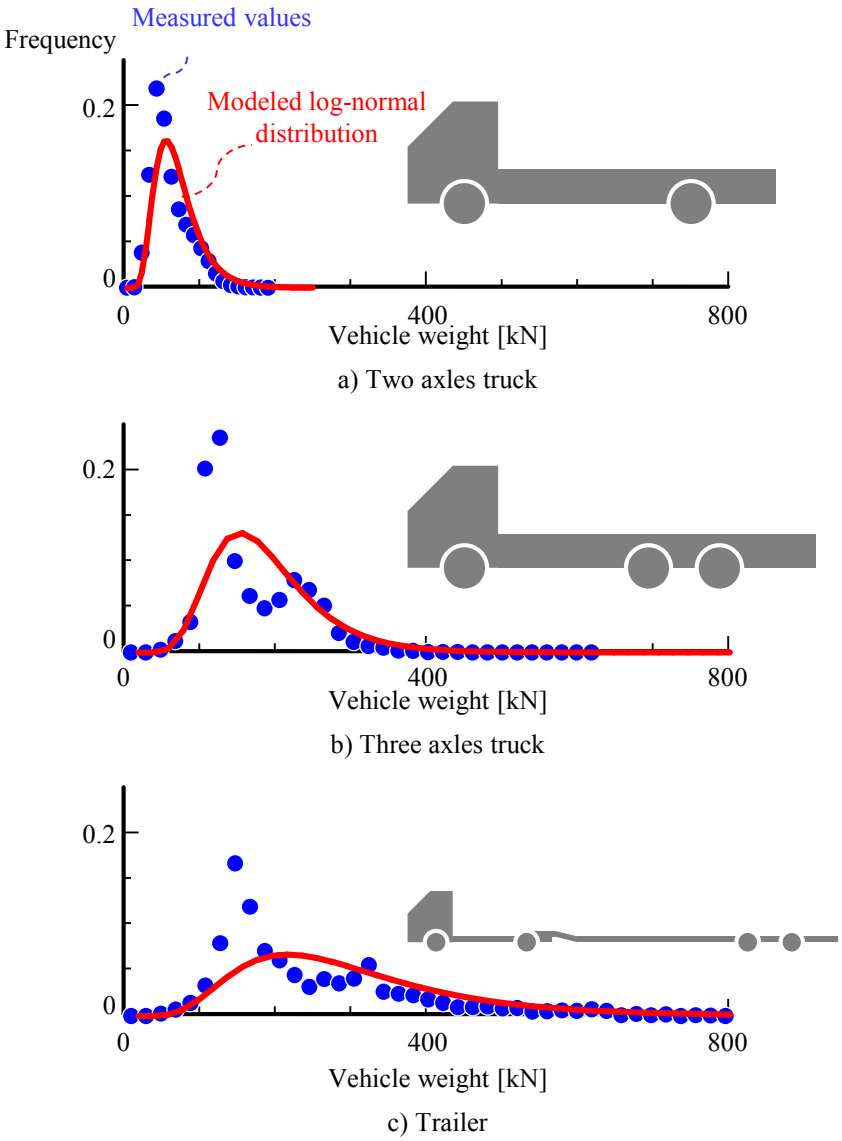

Fig. 5-3 Comparison of model probability distribution of vehicle load and measured values

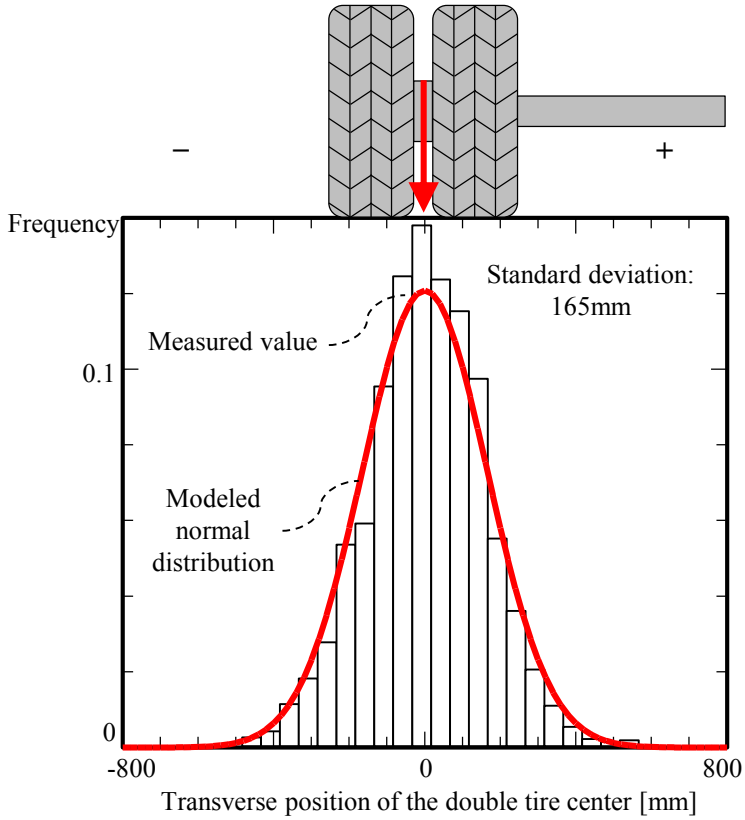

Fig. 5-4 Transverse distributions of tire positions, modeled probability distribution and measured values

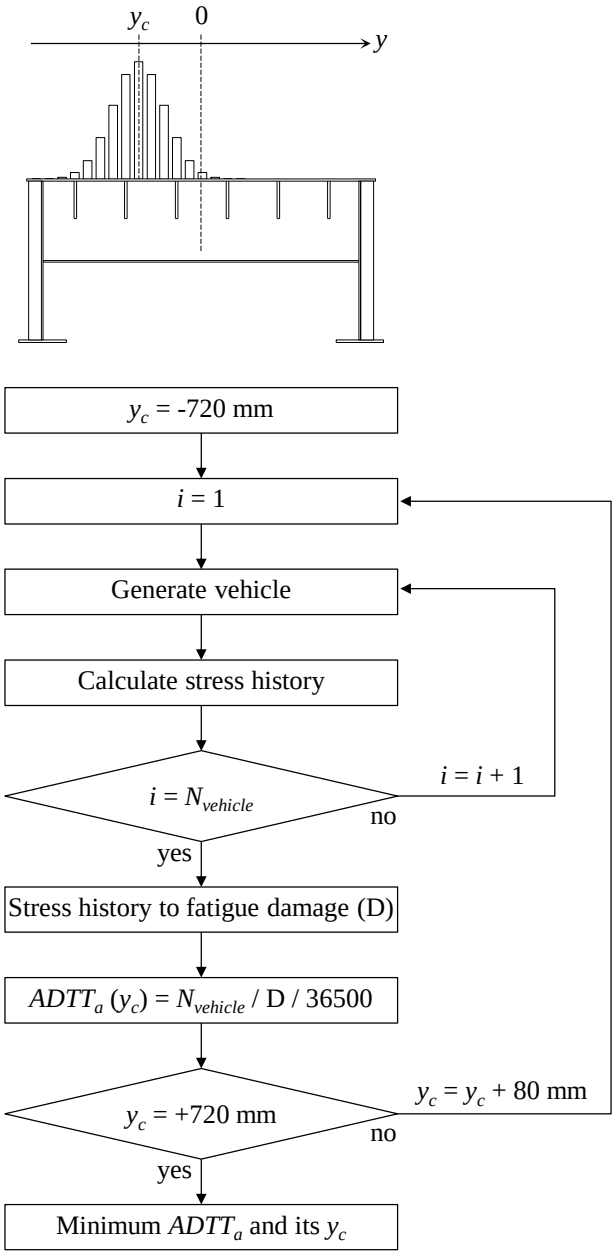

Fig. 5-5 Mote-Carlo simulation procedure

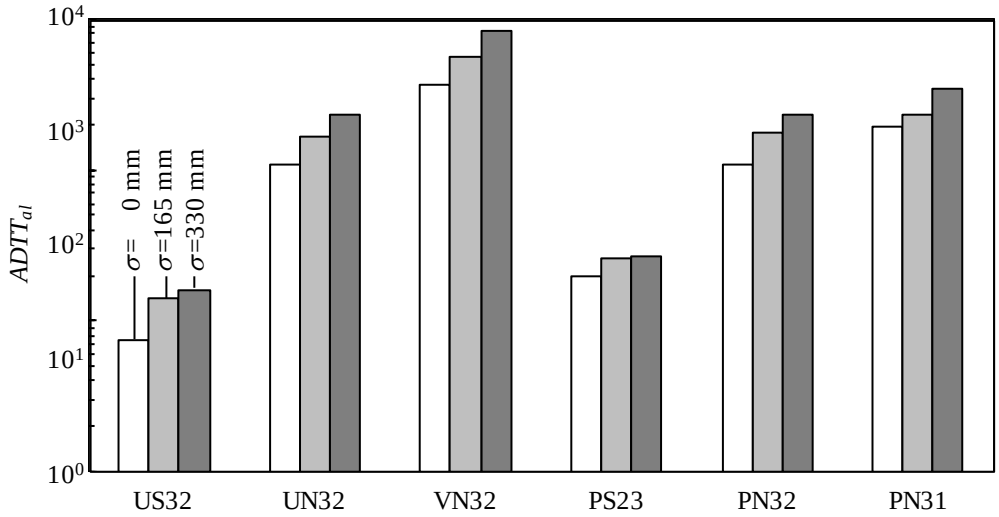

Fig. 5-6 $ADTT_{al}$ for each transverse distributions of tire positions

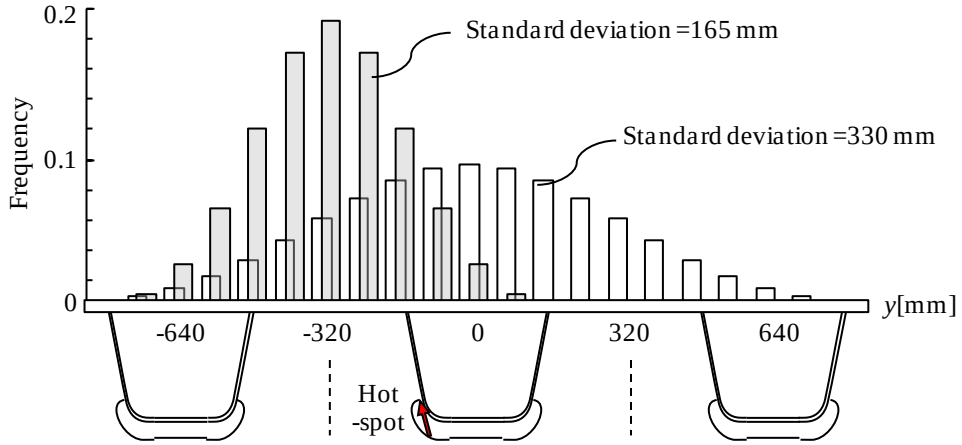

a) Transverse distribution of tire positions causing minimum fatigue lives for each distribution

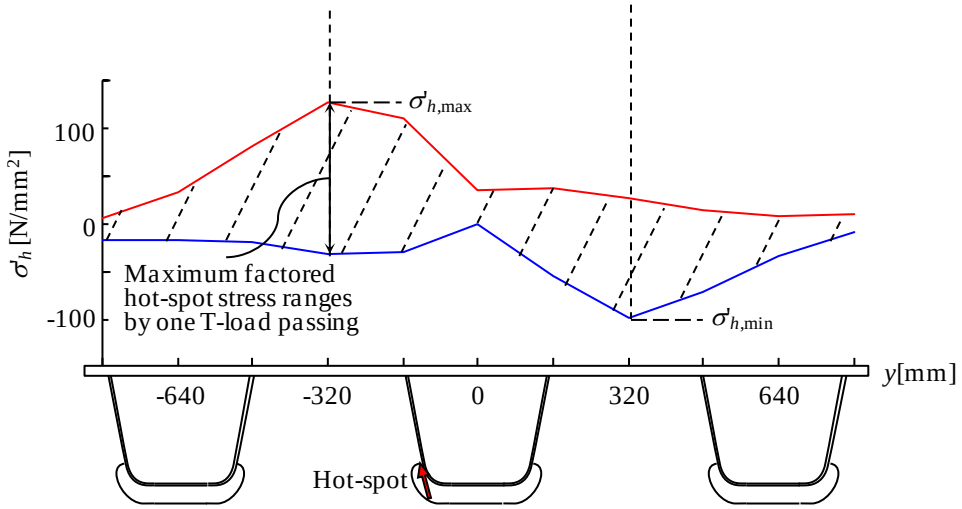

b) Front view of influence surface

Fig. 5-7 Relationships between transverse distributions of tire positions and the influence surface of US32

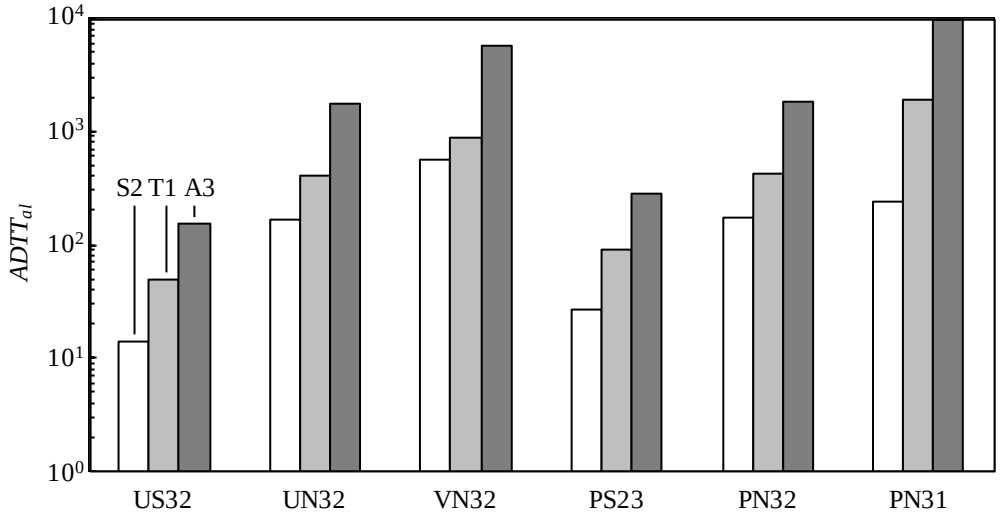

(a) Allowable ADTT for simplified, tandem, and actual traffic models

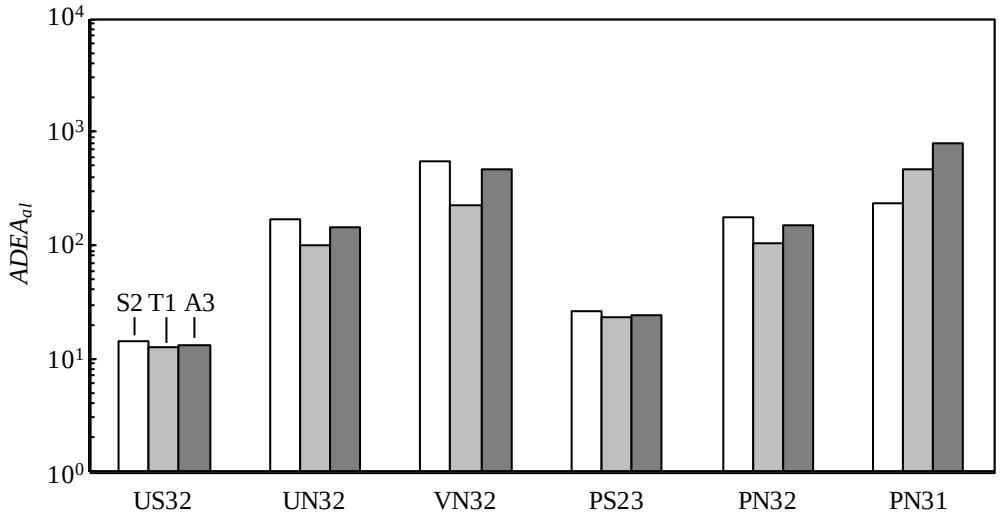

(a) Allowable equivalent axles for simplified, tandem, and actual traffic models

Fig. 5-8 Fatigue life estimation results for each traffic models

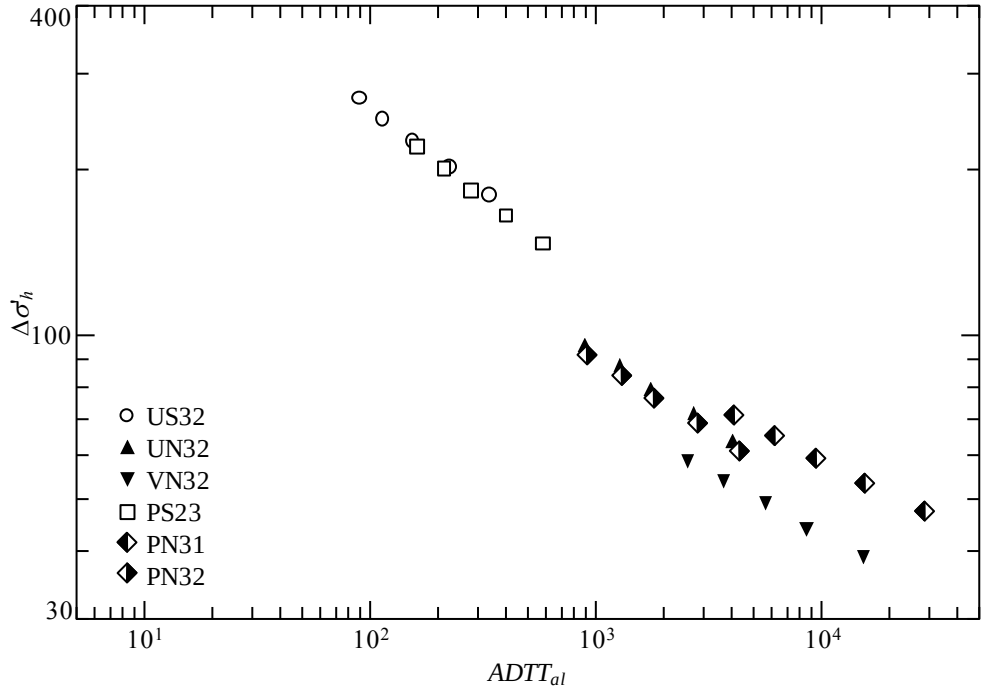

(a) Relationships between allowable ADTT and factored hot-spot stress ranges

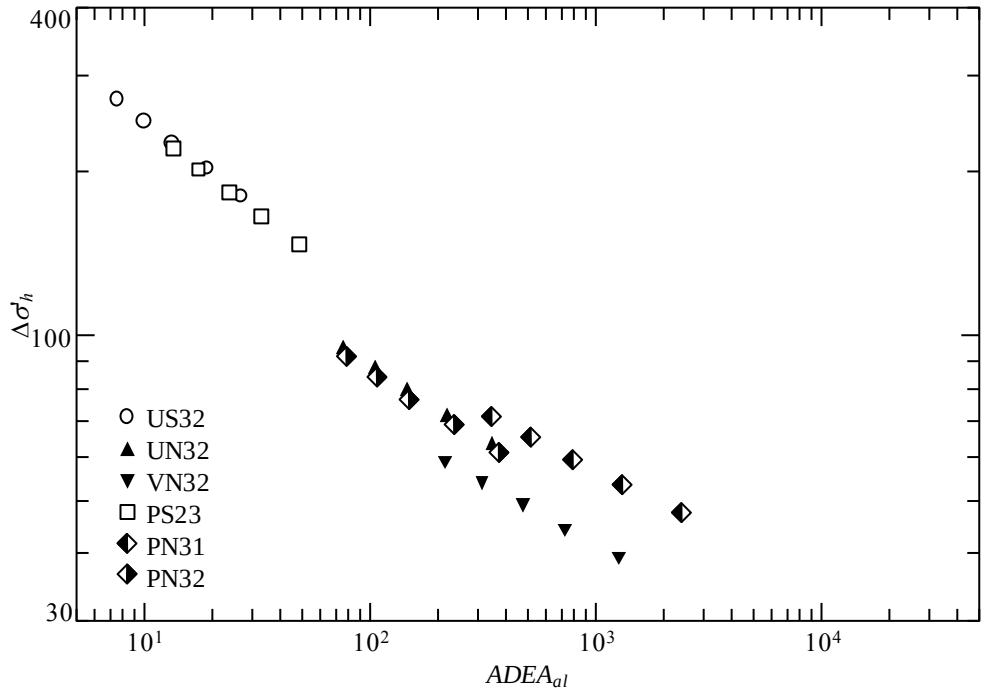

(b) Relationships between allowable equivalent axles and factored hot-spot stress ranges

Fig. 5-9 Relationships between fatigue lives and factored hot-spot stress ranges

6. Conclusion

This study investigated the fatigue strength and the fatigue lives of several types of orthotropic steel decks and proposed a structure with high fatigue strength after clarifying the critical loading conditions for the connections. The critical loading conditions were investigated by the factored hot-spot stress approach and accounting for moving vehicle loads. The fatigue strength of the connections was confirmed by fatigue tests with panel type specimens under critical loading conditions. The fatigue lives were estimated by simulating traffic loadings with transversely distributed running positions. From the investigations above, orthotropic steel decks with connection PN, which is the connection of a plate rib and non-slit transverse rib, were found to achieve 100-year fatigue lives even under heavy traffic conditions. Furthermore, the following results were obtained in the investigations.

2-1) The hot-spot stress approach can be applied for fatigue assessment of longitudinal-rib to transverse-rib connections, where three-dimensional deformations are caused and hot spots move as loading positions move.

2-2) A thickness factor with an exponent of 0.25 and bending stress reduction factor of 0.8 can be applicable to the hot-spot stress approach. The thickness effect could be extended to plates thinner than 25 mm. In addition, the width between the lower and upper 95% survival curves of fatigue data in terms of factored hot-spot stresses was 30% smaller than that in terms of hot-spot stresses.

2-3) JSSC-E class can provide safe estimations of fatigue strength and fatigue lives for the factored hot-spot stresses, except for type C hot spots under a relatively high stress range approximately equal to or higher than 100 N/mm^2 and type B hot spots under stress ranges lower than the constant amplitude fatigue limit of JSSC-E class.

3-1) Critical loading positions causing maximum and minimum hot-spot stresses on longitudinal-rib to transverse-rib connections are located at a distance away from the evaluated connections. Furthermore, those positions are different depending on the longitudinal-rib type and the slit existence on the transverse-rib webs.

3-2) Eliminating the slit on the transverse-rib webs can improve the fatigue strength of the longitudinal-rib to transverse-rib connections. The hot-spot stress ranges of connection UN and PN were smaller than those of US and PS by 65% and 58%, respectively, where the inner diaphragms were attached in the U-ribs at 400 mm from the transverse-rib.

3-3) Using V-ribs would further enhance the fatigue strength of non-slit connections. The hot-spot stress range of connection VN was 39% smaller than that of connection UN.

3-4) Hot-spot stresses of the connections between U-ribs and transverse-rib webs are significantly affected by the existence of inner diaphragms adjacent to the connections. The hot-spot stresses ranges of connection US and UN were increased and decreased by the inner diaphragms.

4-1) Clarify the fatigue strength of longitudinal-rib to transverse-rib connections by fatigue tests simulating critical loading conditions.
4-2) Investigate the applicability of the factored hot-spot stress approach to longitudinal-rib to transverse-rib connections.
4-3) Validate shell element FEA applicability by comparing the stress conditions of analyses and experiments to confirm the validity of critical loading conditions determined by FEA and applied to fatigue test conditions.

5-1) Actual traffic simulations showed that the allowable average daily truck traffic for connection PN was 9,500 vehicles.
5-2) Fatigue lives of longitudinal-rib to transverse-rib connections can be designed by the hot-spot stress approach and traffic simulations.
5-3) Fatigue lives were affected by not only the factored hot-spot stress ranges but also the shapes of the influence surfaces.
5-4) Fatigue lives of longitudinal-rib to transverse-rib connections decrease as the transverse distribution of tire positions becomes narrow.

References

American Association of State Highway and Transportation Officials (2010). "AASHTO LRFD Bridge Design Specifications." American Association of State Highway and Transportation Officials, Washington, DC

Anami, K. and Miki, C. (2001). "Fatigue strength of welded joints made of high-strength steels." *Progress in Struct. Eng. and Materials*, 3(1), 86-94

Araki, Y. (2011). "Fatigue strength of welded joint under plate bending and axial force." *法政大学大学院紀要*, 52 [in Japanese]

Aygul, M., Al-Emrani, M., and Urushadze, S. (2012). "Modelling and fatigue life assessment of orthotropic bridge deck details using FEM." *Int. J. Fatigue*, 40, 129-142

Beales C. (1990). "Assessment of trough to crossbeam connections in orthotropic steel bridge decks." *TRRL Report*, RR276

Bruls, A. (1991) "Measurements and interpretation of dynamic loads in bridges, Phase 3 Fatigue behavior of orthotropic steel decks." Commissions of European Committees, EUR 13378, Brussels

Buitellar, P., Braam, R., and Kaptijn, N. (2004). "Reinforced high performance concrete overlay system for rehabilitation and strengthening of orthotropic steel bridge decks." *Proc. First Int. Orthotropic Bridge Conf.*, Aug. 23-27, 2004, Sacramento, 384-401

Buckland, P. G. (2004). "Four decades of experience with orthotropic steel decks." *Proc. First Int. Orthotropic Bridge Conf.*, Aug. 23-27, 2004, Sacramento, 89-98

Cheng, X., Murakoshi, J., Nishikawa, K., and Ohashi, H. (2004a). "Local stresses and fatigue durability of asphalt paved orthotropic steel decks." *Proc. First Int. Orthotropic Steel Bridge Conf.*, Sacramento, Aug. 25-27, 2004, 543-555

Cheng, X., Murakoshi, J., and Moriyama, A. (2004b). "Fill-scale fatigue test of orthotropic steel deck under running wheel loading." *Proc. First Int. Orthotropic Steel Bridge Conf.*, Sacramento, Aug. 25-27, 2004, 689-704

Connor, R. J., and Fisher, J. W. (2006). "Consistent approach to calculating stresses for fatigue design of welded rib-to-web connections in steel orthotropic bridge decks." *J. Bridge Eng.*, 11(5), 517-525

Cullimore, M. S. G., and Smith, J. W. (1981). "Local stresses in orthotropic steel bridge decks caused by wheel loads." *J. Constructional Steel Research*, 1(2), 17-26

Cuninghame, J. R. (1982). "Steel bridge decks: Fatigue performance of joints between longitudinal stiffeners." *TRRL Report*, LR1066

Cuninghame, J. R. (1990). "Fatigue classification of welded joints in orthotropic steel bridge decks." *TRRL Report*, RR259

Delesie, C., and Bogert, P. V. (2008). "The effect of stiffener distortion of orthotropic steel bridge decks on load dispersal behavior and stress concentrations." *Proc. Second Int. Orthotropic Bridge Conf.*, Aug. 25-29, 2008, Sacramento, 306-326

Dieng, L., Marchand, P., Gomes, F., Tessier, C., and Toutlemonde, F. (2013). "Use of UHPFRC overlay to reduce stresses in orthotropic steel decks." *J. Constructional Steel Research*, 89, 30-41

DNV (2006.) "Recommended practice DNV-RP-C203, Fatigue Design of Offshore Steel Structure." Det Norske Veritas, Norway

Endo, T. and Anzai, H. (1981). “Refined rainflow algorithm: P/V difference method.” Journal of the Society of Materials Science, Japan 30(328), 89-93

European Committee for Standardisation (2003). "EN 1991-2: Eurocode 1: Actions on structures - Part 2: Traffic loads on bridges."

European Committee for Standardisation (2005). "EN 1993-1-9: Eurocode 3: Design of steel structures - Part 1-9: Fatigue."

European Committee for Standardisation (2006). "EN 1993-2: Eurocode 3: Design of steel structures - Part 2: Steel bridges."

Federal Highway Administration (2012). "Manual for Design, Construction, and Maintenance of Orthotropic Steel Deck Bridges." FHWA

Fiedler, E. (2009). "Die Entwicklung der orthotropen Fahrbahnplatte in Deutschland." *Stahlbau*, 78, 562-576

Fischer, C., Fricke, W. (2014). “Consideration of stress gradient effects for complex structures in local fatigue approaches.” *IIW document*, XIII-2543-14

Fricke, W., Doerk, O. (2004). “Simplified approach to fatigue strength assessment of fillet-welded attachment ends” *Int. J. Fatigue*, 28, 141-150

Fricke, W., and Paetzold, H. (2010). “Full-scale fatigue tests of ship structures to validate the S–N approaches for fatigue strength assessment.” *Mar. Struct.*, 23, 115–130.

Fryba, L., and Gajdos, L. (1999). "Fatigue properties of orthotropic decks on railway bridges." *Eng. Struct.*, 21(7), 639-652

Fujii, Y., Matsumoto, T., Miki, C., and Ono, S. (1993). "The compressive fatigue strength of longitudinal joints in orthotropic steel decks." *J. Struct. Eng. A (JSCE)*, 39(3), 999-1009 [in Japanese]

Gurney, T. R. (1997). “Thickness effect in 'Relatively thin' welded joints.” The Welding Institute, Cambridge

Hanji, T., Kato, K., Tateishi, K., Choi, S., and Hirayama, S. (2013). "Local stress characteristics at cross-beam web cutout in closed rib orthotropic deck." *Proc. Third Int. Orthotropic Bridge Conf.*, Jun. 24-30, 2013, Sacramento, 262-277

Harada, H., Murakoshi, J., Hirano, S., and Kinomoto, T. (2016). "Analytical study on local stress behavior of welded connection between U-shaped rib and crossbeam of orthotropic steel deck using whole bridge model." *Steel Construction Eng. (JSSC)*, 23(89), 37-49 [in Japanese]

Haibach, E., and Plasil, I. (1983). “Untersuchen sur betriebsfestigkeit von stahlleichtfahrbahnen mit trapezhohlsteifen im eisembahnbrückenbau.” *Stahlbau*, 9, 269-274

Hirayama, S., Uchida, D., Ogasawara, T., Inokuchi, S., and Onichi, H. (2015). "Study on initiating mechanism of bead-through cracks occurred from weld root between deck plates and U-ribs in orthotropic steel deck." *Steel Construction Eng. (JSSC)*, 22(85), 71-84 [in Japanese]

Hobbacher, A. (2007) “Recommendations for fatigue design of welded joints and components.” IIW Document IIW-2259-15, Springer

Huo, L., Wang, D., and Zhang, Y. (2005). "Investigation of the fatigue behavior of the welded joints treated by TIG dressing and ultrasonic peening under variable-amplitude load." *Int. J. Fatigue*, 27, 95–101

Inokuchi, S., Kainuma, S., Kawabata, A., and Uchida, D. (2008) “Field measurement and development of an experimental system for fatigue-cracking from weld root

between deck plate and U-rib in orthotropic steel decks.” *Proc. Second Int. Orthotropic Steel Bridge Conf.*, Aug. 25-29, 2008, Sacramento, 345-357

Inokuchi, S., Uchida, D., Hirayama, S., and Kawabata, A. (2011). "Evaluation method for fatigue life of welding joint between deck plate and u-shaped rib in orthotropic steel decks." *J. JSCE Ser. A1*, 67(3), 464-476 [in Japanese]

Iwasaki, M., Terada, K., and Fukazawa, M. (1992). "Study of prevention of fatigue damage in floor rib using open section type longitudinal rib on orthotropic steel deck bridges." *J. Struct. Eng. A (JSCE)*, 38(3), 1021-1029 [in Japanese]

Iwasaki, M., Nagata, K., Nishikawa, Y., Ojio, T., and Yamada, K. (1997). "Field measurement and fatigue assessment of orthotropic steel deck with asphalt pavement." *J. JSCE*, (563), 161-171 [in Japanese]

Japan Road Association (1980). "Specification for highway bridges (ver. 1980), Part2 steel bridges." Maruzen [in Japanese]

Japan Road Association (2014). "Specification for highway bridges (ver. 2014), Part2 steel bridges." Maruzen [in Japanese]

Japanese Society of Steel Construction (2012). “Fatigue design recommendation for steel structure.” Gihodo, Tokyo

Jong, F. B. P. (2004). "Overview fatigue phenomenon in orthotropic bridge decks in the Netherland." *Proc. First Int. Orthotropic Bridge Conf.*, Aug. 23-27, 2004, Sacramento, 489-512

Jong, F. B. P., and Kolstein, M. H. (2004). "Strengthening a bridge deck with high performance concrete." *Proc. First Int. Orthotropic Bridge Conf.*, Aug. 23-27, 2004, Sacramento, 328-345

JSCE Subcommittee on Fatigue of Steel Orthotropic Deck (1989). "Fatigue of orthotropic steel bridge deck." *Proc. JSCE*, (410), 25-36 [in Japanese]

Kainuma, S., Onoue, S., Miura, K., Inokuchi, S., Kawabata, A., and Uchida, D. (2008). "Development of an experimental system for fatigue-cracking from weld roots between deck plate and u-rib in orthotropic steel decks." *J. JSCE Ser. A*, 64(2), 297-302 [in Japanese]

Kainuma, S., Yang, M., Jeong, Y., Inokuchi, S., Kawabata, A., and Uchida, D. (2016). "Experiment on fatigue behavior of rib-to-deck weld root in orthotropic steel decks." *J. Constructional Steel Research*, 119, 113-122

Kamakura, M., Hihei, M., Sasaki, E., Kanao, M., and Inagaki, M. (1979). “Effect of specimen size on fatigue properties of SM50B non-load carrying fillet welded joints.” *Journal of the Japan Welding Society*, 48(12), 1060-1064 [in Japanese]

Kang, S. W., Kim, W. S., and Paik, Y. M. (2002) “Fatigue strength of fillet welded steel structure under out-of-plane bending load.” *Int. J. Korean Welding Soc*. 6, 33–39

Katsumata, M., Ogasawara, T., Machida, F., Kawase, A., and Mizoe, Y. (1999). "Local stress of trapezoidal ribs to floor beams joint in rational orthotropic steel decks." *J. Struct. Eng. A (JSCE)*, 45(3), 1241-1252 [in Japanese]

Katsumata, M., Ogasawara, T., Machida, F., Kawase, A., and Mizoe, Y. (2000). "Structural Details' Experimental Study Regarding a Simplified Orthotropic Steel Deck's Trapezoidal Ribs and Floor Beam Intersections." *J. Struct. Eng. A (JSCE)*, 46(3), 1233-1240 [in Japanese]

Kihl, D. P., Sarkani, S. (1997). “Thickness effects on the fatigue strength of welded steel cruciform.” *Int. J. Fatigue*, 19(1), 311-316

Kim, I. T. (2013). "Fatigue strength improvement of longitudinal fillet welded

out-of-plane gusset joints using air blast cleaning treatment." *Int. J. Fatigue*, 48, 289–299

Kodama, T., Ichinose, Y., Kagata, M., Ohta, K., and Niinobe, Y. (2010). "Effect of reducing strains by SFRC pavement on orthotropic steel deck of ohira viaduct." *J. Struct. Eng. A (JSCE)*, 56, 1249-1258 [in Japanese]

Kolstein, M. H. (2001). "Measurements and interpretations of dynamic loads on bridges, Phase 4: fatigue design of European orthotropic steel bridge decks." Commissions of European Committees, EUR 20032, Brussels

Kolstein, M. H. (2007). "Fatigue classification of welded joints in orthotropic steel bridge decks." Delft Univ.

Kondo, A., Yamada, K., and Kikuchi, Y. (1984). "Fatigue strength of field-welded rib joints of orthotropic steel decks." *Proc. IABSE colloquium, Fatigue of steel and concrete structure*, IABSE, Lausanne

Kozy, B. M., Connor, R. J., Paterson, D., and Mertz, D. R. (2011). "Proposed revisions to AASHTO-LRFD bridge design specifications for orthotropic steel deck bridges." *J. Bridge Eng.*, 16(6), 759-767

Leendertz, J. S. (2008). "Fatigue Behaviour of Closed Stiffener to Crossbeam Connections in Orthotropic Steel Bridge Decks." Delft Univ.

Lehrke, H. P. (1997). "Measurements and interpretation of dynamic loads on bridges, Final report." Commissions of European Committees, EUR 16851, Brussels

Leonard, D. R. (1969). "A traffic loading and its use in the fatigue life assessment of highway bridges." *TRRL Report*, LR252

Lotsberg, I., and Sigurdsson, G. (2006) "Hot spot stress S–N curve for fatigue analysis of plated structures." *J. Offshore Mech. Arct. Eng.*, 128(11), 330–336

Lyse, I., and Madsen, I. E. (1938). "Structural behavior of battle-deck floor systems." *ASCE Proc.*, 64, 99-121

Machida, S., Matoba, M., Yoshinari, H., and Nishimura, R. (1992) "Definition of Hot Spot Stress in Welded Structure for Fatigue Assessment (3rd Report)." *J. Society of Naval Architects of Japan*, 171, 477-484

Maddox, S. J. (1974). "Fatigue of welded joints loaded in bending." *TRRL Report*, SR84

Maddox, S. J. (1987) "The effect of plate thickness on the fatigue strength of fillet welded joints." The Welding Institute, Camnridge

Maddox, S. J. (2002) "Hot spot stress design curves for fatigue assessment of welded structures." *Int. J. Offshore Polar Eng.*, 12(2), 134–141

Maddox, S. J., Doré, M. J., and Smith, S. D. (2011). "A case study of the use of ultrasonic peening for upgrading a welded steel structure." *Welding in the World*, 55(9), 56-67

Marquis, G., Mikkola, T. (2002). "Analysis of welded structures with failed and non-failed welds based on maximum likelihood", Welding in the World, 46(1–2), 15-22

Mehue, P. (1990). "Cracks in steel orthotropic decks." Int. Conf. of Bridge Management, *Proc. First Int. Conf. on Bridge Management*, Mar, 1990, University of Surrey, 633-642

Miki, C., Goto, Y., Murakoshi, J., and Tateishi, K. (1986). "Computer simulation studies on the fatigue load of highway bridges", *J. Struct. Eng. A (JSCE)*, 32, 597-608 [in Japanese]

Miki, C., Mori, T., Sakamoto, K., and Kashiwagi, H. (1987). "Size effect on the fatigue

strength of transverse fillet welded joints." *J. Struct. Eng. A (JSCE)*, 33, 393-402.
Miki, C., Tateishi, K., and Takagi, S. (1991). "Field stress measurements at the connection between longitudinal and transverse ribs of steel deck plates." *J. Struct. Eng. A (JSCE)*, 37(3), 1163-1168 [in Japanese]
Miki, C., Tateishi, K., Ishihara, K., and Kajimoto, K. (1994). "Fatigue strength of scallop details in steel bridges" *J. JSCE*, 483 / I-26, 79-86
Miki, C., Tateishi, K., Okukawa, A., and Fujii, Y. (1995). "Local stress and fatigue strength of the joint between longitudinal and transverse ribs in orthotropic steel deck plate." *J. JSCE*, (519), 127-137 [in Japanese]
Miki, C. (2006). "Fatigue damage in orthotropic steel bridge decks and retrofit works." *Int. J. Steel Struct.*, 6(2), 255-267
Miki, C., Suzuki, K., Kano, T., Sasaki, E., Ishida, M., and Takamori, H. (2007). "Preventive works for fatigue damage in orthotropic steel bridge deck by SFRC pavement and long term monitoring of the composite action." *J. JSCE Ser. A*, 62(4), 950-963 [in Japanese]
Miki, C., Konishi T., Tokida H., and Sasaki, K. (2009). "Inspection and retrofitting of fatigue damaged orthotropic steel deck." *Proc. Second Int. Conf. on Fatigue and Fracture in the Infrastructure*, Philadelphia, July 26-29, 2009
Miki, C., and Suganuma, H. (2014). "Rehabilitation of strengthening of orthotropic steel bridge decks." In: Chen, W. F., and Duan, L. (2014). "Bridge Engineering Handbook, Second Edition: Construction and Maintenance." CRC Press
Mizuguchi, K., Nakasu, M., Furukawa, M., and Iguchi, S. (2000). "Influence of rib span and detail on local stress of orthotropic steel deck using large u-shaped rib." *J. Struct. Eng. A (JSCE)*, 46(3), 1225-1232 [in Japanese]
Mizuguchi, K., Yamada, K., Iwasaki, M., and Inokuchi, S. (2004), "Rationalized steel deck structure and large model test for developing new type of structure." *Proc. First Int. Orthotropic Bridge Conf.*, Aug. 23-27, 2004, Sacramento, 675-668
Mori, T. (2010). "Fatigue of Orthotropic Steel Deck." Subcommittee on Fatigue of Orthotropic Steel Bridge Deck [in Japanese]
Mori, T., Shimanuki, H., and Tanaka, M. (2012). "Effect of UIT on fatigue strength of web-gusset welded joints considering service condition of steel structures." *Welding in the World*, 56(9), 141-149
Murakoshi, J., Yanadori, N., Ishizawa, T., Toyama, N., and Kosuge, T. (2012). "Study on effect of deck thickness of orthotropic steel deck on fatigue durability." *Steel Construction Eng. (JSSC)*, 19(75), 55-65 [in Japanese]
Nunn, D. E. (1974). "An investigation into the fatigue of welds in an experimental orthotropic bridge deck panel." *TRRL Report*, LR629
Nunn, D. E., and Cuninghame, J. R. (1974a). "Stresses under wheel loading in steel orthotropic decks with trapezoidal stiffener." *TRRL Report*, SR53
Nunn, D. E., and Cuninghame, J. R. (1974b). "Stresses under wheel loading in a steel orthotropic deck with v-stiffeners." *TRRL Report*, SR59
Ohashi, H., Fujii, Y., Miki, C., Ono, S., and Murakoshi, J. (1997). "Local Stress and Deformation at Field Joints of Orthotropic Steel Deck." *J. JSCE*, (556), 65-76 [in Japanese]
Ohashi, H., Miki, C., Yanadori, N., and Ono, S. (2000). "Structural Performance Study by Truck Loading on a Full-scale Test Specimen of Orthotropic Steel Deck with Thickened Deck Plate and Large Size Trough Ribs." *J. JSCE*, (647), 295-303 [in

Japanese]
Ono, S., Shimozato, T., Masui, T., Machida, F., and Miki, C. (2005). "Retrofitting method for existing orthotropic steel deck." *J. JSCE*, (801), 213-226 [in Japanese]
Ono, S., Hirabayashi, Y., Simozato, T., Inaba, N., Murano, M., and Miki, C. (2009). "Fatigue properties and retrofitting of existing orthotropic steel bridge decks." *J. JSCE Ser. A*, 65(2), 335-347 [in Japanese]
Park, W., and Miki, C. (2008). "Fatigue assessment of out-of-plane attachments with various angles by using local stress approaches." *J. Struct. Eng. A (JSCE)*, 54, 685-694
Radaj, D., Soncino, C. M., and Fricke, W. (2006). "Fatigue Assessment of Welded Joints by Local Approaches (Second Edition)." Woodhead
Saito, S., Kudo, Y., Hayashi, N., Uchida, D., and Mori, T. (2013). "Fatigue durability improvement of welded joint by increasing deck plate thickness." *Proc. Third Int. Orthotropic Bridge Conf.*, Jun. 24-30, 2013, Sacramento, 134-145
Sakano, M., Mikami, I., Arai, M., Yonemoto, E., and Takagaki, N. (1994). "Fatigue test on thickness effect of out-of-plan welded gusset joint." *J. Struct. Eng. A (JSCE)*, 40, 1255-1264 [in Japanese]
Sakano, M., Arai, M. (2004). "Thickness effect on fatigue strength of out-of-plane welded gusset joints" *J. JSCE*, 766 / I-68, 351-356 [in Japanese]
Sakino, Y., and Nakamae, K. (2015). "Effect of base-plate size on bending fatigue life in box-welded joint." P*reprints of the National Meeting of JWS*, 97, 186-187 [in Japanese]
Seeger, K. H. (1964). "Neuere Flachblechfahrbahnen, insbesondere bei Strassenbruecken." *Bauingenieur*, 39, 173-179 [in Germany]
Shimokawa, H., Takena, K., Itoh, F., and Miki, C. (1985). "Fatigue strength of large-size gusset joints of 800 MPa class steels." *Proc. JSCE*, 356 / I-3, 279-287
Sim, H., Uang, C., and Sikorsky, C. (2009). "Effects of fabrication procedures on fatigue resistance of welded joints in steel orthotropic decks." *J. Bridge Eng.*, 14(5), 366-373
Subcommittee on Fatigue of Steel Orthotropic Deck (1989). "Fatigue of orthotropic steel bridge deck." *Proc. JSCE*, (410/I-12), 25-36 [in Japanese]
Suganuma, H., and Miki, C. (2006). "Investigation of the high fatigue resisted slit form on the cross of trough rib and transverse rib on the orthotropic steel deck." *IIW document*, XIII-2121-06
Suganuma, H., and Miki, C. (2007a). "Full size fatigue tests of the new orthotropic steel deck system." *IIW document*, XIII-2164-2007
Suganuma, H., and Miki, C. (2007b). "Fatigue strength evaluation with effective notch stress of the weld between trough rib and deck plate on orthotropic steel deck." *J. JSCE Ser. A*, 63(1), 35-42 [in Japanese]
Sugisaki, M., and Kobayashi H. (1991). "Various repairing methods employed for damaged RC (reinforced concrete) deck slabs." Ishikawajima-Harima engineering review, 31(2), 67-73 [in Japanese]
Sugiyama, H., Tabata, A., Kasugai, T., Ishii, H., Inokuch, S., Kiyokawa, S., and Ikezue, K. (2014). "Improving fatigue resistance of cutout on diaphragm in orthotropic steel deck." *J. JSCE Ser. A1*, 70(1), 18-30 [in Japanese]
Suzuki, I., Kagayama, T., and Iwasaki, M. (1991). "Effect of longitudinal rib spacing on deformation of asphalt pavement and fatigue of welds in orthotropic steel deck

bridge." *Proc JSCE*, (432), 1-10

Takada, Y., Kishiro, M., Nakashima, T., and Usui, K. (2009a). "Fatigue failure assessment of actual-working load and run location on orthotropic steel deck applied in BWIM." *J. Struct. Eng. A (JSCE)*, 55, 1456-1467 [in Japanese]

Takada, Y., Tabata, A., Usui, K., and Motoi, K. (2010). "Analysis of stress change for the temperature effect of orthotropic steel deck." *Steel Construction Eng. (JSSC)*, 17(67), 13-27 [in Japanese]

Tamakoshi, T., Nakasu, K., and Ishio, M. (2006), "Actual datas of live loads on highway bridges" Technical Note of National Institute for Land and Infrastructure Management, 295, National Institute for Land and Infrastructure Management, "Ministry of Land, Infrastructure and Transport, Japan"

Tateishi, K., Takenouchi, H., and Miki, C. (1995). "Mechanism for Developing Local Stress at the Connection Details in Steel Bridge Structures." *J. JSCE*, (507), 109-119 [in Japanese]

Taskopoulos, P., and Fisher, J. W. (2003). "Full-scale fatigue tests of steel orthotropic decks for the williamsburg bridge." *J. Bridge Eng.*, 8(5), 323-333

Vosikovsky, O., Bell, R., Burns, D. J., and Mohaupt U. H. (1989). "Thickness effect on fatigue life of welded joints – review of the Canadian program." *Proc. 8th Int. Conf. Offshore Mech. and Arctic Eng.,Volume 3*, 9-19

Wang, C., and Feng, Y. (2008). "Review of fatigue behaviors and finite element analysis of orthotropic steel bridge decks." *Proc. Second Int. Orthotropic Bridge Conf.*, Aug. 25-29, 2008, Sacramento, 290-303

Wang, T., Wang D., Huo L., and Zhang Y. (2009). "Discussion on fatigue design of welded joints enhanced by ultrasonic peening treatment (UPT)" *Int. J. Fatigue* 31, 644–650

Wolchuk, R. (1987). "Application of orthotropic decks in bridge rehabilitation." *Eng. J.*, 24(3), 113-121

Wolchuk, R., and Ostapenko, A. (1992). "Secondary stresses in closed orthotropic deck ribs at floor beams." *J. Struct. Eng.*, 118(2), 583-595

Wolchuck, R. (2004). "Orthotropic decks with long rib spans." *Proc. First Int. Orthotropic Bridge Conf.*, Aug. 23-27, 2004, Sacramento, 44-56

Yuge, T., Machida, F., Morikawa, H., Miki, C., Kamiki, T., and Matsui, T. (2004). "Analysis of fatigue damage patterns in orthotropic steel deck of Tokyo Metropolitan Expressway." *Proc. First Int. Orthotropic Bridge Conf.*, Aug. 23-27, 2004, Sacramento, 531-542

Yagi, J., Machida, S., Tomita, Y., Matoba, M., and Soya, I. (1993) "Thickness effect criterion for fatigue strength evaluation of welded steel structures." *J. Offshore Mech. and Arctic Eng.*, 115, 58-65

Yamaoka, D., Sakano, M., Natsuaki, Y., Nonaka, S., Nakagawa, Y., and Nakamura, S. (2010). "Fatigue behavior and countermeasure of intersection between bulb ribs and lateral rib of A bridge type orthotropic steel deck." *J. Struct. Eng. A (JSCE)*, 56, 838-849 [in Japanese]

Yan, F., Chen, W., and Lin, Z. (2016). "Prediction of fatigue life of welded details in cable-stayed orthotropic steel deck bridges." *Eng. Struct.*, 127, 344-358

Yuge, T., Machida, F., Morikawa, H., Miki, C., Kamiki, T., and Matsui, T. (2004) "Analysis of fatigue damage patterns in orthotropic steel deck of Tokyo Metropolitan Expressways." *Proc. First Int. Orthotropic Bridge Conf.*, Aug. 23-27,

2004, Sacramento, 531-542
Zhang, S., Shao, X., Cao, J., Cui, J., Hu, J., and Deng, L. (2016). "Fatigue Performance of a Lightweight Composite Bridge Deck with Open Ribs." *J. Bridge Eng.*, 21(7)
鋼床構造の進捗調査分科会 (1982). "鋼床版の発展と現況." *J. JSCE,* 67(10), 34-40 [in Japanese]
日本道路協会 (2002). “鋼道路橋の疲労設計指針”, 5章, 丸善 [in Japanese]

Appendix-A Fatigue data used in Chapter 2

A.1. Corrected literature fatigue data

Table A-1 and Table A-2 show fatigue data of the non-load-carrying cruciform and the out-of-plane gusset joints, and Fig. A-1 shows these models. Though materials of fatigue data were varied from mild to high strength steels such as HT780 or HT80 (Shimokawa 1985; Anami 2001), the effect of material strength on the fatigue strength of welded joints was not significant. The load types were axial, and 4- and 3-point bending cyclic loads had stress ratios of zero or larger than zero (Fig. A-2). The numbers of models in the table are not the numbers of models in the literature, but are the numbers of models used to calculated fatigue strength at 2.0×10^6 cycles in this study, because data of fatigue lives shorter than 10^5 cycles and run-out were eliminated, as described in the following paragraph. In addition, fatigue data sets with fatigue lives only shorter than 10^6 cycles were not used in this study because those fatigue data sets may not have long enough cycles to estimate fatigue strength at 2.0×10^6 cycles.

The mean fatigue strength of 2.0×10^6 cycles in terms of the nominal stress ($\Delta\sigma_f$) was determined based on the IIW recommendation (Hobbacher 2007). The fatigue strength was calculated with linear regressions of the literature data, where fatigue lives were regarded as dependent variables, and data of fatigue lives shorter than 10^5 cycles and run-out were eliminated. Since short fatigue lives might indicate a different result than that of high cycle fatigue data, test results under high stress ranges that could cause fatigue lives shorter than 10^5 cycles were eliminated from analyses in this study. On the other hand, it was indicated that run-out data should be used to estimate mean curves of the test results in the S-N diagram (Marquis). However, since some fatigue data sets did not include run-out data, all fatigue data sets were analyzed without run-out data. Those analyses would provide conservative estimations of the mean curves.

Fatigue strength at 2.0×10^6 cycles in terms of the hot-spot stress ($\Delta\sigma_{f,h}$) were determined by multiplying stress concentration factors (SCFs), ratios of hot-spot stresses to nominal stresses, into the fatigue strength in terms of nominal stresses. In the case that the literature included enough data of hot-spot stresses, $\Delta\sigma_{f,h}$ was determined by linear regressions of the data, with elimination of data of fatigue lives shorter than 10^5 cycles and run-out.

Table A-3 shows fatigue data of component models with fatigue crack initiation points at the plate edges, which means type B hot spots. Fatigue tests were conducted with in-plane gusset joints by Yamada (1984) and Kondo (2002) and gusset models by Miki (1994) and Fricke (2006) (Fig. A-3). The literature used different crack lengths as fatigue failure, N_f, as twice of the surface crack length, as shown in Table A-3. Cracks at plate edges were treated as half cracks in this study.

Table A-4 shows fatigue data of structural models with fatigue crack initiation points at three types of hot spots, type A, -B and -C. Fatigue data of type A hot spots is a bracket model for ships, tested by Yagi (1991), and a bridge plate girder model having an out-of-plane gusset, tested by Kim (2013) (Fig. A-4 and Fig. A-5). Fatigue data of type B hot spots is an open-rib to transverse-rib connection model for orthotropic steel

bridge decks, tested by Yamaoka (2010) (Fig. A-6). Fatigue data of type C hot spots is pipe-to-pipe K-joints for truss bridges, tested by Schumacher (2006), and rectangular pipe-to-pipe T joints, tested by Cheng (2015) (Fig. A-7). The literature used different crack lengths as fatigue failure, N_f, as shown in Table A-4.

The 95% survival fatigue strength for the data sets was determined based on the IIW recommendation (Hobbacher 2007).

A.2. Computed stress concentration factors

Fig. 2-6 shows graphs of stress concentration factors (SCFs) of cruciform, T, and out-of-plane gusset joints as the vertical axis and thicknesses and width-thickness ratios of component joint models as the horizontal axis. Table A-5 and Table A-6 summarize the numerical data.

A.3. Thickness effects investigation

Fig. A-8a and b show the relations between corrected thicknesses and fatigue strength of cruciform joints in terms of nominal and hot-spot stress, respectively, and Table A-5 summarizes the fatigue strengths. The corrected thicknesses were determined by Equation 2-2. Fig. A-8 also shows the mean lines obtained by linear regressions.

The thickness effects on axially loaded cruciform joints existed down to 6-mm thickness with exponents of 0.25 and 0.23 in terms of nominal and hot-spot stress (Fig. A-8a, b). The relation in terms of hot-spot stress was similar to that of nominal stress due to small stress concentrations of cruciform joints regardless of plate thickness. The result that the thickness effect on cruciform joints was extended to relatively thinner plates was also suggested in previous research (Miki 1987; Gurney 1995; Kihl and Sarkani 1997).

The thickness effects on bending loaded T joints also existed down to 6-mm thickness, but its exponents, which were 0.34 and 0.35 in terms of nominal and hot-spot stress, respectively, were larger than those under axial loads. The steeper thickness exponents mean that the fatigue strength of plates thinner than the basic thickness can increase more under a bending load than the fatigue strength under an axial load. The steeper thickness exponents of bending loaded T joints were obtained by Yagi (1991) with fatigue tests on geometrically similar component models under both axial and bending loads. The relations in terms of nominal and hot-spot stress were again similar, due to the small stress concentrations.

From Fig. A-8 and previous results, the thickness effects in terms of hot-spot stress, with an exponent of 0.25, could be extended to 6 mm for cruciform joints. Thickness effects of cruciform and T joints, in terms of hot-spot stress, were similar to those of nominal stress. Thickness effects down to 6 mm are shown in Fig. A-8 and in previous studies. Though the thickness exponents of bending loaded T joints were steeper than 0.25, the lower exponent applied to plates thinner than the basic thickness can provide safe estimations. The corrected thickness indicated in Equation 2-2 can be applied to

determine the thickness factor, but simply using the main plate thickness, which is equal to or larger than the corrected thickness would give safe fatigue estimations.

Fig. A-9a and b show relations between thickness and fatigue strength of out-of-plane gusset joints in terms of nominal and hot-spot stress, respectively, and Table A-6 summarizes the fatigue strengths. Fig. A-9 also shows the mean lines obtained by linear regressions.

The thickness effects on axially loaded out-of-plane gusset joints existed down to 8-mm thickness, as is similar to the effects on cruciform joints, and its exponents were 0.29 and 0.28 in terms of nominal and hot-spot stress. The existence of thickness effects in terms of nominal stress has already been indicated in the literature (Sakano 1994, 2004; Hobbacher 2007), and these effects can be applied to out-of-plane gusset joints with relatively thicker plates. Fig. A-9 shows that the thickness effects extended to relatively thin plates in terms of hot-spot stress. Though SCFs of axially loaded out-of-plane gusset joints had ranges from 1.20 to 1.43, the mean thickness exponents in terms of nominal and hot-spot stress were similar. This result might mean that structural stress concentrations calculated by using reference points of 0.4t and 1.0t do not have significant effects on the thickness effects of axially loaded out-of-plane gusset joints.

The thickness effects on bending loaded out-of-plane gusset joints also existed down to 12-mm thickness and its exponents were 0.27 and 0.35 in terms of nominal and hot-spot stress, respectively. The steeper thickness exponents in terms of hot-spot stress could be obtained due to the relatively smaller SCFs of fatigue data at 75-mm thickness, which were 1.14 and 1.15, whereas the other bending loaded out-of-plane gusset joints had SCFs of 1.25 to 1.60. The two fatigue data at 75-mm thickness could have affected the mean thickness exponent, since only those two data existed for bending loaded out-of-plane gusset joints with a thickness >25 mm.

From Fig. A-9, the thickness effects in terms of hot-spot stress with an exponent of 0.25 could be extended to 8 mm for cruciform joints. Fig. A-9 shows thickness exponents steeper than 0.25. This result shows exponent 0.25 applied to plates thinner than the basic thickness can provide safe fatigue estimations. Though fatigue data was limited in numbers and thickness ranges down to 8 and 12 mm for the axially and the bending loaded joints, respectively, the thickness effect could be extended to 6-mm thickness, which is the minimum thickness commonly applied to orthotropic steel decks.

A.4. Bending effect investigation

Fig. A-10a and b show fatigue data of axially and bending loaded cruciform joints with thicknesses of 6-25 mm, in the S-N diagrams with the vertical axis of nominal stress and hot-spot stress modified by the thickness effect factor $(t/25)^{0.25}$, respectively. The figures do not include fatigue data of plates thicker than 25 mm, which are rarely used for orthotropic steel decks and can cause non-conservative fatigue estimations by thickness exponents of 0.25, according to Fig. A-8. Fig. A-10 also shows 95% survival curves connected to constant amplitude fatigue limits, and the axial-bending ratios are shown in Equation 2-3

Comparing the 95% survival curves, the reduction factor of 0.8 for bending stresses

could be applicable to cruciform joints evaluated by the hot-spot stress approach. The axial-bending ratios in terms of nominal stress, which were 0.89 and 0.88 at 2.0×10^6 cycles and constant amplitude fatigue limits, were smaller value than 0.8 as suggested by JSSC (2012), or 0.6 as suggested by Lotsberg and Sigurdsson (2006). On the other hand, the axial-bending ratios in terms of hot-spot stress were 0.74 and 0.76 at 2.0×10^6 cycles and constant amplitude fatigue limits, respectively. Those ratios were closer values to those provided by the literature and indicate that the reduction factor of 0.8 for bending stress suggested by JSSC (2012) can give safe fatigue estimations to the hot-spot stress approach. The reason why the axial-bending ratios in terms of hot-spot stress decrease might be that the fatigue life distribution of bending loaded cruciform joints in the relatively short fatigue life region were narrowed by taking account of structural stress concentrations.

Fig. A-11a and b show S-N diagrams of the fatigue data of axially and bending loaded out-of-plane gusset joints with thicknesses of 8-25 mm. Explanations for Fig. A-11 are the same as those for Fig. A-10.

Comparing the 95% survival curves, the reduction factor of 0.8 for bending stresses could be applicable to out-of-plane gusset joints evaluated by the hot-spot stress approach, with an appropriate constant amplitude fatigue limit. The axial-bending ratios at 2.0×10^6 cycles in terms of nominal and hot-spot stress were 0.79 and 0.68, respectively. This result indicates that the reduction factor of 0.8, suggested by JSSC (2012), can give safe fatigue estimations to both the nominal and the hot-spot stress approaches. The axial-bending ratios at constant amplitude fatigue limits in terms of nominal and hot-spot stress were 1.07 and 0.86, both of which are larger than 0.8. However, 0.8 times the constant amplitude fatigue limits, $0.8 \times 56 = 45$ and $0.8 \times 84 = 67$ N/mm^2, were larger than the corresponding design values, 32 and 62 N/mm^2, provided by JSSC (2012).

A.5. Fatigue design curve selection

Fig. A-12 to Fig. A-15 show fatigue strengths of literature data and fatigue class JSSC-E provided by the JSSC recommendation, plotted in S-N diagrams with vertical axes of hot-spot stresses modified by the equations below.

$$\sigma'_{\boldsymbol{h}} = (\boldsymbol{t}/25)^{0.25}\left(\sigma_{\boldsymbol{h},\mathrm{m}} + 0.8\sigma_{\boldsymbol{h},\mathrm{b}}\right) \qquad \text{6-1a}$$

$$\sigma_{\boldsymbol{h},\mathrm{m}} = \left(\sigma_{\boldsymbol{h},\mathrm{obv}} + \sigma_{\boldsymbol{h},\mathrm{rev}}\right)/2 \qquad \text{2-4b}$$

$$\sigma_{\boldsymbol{h},\mathrm{b}} = \left(\sigma_{\boldsymbol{h},\mathrm{obv}} - \sigma_{\boldsymbol{h},\mathrm{rev}}\right)/2 \qquad \text{2-4c}$$

where $\sigma_{h,\,\mathrm{m}}$ and $\sigma_{h,\,\mathrm{b}}$ are membrane and bending components of hot-spot stresses, respectively, and $\sigma_{h,\,\mathrm{obv}}$ and $\sigma_{h,\,\mathrm{rev}}$ are hot-spot stresses calculated based on obverse and reverse surface stresses. The hot-spot stress and their bending components were computed by finite element analyses and are summarized in Table A-5 to Table A-7. As the results of the previous section, the thickness factor and the bending reduction factor were determined to be those provided by the JSSC recommendation. The thickness factor was applied to any type of joint with all thickness ranges, though JSSC recommendations provide the thickness factor for only cruciform and butt welded joints

with plates thicker than 25 mm. Fig. A-12 to Fig. A-15 only show fatigue strengths of joints with plates thinner than 25 mm, since the thickness exponents of 0.25 can be non-conservative for plates thicker than 25 mm, which is a thickness rarely applied to orthotropic steel decks.

All fatigue data, except some plots of in-plane gusset joints at fatigue lives $>9.0 \times 10^6$, satisfied fatigue class JSSC-E. Fatigue data sets of component joints had 95% survival curves above or across JSSC-E (Fig. A-12 to Fig. A-15). In addition, all fatigue data of structural models were plotted above JSSC-E (Fig. A-15). However, 95% survival curves of both axially and bending loaded cruciform joints were below JSSC-E in relatively short fatigue life regions of approximately $\leqq 1.0 \times 10^6$ cycles, which corresponds to the factored hot-spot stress ranges of $\geqq 100$ N/mm^2 (Fig. A-12). Furthermore, some in-plane gusset joints were plotted below the constant amplitude fatigue limit of JSSC-E. Therefore, the fatigue evaluation using the hot-spot stress modified by Equation 2-4a and the fatigue design curve of JSSC-E could be applicable for type A and C hot spots, but can result in non-conservative fatigue evaluations in the case that the hot-spot stress ranges are equal or higher than 100 N/mm^2. In addition, the fatigue evaluation could be applicable to type B hot spots, whereas the constant amplitude fatigue limit of JSSC-E would not applicable to the evaluations of in-plane gusset joints.

Table A-1 Fatigue data of cruciform and T joints

Reference	Material	Load	Series	t_1 [mm]	t_2 [mm]	a [mm]	N
Kamakura (1979)	SM50B	Axial	1	9	9	6	5
			2	9	9	6	5
			3	9	9	6	7
			4	20	9	9	7
			5	20	9	9	6
			6	20	9	9	5
			7	20	20	9	7
Maddox (1987)	Grade50	Axial	1	13	10	8	4
			2	50	50	16	6
			3	100	50	16	4
Yagi (1991)	EH36	Axial	1	10	5	4	5
			2	10	10	9	7
			3	10	22	16	7
			4	22	10	9	6
			5	22	22	16	8
			6	22	40	32	8
			7	40	10	9	7
			8-9	40	22	16	6+6
			10	40	40	32	8
			11	80	10	9	7
			12	80	22	16	5
			13	80	40	32	7
Miki (1987)	SM58	Bending*	1	9	16	6	8
			2	15	16	6	8
			3	24	16	6	6
			4	34	16	6	6
			5	50	16	6	7
			6	50	50	19	7
Vosikovsky (1989)	350 Grade	Bending*	1	16	16	10**	7
			2	26	26	16**	8
			3	52	52	28**	4
			4	78	78	39.5**	5
			5	103	103	54.5**	7
Yagi (1993)	EH36	Bending*	1	22	10	9	6
			2	22	22	16	5
			3	40	22	16	6
			4	80	22	16	7
			5	80	40	32	7

t_1, t_2: main and attached plate thicknesses, a: weld leg length, N: number of data except $\leqq 10^5$ and run-out
* Miki (1987): 4-point bending, Vosikovsky (1989) and Yagi (1993): 3-point bending, **Average value

Table A-2 Fatigue data of out-of-plane gusset joints

Reference	Material	Load	Series	t_1 [mm]	t_2 [mm]	a [mm]	N
Shimokawa (1985)	HT80	Axial	1	30	36	9	3
Anami (2000)	SM570	Axial	1	16	12	9[a]	26
Huo (2005)	16Mn	Axial	1	8	8	5[a]	9
Park (2008)	BHS500	Axial	1	20	20	11.15/8.01 [b]	3
Wang (2009)	SS800	Axial	1	8	8	5[a]	16
Maddox (2011)	Grade 355J2+N	Axial	1	30	30	8	3
Araki (2012)	SM490YA	Axial	1	12	12	9	9
Mori (2012)	SBHS500	Axial	1	12	12	10.8/8.2 [b]	14
Kim (2013)	SM400 or 490	Axial	1	10	10	6	13
Sakano (1994)	SM570Q	Bending	1	25	25	8	3
			2	75	75	13	4
Sakano (2004)	SM570Q	Bending	1	75	25	13	3
Araki (2012)	SM490YA	Bending	1	12	12	9	13
Kim (2013)	SM400 or 490	Bending	1	14	14	6	3
Sakino (2015)	HT780	Bending	1	15	6	8	14

t_1, t_2: main and attached plate thicknesses, a: weld leg length, N: number of data except $\leqq 10^5$ and run-out
[a] Not found in the literature and set to $t_2/\sqrt{2}$, [b] Main plate side / Attached plate side

Table A-3 Fatigue data of other component joints

Reference	Material	Type	Stress	t_1 [mm]	N	Crack
Yamada (1984)	SM50A	B	Membrane	10	19	20 mm (2.0) [a]
Miki (1993)	No info. available	B	Membrane	9	7	40 mm (4.4) [a]
Kondo (2002)	SM520B	B	Membrane	10	18	20 mm (2.0) [a]
	SM490A	B	Membrane	10	8	20 mm (2.0) [a]
Fricke (2006)	No info. available	B	Membrane	12	3	No info. available

[a] twice of plate edge crack length at fatigue failure (c / t_1)

Table A-4 Fatigue data of structural models

Reference	Material	Type	Stress	t_1 [mm]	N	Crack
Yagi (1991)	TMCP (YP353)	A	Membrane	22	12	100 mm (4.5) [a]
Kim (2013)	SM400A	A	Membrane	9	8	30 mm (3.3) [a]
Yamaoka (2010)	SM400A	B	Membrane	9	2	40 mm (2.5) [b]
Schumacher (2006)	S 355 J2 H	C	Bending	20	8	Through-thickness
				12.5	4	Through-thickness
Cheng (2015)	Q420	C	Bending	12	2	Through-thickness
				10	2	Through-thickness
				8	2	Through-thickness

[a] surface crack length c at fatigue failure (c / t_1)
[b] twice of plate edge crack length at fatigue failure (c / t_1)

Table A-5 Fatigue strength of non-load-carrying cruciform joints

Reference	Series	Thickness [mm]		SCF	m	Fatigue strength [N/mm^2]	
		t_1	$L/2$			Nominal	Hotspot stress
Axial loading test							
Kamakura (1979)	1	9	10.5	1.04	3.0	124	129
	2	9	10.5	1.02	3.0	130	132
	3	9	10.5	1.00	3.0	129	129
	4	20	13.5	1.04	3.0	100	104
	5	20	13.5	1.02	3.0	106	108
	6	20	13.5	1.01	3.0	96	97
	7	20	19	1.04	3.0	91	95
Maddox (1987)	1	13	13	1.01	3.0	99	100
	2	50	41	1.02	3.0	76	77
	3	100	41	1.02	3.0	71	73
Yagi (1991)	1	10	6.5	0.99	3.0	137	135
	2	10	14	0.98	3.0	108	106
	3	10	27	1.00	3.0	120	119
	4	22	14	1.03	3.0	121	125
	5	22	27	1.03	3.0	88	90
	6	22	52	1.02	3.0	91	94
	7	40	14	1.04	3.0	109	113
	8	40	27	1.05	3.0	97	101
	9	40	27	1.05	3.0	91	96
	10	40	52	1.05	3.0	94	98
	11	80	14	1.03	3.0	87	89
	12	80	27	1.04	3.0	99	103
	13	80	52	1.05	3.0	87	91
Bending test							
Miki (1987)	1	9	14	0.94	3.0	213	199
	2	15	14	0.94	3.0	179	167
	3	24	14	0.94	3.0	130	122
	4	34	14	1.03	3.0	150	155
	5	50	14	1.03	3.0	139	143
	6	50	44	1.03	3.0	116	120
Vosikovsky (1989)	1	16	18	0.96	3.0	143	137
	2	26	29	0.97	3.0	119	115
	3	52	54	0.93	3.0	92	85
	4	78	78.5	0.93	3.0	88	82
	5	103	106	0.93	3.0	81	75
Yagi (1991)	1	22	14	0.94	3.0	127	120
	2	22	27	0.93	3.0	115	107
	3	40	27	0.95	3.0	95	90
	4	80	27	0.98	3.0	100	99
	5	80	52	0.96	3.0	83	79

t_1, t_2: thicknesses of main and attached plates, L: t_2+2a as shown in, a: weld leg length
$\Delta\sigma_f$, $\Delta\sigma_{f,h}$: fatigue strength corresponding to nominal and hot spot stresses

Table A-6 Fatigue strength of out-of-plane gusset joints

Reference	Series	t_1 [mm]	SCF	m	Fatigue strength [N/mm^2]	
					$\Delta\sigma_f$	$\Delta\sigma_{f,h}$
Axial loading test						
Shimokawa (1985)	1	30	1.43	3.0	72	103
Anami (2000)	1	16	1.22	3.0	98	120
Huo (2005)	1	8	1.23	3.0	113	138
Park (2008)	1	20	1.22	3.0	88	108
Wang (2009)	1	8	1.23	3.2	104	127
Maddox (2011)	1	30	1.20	3.0	68	82
Araki (2012)	1	12	1.34	3.0	84	113
Mori (2012)	1	12	1.32	3.8	91	120
Kim (2013)	1	10	1.37	3.6	99	136
Bending test						
Sakano (1994)	1	25	1.60	3.0	112	180
	2	75	1.15	3.0	80	91
Sakano (2004)	1	75	1.14	3.0	82	94
Araki (2012)	1	12	1.25	3.1	136	169
Kim (2013)	1	14	1.37	3.0	129	177
Sakino (2015)	1	15	1.30	2.8	120	156

t_1: thicknesses of main plates, $\Delta\sigma_f$, $\Delta\sigma_{f,h}$: fatigue strength corresponding to nominal and hot spot stresses

Table A-7 Fatigue strength of component joints with cracks at type B hot spots

Reference	Series	t_1 [mm]	SCF	m	Fatigue strength [N/mm^2]	
					$\Delta\sigma_f$	$\Delta\sigma_{f,h}$
In-plane gusset						
Yamada (1984)	G5	10	1.64	3.0	105	173
	G1	10	1.92	3.0	99	190
	G2	10	2.27	3.0	97	220
Kondo (2002)	GS	10	1.80	3.0	124	223
	GL	10	1.88	3.0	113	213
	GLL	9	2.26	3.0	95	215
Plate edge to plate surface						
Miki (1993)	Gap 25mm	9	8.7	3.0	25	215
	Gap 30mm	9	9.7	3.0	23	224
	Gap 35mm	9	9.3	3.0	29	267
	Gap 40mm	9	7.7	3.0	24	188
Fricke (2006)	A	12	1.5	3.0	125	188

t_1: thicknesses of main plates, $\Delta\sigma_f$, $\Delta\sigma_{f,h}$: fatigue strength corresponding to nominal and hot spot stresses

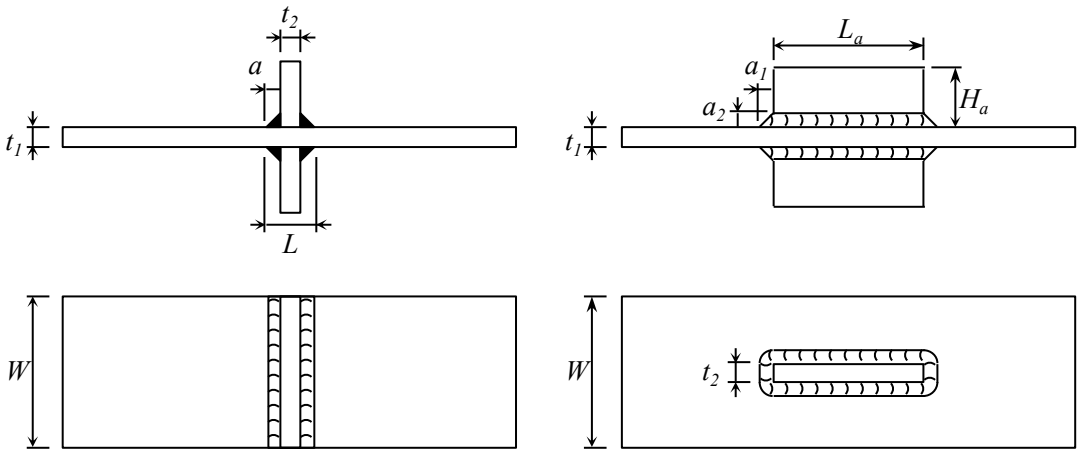

(a) Cruciform joints (b) Out-of-plane gusset joints

Fig. A-1 Basic component specimens

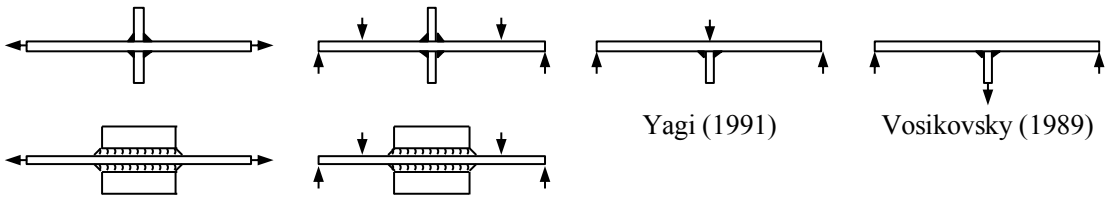

(a) Axial (b) 4-point bending (c) 3-point bending (d) 3-point bending

Fig. A-2 Loadings on cruciform, T and out-of-plane gusset joints

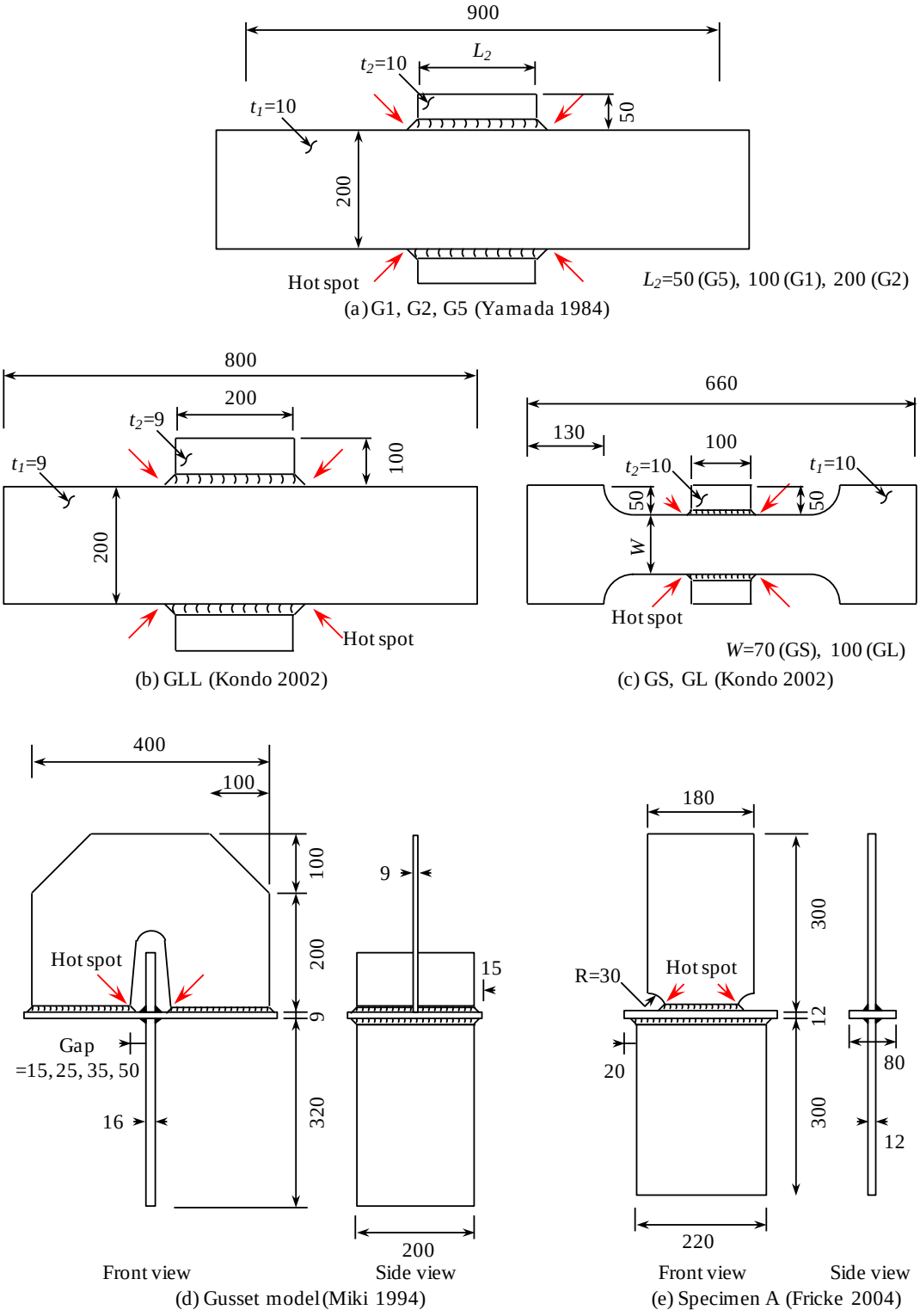

(a) G1, G2, G5 (Yamada 1984)

(b) GLL (Kondo 2002)

(c) GS, GL (Kondo 2002)

(d) Gusset model (Miki 1994)

(e) Specimen A (Fricke 2004)

Fig. A-3 Component models for fatigue cracks from type B hot spots

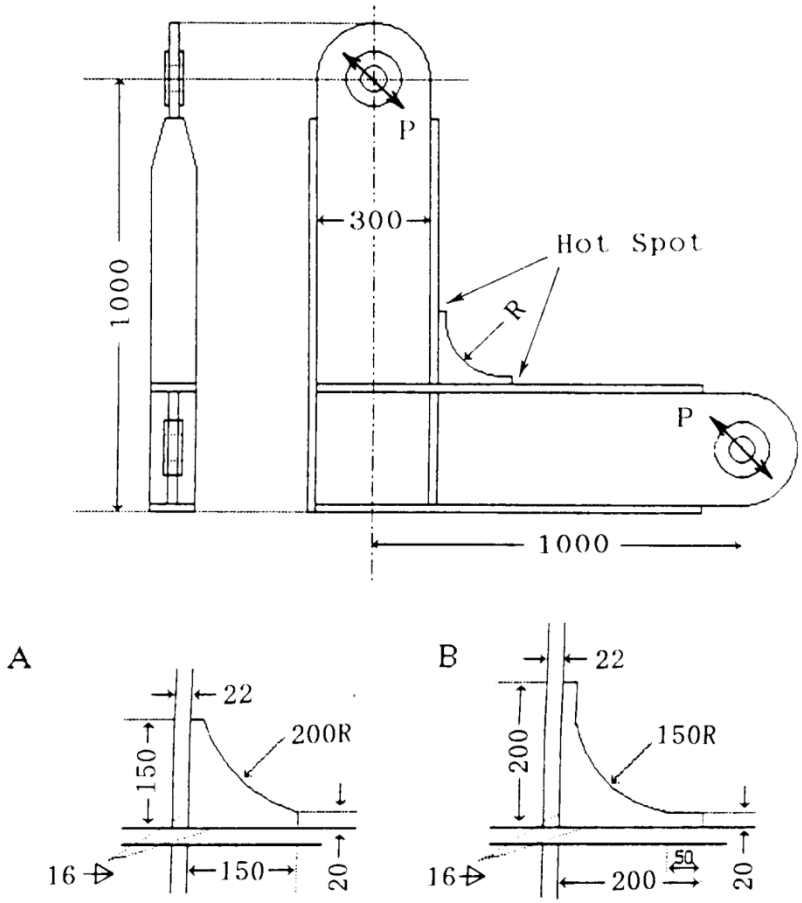

Fig. A-4 Structural model (Yagi, 1991)

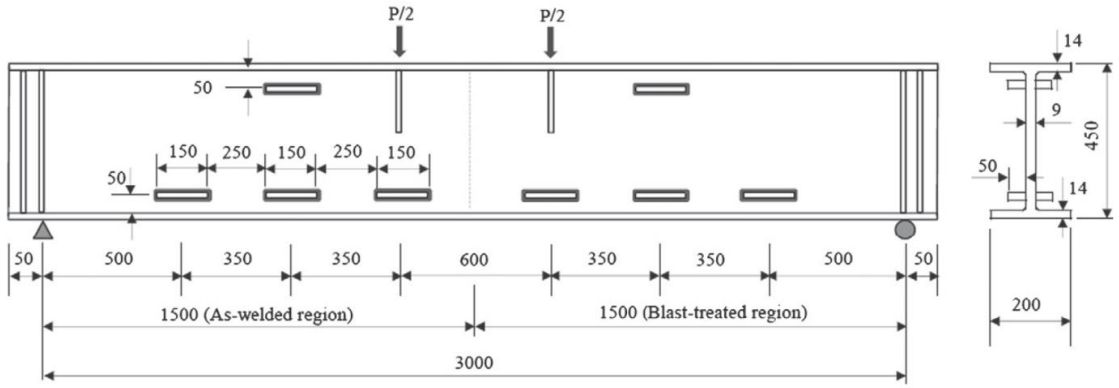

Fig. A-5 Structural model (Kim, 2013)

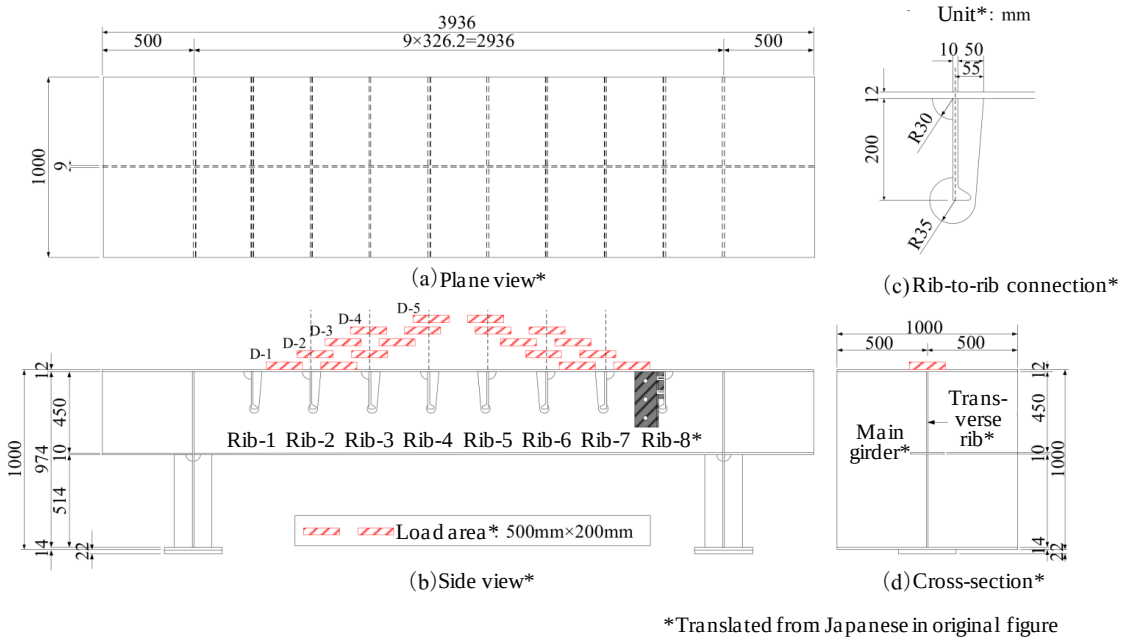

*Translated from Japanese in original figure

Fig. A-6 Structural model (Yamaoka, 2010)

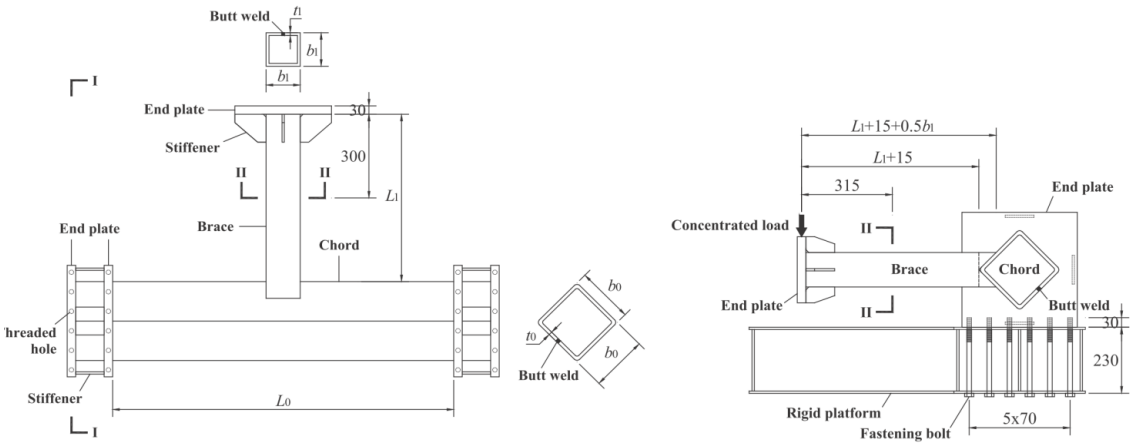

Fig. A-7 Structural model (Cheng, 2015)

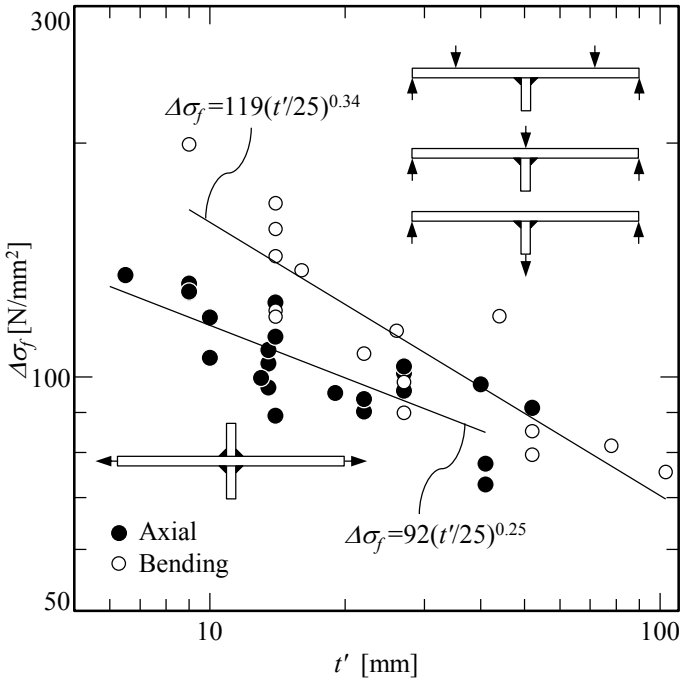

(a) Nominal stress approach

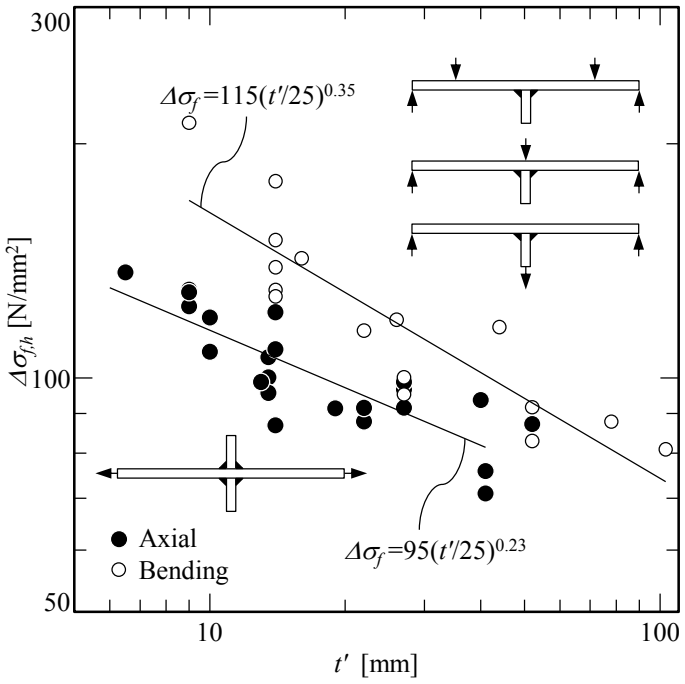

(b) Hot spot stress approach

Fig. A-8 Relationships between thicknesses and fatigue strength of cruciform and T joints

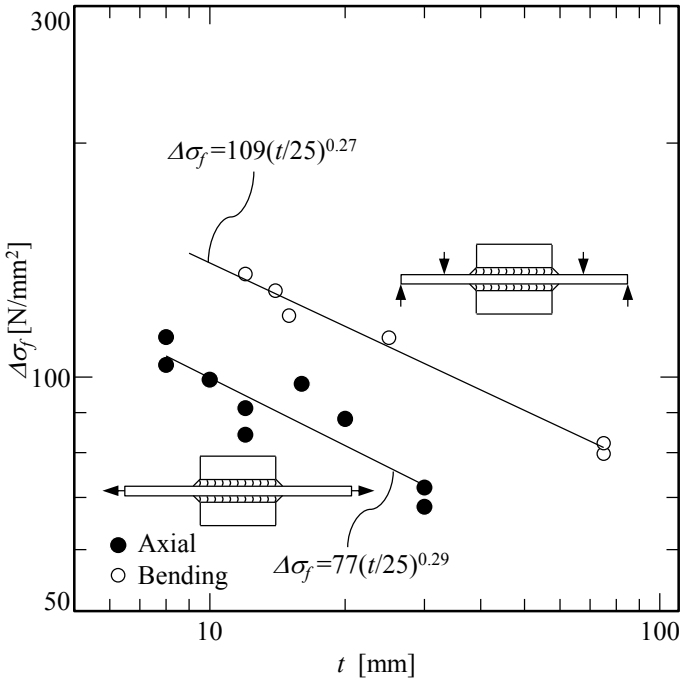

(a) Nominal stress approach

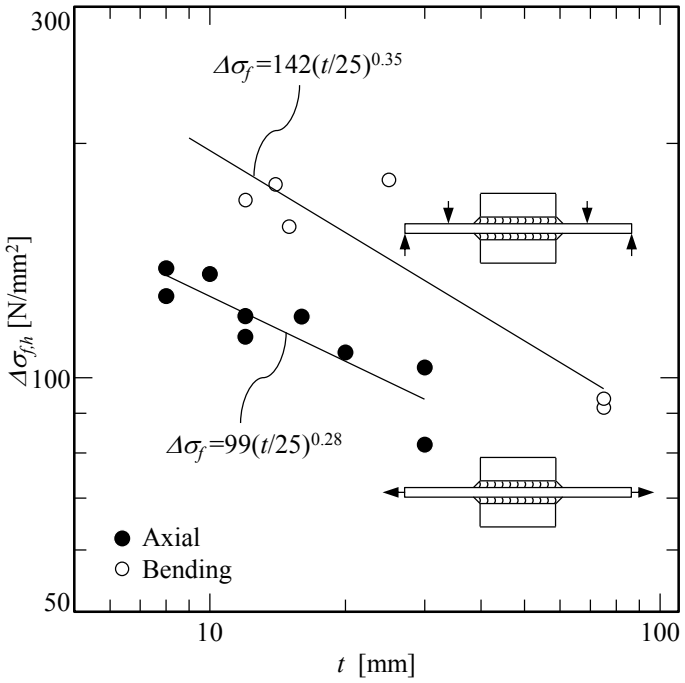

(b) Hot spot stress approach

Fig. A-9 Relationships between thicknesses and fatigue strength of out-of-plane gusset joint

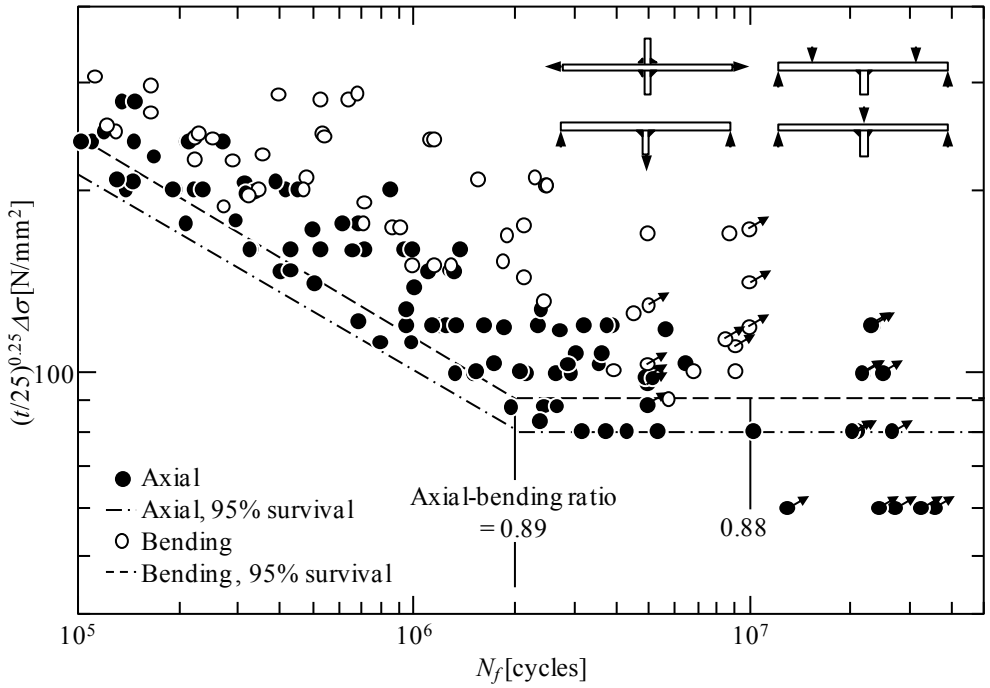

(a) Nominal stress approach

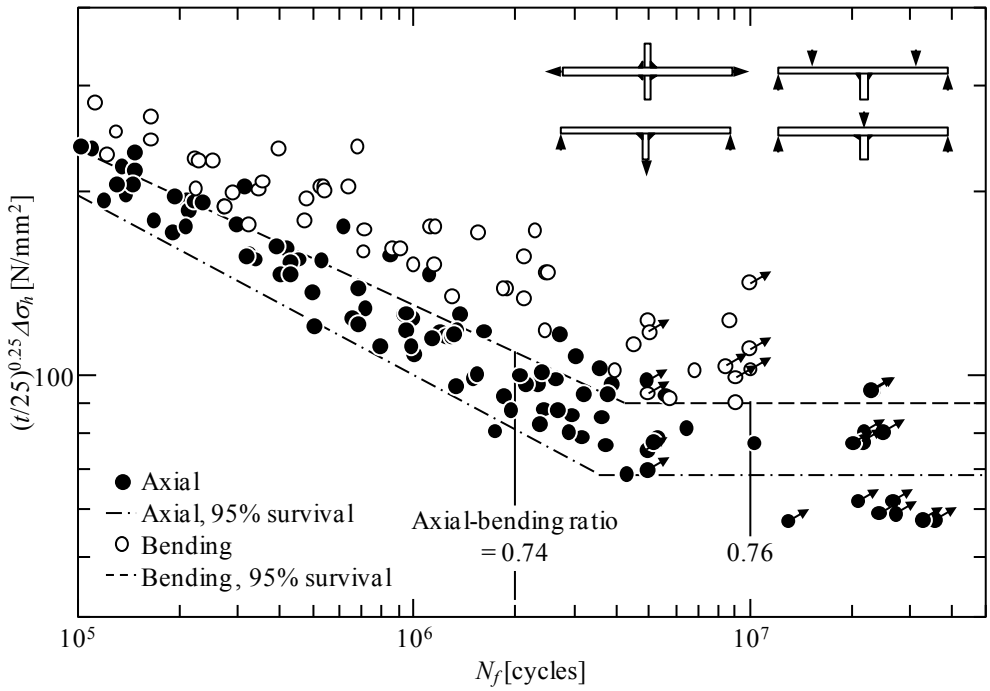

(b) Hot spot stress approach

Fig. A-10 Comparison between axially- and bending-loaded cruciform joints (T joints)

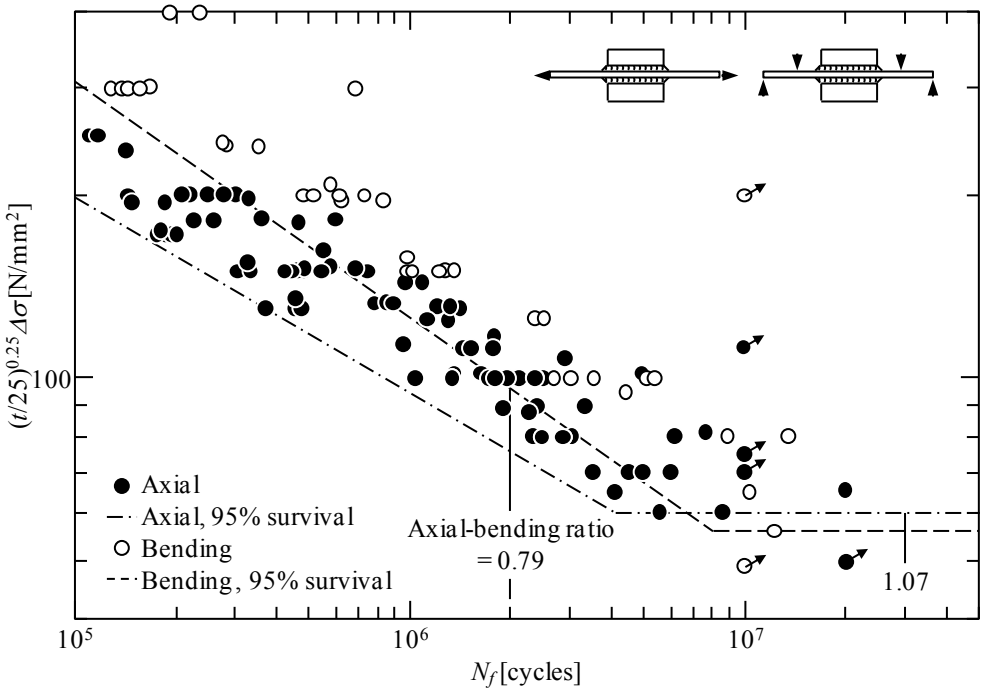

(a) Nominal stress approach

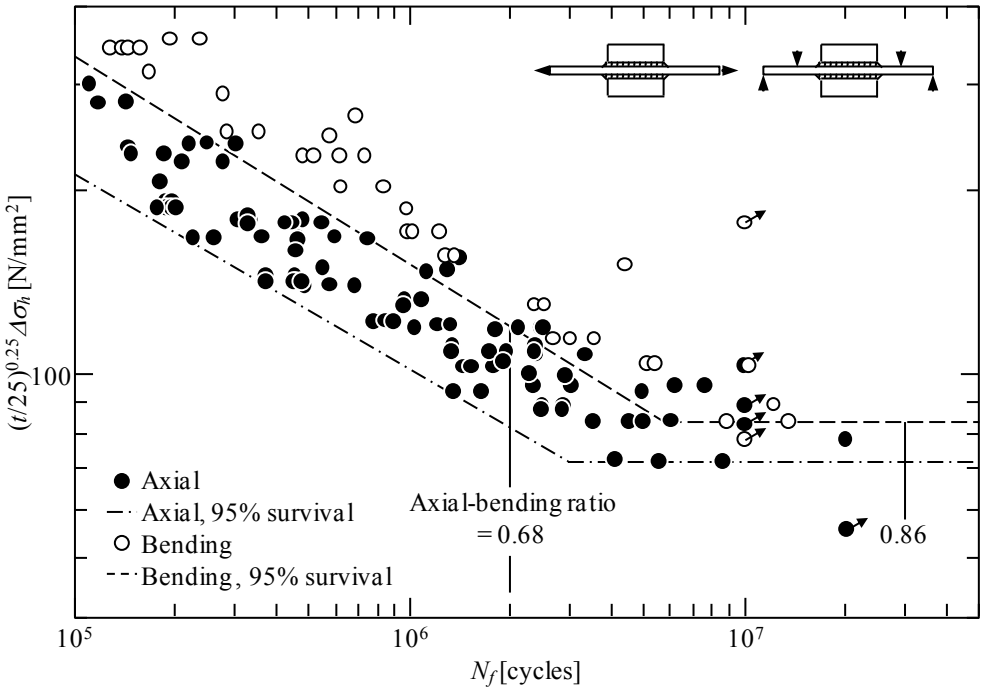

(b) Hot spot stress approach

Fig. A-11 Comparison between axially- and bending-loaded out-of-plane gusset joints

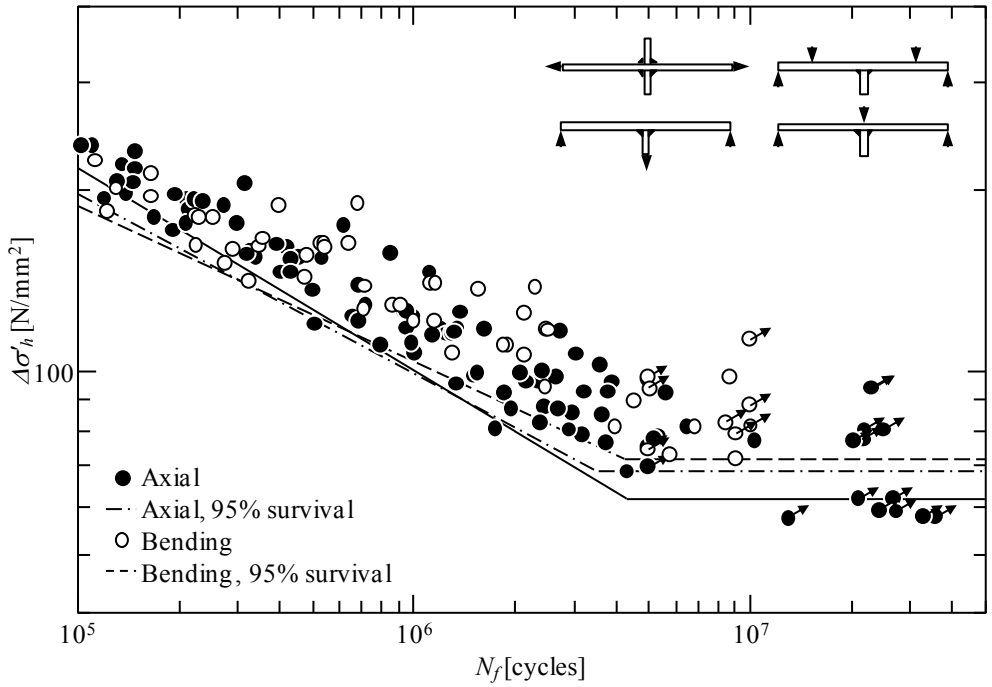

Fig. A-12 Fatigue strength in terms of factored hot spot stress – cruciform and T joints

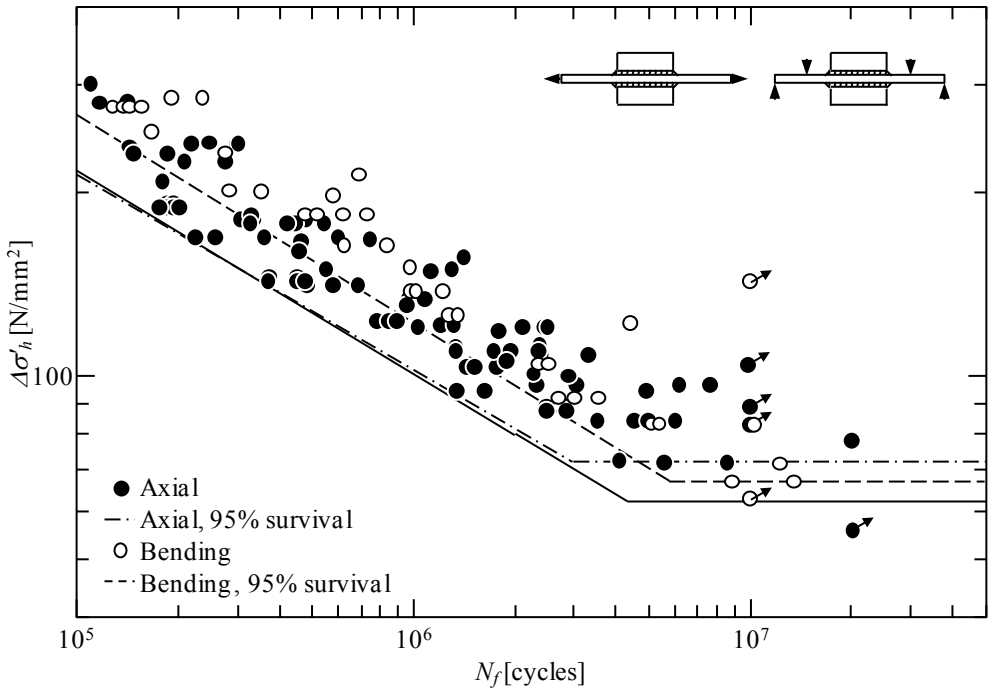

Fig. A-13 Fatigue strength in terms of factored hot spot stress – out-of-plane gusset joints

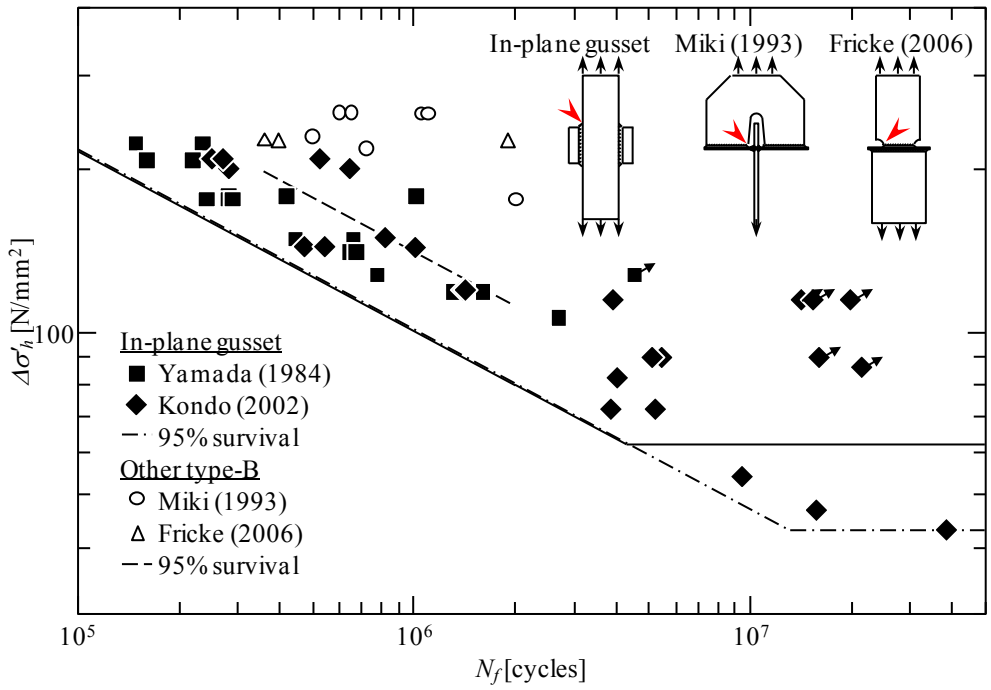

Fig. A-14 Fatigue strength in terms of factored hot spot stress – component joints with cracks at type B hot spots

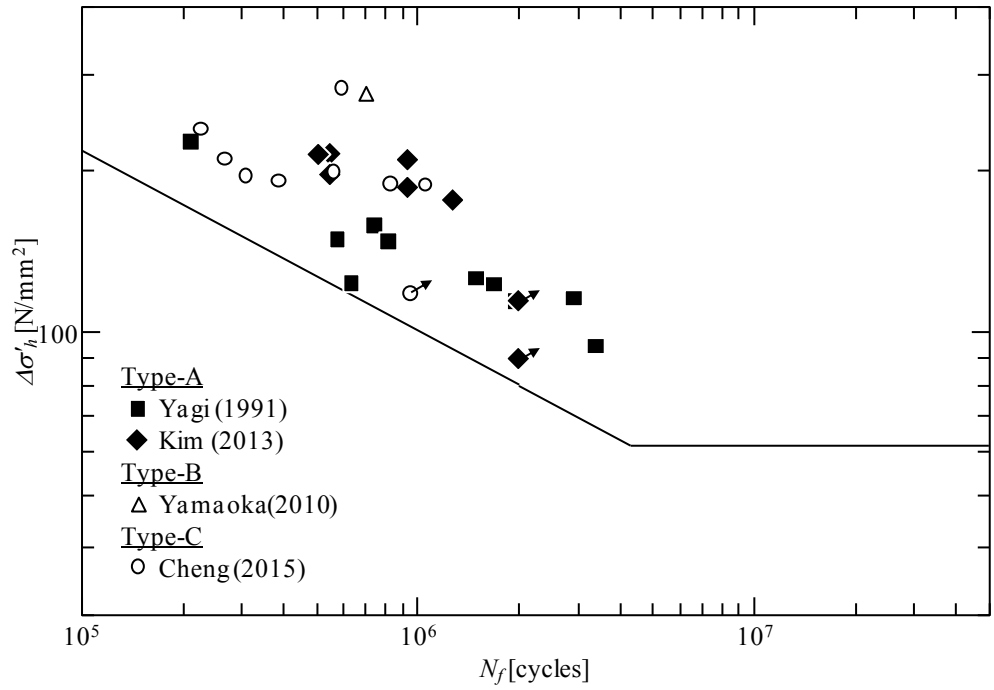

Fig. A-15 Fatigue strength in terms of factored hot spot stress – Structural models

Appendix-B Deck panel model experiment records

B.1. Order of loading in deck panel model experiments

Table B-1‑B-4 shows all loading records of deck panel model experiments. Loading positions are shown in Fig. B-1–B-4. Though it is not displayed in the tables, all constant amplitude fatigue tests and running wheel tests include static loading before and after fatigue loading with the same loading position and the same maximum loads as the fatigue tests.

Since order of loading can affect residual stress conditions and fatigue test results, all loading histories should be considered. Welding residual stresses around welded joints can redistribute when local yielding of areas around the welded joints occur by loading. Therefore relations between load and measured strain can change depending on previous loading histories.

B.1. Fatigue crack locations

Fig. B-5–B-8 shows all fatigue crack locations including the cracks which were not used in Chapter 4, such as the cracks of rib-to-deck joints underneath the loading positions. The loading positions and cycles, which caused the cracks, were summarized in Table B-1‑B-4. “Crack detection” in the tables means visual detection of the cracks. Cracks initiated at rib-to-deck joints of model U were root cracks and could not be detected visually. Cracks initiated at rib-to-deck joints of model V were detected visually. Cracks at VW-35 and VW-45 were initiated from weld root but propagated to deck plate surface. Crack at VW-46 were detected on weld bead surfaces as shown in Fig. B-9.

Table B-1 Test conditions and results of model U

Load case	Test type	Load [kN] Min.	Max.	Range	Freq.	Cycle [×10^6]	Status[a]
UWa	Static	0	50	50	-	-	
UWb	Static	0	100	100	-	-	
UNa	Static	0	100	100	-	-	
UNc	Static	0	100	100	-	-	
USc	Static	0	100	100	-	-	
USd	Static	0	100	100	-	-	
USb	Static	0	100	100	-	-	
USa	Static	0	100	100	-	-	
UNb	Static	0	100	100	-	-	
UNd	Static	0	100	100	-	-	
USe	Static	0	100	100	-	-	
USa	Cyclic	5	105	100	2.6 Hz	0.70	Failure at US-22
						0.70	Crack detection at US-32
						1.48	Failure at US-32
						3.00	Fatigue test stop
UWa	Cyclic	5	80	75	2.5 Hz	0.20	15 % strain drop at UW-35
						0.35	15 % strain drop at UW-45
						3.00	Fatigue test stop
UNa	Cyclic	5	105	100	2.7 Hz	4.62	Fatigue test stop

[a] crack detection means visual detection, fatigue failure definition are explained in section 4.4.1,

Table B-2 Test conditions and results of model V

Load case	Test type	Load [kN] Min.	Max.	Range	Freq.	Cycle [×10^6]	Status[a]
VNb	Static	0	100	100	-	-	
VNd	Static	0	100	100	-	-	
VNc	Static	0	100	100	-	-	
VNa	Static	0	120	120	-	-	
VWa	Static	0	75	75	-	-	
VWa	Cyclic	5	80	75	5.1 Hz	2.25	15 % strain drop at VW-35'
						5.50	Fatigue test stop
VNa	Cyclic	5	125	120	3.5 Hz	5.00	Fatigue test stop
VNa	Cyclic	5	250	245	2.8 Hz	3.00	Failure at VN-32, 32'[c]
						3.00	Crack detection at VW-46
VNra	Running	0	198	198	5.5 rpm[b]	0.30	Crack detection at VW-35, 45[d]
						1.01	Fatigue test stop
VNrb	Running	0	198	198	5.4 rpm[b]	0.34	Fatigue test stop

[a] crack detection means visual detection, fatigue failure definition are explained in section 4.4.1,
[b] rpm means revolution per minute, or round trip per minute,
[c] though the cracks were detected after 0.05 million cycles of the wheel running fatigue test, the cracks were considered to be caused by load VNa,
[d] fatigue cracks initiated from weld root of rib-to-deck joints were penetrated the deck plate and detected as surface cracks on the deck plate

Table B-3 Test conditions and results of model P

Load case	Test type	Load [kN] Min.	Max.	Range	Freq.	Cycle [×10^6]	Status[a]
PSa	Static	0	100	100	-	-	In-elastic strain at PS-43, 43', 53, 53'
PSc	Static	0	100	100	-	-	In-elastic strain at PS-33, 34'
PSd	Static	0	100	100	-	-	
PSe	Static	0	100	100	-	-	
PSf	Static	0	100	100	-	-	
PSb	Static	0	100	100	-	-	
PNb	Static	0	100	100	-	-	
PNc	Static	0	100	100	-	-	
PNd	Static	0	100	100	-	-	
PNe	Static	0	100	100	-	-	
PSf	Static	0	100	100	-	-	
PSa	Cyclic	5	200	195	3.6 Hz	0.35	Crack detection at PW-25
PNb	Cyclic	5	200	195	3.0 Hz	0.25	Crack detection at PW-36 and PW-36*
						0.25	Repairing of PW-36 and PW-36*
						5.35	Fatigue test stop
PSa	Cyclic	10	300	290	3.0 Hz	1.25	Failure at PS-14
						1.48	Crack detection at PS-23
						2.33	Failure at PS-23
						3.48	Failure at PS-24
						5.30	Fatigue test stop
PNa	Static	0	210	205	3.0 Hz		In-elastic strain at PN-42, 42'
PNa	Cyclic	5	210	205	3.0 Hz	0.35	Crack detection at PW-46 and PW-46*
						0.35	Repairing of PW-46 and PW-46*
						5.40	Fatigue test stop
PNa	Cyclic	5	415	410	1.6 Hz	1.04	Fatigue test stop

[a] crack detection means visual detection, fatigue failure definition are explained in section 4.4.1,

Table B-4 Test conditions and results of model PL

Load case	Test type	Load [kN] Min.	Max.	Range	Freq.	Cycle [×10^6]	Status[a]
PLr	Running	0	198	198	3.6 rpm[b]	2.00	Fatigue test stop
PLa	Static	0	856	856			In-elastic strain at PL-32, 32'
PLa	Cyclic	10	856	846	1.0 Hz	0.41	Failure at PL-31
						0.49	Fatigue test stop
PLb	Static	0	633	633			In-elastic strain at PL-42, 42'
PLb	Cyclic	10	633	623	1.2 Hz	0.37	Stop hole drilling for crack at PL-31
						0.67	Crack detection at PL-41 and PL-41'
						0.86	Failure at PL-41
						0.86	Fatigue test stop

[a] crack detection means visual detection, fatigue failure definition are explained in section 4.4.1,
[b] rpm means revolution per minute, or round trip per minute,

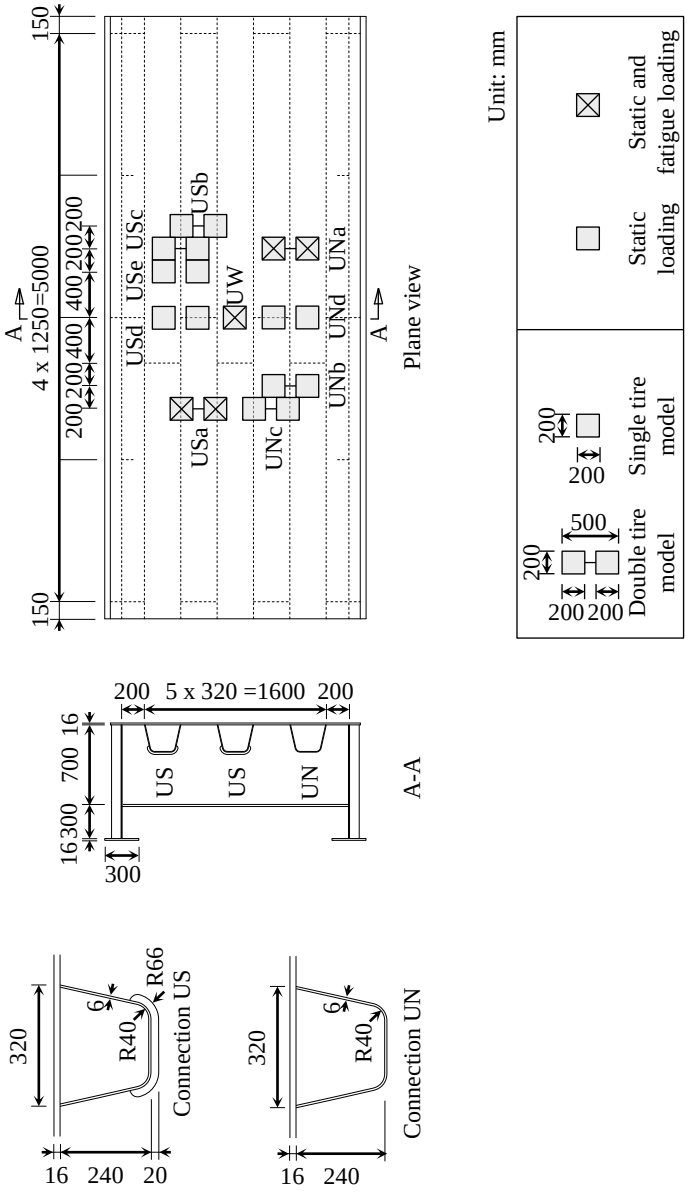

Fig. B-1 Shapes and loading positions of model U

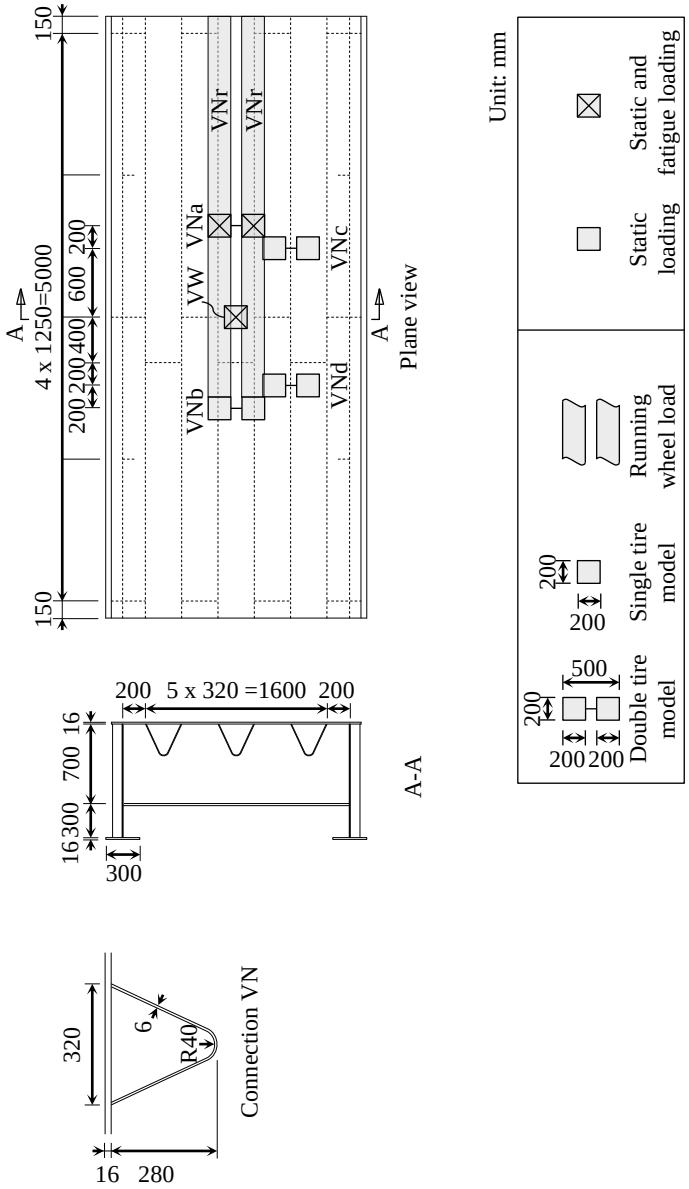

Fig. B-2 Shapes and loading positions of model V

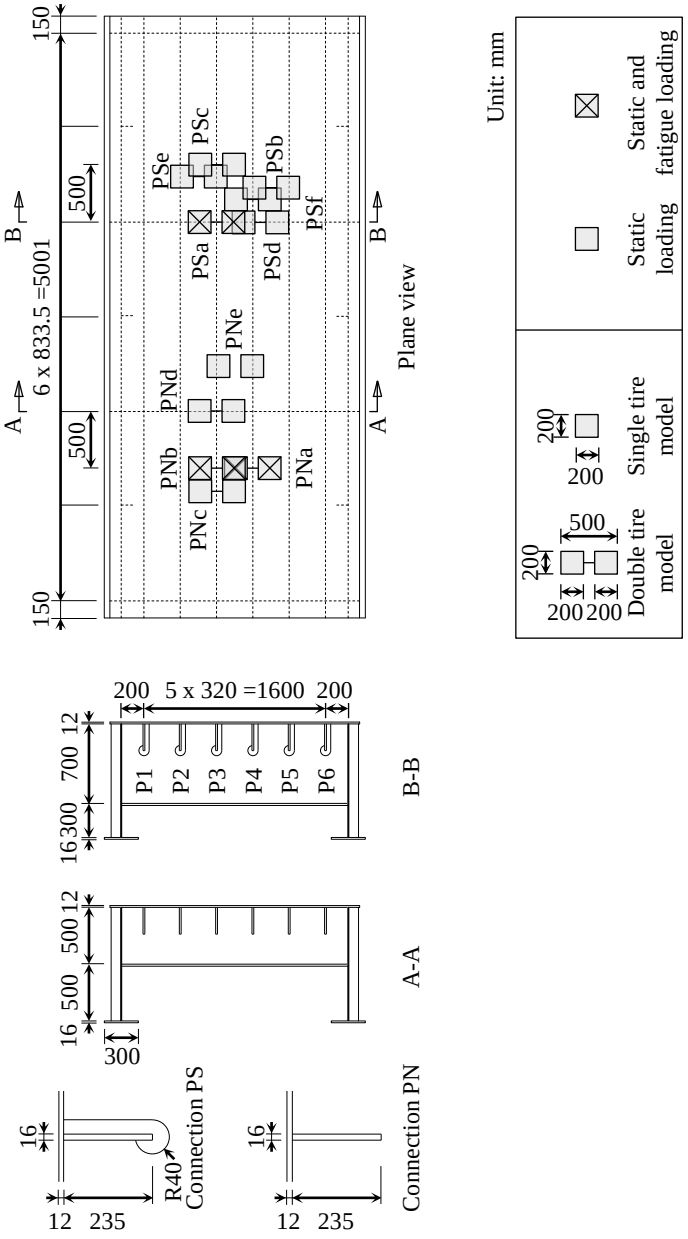

Fig. B-3 Shapes and loading positions of model P

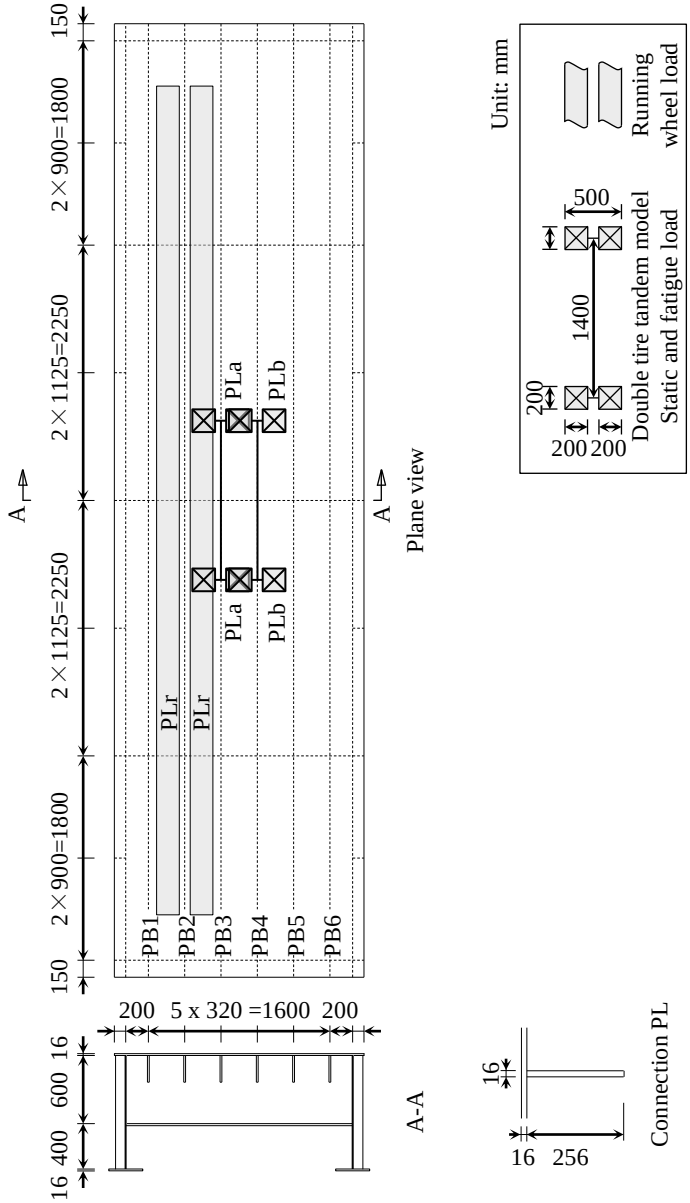

Fig. B-4 Shapes and loading positions of model PL

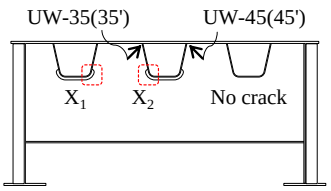

(a) Center transverse-rib cross section of model U

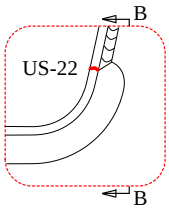

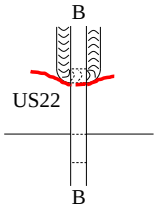

(b) Enlarged view of X_1

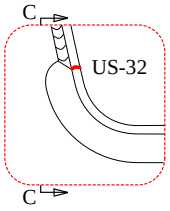

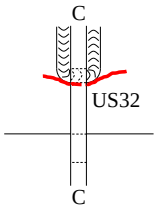

(c) Enlarged view of X_2

Fig. B-5 Location of racks in model U

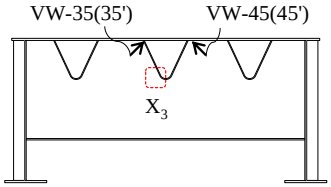

(a) Center transverse-rib cross section of model V

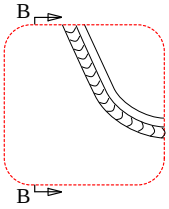

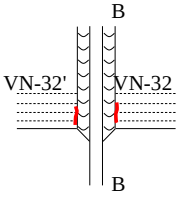

(b) Enlarged view of X_3

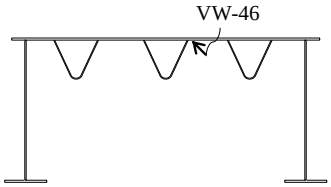

(c) Cross section underneath load VNb of model V

Fig. B-6 Location of racks in model V

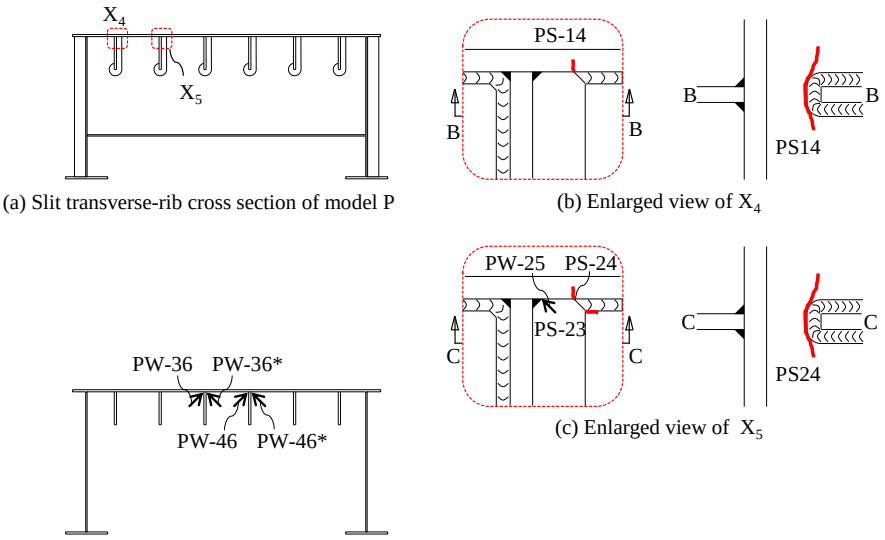

(a) Slit transverse-rib cross section of model P (b) Enlarged view of X_4

(c) Enlarged view of X_5

(d) Cross section underneath load PNa and PNb of model P

Fig. B-7 Location of racks in model P

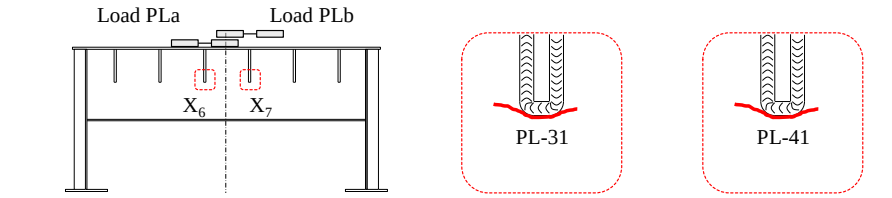

(a) Center transverse-rib cross section of model PL (b) Enlarged view of X_6 (c) Enlarged view of X_7

Fig. B-8 Location of racks in model PL

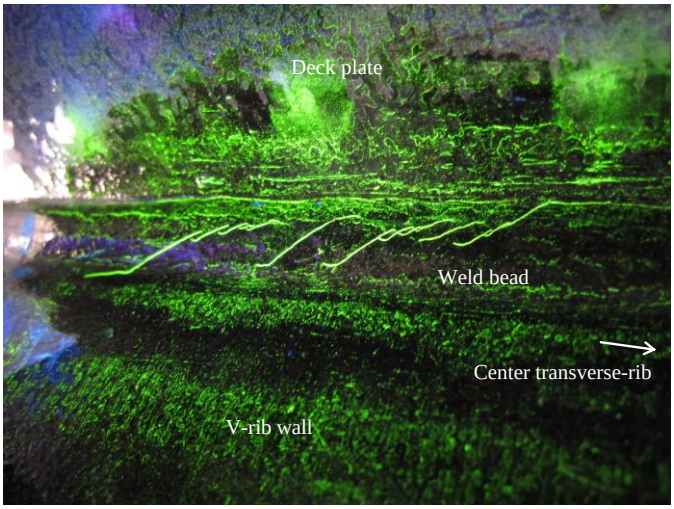

Fig. B-9 Crack at rib-to-deck joints, VW-46, of model V